Non-self-similar Cavity Expansion in Elastoplastic Soils: Theory and Applications

He YANG

Submitted in accordance with the requirements for the degree of

Doctor of Philosophy

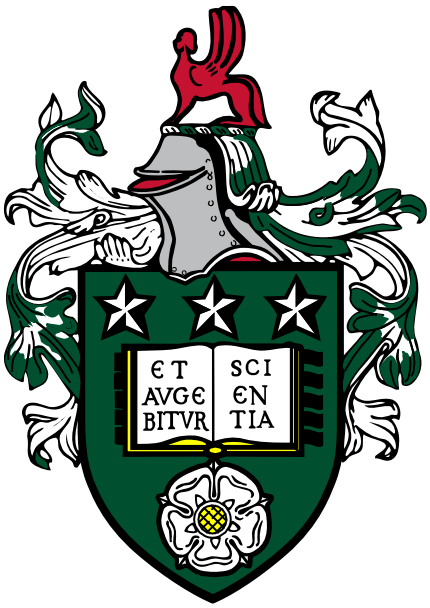

The University of Leeds

School of Civil Engineering

October, 2024

Intellectual Property and Publication Statements

The candidate confirms that the work submitted is his own, except where work which has formed part of jointly authored publications has been included. The contribution of the candidate and the other authors to this work has been explicitly indicated below. The candidate confirms that appropriate credit has been given within the thesis where reference has been made to the work of others.

Publications 1, 2 and 3 have been reproduced based on chapters 2, 3, 4 and 5.

1. **Yang, H.**, Zhuang, P.-Z., Zhang, J.-L., Ma, Y., Yu, H.-S. and Chen, X. 2024. A hybrid Eulerian-Lagrangian approach for non-self-similar expansion analysis of a cylindrical cavity in saturated and unsaturated critical state soils. *Acta Geotechnica*. **19**(5), pp.2361-2380. https://doi.org/10.1007/s11440-023-02189-5. (Chapters 2 and 3).
2. **Yang, H**., Zhuang, P.-Z., Yu, H.-S, Mo, P.-Q., Ma, Y., Chen, X. and Schnaid, F. 2024. Cylindrical cavity expansion analysis under partially drained conditions for normalisation of excess water pressure in CPTU. *Canadian Geotechnical Journal*. (Under review). (Chapters 2 and 4).
3. **Yang, H.**, Chen, X., Mo, P.-Q., Yu, H.-S. and Zhuang, P.-Z. 2024. Transient thermo-elastic solution for radial interaction between energy piles and soils. *Geomechanics for Energy and the Environment*. **39**, article no: 100572 [no pagination]. https://doi.org/10.1016/j.gete.2024.100572. (Chapters 2 and 5).

In the first publication, the candidate carried out the mathematical derivation, methodology, validation, software and data analysis, draft writing, and draft revising. Prof Pei-Zhi Zhuang gave the conceptualisation and draft revising. Mr Jia-Liang Zhang conducted validation of the HEL approach by numerical simulation software. Dr Yue Ma helped to revise the draft. Prof Hai-Sui Yu and Dr Xiaohui Chen provided supervision and comments.

In the second submission, the candidate carried out the mathematical derivation, methodology, validation, software and data analysis, draft writing, and draft revising. Prof Pei-Zhi Zhuang revised the draft and gave useful comments. Dr Pin-Qiang Mo and Dr Yue Ma reviewed the draft and provided some comments, especially for the Introduction Section. Dr Xiaohui Chen and Prof Hai-Sui Yu provided supervision in the whole process and helped review the draft. Prof Fernando Schnaid helped with the draft reviewing and gave comments on the application part.

In the third submission, the candidate carried out the mathematical derivation, methodology, validation, software and data analysis, energy pile-soil interaction analysis, draft writing, and draft revising. Dr Xiaohui Chen contributed to supervision, reviewing the draft, and comments. Dr Pin-Qiang Mo helped review the draft. Prof Hai-Sui Yu provided supervision and comments. Prof Pei-Zhi Zhuang reviewed and revised the draft.

Acknowledgements

The research shown in this thesis was finished at the School of Civil Engineering, University of Leeds during the period from October 2021 to September 2024 with the help of many people from several institutions. It was financially supported by China Scholar Council (CSC)-the University of Leeds Scholarship which is sincerely acknowledged.

First and foremost, I wish to express my profound gratitude to my supervisors, Dr Xiaohui Chen and Prof Hai-Sui Yu, for their invaluable guidance, constant help and generous encouragement throughout this period. I would also like to sincerely thank Prof Pei-Zhi Zhuang at Shandong University, who provided essential guidance, comments, reviewing and revising for this thesis.

I want to appreciate the discussion and comments from Prof Fernando Schnaid at Universidade Federal do Rio Grande do Sul for CPTU, Dr Pin-Qiang Mo at China University of Mining and Technology for CPTU and energy pile-soil interaction. Moreover, it was Dr Yue Ma's suggestions that helped improve the quality of Chapters 3 and 4 in this thesis. I would also like to thank Dr Ren-Rong Li, the former visiting PhD student from Hohai University, for his kind comments on the energy pile-soil interaction.

The help from the members of Geomodelling and AI Centre (GAIC) is also acknowledged. I want to express my special thanks to Dr Kai Wang for teaching me Comsol Multiphysics software. Also, the discussion with Dr Kai Wang, Dr Li-Yang Xu, Dr Shang-Qi Ge and Dr Jiang-Wei Zhang is very important for me to understand the Thermo-Hydro-Mechanical coupling theory. I want to thank Mr Yan-Jie Song, the PhD Candidate at the University of Leeds, for his checking on Chapter 1 and Chapter 2.

I am very thankful to Mr En-Ci Sun, Mr Jia-Liang Zhang and Mr Kang-Xu Wang, the

postgraduate students at Shandong University. Their support for unsaturated soil mechanics and numerical simulations can never be overestimated.

During the past three years, Dr Ashani Ranathunga has also given fruitful suggestions and her contributions to the thesis are vital to enhance the quality of this thesis.

Last but not least, I want to sincerely thank the endless support and continuous love from my family members: my grandfather, my late grandmother, my parents and my brother. I cannot imagine how I can face these challenging years without them.

Abstract

Cavity expansion theory (CET) is a simplified theoretical method in geomechanics and has been widely applied to many geotechnical problems. Traditional CET are mainly concentrated on self-similar cavity expansion problems, in which all material points follow the same stress/deformation paths. However, non-self-similar CET is developed much more slowly due to limitations of traditional methods, especially when constitutive models are complex and multi-fields are taken into consideration. In this thesis, three three non-self-similar cavity expansion problems are investigated by developing novel solution methods, where the non-self-similarity is induced by finite cylinder thickness, hydro-mechanical coupling and thermo-mechanical coupling, respectively. The main work of the thesis is briefly summarised as follows.

A hybrid Eulerian-Lagrangian (HEL) approach is proposed and applied to analyse the non-self-similar expansion process of a hollow cylinder with critical state models, considering arbitrary saturation states of soils under both drained and undrained conditions. A closed-form solution for the stresses and displacements in the elastic zone is presented, taking the state-dependent soil moduli and outer boundary effect of the soil cylinder into account. Adopting large strain theory in the plastic zone, the non-self-similar cavity expansion process is formulated into a set of partial differential equations (PDEs) in terms of both Eulerian and Lagrangian descriptions, which is solved by a newly proposed algorithm. Then, the expansion process is proven to be non-self-similar by showing the stress and deformation paths, and the finite thickness of soil cylinders may greatly influence the cavity expansion behaviour, especially with a small thickness ratio. Finally, an example application of the new solution shows that the boundary effect in pressuremeter tests can be generally captured by the cavity expansion solution in bounded soils.

A hydro-mechanical coupled solution is proposed for cylindrical cavity expansion under

partially drained conditions. The mechanical behaviour of soils is modelled by the perfectly elastoplastic model with the Tresca yield criterion and water flow within porous soils is assumed to obey Darcy's law. Two PDEs are established in the elastic and plastic zones, respectively, transforming the cavity expansion analysis under partially drained conditions into a typical Stefan problem with moving boundary conditions. Then an approximate solution for the PDEs is derived by the variable transformation method. Based on the new solution, a novel normalised penetration rate is defined considering the rigidity index of soils, with which a unique backbone curve for CPTU is found. Finally, the backbone curve is compared with a database consisting of 109 in-situ experimental tests, 101 centrifuge modelling tests, and numerical simulation results.

Considering the thermo-mechanical coupling, a cavity expansion solution is developed to investigate the radial interaction between energy piles and soils (RIEPS). Firstly, transient temperature distributions are shown by assuming heat conduction in the radial direction and constant temperature at the pile-soil interface. Then the temperature distributions are applied to soils to obtain an analytical solution for thermo-elastic stresses and displacements. It is found that the solution under the combined thermal-mechanical loading pattern is the linear superposition of those under the purely thermal loading and mechanical loading. Hence, the stresses, strains and displacements in soils are determined by the competitive relationships between thermal loading and mechanical loading. Finally, the expression for radial stress change at the pile-soil interface is revisited by the cavity expansion analysis and comparison with field data. This expression could be quite general for typical soil and pile parameters considering transient temperature distributions and soil/pile moduli.

Keywords: cavity expansion; non-self-similar; finite soil thickness; hydro-mechanical coupling; thermo-mechanical coupling; piezocone penetration test; CPTU; energy pile; energy pile-soil interaction

Table of Contents

List of Tables

List of Figures

Abbreviations

Abbreviations	Full names
CASM	clay and sand model
CET	cavity expansion theory
CM6	Comsol Multiphysics 6.0
CPT	cone penetration test
CPTU	piezocone penetration test
CSL	critical state line
DP	Drucker-Prager model
EWP	excess water pressure
FEM	finite element method
HEL	hybrid Eulerian-Lagrangian
LC	loading collapse
MCC	modified Cam Clay model
MUMPS	Multifrontal Massively Parallel Sparse Direct Solver
NCL	normally consolidated line
OCC	original Cam Clay model
ODE	ordinary differential equation
PDE	partial differential equation
RIEPS	radial interaction between energy pile and soil
SBP	self-boring pressuremeter test
SL	swelling line
SWRC	soil water retention curve
SWCC	soil water characteristic curve
UCSM	unsaturated critical state model

List of Notations

a_0, a	initial and current radii of the inner cavity wall
$\tilde{a}$	normalised inner radius at the inner cavity wall
a_{end}	final inner radius at the end of the cavity expansion process
A_a	integral constant that should be determined by the boundary condition at the inner cavity wall
A_e	integral constant for excess water pressure
A_{ii}	derivative of the yield function with respect to the effective stress σ'_{ii} $(ii = r, \theta, z)$
A_s	derivative of the yield function with respect to the suction
A_v	derivative of the yield function with respect to the specific volume
b_0, b	initial and current radii of the outer cavity wall
B_{ii}	derivative of the plastic potential with respect to the effective stress σ'_{ii} $(ii = r, \theta, z)$
c_{h}, c_{v}	horizontal and vertical coefficients of consolidation
c_{he}, c_{hp}	elastic and plastic coefficients of consolidation
c_{ht}	thermal diffusivity of soil
C_ρ	integration constant and is the function of the elastoplastic boundary
$\text{d}(\bullet)$	spatial differential of $(\bullet)$ for a given time
$\text{D}(\bullet)$	material time differential of $(\bullet)$ for a given material point
D	piezocone diameter
E	elastic modulus of the soil
E_{pile}	elastic modulus of energy pile

E_0	constant elastic modulus
E_1	exponential integral
f	yield function
g	plastic potential
G	shear modulus of soils
k	permeability coefficient of soils
$\mathbf{K}$	stiffness matric
K_{p}	plastic modulus
(i)	node number
I_{r}	rigidity index of soils
(j)	load step number
$J_0(r),\ J_1(r)$	the first kind of Bessel functions of zero and first orders
m	maximum node numbers
$\bar{m}$	curve fitting parameter for backbone curve
M	critical state parameter of Cam Clay models; slope of the CSL in the v-$\ln p'$ plane.
n^*	material constant of the CASM
$r_0,\ r$	initial and current positions of a material point in the cylindrical coordinate
$\tilde{r}$	normalised radial position of a material point
$r_{(i)}^{(0)}$	initial radius of the i-th node
r^*	material constant of the CASM
R_0	initial overconsolidation ratio
p'	mean effective stress, one of the stress invariants
p'_0	initial mean effective stress
p'_ρ	mean effective stress at the elastoplastic boundary

p_{net0}	initial mean net stress
$p'_c(s)$	isotropic consolidation pressure at the suction of *s*
$p'_c(0)$	isotropic consolidation pressure at the suction of 0
$p'_{c0}(s)$	initial isotropic consolidation pressure at the suction of *s*
q	deviatoric stress, one of the stress invariants
q_0	initial deviatoric stress
q_ρ	deviatoric stress at the elastoplastic boundary
s	suction
s_u	shear strength of soils
t	time and t=0 at the in-situ stress state
T	soil temperature
T_a	soil temperature at the energy pile-soil interface
S_{r0}, S_r	initial and current degrees of saturation
u	radial displacement of a material point
u_a	pore air pressure
u_w	pore water pressure
u_{w0}	initial pore water pressure
U	excess water pressure
$U_0(r)$, $U_1(r)$	composite Bessel functions of zero and first order
U_ρ	excess water pressure at the elastoplastic boundary
U_{ref}, $\bar{U}$	reference and normalised excess water pressures
v_0, v	initial and current specific volumes of soils
V_a, V_{cptu}	rates of cavity expansion and penetration
$\bar{V}_0$, $\bar{V}$	normalised penetration rates with and without modifications

$\mathbf{x}_{(i)}^{(j)}$	information vector for the *i*-th node in the *j*-th load step
$Y_0(r),\ Y_1(r)$	the second kind of Bessel functions of zero and first orders
z	vertical direction in the cylindrical coordinate
α	thermal expansion coefficient of soils
α_{pile}	thermal expansion coefficient of energy pile
α, β	material constants for unsaturated soils
β_n	*n*-th root of a composite Bessel function
Λ	scalar multiplier for plasticity
δ	constant controlling cavity expansion rate
δ_{ij}	Kronecker's delta
Δ	changes of stresses, displacement or temperature regarding the initial state
$\varepsilon_r,\ \varepsilon_\theta,\ \varepsilon_z$	radial, circumferential, and vertical strains
$\varepsilon_r^{\text{e}},\ \varepsilon_\theta^{\text{e}},\ \varepsilon_z^{\text{e}}$	elastic radial, circumferential, and vertical strains
$\varepsilon_r^{\text{p}},\ \varepsilon_\theta^{\text{p}},\ \varepsilon_z^{\text{p}}$	plastic radial, circumferential, and vertical strains
ε_v	total volumetric strain
$\varepsilon_v^{\text{e}},\ \varepsilon_v^{\text{p}}$	elastic and plastic volumetric strains
ε_q	deviatoric strain
$\varepsilon_q^{\text{e}},\ \varepsilon_q^{\text{p}}$	elastic and plastic deviatoric strains
η	stress ratio, the ratio of deviatoric stress to mean effective stress
φ_{cs}	friction angle of soil at the critical state
γ_{w}	specific gravity of water
Γ	critical state parameter of Cam Clay models; critical specific volume at p'=1kPa

κ	critical state parameter of Cam Clay models; slope of the swelling line
ξ_0	initial state parameter
$\lambda(s)$	slope of the CSL in the $v-\ln p'$ plane for unsaturated soils
$\lambda(0)$	slope of the CSL in the $v-\ln p'$ plane for saturated soils
μ	Poisson's ratio of soils
μ_{pile}	Poisson's ratio of energy pile
ω	soil parameter dependent on Poisson's ratio and rigidity index
ρ, ρ_0	current radius of the elastoplastic boundary and its initial value
$\tilde{\rho}$, $\tilde{\rho}_0$	normalised radius of the elastoplastic boundary and its initial value
σ_{ij}, σ'_{ij}, $\bar{\sigma}_{ij}$	total stress tensor, effective stress tensor, and net stress tensor
σ_a	total radial stress at the inner wall of the cylinder
σ'_{h}	radial effective stress at the outer boundary of the cylinder
σ_{h0}	initial (in-situ) horizontal total stress
σ'_{h0}	initial (in-situ) horizontal effective stress
σ_{n}	radial contact stress at the energy pile-soil interface
σ_r, σ_θ, σ_z	total radial, circumferential, and vertical stresses
σ'_r, σ'_θ, σ'_z	radial, circumferential, and vertical effective stresses
$\sigma'_{r\rho}$, $\sigma_{r\rho}$	effective and total radial stress at the elastoplastic boundary
σ_{v0}	initial (in-situ) vertical total stress
σ'_{v0}	initial (in-situ) vertical effective stress
$\sigma'_{\theta\rho}$	effective circumferential stress at the elastoplastic boundary

χ	Bishop's effective stress parameter
θ	circumferential direction in the cylindrical coordinate
ϑ	piezocone tip angle

List of Publications

Main publications related to the thesis

1. **Yang, H.**, Zhuang, P.-Z., Zhang, J.-L., Ma, Y., Yu, H.-S. and Chen, X. 2024. A hybrid Eulerian–Lagrangian approach for non-self-similar expansion analysis of a cylindrical cavity in saturated and unsaturated critical state soils. *Acta Geotechnica*. **19**(5), pp.2361-2380. https://doi.org/10.1007/s11440-023-02189-5.
2. **Yang, H.**, Zhuang, P.-Z., Yu, H.-S., Mo, P.-Q., Ma, Y., Chen, X. and Schnaid, F. 2024. Cylindrical cavity expansion analysis under partially drained conditions for normalisation of excess water pressure in CPTU. *Canadian Geotechnical Journal*. (Under review)
3. **Yang, H.**, Zhuang, P.-Z., Mo, P.-Q., Yu, H.-S. and Chen, X. 2024. Analytical solution for transient radial interaction between energy piles and soils: Thermo-elastic cavity expansion analysis. *Geomechanics for Energy and the Environment*. **39**, article no: 100572 [no pagination]. https://doi.org/10.1016/j.gete.2024.100572.
4. **Yang, H.**, Zhang, J.-L., Yu, H.-S. and Zhuang, P.-Z. 2024. Semi-analytical solution for drained expansion analysis of a hollow cylinder of critical state soils. *Journal of Rock Mechanics and Geotechnical Engineering*. **16**(6), pp.2326-2340. https://doi.org/10.1016/j.jrmge.2023.10.018.

Other publications not related to the thesis

1. **Yang, H**., Yu, H.-S., Chen, X. and Zhuang, P.-Z. 2023. Rigorous solution for drained analysis of spherical cavity expansion in soils of finite radial extent. *Computers and Geotechnics*. **160**, article no: 105516 [no pagination]. https://doi.org/10.1016/j.compgeo.2023.105516.
2. **Yang, H.**, Ren, F., Song, Y.-J., Yu, H.-S. and Chen, X. 2024. Physics-informed neural network solution for thermo-elastic cavity expansion problem. *Geomechanics and Geoengineering*. pp.1-11. https://doi.org/10.1080/17486025.2024.2414849.

3. **Yang, H.**, Chen, S.-L., Wang, X., Zhuang, P.-Z. and Yu, H.-S. 2024. Revisiting undrained cavity expansion in Mohr-Coulomb soils: consideration of limited dilatation. *International Journal for Numerical and Analytical Methods in Geotechnical Engineering*. (Under review).

4. Zhuang, P.-Z., Sun, E.-C., Zhang, J.-L., Yu H.-S. and **Yang H**.*. 2024. CASM-U: A critical state model for unsaturated clay and sand. *Acta Geotechnica*. https://doi.org/10.1007/s11440-024-02462-1.

5. Zhang, J.-L., Sun, E.-C., Zhuang, P.-Z., Yu, H.-S. and **Yang, H**.*. 2024. Elastoplastic solution for cylindrical cavity contraction in unsaturated soils. *Geotechnique Letters*. **14**(1), pp.1-7. https://doi.org/10.1680/jgele.23.00080.

6. Zhuang, P.-Z., Wang, K.-X., Song, X.-G., Geng, X. and **Yang, H.***. 2024. Thermo-mechanical behaviour of energy pile considering nonuniform initial ground temperature. *Proceedings of the Institution of Civil Engineers - Geotechnical Engineering*. https://doi.org/10.1680/jgeen.24.00363.

7. Ma, Y., Ge S.-Q., **Yang H**. and Chen X. 2022. Coupled thermo-hydro-mechanical-chemical processes with reactive dissolution by non-equilibrium thermodynamics. *Journal of the Mechanics and Physics of Solids*. **169**, article no: 105065 [no pagination]. https://doi.org/10.1016/j.jmps.2022.105065.

12. Li, G.-Y., Mo P.-Q., Lu Z., Yuan R., **Yang H**. and Yu H.-S. 2024. Drained Cavity Expansion-Contraction in CASM and Its Application for Pressuremeter Tests in Sands. *Journal of Geotechnical and Geoenvironmental Engineering*. **150**(9), article no: 04024073 [no pagination]. https://doi.org/10.1061/JGGEFK/GTENG-12417.

13. Song, Y.-J., Wang, H., **Yang, H**., Taccari, M.L. and Chen, X. 2024. Loss-Attentional Physics-Informed Neural Networks. *Journal of Computational Physics*. **501**, article no: 112781 [no pagination]. https://doi.org/10.1016/j.jcp.2024.112781.

14. Li, G.-Y., Mo P.-Q., **Yang H.**, Yu H.-S. and Qin Y.-J. 2024. Undrained cavity expansion-contraction analysis in CASM and its application for pressuremeter tests. *Canadian Geotechnical Journal*. https://doi.org/10.1139/cgj-2024-0011.

Chapter 1 Introduction

1.1 Background

Stability and deformation analyses are normally two major concerns when designing and constructing geo-structures on/under soil ground. The stability analysis is necessary to avoid the failure of geo-structures, while the deformation analysis is to avoid large movement of geo-structures and soils ADDIN EN.CITE (. In previous studies, various methods have been available to conduct stability and deformation analyses, which may be roughly categorised into four groups: the empirical method, physical model tests, numerical simulations (e.g. the finite element/difference method and the discrete element method), and the analytical/semi-analytical method. Compared with the former three methods, the last method formulates geotechnical problems into closed-form equations with simplified model geometry, boundary conditions, applied forces/stresses, and/or constitutive behaviour of soils (Gibson, 1974; Vaughan, 1994; Yu, 2000; Potts, 2003; Yu, 2007). Although this kind of theoretical method may be restricted to some specific applications, it can be useful to provide a first estimation of stability and deformation of geo-structure with less time and expense.

Cavity expansion theory (CET) is an important branch of analytical/semi-analytical methods in geomechanics. It is mainly concerned with the stress and displacement fields around an expanding cylindrical/spherical cavity that is embedded in the linear/nonlinear solid media (Yu, 2000). Since the 1960s, the CET have served as a simple but powerful theoretical tool for some problems in geotechnical engineering such as the interpretation of self-boring pressuremeter tests (SBPs) and cone penetration tests (CPTs), and bearing capacity estimation of piles and plate anchors (Gibson and Anderson, 1961; Vesic, 1972; Hughes et al., 1977; Randolph et al., 1994; Yu and Mitchell, 1998; Ghafghazi and Shuttle, 2008; Zhuang and Yu, 2018).

Traditional CET usually focuses on cavity expansion problems in an infinite soil thickness and neglects the influence of hydraulic and thermal fields. Therefore, if all solid material points are initially subjected to the same stress state, they will follow the same stress/deformation paths under monotonic loading, which means that the cavity expansion process is "self-similar" (Hill, 1950; Collins et al., 1992; Yu and Carter, 2002; Chen, S.L. and Abousleiman, Y.N., 2013; Carter and Yu, 2022). A few factors may result in non-self-similar properties during the cavity expansion process (namely, material points at different radial positions do not follow the same stress and deformation paths). For example, to interpret SBPs and CPTs in small-sized calibration chambers (see Figure 1.1), the possible outer boundary effect of the chamber cannot be ignored and it may affect the stress state of a material point (and then cause the non-self-similarity) (Jewell et al., 1980; Fahey, 1986; Sladen, 1989; Schnaid and Houlsby, 1991; Alsiny et al., 1992; Salgado et al., 1998; Zhuang et al., 2021; Song et al., 2022). In the jet grouting process and piezocone penetration tests (CPTU), the generation and dissipation of pressurised fluids are time-dependent and will affect the stress state of the surrounding soil due to the hydro-mechanical coupling (Liu, H. et al., 2017; Wang, Z.-F. et al., 2020), as shown in Figure 1.2. Similarly, the heat exchange between energy piles and soil ground will generate a temperature gradient that will back-affect the bearing capacity of energy piles (Bourne-Webb, P.J. et al., 2009; Bourne-Webb, P.J. et al., 2016; Zhou et al., 2018; Faizal et al., 2022). Although the non-self-similar CET is required for these geotechnical problems, this theory has developed slowly owing to the non-self-similarity. Overall, it can be realised that the CET as well as its applications to geotechnical engineering could be enlarged if it can be extended to non-self-similar problems.

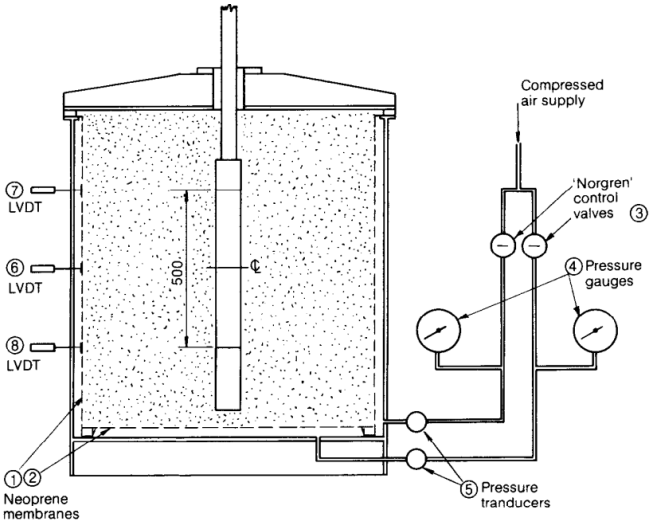

Figure 1.1 Pressuremeter test in small-size calibration chamber (Jewell et al., 1980).

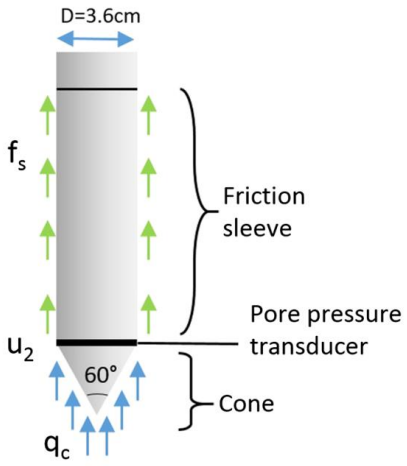

Figure 1.2 Schematic representation of CPTU device (Ceccato et al., 2016).

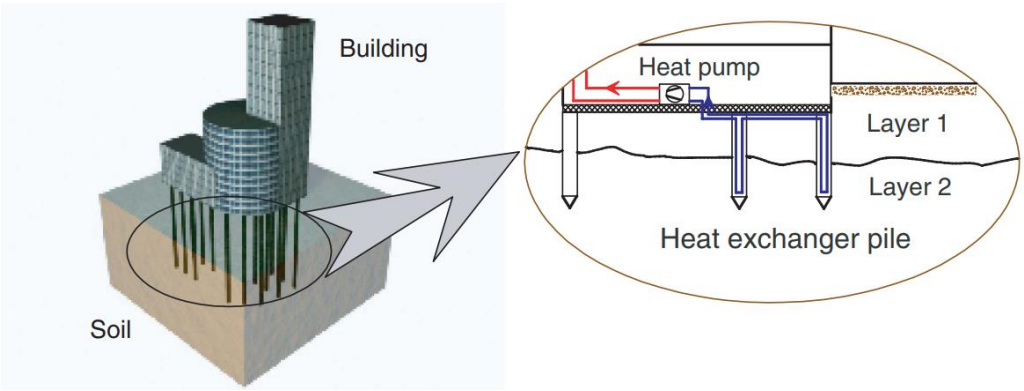

Figure 1.3 Schematic representation of a heat exchanger pile system and pile foundation (Knellwolf et al., 2011).

1.2 Research aims

This thesis aims to investigate the non-self-similar cavity expansion problems in geomechanics from the aspects of theoretical analyses and applications to geotechnical engineering. This overall aim will be achieved by developing different solution methods for solving non-self-similar problems induced by the finite soil thickness around a cavity, hydro-mechanical coupling effect and thermo-mechanical coupling effect. Correspondingly, three applications of the non-self-similar CET will be explored with the aid of the new cavity expansion solutions, including the analyses of SBP in small-size calibration chambers, partially drained effect in CPTU and radial interaction between energy pile and surrounding soil (RIEPS).

1.3 Research objectives

There are four major objectives to achieve the aims of this thesis:

(i) To develop a unified hybrid Eulerian-Lagrangian (HEL) approach for cavity expansion in a finite soil thickness.

(ii) To develop a variable transformation method for cavity expansion in poro-elasto-plastic soil with Tresca failure criterion considering hydro-mechanical coupling.

(iii) To quantify the excess water pressure (EWP) in CPTU consiering the partially drained effect.

(iv) To develop a thermo-elastic solution for cavity expansion under transient temperature fields.

1.4 Thesis structure

This thesis is organised in 6 chapters, and Chapters 3, 4 and 5 are also summarised in Table 1.1.

In Chapter 1 the background, research aims and objectives are introduced.

Chapter 2 consists of an in-depth review of the development of CET and its applications. The literature pays attention to: (i) the currently available solution approaches for CET as well as their limitations; (ii) the development of non-self-similar CET; (iii) the applications of CET in SBP, CPT and CPTU, and energy pile-soil interaction.

Chapter 3 shows a unified HEL approach for non-self-similar cavity expansion problems caused by the finite cylinder thickness, considering various drained/undrained conditions, saturated/unsaturated soil states, and critical state soil models. The HEL approach is firstly introduced, including problem definition and assumptions, establishment of governing equations, and solution algorithms and procedures. Then the HEL approach is validated by comparison with published solutions in special cases and finite element method (FEM). Later the non-self-similar characteristics and boundary effect are highlighted for cavity expansion in completely dry, fully saturated, and unsaturated soils. Finally, the boundary effect during SBP in small-size calibration chambers is captured on the basis of the solution in this chapter.

In Chapter 4 a hydro-mechanical solution is proposed for cavity expansion in poro-elasto-plastic soils with Tresca yield criterion under partially drained conditions. The problem definition and assumptions are defined at first, after which two partial differential equations (PDEs) for the cavity expansion problem are derived with the moving boundary conditions at the elastoplastic boundary. Then an approximate solution for the PDEs is obtained by the variable transformation approach and is validated by comparison with FEM. Based on the solution, a modified normalised penetration rate is defined for normalisation of excess water pressure (EWP) in CPTU under partially drained conditions. Finally, a unique backbone curve is found with the new normalised penetration rate and is proven by comparing with a database of in-situ tests, centrifuge tests and numerical simulation results.

In Chapter 5 a thermo-elastic solution is shown for cavity expansion under transient temperature fields with an application to the radial interaction between energy piles and soils (RIEPS). At first, the research problem is defined and the assumptions are summarised. Then a solution for transient temperature distributions is shown, which is incorporated into the stress-strain relationship to obtain the stress and displacement distributions in the surrounding soil. A parametric study is conducted after solution validation, and the change of radial contact stress at the energy pile-soil interface is quantified.

Chapter 6 is the final chapter that gives the summary of key conclusions and recommendations for future research.

Table 1.1. Summary of Chapters 3, 4 and 5.

Chapter	Chapter 3	Chapter 4	Chapter 5
CET	Finite cylinder thickness	Hydro-mechanical coupling	Thermo-mechanical coupling
Novelty	HEL approach	Stefan problem and variable transformation approach	Analytical transient solution
Application	In-lab SBP	CPTU interpretation	Energy pile-soil interaction

Chapter 2 Literature Review

The literature review for CET is shown in this chapter. Firstly, the development of CET in geotechnical engineering is briefly introduced. Then, two commonly used approaches for self-similar CET are discussed, highlighting their advantages and disadvantages. Later, the theoretical development of non-self-similar cavity expansion problems is reviewed. Finally, three applications of non-self-similar CET are reviewed, including interpretation of SBP, EWP nomalisation in CPTU under partially drained conditions, and interaction between energy piles and surrounding soils.

2.1 Introduction

The CET was perhaps firstly proposed by Bishop, R.F. et al. (1945) to solve the mental indentation problem and later was applied in geotechnical engineering by Gibson and Anderson (1961) for the interpretation of pressuremeter tests. Over the past seven decades, a large number of analytical/semi-analytical solutions for cavity expansion problems have been derived, which may be distinguished from each other in five aspects (Yu, 2000; Zhou et al., 2021a):

(i) Small and large strain definitions. The small strain definition was adopted to simplify the elastoplastic cavity expansion analysis in the early days of the CET, while the logarithmic definition of large strains is particularly popular to consider large plastic deformation. Nowadays it has been commonly accepted that the small strain theory can be used in the elastic zone while the logarithmic large strain definition is preferred in the plastic zone, which is also followed in this thesis (Yu and Houlsby, 1991; Chen, S. and Abousleiman, Y., 2013).

(ii) Different constitutive models of soils. The complexity of the cavity expansion solutions is heavily dependent on the selected constitutive models of soils such as elastic models and elastoplastic models (e.g. elastic-perfectly plastic Tresca or Mohr-Coulomb models, critical state models, hypo-plasticity models).

(iii) Fully drained/undrained conditions. For saturated/dry soils, it is assumed that

there is no generation of excess water pressure (EWP) for fully drained conditions and no volume change (or EWP dissipation) for fully undrained conditions, respectively.

(iv) Finite/infinite magnitude of soil. The infinite magnitude of soil around the cavity is usually assumed, but a few studies focused on the influence of finite magnitude of soil on the cavity expansion behaviour (Yu, 1992; Yu, 1993; Pournaghiazar et al., 2013; Cheng and Yang, 2019; Zhuang et al., 2021). As aforementioned, the finite soil thickness will result in the non-self-similarity during the cavity expansion process, and it will be discussed in Chapter 3 of the thesis.

(v) Special cavity expansion problems. Some research considered layered soil effects (Mo et al., 2014), non-circular cavity shapes (Liang, 2010; Zhou et al., 2016a; Zhuang, 2017; Zhou, H. et al., 2022a; Zhou, H. et al., 2022b) and dynamic expansion effect (Davis et al., 1984; Zhou et al., 2019). Note that these special problems are beyond the scope of this thesis.

While there are hundreds of large strain solutions being published, the equations that are solved for stresses and displacements are quite similar. These equations mainly include:

(i) Stress equilibrium equations in the radial direction.

$$\frac{\mathrm{d}\sigma_r}{\mathrm{d}r}+\frac{\sigma_r-\sigma_\theta}{r}=0 \qquad \text{(for a cylindrical cavity)} \tag{2.1}$$

$$\frac{\mathrm{d}\sigma_r}{\mathrm{d}r}+2\frac{\sigma_r-\sigma_\theta}{r}=0 \qquad \text{(for a spherical cavity)} \tag{2.2}$$

(ii) Constitutive equations for elastic/elastoplastic soil behaviour.

(iii) Stress boundary conditions and drainage conditions.

(iv) Compatibility equations.

$$\varepsilon_r=\varepsilon_r\left(r,r_0\right) \tag{2.3}$$

$$\varepsilon_\theta=\varepsilon_\theta\left(r,r_0\right) \tag{2.4}$$

$$\varepsilon_z=0 \qquad \text{(for a cylindrical cavity under plane strain conditions)} \tag{2.5}$$

where r is the radial position of a soil material point whose initial position is r_0; σ_r and

σ_θ are the total radial and circumferential stress, respectively; the symbol "$\mathrm{d}(\bullet)$" means the spatial differential of $(\bullet)$ at a given time (i.e. Eulerian description). It should be mentioned that both the stresses and strains are taken as positive when compression.

Available methods that solve these equations can be broadly categorised into two groups, namely the total strain approach and the auxiliary variable approach (Yu and Carter, 2002; Carter and Yu, 2022; Yang, H. et al., 2023). The advantages and limitations of each approach will be discussed in the following state-of-the-art review for both self-similar and non-self-similar cavity expansion problems.

2.2 Self-similar cavity expansion problems

Although the non-self-similar characteristics during the cavity expansion are focused in this thesis, studies on self-similar problems are firstly reviewed in this section to provide fundamental information for the development of CET and clarify the novelties of the thesis. For self-similar problems, rigorous solutions can be derived by both the total strain approach and the auxiliary variable approach. Therefore, the review is divided into two parts according to these two approaches.

2.2.1 Total strain approach

In the total strain approach, the loading history of a given material point is tracked and the incremental form of constitutive equations is integrated directly to result in an analytical expression of total strains (sums of elastic and strains) with respect to the current effective stresses. Then the Eulerian (current) stresses for a given time can be readily linked with the motion of each material point by the logarithmic strains (Chadwick, 1959). Therefore, the total strain approach may also be termed as the Lagrangian approach as the movement of a material point is followed.

It has been proven that this approach can provide elegant analytical solutions for cavity expansion with elastoplastic Tresca, Mohr-Coulomb, Hoek-Brown, Drucker–Prager (DP)

models (Bigoni and Laudiero, 1989; Yu and Houlsby, 1991; Mo et al., 2014), as summarised in Table 2.1. In these studies:

(i) for the fully drained case, the distribution of the current stress fields can be analytically solved by combining the stress equilibrium equation and the yield function. Afterwards, the particle displacement can be calculated from the integration of the stress-total strain relationship.

(ii) For the fully undrained case, the current strain field can be firstly known because the soil volume is assumed constant. Then the current effective stress fields and distribution of EWP can be back-calculated from the analytical relationship between total strain and effective stresses (if analytical relationship can be derived).

Table 2.1 CET developed by the total strain approach with elastoplastic models

References	Soil model	Cavity shape	Drainage conditions	Remarks
Chadwick (1959)	Mohr-Coulomb	Spherical	Drained	Associated flow rule
Gibson and Anderson (1961)	Tresca and Mohr-Coulomb	Cylindrical	Undrained	No volume change for sand
Hughes et al. (1977)	Mohr-Coulomb	Cylindrical	Drained	Small strain assumption
Carter et al. (1986)	Mohr-Coulomb	Cylindrical/spherical	Drained	Non-associated flow rule; ignoring convective terms
Bigoni and Laudiero (1989)	Mohr-Coulomb	Cylindrical/spherical	Drained	Semi-analytical solution; non-associated flow rule
Yu and Houlsby (1991)	Mohr-Coulomb	Cylindrical/spherical	Drained	Analytical solution
Durban, David and Fleck (1997)	Drucker–Prager	Spherical	Drained	Non-associated flow rule
Mo et al. (2014)	Mohr-Coulomb	Cylindrical/spherical	Drained	Two layer soils
Gharsallaoui et al. (2020)	Hoek-Brown	Cylindrical/spherical	Drained	Non-associated flow rule
Zhang, Q. et al. (2021)	Strain-hardening/softening	Cylindrical	Drained	
Chen, S.-L. and Wang (2022)	Mohr-Coulomb	Cylindrical	Undrained	Graphic method
Chen, S.-L. (2024)	Mohr-Coulomb	Cylindrical	Drained/Undrained	Graphic method

The total strain approach may also be helpful when critical state models are considered in the cavity expansion analyses (Collins and Yu, 1996; Cao et al., 2001; Silvestri and Abou-Samra, 2011; Silvestri and Abou-Samra, 2012; Nanda and Patra, 2015; Vrakas, 2016; Mo and Yu, 2017), as summarised in Table 2.2. But it is mainly restricted to those analyses for saturated soils under fully undrained conditions where the soil volume is always a constant. For cavity expansion in completely dry or unsaturated soils, the soil volume changes with loading and the stress-strain relationship can hardly be directly integrated. Therefore, the total strain approach can hardly be used for cavity expansion in dry and unsaturated soils. Meanwhile, the advantage of the total strain approach lies in that the self-similar assumption is not necessary for the cavity expansion analysis, which means that this approach is suitable for both the self-similar and non-self-similar cavity expansion problems.

Table 2.2 CET developed by the total strain approach with critical state models

References	Soil model	Cavity shape	Drainage conditions	Remarks
Collins and Yu (1996)	OCC[&]; MCC[*]	Cylindrical/spherical	Undrianed	Approximate definition of stress invariants; numerical solution for MCC
Cao et al. (2001)	MCC	Cylindrical	Undrianed	Constant shear modulus
Silvestri and Abou-Samra (2011)	MCC	Spherical	Undrianed	Constant shear modulus or Poisson's ratio
Nanda and Patra (2015)	Structured Cam Clay	Cylindrical	Undrianed	Considering soil structure
Vrakas (2016)	MCC	Cylindrical	Undrianed	
Mo and Yu (2017)	CASM[#]	Cylindrical/spherical	Undrianed	Approximate definition of stress invariants
Chen, S. and Abousleiman (2023)	MCC	Cylindrical	Undrianed	Graphic method

[&]original Cam Clay model

*modified Cam Clay model

[#]Clay and Sand model

2.2.2 Auxiliary variable approach

The auxiliary variable approach highly relies on the self-similar nature of cavity expansion that all material points go through the same stress and deformation paths (Hill, 1950; Collins et al., 1992; Yu and Carter, 2002; Carter and Yu, 2022; Yang, H. et al., 2023). As a result, the incremental stresses and strains related to loading history (i.e. time or Lagrangian description) and field distribution (i.e. space or Eulerian description) are equivalent to each other under a special loading pattern. An auxiliary variable or a normalised timescale can be chosen to transform the governing PDEs with respect to material time derivative and spatial derivative into ordinary differential equations (ODEs) in either Lagrangian or Eulerian description. According to the different descriptions of ODEs, there are two branches of the auxiliary variable approaches.

One branch of this approach, also known as the similarity technique or the incremental velocity method, was firstly proposed by Hill (1950) (also known as Hill's incremental velocity approach) for the cavity expansion analysis in perfectly elastoplastic materials with Tresca yield criterion. Later, it was extended to the analyses of cavity expansion with Mohr-Coulomb models (Yu and Carter, 2002; Carter and Yu, 2022) and critical state models (Collins et al., 1992; Collins and Stimpson, 1994; Zhou et al., 2021a). In this branch the PDEs are transformed into ODEs in terms of space (i.e. Eulerian description) by setting the movement of the elastoplastic boundary as the normalised timescale (Hill, 1950; Collins et al., 1992; Yu and Carter, 2002; Zhou et al., 2021a; Carter and Yu, 2022). For example, the stress equilibrium equation for cylindrical cavity can be expressed as:

$$\mathrm{d}\sigma_r + \left(\sigma_r - \sigma_\theta\right)\frac{\mathrm{d}r}{r} = 0 \tag{2.6}$$

The constitutive equations are transformed from the Lagrangian description into Eulerian description, as

$$\mathbf{A}\begin{bmatrix} \mathrm{D}\sigma_r' \\ \mathrm{D}\sigma_\theta' \\ \mathrm{D}\sigma_z' \\ \mathrm{D}v \end{bmatrix} = \begin{bmatrix} \mathrm{D}\varepsilon_r \\ \mathrm{D}\varepsilon_\theta \\ \mathrm{D}\varepsilon_z \end{bmatrix} \overset{\text{Transformed}}{\rightarrow} \mathbf{A}\begin{bmatrix} \mathrm{d}\sigma_r' \\ \mathrm{d}\sigma_\theta' \\ \mathrm{d}\sigma_z' \\ \mathrm{d}v \end{bmatrix} = \begin{bmatrix} \mathrm{d}\varepsilon_r \\ \mathrm{d}\varepsilon_\theta \\ \mathrm{d}\varepsilon_z \end{bmatrix} \tag{2.7}$$

where the symbol "$\mathrm{D}(\bullet)$" means the material time differential of $(\bullet)$ for a given material point (i.e. Lagrangian description); v=specific volume; $\mathbf{A}$ is the constitutive matric; σ_z is the total vertical stress; σ' means effective stress. Now the PDEs in both the Euerian and Lagrangian descriptions are transformed into ODEs in the Eulerian description.

Another branch formulates the self-similar cavity expansion problem into ODEs in terms of time (i.e. Lagrangian description) by introducing auxiliary variables. This method was firstly proposed by Chen, S.L. and Abousleiman (2012) and Chen, S.L. and Abousleiman, Y.N. (2013) when they studied cylindrical cavity expansion problems in the modified Cam Clay soils under undrained and drained conditions. They adopted a novel auxiliary variable for drained cavity expansion analysis, which is defined by $(r-r_0)/r$. Later, Su and Yang (2019) found that r/r_0 can also serve as the auxiliary variable to facilitate mathematic formulations for self-similar cavity expansion analyses. Taking cylindrical cavity as an example again, this branch can be expressed as

$$\mathrm{d}\sigma_r + (\sigma_r - \sigma_\theta)\frac{\mathrm{d}r}{r} = 0 \overset{\text{transformed}}{\rightarrow} \mathrm{D}\sigma_r + (\sigma_r - \sigma_\theta)\frac{\mathrm{D}[f(r)]}{r} = 0 \tag{2.8}$$

$$\mathbf{A}\begin{bmatrix} \mathrm{D}\sigma_r' \\ \mathrm{D}\sigma_\theta' \\ \mathrm{D}\sigma_z' \\ \mathrm{D}v \end{bmatrix} = \begin{bmatrix} \mathrm{D}\varepsilon_r \\ \mathrm{D}\varepsilon_\theta \\ \mathrm{D}\varepsilon_z \end{bmatrix} \tag{2.9}$$

where $f(r)$ is the function of r. Now the PDEs in both the Euerian and Lagrangian descriptions are transformed into ODEs in the Lagrangian description.

Overall, the auxiliary variable approach is quite powerful and has recently been used to study cavity expansion problems considering anisotropy, structure, viscoplastic, particle crushing, etc. (Russell and Khalili, 2006; Silvestri and Tabib, 2018; Liu, Kai and Chen, 2019; Sivasithamparam and Castro, 2020; Liu, H. et al., 2021; Zhou et al., 2021b; Castro and Sivasithamparam, 2022; Chen, H. and Mo, 2022; Chen, S. et al., 2022; Cheng, W. et al., 2022; Mo et al., 2022; Wang, H. et al., 2022a). Some of the published cavity expansion solutions that adopting the auxiliary variable approach are summaried in Table 2.3. Unfortunately, this approach is rigorous and valid only if the self-similar assumption is satisfied, meaning that it cannot be applied to the targeted problems in this thesis. This is the main shortcoming of the auxiliary variable approach.

Table 2.3 CET developed by the auxiliary variable approach

References	Soil model	auxiliary variable	Drainage conditions	Remarks
Hill (1950)	Tresca	Elastoplastic boundary	Undrained	The first one that proposed this method
Collins et al. (1992)	state-dependent model	Elastoplastic boundary	Drained	Approximate definition of stress invariants; the first one that transform the the governing ODEs into Eulerian description
Collins and Stimpson (1994)	MCC	Elastoplastic boundary	Drained/undrained	Approximate definition of stress invariants
Yu and Carter (2002)	Mohr-Coulomb	Elastoplastic boundary	Drained	
Russell and Khalili (2006)	Unsaturated model	Elastoplastic boundary	Drained	Approximate definition of stress invariants; first one considering unsaturated effect
Chen, S.L. and Abousleiman (2012)	MCC	$\ln r + \text{constant}$		
Chen, S.L. and Abousleiman, Y.N. (2013)	MCC	$(r - r_0)/r$	Drained	The first one that transform the the governing ODEs into Lagrangian description
Li et al. (2017)	Anisotropic MCC	$(r - r_0)/r$	Drained	
Rao et al. (2017)	MCC	$(r - r_0)/r$	Drained	Spherical cavity shape
Sivasithamparam and Castro (2018)	MCC considering fabric anisotropy	$\ln r + \text{constant}$	Undrained	

Chen, S. and Abousleiman (2018)	strain hardening model	$(r-r_0)/r$	Drained	
Mo and Yu (2018)	CASM	$(r-r_0)/r$	Drained	Approximate definition of stress invariants for cylindrical senario
Zhou et al. (2018)	ACMEG-T	Elastoplastic boundary	Drained/undrained	Consider thermal effect
Chen, S.-L. and Liu (2019)	Anisotropic MCC	$\ln r + \text{constant}$	Undrained	
Zhou et al. (2019)	MCC	Elastoplastic boundary	Drained	Consider dynamic effect
Chen, H. et al. (2020a)	Unsaturated model	$(r-r_0)/r$	Drained/undrained	
Huang et al. (2021)	State-dependent model	$(r-r_0)/r$	Drained	Spherical cavity
Yang, C. et al. (2020)	Anisotropic MCC	$(r-r_0)/r$	Drained	Consider 3-dimensional strength
Zhou et al. (2021b)	MCC		Undrained	Consider rate-depedent properties
Li, L. et al. (2021)	Unsaturated model	$(r-r_0)/r$	Undrained	Consider anisotropic effect
Su (2021)	MCC	r/r_0	Drained	Plane stress conditions
Zhou et al. (2021a)	MCC	Elastoplastic boundary	Drained/undrained	Try to present solutions in a unified form
Carter and Yu (2022)	Mohr-Coulomb	Elastoplastic boundary	Drained	Consider limited dilatation
Chen, H. et al. (2022)	Unsaturated model	$(r-r_0)/r$	Undrained	Consider anisotropic and plane stress effects

Mo et al. (2022)	SANICLAY	$\ln r + \text{constant}$	Undrained	Consider anisotropy and destructuration
Wang, H. et al. (2022b)	Unsaturated model	$(r - r_0)/r$	Drained	Consider overconsolidation effect
Pang et al. (2023)	SANISAND	$(r - r_0)/r$	Drained	Consider fabric change effect
Wang, Yanzhi and Russell (2023)	Unsaturated model	Elastoplastic boundary	Drained/undrained	Consider four different drainage conditions
Tian et al. (2024)	Unified hardening model	$\ln r + \text{constant}$	Undrained	Consider thermal effect and overconsolidation effect
Jing et al. (2024)	Unsaturated model	$(r - r_0)/r$	Undrained	Consider various initial hydraulic state

2.3 Non-self-similar cavity expansion problems: theory

In this section, theoretical studies on non-self-similar cavity expansion problems are briefly reviewed, focusing on non-self-similar cavity expansion problems caused by finite soil thickness, hydro-mechanical coupling and thermo-mechanical coupling.

2.3.1 Cavity expansion in a finite soil thickness

The mostly discussed factor for non-self-similarity is the finite thickness of the cylinder/sphere (i.e. the cavity is embedded in a finite soil thickness). Investigations on this factor may date back to the 1950s and were mainly related to cavity expansion in metal materials such as steels (Hill, 1950; Chadwick, 1963; Bhargava and Sharma, 1964). A summary of relevant publications in these two decades can refer to Johnson, William and Mellor (1983). In these analyses the elastoplastic behaviour of solid media was modelled either by Tresca or by von Mises models and the small strain assumption was frequently adopted.

It was not until 1980 that the CET in a finite soil thickness was applied to geotechnical engineering to interpret SBPs in small-sized calibration chambers (Jewell et al., 1980). The perfectly elastoplastic Mohr-Coulomb model with a non-associated flow rule (Rowe, 1962) was adopted in Jewell et al. (1980), but the small strain deformation was assumed and the elastic deformation in the plastic zone was also neglected. Later, Yu (1992) and Yu (1993) proposed large strain analytical solutions for the expansion of thick-walled cylinders and spheres of Mohr-Coulomb soils, respectively. The total strain approach was particularly interesting in these analyses with the perfectly elastoplastic Mohr-Coulomb model. This is because the stress-total strain relationship can be easily established when the strength, dilatancy, and stiffness parameters are taken as constants. To study the chamber boundary effect on CPT results, Salgado et al. (1998) derived a semi-analytical solution for drained cylindrical cavity expansion using a modified Mohr-Coulomb model

that considers the state-dependent properties of sands (Bolton, 1986), whereas the cavity expansion response needed to be calculated step-by-step by discretizing the soil thickness into finite elements and the load history into load steps. In general, these published solutions demonstrated that the finite soil thickness may result in a smaller internal support pressure and a softening cavity expansion curve (constant stress at the outer boundary), as shown in Figure 2.1.

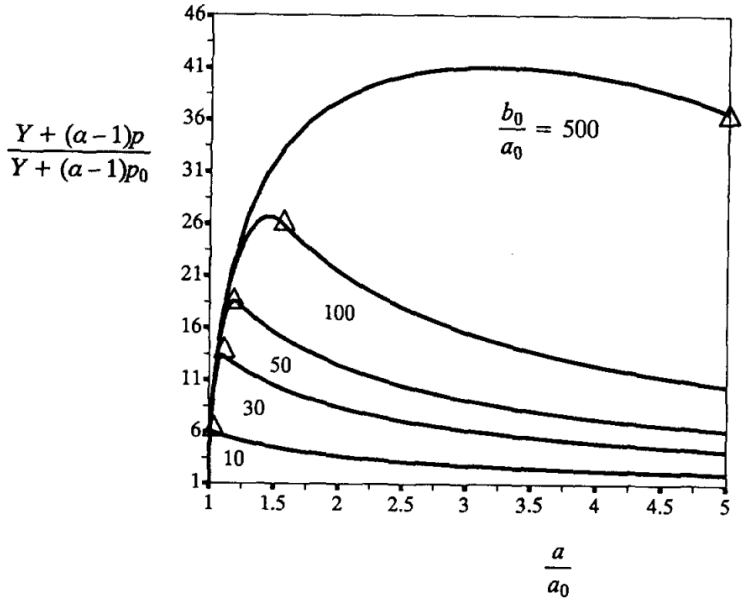

Figure 2.1 Internal support pressure versus cavity expansion radius (Yu, 1992)

Note: In this figure, b_0/a_0 is the ratio of outer to inner cylinder radius; a/a_0 is the ratio of current to initial inner cylinder radius; $\left[Y+(\alpha-1)p\right]/\left[Y+(\alpha-1)p_0\right]$ denotes the normalised internal support pressure, and the larger the value, the larger internal support pressure is required.

For cavity expansion in a finite soil thickness, a few approximate solutions have been developed by the auxiliary variable approach or the total strain approach. Among them, Zhuang et al. (2021) firstly presented a general analytical solution for cylindrical/spherical cavity expansion with Cam-Clay-type soil models under fully undrained conditions using the total strain approach, but approximate definitions of two stress invariants were chosen in the cylindrical scenario. For cavity expansion in dry and unsaturated soil, a few studies showed semi-analytical solutions by simply applying the auxiliary variable approach (Pournaghiazar et al., 2013; Pournaghiazar et al., 2014;

Cheng et al., 2018; Cheng and Yang, 2019; Wang, C.-L. et al., 2022). However, the auxiliary variable approach is only valid under the self-similar assumption and cannot provide rigorous solutions for cavity expansion in a bounded soil mass. As shown in Figure 2.2, there is no softening behaviour observed in these curves, which conflicts with the results shown in Figure 2.1 that the inner cavity pressure first increases and then decreases with a/a_0. So far rigorous drained analysis of boundary effect in soils with critical state models has heavily relied on cumbersome numerical methods (Osinov and Cudmani, 2001).

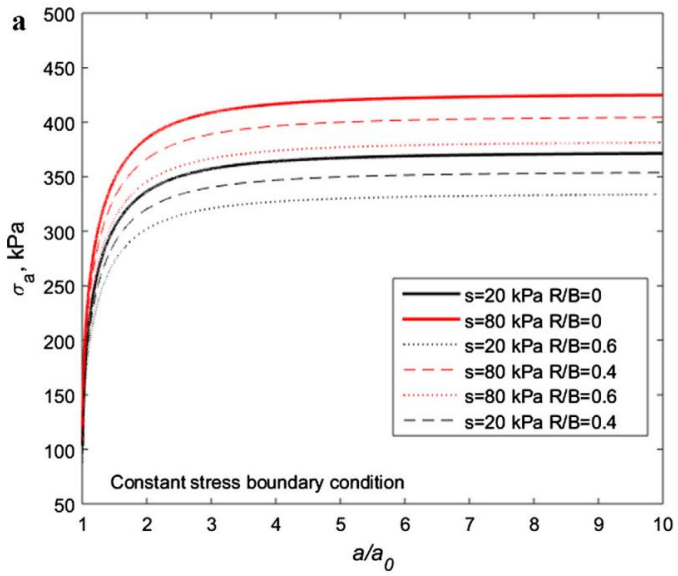

Figure 2.2 Internal support pressure versus cavity expansion radius (Cheng et al., 2018)

Note: In this figure, R/B is the ratio of outer cylinder radius to elastoplastic boundary; a/a_0 is the ratio of current to initial inner cylinder radius; σ_a is the internal support pressure.

It can be found from the literature review that rigorous analytical/semi-analytical solutions for cavity expansion in a finite soil thickness were mainly derived when Mohr-Coulomb models were used. Solutions with critical state models were not rigorous: some solutions were derived by the auxiliary variable approach with the self-similar assumption, while some were derived by the total strain approach with the simplified stress invariant definitions. To fill this gap, a novel HEL approach that combines the total strain approach and auxiliary variable approach is proposed in Chapter 3 of the thesis. The new approach

combines the advantages of the two separate approaches, and a rigorous and general solution will be presented in Chapter 3 for cavity expansion in a finite soil thickness.

2.3.2 Cavity expansion in the hydro-mechanical coupling process

Hydro-mechanical coupling in porous media is the physical interaction between solids and fluids. A clear understanding of the coupling process is important to many engineering problems in soil mechanics, geophysics, material science, the petroleum industry, chemical engineering, agricultural engineering and biomechanics (Coussy, 2004; De Boer, 2012).

Water flow in porous soils is mainly dependent on the EWP gradient and the soil hydraulic conductivity. It is normally described by Darcy's law that assumes the velocity of water flow is proportional to the gradient of EWP. The fully undrained and drained conditions can be seen as two special cases of the lower and upper bounds of soil hydraulic conductivity, respectively:

(i) Under fully undrained conditions, there is nearly no dissipation of EWP for low permeable soils under fast loading.

(ii) Under fully drained conditions, the permeability is large enough and loading process is slow, so EWP is dissipated as soon as it is generated.

The drainage conditions of soils are actually between fully drained and undrained conditions regarding the soil permeability and loading rate. To distinguish them from fully drained/undrained conditions, in this thesis the hydro-mechanical coupling process represents the process of cavity expansion under partially drained conditions and will be focused in Chapter 4 of this thesis.

A majority of these solutions paid much attention to cavity expansion analyses under ideally drained/undrained conditions. In fact, partially drained cavity expansion in poro-elasto-plastic media is also of great significance for the potential applications to fluid

injection, pile installation below the water table, CPTU, bio-inspired robots for burrowing in aquatic environments, among others (Silva et al., 2006; Auton, 2018; Dienstmann et al., 2018a; Auton and MacMinn, 2019; Mo et al., 2020). When considering partially drained effect, cavity expansion analyses have not been published until recent years. Silva et al. (2006) and Zhou et al. (2021a) simulated the cylindrical cavity expansion under partially drained conditions by FEM, where the partially drained effect was emphasised for cavity expansion in Boston blue clay and Kaolin clay. Auton and MacMinn (2019) and Kumar et al. (2024) proposed analytical cylindrical cavity solutions for fluid injection in a poro-elastic-plastic Mohr-Coulomb solid. However, the former neglected the time-dependent cavity expansion behavior by assuming steady-state fluid flow, while the latter adopted small strain definitions in the plastic zone. To investigate the partially drained effect in CPTU, Dienstmann et al. (2017) and Mafra and Dienstmann (2022) developed large strain solutions for cavity expansion in a poro-elastic-plastic Drucker-Prager medium by the time-stepping approach (i.e. discretizing the loading process into finite time intervals). In their studies the EWP distribution was predefined to simplify the hydro-mechanical coupling equations, which should be carefully selected in order to improve solution accuracy. Mo et al. (2020) developed a cavity-expansion-based method that linked the partially drained conditions with fully drained and undrained conditions by empirical relationships. Using a poro-elasto-plastic Cam-Clay model, Russell et al. (2023) presented a time-stepping, large strain cavity expansion solution that consists of seven ordinary differential equations, and iterations are required in each time step to satisfy stress continuity at the elastoplastic boundary.

Overall, only time-stepping solutions are available for large strain cavity expansion when the hydro-mechanical coupling effect is considered, which may involve the cost of calculation time and indirect physical explanations (e.g. obstacles for dimensional analyses). Therefore, it is essential to develop such a solution in fairly straightforward forms to provide more efficient computation and more insightful understanding of inherent mechanisms, for cavity expansion under partially drained conditions. This gap

will be filled in Chapter 4 of the thesis by presenting a straightforward-form solution for cylindrical cavity expansion in a poro-elasto-plastic media under partially drained conditions. With the superiority of the present solution in dimensional analyses, the normalisation of EWP is discussed and applied to the interpretation of CPTU under partially drained conditions.

2.3.3 Cavity expansion in the thermo-mechanical coupling process

Cavity expansion in the thermo-mechanical coupling process is also non-self-similar as thermal stresses can affect the stress paths of particles at various positions. Since the 1950s, stress and deformation analyses of hollow cylinders and spheres under thermal stresses have been studied by many scholars in solid mechanics. For example, Bland (1956) investigated the elastoplastic behaviour of a thick-walled hollow cylinder subjected to the symmetric pressure and temperature gradient. Derrington and Johnson (1958), Cowper (1960), and Durban, David (1983) focused on the elastoplastic behaviour of the hollow sphere considering thermo-mechanical coupling. In the past twenty years, thermo-mechanical coupled analyses of hollow cylinders and spheres made of functionally graded materials have been increasingly popular for their wide applications in aerospace industries, pressure vessels, nuclear reactors, gun tubes, and piping (Jabbari et al., 2002; Shao and Ma, 2008; Ozturk and Gulgec, 2011; Moheimani et al., 2018; Alexandrov and Jeng, 2020; Benslimane et al., 2020; Thakur and Sethi, 2020; Akbari, 2021; Arslan et al., 2021; Saeedi et al., 2021; Sim et al., 2021; Temesgen et al., 2021).

A summary of these studies is listed in Table 2.4. It can be found that stresses and displacements around the cavity were calculated with four assumptions:

(i) Small strain definition. This is mainly because thermal strains are normally elastic.

(ii) Simplified constitutive models. The linearly elastic model and elastoplastic models with Tresca and von Mises yield criteria were frequently adopted.

(iii) Static cavity expansion problems. The internal and external pressures were kept

unchanged, and the temperature distribution was normally calculated with steady state temperature (i.e. temperature field does not change with time).

(iv) Non-stress or constant-stress boundary conditions at the inner cylinder wall. The problem with a radial displacement boundary has seldom been reported.

By modifying assumptions (iv), a few analytical solutions were proposed for cavity expansion with a radial displacement boundary at the inner cavity wall (Zhou et al., 2016b; Zhou et al., 2018; Gaaloul et al., 2021; Tian et al., 2024). Zhou et al. (2018) presented a cavity expansion solution in thermoplastic soils with the ACMEG-T model proposed by Laloui and François (2009). Gaaloul et al. (2021) showed a thermo-mechanical solution for the limit pressure of cavity expansion in Mohr-Coulomb soils. The temperature distribution in soils was ideally assumed to be uniform and time-independent in their solutions. In reality, soil temperatures vary with the radial distance because the heating/cooling effect of energy piles gradually decreases along the radial direction.

Assumptions (iii) and (iv) were modified by Olgun et al. (2014) in order to model the transient radial interaction between energy piles and surrounding soils. The soil around energy piles was modelled by the elastoplastic mode with Tresca yield surface and the transient radial temperature distributions were also considered. Their results were obtained by FEM, and an analytical-form, thermo-mechanical solution for cavity expansion is still not available. To better quantify the transient RIEPS, assumptions (i) and (ii) are followed while assumptions (iii) and (iv) are modified by involving transient temperature distributions and a radial displacement boundary, as detailed in Chapter 5.

Table 2.4 Thermo-mechanical CET solution

Reference	Constitutive model	Cavity shape	Boundary conditions	Thermal field	Remark
Bland (1956)	Tresca	Finite cylinder	Internal and external pressures	Steady	
Derrington and Johnson (1958)	Tresca	Finite sphere	Internal and external pressures	Steady	Discussed the plastic zone
Cowper (1960)	Tresca	Finite sphere	No pressure	Steady	Two thermal plastic zone
Lomakin (1960)	Elastic	Infinite cylinder/sphere	No pressure	Transient	
Johnson, W. and Mellor (1962)	Tresca	Finite sphere	No pressure	Steady	
Ishikawa (1977)	Elastic	Finite sphere	No pressure	Transient	
Durban, David (1983)	von-Mises	Finite sphere	No pressure	Steady	Two thermal plastic zone
Gamer (1988)	von-Mises	Finite sphere	No pressure	Steady	
Aptukov (1991)	Tresca	Infinite sphere	Internal pressure	Steady	Considering dynamic effect
Orçan and Gamer (1994)	Tresca	Finite sphere	No pressure	Steady	Linear hardening law
Jin and Noda (1994)	Elastic	Finite cylinder	No pressure	Transient	Functionally gradient material
Kandil et al. (1995)	von-Mises	Finite cylinder	No pressure	Transient	Increase internal temperature

Şahin (1995)	Tresca	Finite cylinder	Internal pressure	Transient	
Wu (1997)	Elastic	Finite cylinder	No pressure	Transient	
Jahanian and Tavakoli (1998)	Incremental hardening model	Finite sphere	No pressure	Transient	
Lee, Z.-Y. et al. (2001)	Elastic	Finite cylinder	No pressure	Transient	
Jabbari et al. (2002)	Elastic	Finite cylinder	Internal and external pressures	Steady	Functionally gradient material
Eraslan and Orcan (2002)	Tresca	Finite cylinder	No pressure	Transient	FEM
Araki et al. (2004)	Elastic	Finite cylinder	No pressure	Transient	
Schmitt et al. (2007)	Drucker–Prager	Finite cylinder	No pressure	Transient	Functionally gradient material
Shahani and Nabavi (2007)	Elastic	Finite cylinder	Internal temperature/pressure	Transient	
Shao and Ma (2008)	Elastic	Finite cylinder	Internal and external pressures	Transient	Functionally gradient material
Radu et al. (2009)	Elastic	Finite cylinder	No pressure	Transient	
Nabavi and Shahani (2009)	Elastic	Finite cylinder	Internal pressure	Transient	
Asgari and Akhlaghi (2010)	Elastic	Finite cylinder	No pressure	Transient	FEM

Ozturk and Gulgec (2011)	Tresca	Finite cylinder	Internal pressure	Transient	Functionally gradient material
Ehteram et al. (2011)	Elastic	Finite cylinder	No pressure	Transient	
Rash Ahmadi et al. (2011)	Tresca	Finite sphere	Internal pressure	Steady	Functionally gradient material
Mahmoudi and Atefi (2012)	Elastic	Finite cylinder	No pressure	Transient	
Arefi and Rahimi (2013)	Elastic	Finite cylinder	Internal pressure	Steady	Functionally gradient material
KAYA and ERASLAN (2014)	Elastic	Finite cylinder	No pressure	Transient	
Abbas (2014)	Elastic	Finite cylinder	No pressure	Transient	Finite difference method
Shi and Shang (2014)	Tresca	Infinite sphere	No pressure	Transient	
Talaee et al. (2014)	Elastic	Finite cylinder	Internal pressure	Transient	
Dats et al. (2015)	Elastic	Finite cylinder	No pressure	Steady	
Heydari and Kazemi (2015)	von-Mises	Finite sphere	No pressure	Steady	
Kashkoli and Nejad (2015)	Elastic	Finite sphere	Internal and external pressures	Steady	
Parvizi et al. (2016)	Tresca	Finite sphere	Internal and external pressures	Steady	
Takabi (2016)	Elastic	Finite cylinder	Internal and external pressures	Transient	Finite difference method

Eraslan and Apatay (2016)	Tresca	Finite cylinder	No pressure	Transient	
Kamal et al. (2017)	Tresca	Finite cylinder	No pressure	Steady	
Burenin et al. (2018)	von-Mises	Finite cylinder	No pressure	Transient	Finite difference method
Benslimane et al. (2020)	von-Mises	Finite cylinder	Internal and external pressures	Steady	Functionally gradient material
Alexandrov and Jeng (2020)	von-Mises	Finite sphere	Internal and external pressures	Steady	
Sim et al. (2021)	Elastic	Finite sphere	Internal and external pressures	Steady	Functionally gradient material

2.4 Non-self similar cavity expansion problems: applications in geotechnical engineering

Three applications of non-self-similar CET in geotechnical engineering are reviewed in this section to further show the significance of the new CET, including the interpretation of SBP, partially drained effect in CPTU, and interaction between energy piles and surrounding soils. To avoid redundant introductions, only the state-of-the-art review that is most close to the thesis is presented.

2.4.1 Interpretation of SBP

SBP is widely used in the interpretation of in-situ tests due to the simple boundary conditions, convenient measurement of soil strength and stiffness, and low disturbance on in-situ soils (Mair and Wood, 2013). By involving some assumptions, it has been proven that the pressuremeter curves obtained from SBP can be interpreted by CET (Hughes et al., 1977; Houlsby and Withers, 1988; Jefferies, 1988; Yu, 1994; Yu, 1996; Mair and Wood, 2013).

Gibson and Anderson (1961) may be the first ones that applied the CET to the interpretation of soil parameters by modelling the clay and sand as perfectly elastoplastic Tresca and Mohr-Coulomb materials. Nevertheless, Gibson and Anderson (1961) assumed that the volume of sand remianed unchanged during pressuremeter tests, which may lead to the overestimation of soil friction angle. Hughes et al. (1977) modified the solution of Gibson and Anderson (1961) by modelling sand as an elastoplastic Mohr-Coulomb material with constant dilatation angles. Their method is able to get the friction angle and shear modulus from SBP in loose sand, but errors may be noticeable for SBP in dense sand (Jewell et al., 1980; Fahey and Randolph, 1984).

Palmer (1972), Ladanyi (1972) and Baguelin et al. (1972) proposed a CET-based method to directly obtain the stress-strain relationship of undrained clay from pressuremeter

curves. This kind of method was further extended by Manassero (1989) and Silvestri (2001) to get stress-strain relationships of sand. As pointed out in Yu (2000), however, the interpretation accuracy of this interpretation method may be very sensitive to the initial disturbance of pressuremeter installation.

By involving a state-parameter-based soil model, Yu (1994) found that the slopes of SBP curves can be related to initial state parameters of sands by a unique linear relationship in logarithmic coordinates. As shown in Figure 2.3, this linear relationship is not sensitive to the initial stress state and soil stiffness, and therefore it is rather suitable for the back-analysis of SBP results. Yu (1994)'s method faced one challenge that the linear relationship may not exist for pressuremeter curves measured from SBP in small-size calibration chambers. Zhuang et al. (2021) stated that the finite soil thickness around pressuremeter may pose an important impact on the relationship between SBP curve slopes and initial state parameters under undrained conditions, but the relationship for SBP calibration chambers under drained conditions (e.g. dry sand) has not been checked so far. Therefore, it will be discussed in Chapter 3 of this thesis with the benefit of the new solution.

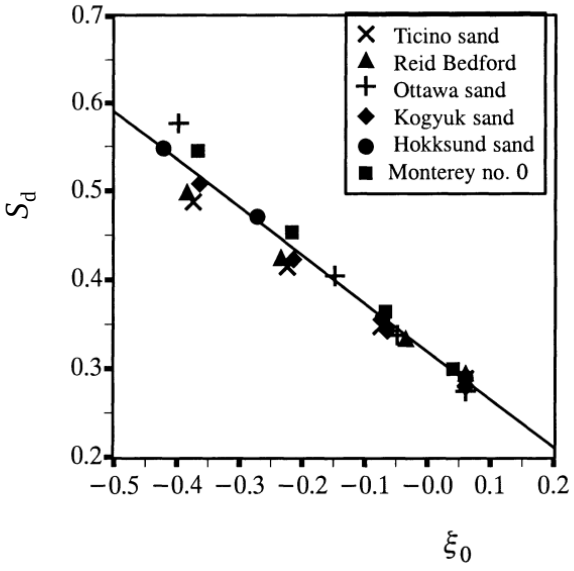

Figure 2.3 Linear relationship between the slopes of SBP curves and initial state parameters of sands (Yu 2000).

Note: In this figure S_d is the slope of SBP curve in the logarithmic coordinate; ξ_0 is the initial state parameter of sand.

2.4.2 Partially drained effect in CPTU

CPTU is an efficient and economic in-situ test method to interpret soil properties such as strength, stiffness and permeability from the measured cone tip resistance and water pressure (Robertson et al., 1992; Ghafghazi and Shuttle, 2008; Lunne, 2012; Mayne and Peuchen, 2022). For a standard penetration rate (i.e. 20mm/s), it is normally assumed that CPTU is conducted under fully undrained conditions in low permeable clays and fully drained conditions in high permeable sands. However, partially drained conditions may prevail for CPTU in intermediately permeable soils, such as silty soils and some silty/clayed tailings (Abu-Farsakh et al., 2003; DeJong and Randolph, 2012; Sheng et al., 2014; Russell et al., 2023). Besides, various penetration rates in a given soil can be another reason for the partially drained effect, namely the rate effect (Silva et al., 2006; Schneider et al., 2007; Kim et al., 2008; DeJong and Randolph, 2012).

Since the last two decades, the partially drained effect in CPTU has been investigated with various methods, including FEM (Liyanapathirana, 2009; Obrzud et al., 2011; Yi et al., 2012; Sheng et al., 2014; Liu, Kehan et al., 2024), material point method (MPM) (Ceccato et al., 2016; Ceccato and Simonini, 2017), particle finite element method (Monforte et al., 2021), in-situ tests (Bedin, 2006; Kim et al., 2008; Klahold, 2013; Suzuki, 2015; Sosnoski, 2016), centrifuge model tests (House et al., 2001; Randolph and Hope, 2004; Schneider et al., 2007; Jaeger et al., 2010), and cavity expansion method (Silva et al., 2006; Dienstmann et al., 2018b; Mo et al., 2020; Reid and Smith, 2021; Zhou et al., 2021a; Mafra and Dienstmann, 2022; Russell et al., 2023). These studies provided important evidence that the partially drained effect has an essential influence on the evolution of measured EWP and cone tip resistance. For example, typical results for normalised cone tip resistance and EWP shown in Figure 2.4 indicate that the normalised EWP increases with the normalised penetration rate, while the the normalised cone tip resistance decreases.

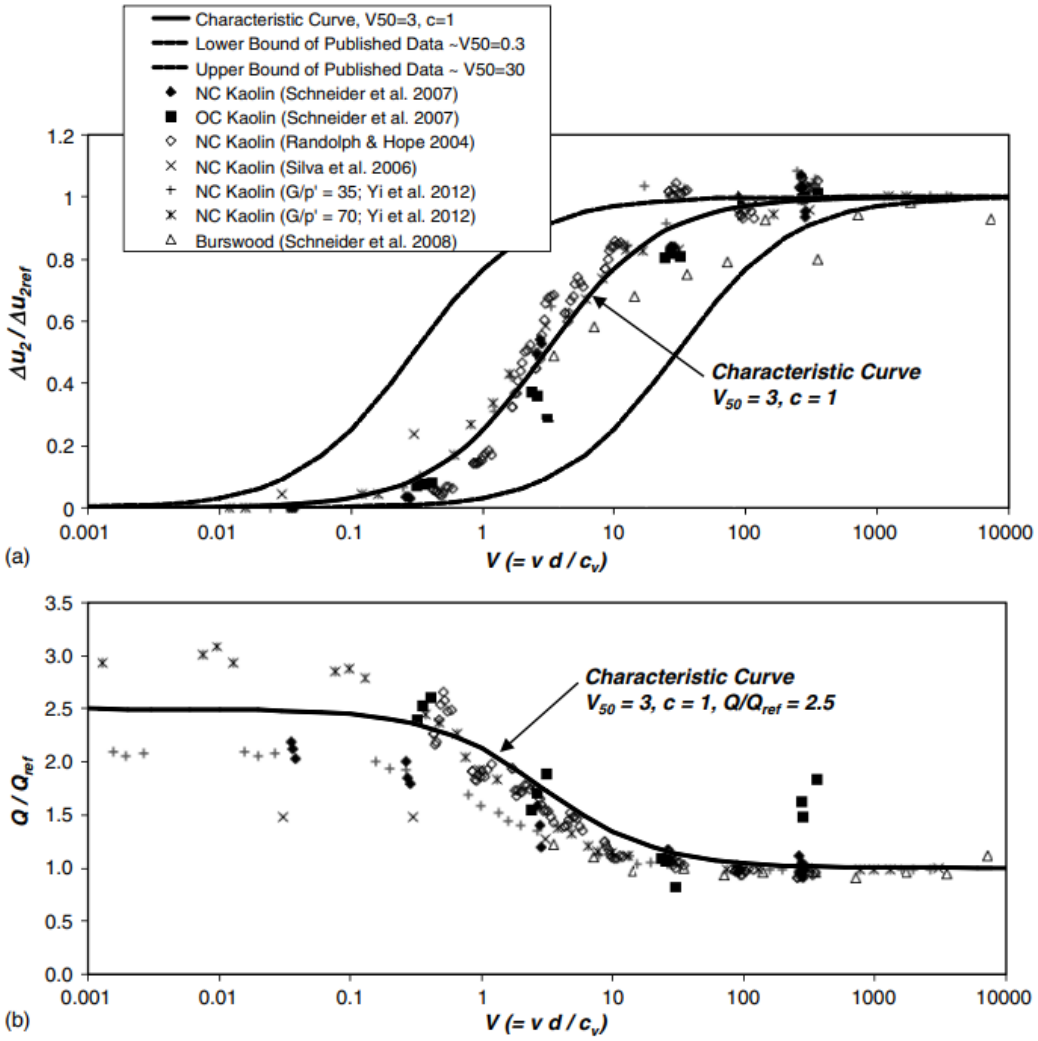

Figure 2.4 Normalised cone tipe resistance and EWP measured in CPTU under partially drained conditions (DeJong and Randolph, 2012): (a) normalised EWP; (b) normalised cone tip resistance

Note: In this figure, V is the normallised penetration rate; $\Delta u_2/\Delta u_{2\text{ref}}$ is the normalised EWP; Q/Q_{ref} is the normalised cone tip resistance.

In the above studies with various methods, the partially drained effect in CPTU was normally estimated by a normalised penetration rate, $\bar{V}_0$, defined as (Randolph and Hope, 2004)

$$\bar{V}_0 = \frac{V_{\text{cptu}} D}{c_{\text{h}}} \text{ or } \frac{V_{\text{cptu}} D}{c_{\text{v}}} \tag{2.10}$$

where V_{cptu} =penetration rate; D =piezocone diameter; c_{h} and c_{v} are the horizontal

and vertical coefficients of consolidation, respectively. It is recognised that CPTU is conducted under partially drained conditions for $\bar{V}_0$=0.01-30, undrained conditions for $\bar{V}_0$>30, and drained conditions for $\bar{V}_0$<0.01 (Randolph and Hope, 2004). However, previous studies indicate the need to improve the normalisation process by incorporating the influence of the rigidity index of soils, I_r, for two reasons.

The first reason lies in that the normalised EWP and cone tip resistance by $\bar{V}_0$ (i.e. the backbone curves in CPTU) were found to be significantly affected by I_r (Dienstmann et al., 2017; Dienstmann et al., 2018b; Mafra and Dienstmann, 2022). One example for the difference can be seen in Figure 2.5.

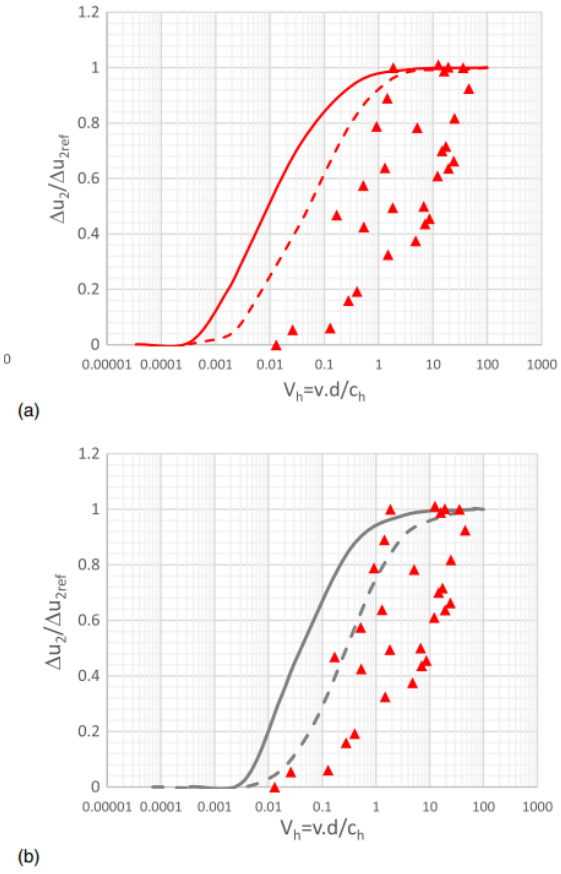

Figure 2.5 Normalised EWP with different I_r (Dienstmann et al., 2018b): (a) I_r=900; (b) I_r=100

Note: In this figure, the solid line represents the analytical resutls and the dashed line means the numerical results. V_h is the normallised penetration rate; $\Delta u_2/\Delta u_{2ref}$ is the normalised EWP;

Q/Q_{ref} is the normalised cone tip resistance.

The second reason lies in the consistency of the penetration process and dissipation process. Since Teh and Houlsby (1991) proposed a method of interpreting consolidation coefficient from CPTU dissipation tests (i.e. holding test that records water pressure dissipation with time at a certain depth), the effect of I_{r} has been widely considered in the interpretation of those dissipation tests (Chai et al., 2012; Cai et al., 2015; Chai et al., 2016; Zhang, Y. et al., 2022; Ecemis et al., 2023), by defining a normalised time factor T^*:

$$T^* = \frac{4c_{\mathrm{h}}t}{D^2\sqrt{I_{\mathrm{r}}}} \tag{2.11}$$

where *t* denotes time. It can be seen from Figure 2.6 that the normalised dissipation curves can become unique with the normalised time factor. By contrast, consideration of I_{r} ought to be equally important for the interpretation of CPTU in the penetration process.

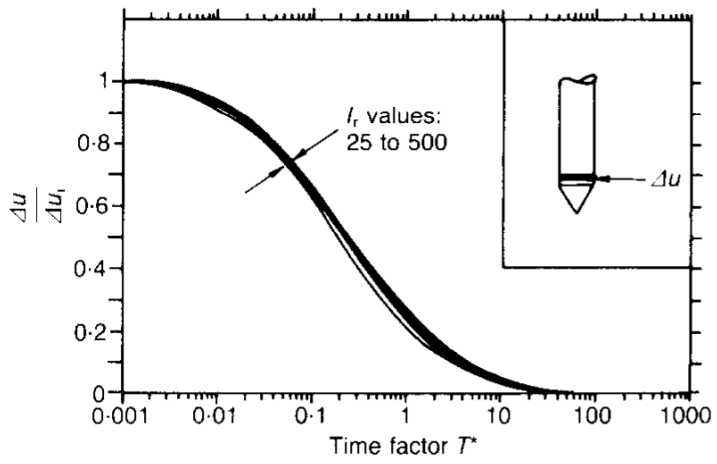

Figure 2.6 Normalised dissipation curves plotted against the normalised time factor (Teh and Houlsby, 1991)

Considering the contributions from these studies, Chapter 4 of the thesis defines a new normalised penetration rate by considering the influence of rigidity index. The soundness of this new normalised rate is theoretically illustrated by a novel hydro-mechanical cavity expansion solution under partially drained conditions. A unique backbone curve exists

with the new normalised rate, and the curve matches well with a database of numerical and experimental results. Obviously, the unique backbone curve can make it easier to estimate the consolidation coefficient of soils from multi-rate CPTU (penetration stage), which can provide guidance and redundancy in the interpretation of CPTU dissipation tests.

2.4.3 Interaction between energy piles and surrounding soils

Energy piles that serve as pile foundations and heat exchangers for superstructures can provide an efficient and sustainable way to make use of geothermal energy. Temperatures of energy piles and surrounding soils will change when the systems are operating in different seasons. This thermal effect may be important for the bearing capacity design of energy piles (Bourne-Webb, P. et al., 2016). For example, a large number of studies have shown that the shaft friction of energy piles increase/decrease in the heating/cooling process (Laloui et al., 2006; Bourne-Webb, P.J. et al., 2009; Stewart and McCartney, 2014; Ng et al., 2015; Ozudogru et al., 2015; Liu, H.-l. et al., 2019; Nguyen et al., 2019; Kong et al., 2021a; Li, R. et al., 2021; Bao et al., 2022; Liu, S.-w. et al., 2022; Zhou, Y. et al., 2022; Wang, Yang et al., 2024).

The radial interaction between energy piles and soils (RIEPS) may be one of the reasons for the shaft resistance change of energy piles (Ouyang et al., 2011; Amatya et al., 2012; Ng et al., 2015; Bourne-Webb, P. et al., 2016; Ng et al., 2016; Xiong et al., 2021). This interaction mechanism has been investigated by various methods such as model tests (Yazdani et al., 2019; Kong et al., 2021a), in-situ tests (Faizal et al., 2018; Faizal et al., 2019a; Lv et al., 2020; Kong et al., 2021b; Xiong et al., 2021), numerical simulation methods (Olgun et al., 2014; Saggu and Chakraborty, 2015; Fuentes et al., 2016), and analytical methods (Zhou et al., 2016b; Zhou et al., 2018; Gaaloul et al., 2021). Some of these studies indicated that the radial contact stress change at the soil-pile interface, $\Delta\sigma_n$, plays a limited role in shaft resistance of energy pile, while some found the thermal-induced $\Delta\sigma_n$ should not be ignored. For instance, a full-scale field test conducted by

Xiong et al. (2021) showed that higher temperatures can result in an increase of $\Delta\sigma_n$ by more than 50kPa at a sand-pile interface (36.5m in depth). The discrepancy in the significance of RIEPS may be dependent on different temperatures, water content, and thermo-mechanical properties of soils and energy piles (e.g. stiffness, strength and thermal expansion coefficients). $\Delta\sigma_n$ may also be affected by temperature circles due mainly to cumulative irreversible deformation of soil (Ng et al., 2016; Faizal et al., 2018; Kong et al., 2021a), but it remains to be validated whether the complex soil temperature distributions under temperature circles have an impact on $\Delta\sigma_n$.

To better describe the radial interaction between energy piles and soils, it is necessary to develop an explicit analytical solution, considering two physics-based factors:

(i) the radial thermal expansion of energy piles, which will squeeze the surrounding soils;

(ii) soil temperature changes, which will generate thermal strains in soils.

There have been a few analytical solutions for modelling the RIEPS (Zhou et al., 2016b; Zhou et al., 2018; Gaaloul et al., 2021). These solutions are developed primarily based on the cavity expansion theory and assumed that the temperature distribution in soils was uniform and time-independent. As aforementioned, soil temperatures vary with the radial distance because the heating/cooling effect of energy piles gradually decreases along the radial direction. On the other hand, some thermo-mechanical solutions were proposed in the fields of solid and structure mechanics to study the transient thermo-mechanical behaviour of hollow cylinders (Kandil et al., 1995; Wu, 1997; Shahani and Nabavi, 2007; Radu et al., 2008; Ehteram et al., 2011; Teixeira et al., 2023). These solutions may not be directly applied to the analysis of RIEPS because free-stress or constant-stress boundary conditions were assumed at the inner cylinder wall (i.e. pile-soil interface).

To fill this gap, Chapter 5 proposes an analytical solution for the calculation of thermo-elastic stresses and displacements during cavity expansion under transient temperature

fields. The solution is a modification of Kandil et al. (1995) considering a radial displacement boundary at the pile-soil interface and is shown in an analytical form. It is therefore more suitable for RIEPS analysis in geotechnical engineering considering the combined effects of transient soil temperatures and energy pile expansion.

Chapter 3 Cavity expansion in finite soil thickness: a hybrid Eulerian-Lagrangian approach

This chapter proposes a new approach, termed as the hybrid Eulerian-Lagrangian (HEL) approach, for non-self-similar cavity expansion in bounded soils. With the HEL approach, a unified framework is established for the quasi-static expansion analysis of a cylindrical cavity, considering finite/infinite magnitude of soil, drained/undrained conditions, saturated/unsaturated soil states, and various critical state soil models. The HEL approach is validated by comparing with FEM and existing solutions in special cases. Later, the non-self-similar cavity expansion behaviour and outer boundary effect of the cylinder are highlighted by parametric studies. Finally, an example application of the non-self-similar CET is illustrated regarding the boundary effect of SBP in small-size calibration chambers.

Related publications	(i) **Yang, H.**, Zhuang, P.-Z., Zhang, J.-L., Ma, Y., Yu, H.-S. and Chen, X. 2024. A hybrid Eulerian-Lagrangian approach for non-self-similar expansion analysis of a cylindrical cavity in saturated and unsaturated critical state soils. *Acta Geotechnica*. **19**(5), pp.2361-2380. (ii) **Yang, H.**, Zhang, J.-L., Yu, H.-S. and Zhuang, P. 2024. Semi-analytical solution for drained expansion analysis of a hollow cylinder of critical state soils. *Journal of Rock Mechanics and Geotechnical Engineering*. **16**(6), pp.2326-2340.

3.1 Problem definition and assumptions

The expansion of a hollow thick-wall cylinder of soils upon loading at the inner cavity wall is considered, as shown in Figure 3.1. The soil cylinder is of an infinite length (out of plane), and the inner and outer radii of the cylinder are a_0 and b_0, respectively, at the initial state. A horizontal total stress and a vertical total stress σ_{v0} act throughout the surrounding soil which is assumed to be isotropic and homogenous. When the inner pressure gradually increases from σ_{h0} to σ_a. ($\sigma_a > \sigma_{h0}$), the hollow cylinder will expand outwards with the current inner and outer radii becoming a and b, respectively, and the total vertical stress will change from σ_{v0} to σ_z.

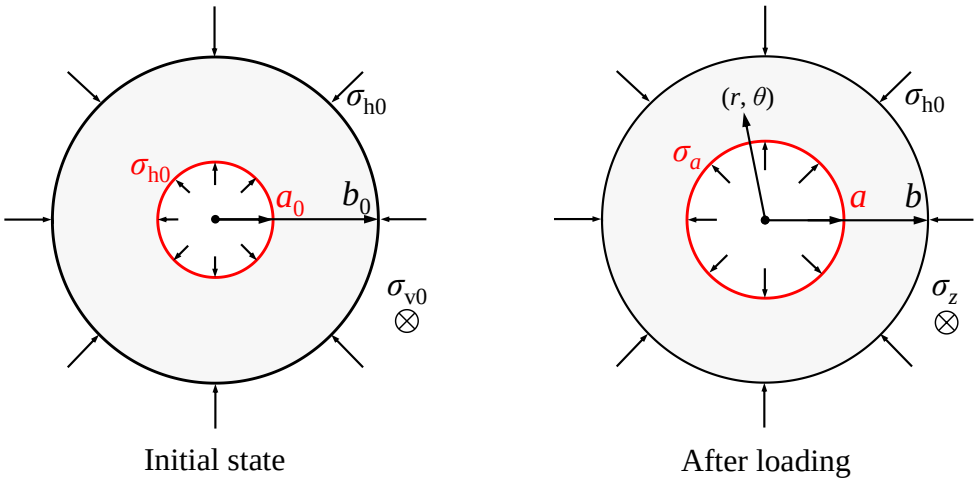

Figure 3.1 Expansion of a thick-wall cylinder of soils

Under the geometry and stress boundary conditions defined in Figure 3.1, the expansion process can be regarded as an axial-symmetric plane strain problem with respect to the vertical direction. For convenience the problem is investigated in the cylindrical coordinate system (r, θ, z) with the origin at the cylinder centre. The stress boundary conditions can be expressed as

$$\sigma_r\big|_{r=a} = \sigma_a \tag{3.1}$$

$$\sigma_r\big|_{r=b} = \sigma_{h0} \tag{3.2}$$

where σ_r =total radial stress; r=current radial position of a material point.

Neglecting body forces, the stress equilibrium equation in the radial direction is

$$\frac{\mathrm{d}\sigma_r}{\mathrm{d}r}+\frac{\sigma_r-\sigma_\theta}{r}=0 \tag{3.3}$$

Unsaturated soils consist of three phases: soil particles, water, and air. The effective stress is then affected by the degree of saturation (S_r) of soil defined by the volume fraction of water to the pores. In this chapter, the initial saturation state of the surrounding soil is assumed to be arbitrary (e.g. saturated or unsaturated). For a smooth transition of soil state between saturated and unsaturated, the simplified Bishop's definition (Bishop, A.W. and Blight, 1963; Schrefler, 1984; Borja, 2004) for the effective (average skeleton) stresses is used as

$$\sigma'_{ij}=\sigma_{ij}-u_a\delta_{ij}+\chi s\delta_{ij} \tag{3.4}$$

$$\bar{\sigma}_{ij}=\sigma_{ij}-u_a\delta_{ij} \tag{3.5}$$

$$s=u_a-u_w \tag{3.6}$$

where σ'_{ij} = effective stress tensor; σ_{ij} = total stress tensor; u_a = pore air pressure; u_w = pore water pressure; δ_{ij} = Kronecker's delta; χ =Bishop's effective stress parameter; s = suction stress; $\bar{\sigma}_{ij}$ =net stress tensor. In this thesis u_a is assumed to equal the atmospheric pressure, and therefore the net stress equals the total stress. χ is the function of the degree of saturation, S_r, and is affected by stress paths, hydraulic hysteresis, soil type, etc. A summary of the relationships between χ and S_r can refer to Khalili, Nasser et al. (2022). Among these relationships, the simplest definition of χ may be χ=S_r and has been widely used in constitutive modelling of unsaturated soils for its simplification (Sheng et al., 2003; Wheeler et al., 2003; Chen, X., 2013). Therefore, χ=S_r is selected in this chapter without loss of generality of the HEL approach.

Two stress invariants (p', q), namely the mean effective stress and deviatoric stress, are rigorously defined respectively as

$$p' = \frac{\sigma'_{ij}\delta_{ij}}{3} = \frac{\sigma'_r + \sigma'_\theta + \sigma'_z}{3} \tag{3.7}$$

$$\begin{aligned} q &= \sqrt{\frac{3}{2}\left(\sigma'_{ij} - p'\delta_{ij}\right)\left(\sigma'_{ij} - p'\delta_{ij}\right)} \\ &= \frac{1}{\sqrt{2}}\sqrt{\left(\sigma'_r - \sigma'_\theta\right)^2 + \left(\sigma'_r - \sigma'_z\right)^2 + \left(\sigma'_\theta - \sigma'_z\right)^2} \end{aligned} \tag{3.8}$$

where σ'_z denotes the vertical effective stress. The work-conjugated volumetric strain (ε_v) is defined as

$$\varepsilon_v = \varepsilon_r + \varepsilon_\theta + \varepsilon_z \tag{3.9}$$

in which ε_r, ε_θ and ε_z are radial, circumferential and vertical strains, respectively, and ε_z remains zero for the present plane strain problem.

3.2 Constitutive modelling of soils

In this chapter the critical state unsaturated models are utilised for the elastoplastic cavity expansion analysis, and thery are shown in a general form. Fully saturated and completely dry states of soils can be seen as two limit conditions of unsaturated soils.

3.2.1 Soil water retention curve (SWRC)

SWRC reflects the hydraulic behaviour of unsaturated soils, and it may be affected by the hydraulic hysteresis, pore size distribution, and stress states (Sheng, 2011; Ng et al., 2020; Khalili, Nasser et al., 2022). A general form of SWRC may be expressed as

$$\mathrm{D}S_\mathrm{r} = \frac{\partial S_\mathrm{r}}{\partial v}\mathrm{D}v + \frac{\partial S_\mathrm{r}}{\partial s}\mathrm{D}s \tag{3.10}$$

Taking the expression of Sun, De'An et al. (2007) as an example, the evolution of S_r with the suction and volume of soils is defined as

$$\mathrm{D}S_\mathrm{r} = -\lambda_{se}\mathrm{D}v - \left(\lambda_{sr}/s\right)\mathrm{D}s \qquad \text{(for the main drying/wetting curve)} \tag{3.11}$$

$$\mathrm{D}S_{\mathrm{r}} = -\lambda_{\mathrm{se}}\mathrm{D}v - \left(\kappa_{\mathrm{sr}}/s\right)\mathrm{D}s \qquad \text{(for the scanning curve)} \tag{3.12}$$

where λ_{se} =slope of S_{r}-v curve at a constant suction; λ_{sr} and κ_{sr} are the slopes of the main drying/wetting curve and the scanning curve, respectively (see Figure 3.2).

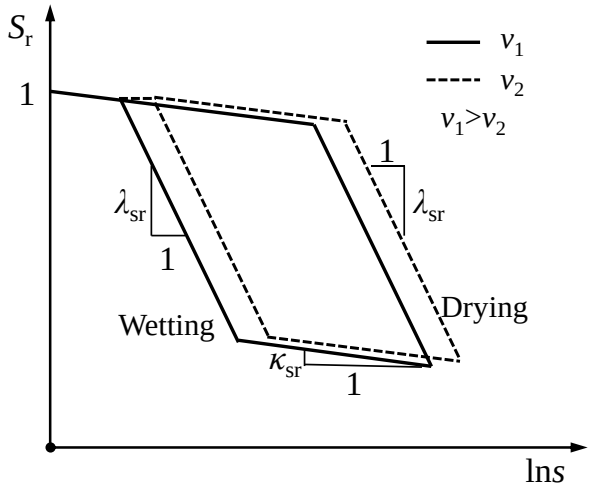

Figure 3.2 Void-ratio dependent SWRC

For constant suction (i.e. Ds=0), Eq. (3.10) can be simplified as

$$\mathrm{D}S_{\mathrm{r}} = \frac{\partial S_{\mathrm{r}}}{\partial v}\mathrm{D}v \tag{3.13}$$

For constant water content (i.e. $\mathrm{D}\left[\left(v-1\right)S_{\mathrm{r}}\right]=0$), the amount of water remains unchanged, which gives

$$\begin{cases} \mathrm{D}S_{\mathrm{r}} = -\dfrac{S_{\mathrm{r}}}{v-1}\mathrm{D}v \\ \mathrm{D}s = \dfrac{-1}{\partial S_{\mathrm{r}}/\partial s}\left(\dfrac{S_{\mathrm{r}}}{v-1} + \dfrac{\partial S_{\mathrm{r}}}{\partial v}\right)\mathrm{D}v \end{cases} \tag{3.14}$$

It can be summarised that the changes in S_{r} and s can be determined by the change in v for both constant suction and constant water content. This conclusion will be important for the elastoplastic cavity expansion analysis in Sections 3.3 and 3.4. Moreover, water flow in porous soils is not considered in this chapter in order to develop semi-analytical solutions with complex critical state models.

3.2.2 Mechanical behaviour

Since the milestone work of Alonso et al. (1990) that proposed Barcelona Basic Model

for unsaturated soils, various unsaturated soil models have been developed based on MCC, CASM, among others (Cui and Delage, 1996; Sun, De' An et al., 2000; Khalili, N. et al., 2008; Sheng et al., 2008; Lai et al., 2016; Zhuang et al., 2024). The stress-strain relationship of saturated/unsaturated soils consists of the yield function, plastic potential, hardening law, and elastic behaviour. For typical two invariant critical state models, the loading collapse (LC) yield function *f* and plastic potential *g* can be expressed respectively as

$$f = f\left[p', q, p'_{\mathrm{c}}(s)\right]=0 \tag{3.15}$$

$$g = g\left[p', q, p'_{g}(s)\right]=0 \tag{3.16}$$

where $f = g$ for the associated plastic flow rule while $f \neq g$ for the non-associated; $\eta = q/p'$ is known as the stress ratio; M =slope of the critical state line (CSL) in the p'-q plane; $p'_g(s)$ =size parameter for the plastic potential; $p'_{\mathrm{c}}(s)$ denotes the isotropic yield stress for unsaturated soils at suction *s*, which is the function of the isotropic yield stress for saturated soils ($p'_{\mathrm{c}}(0)$) and the suction. Following the Barcelona Basic Model (Alonso et al., 1990), $p'_{\mathrm{c}}(s)$ is expressed as:

$$\left[\frac{p'_{\mathrm{c}}(s)}{p'_{\mathrm{n}}}\right]^{\lambda(s)-\kappa} = \left[\frac{p'_{\mathrm{c}}(0)}{p'_{\mathrm{n}}}\right]^{\lambda(0)-\kappa} \tag{3.17}$$

$$\lambda(s)=\lambda(0)\left[(1-\alpha)e^{-\beta s}+\alpha\right] \tag{3.18}$$

where p'_{n} =reference stress; $\lambda(s)$ and $\lambda(0)$ are the slopes of CSLs in the v-$\ln p'$ plane at suction *s* and 0, respectively; α and β are material constants for soils in unsaturated states. The yield function f and $p'_{\mathrm{c}}(s)$ for the MCC-based and CASM-based models are listed in Table 3.1.

Table 3.1 f **and** $p'_{\mathrm{c}}(s)$ **for the selected Cam Clay models**

Model	$f\left[p', q, p'_{\mathrm{c}}(s)\right]$	$p'_{\mathrm{c}}(s)$	Plastic flow rule
MCC	$(\eta/M)^2-(p'_{\mathrm{c}}/p'-1)$	$p'\left[1+(\eta/M)^2\right]$	Associated
CASM	$(\eta/M)^{n^*}-\dfrac{\ln(p'_{\mathrm{c}}/p')}{\ln r^*}$	$p'\exp\left[\ln r^*(\eta/M)^{n^*}\right]$	Non-associated

Note: n^* and r^* are material constants of the CASM, which control the curvature of the yield surface and the intersection point of the CSL and the yield surface, respectively.

The isotropic volumetric hardening law is used to describe the evolution of the yield surface, as

$$\mathrm{D}\varepsilon_v^{\mathrm{p}}=\frac{\lambda(0)-\kappa}{v}\frac{\mathrm{D}p'_{\mathrm{c}}(0)}{p'_{\mathrm{c}}(0)} \tag{3.19}$$

in which $\varepsilon_v^{\mathrm{p}}$=plastic volumetric strain; κ=slope of the swelling line in the v-$\ln p'$ plane and is assumed to be suction-independent (Alonso et al., 1990).

In the elastic loading stage, the volume change can be expressed as

$$\begin{cases}\mathrm{D}\varepsilon_v^{\mathrm{e}}=\dfrac{\kappa}{vp'}\mathrm{D}p'\\ v=v_0-\kappa\ln(p'/p'_0)\end{cases} \tag{3.20}$$

where $\varepsilon_v^{\mathrm{e}}$ =elastic volumetric strain; v_0 =initial specific volume; p'_0 =initial mean effective stress.

3.3 Solutions in the elastic zone

During the elastoplastic expansion process, there will be an elastic zone ($\rho\le r\le b$, ρ denotes the current radius of the elastoplastic boundary) and a plastic zone ($a\le r\le\rho$) forming around the cavity. In the elastic zone, the particle displacement is usually small so that the stress-strain relationship can be simplified by the small strain theory:

$$\begin{bmatrix} \mathrm{D}\varepsilon_r^{\mathrm{e}} \\ \mathrm{D}\varepsilon_\theta^{\mathrm{e}} \\ \mathrm{D}\varepsilon_z^{\mathrm{e}} \end{bmatrix} = -\begin{bmatrix} \mathrm{d}(\mathrm{D}u)/\mathrm{d}r \\ \mathrm{D}u/r \\ 0 \end{bmatrix} = \frac{1}{E(v,p')}\begin{bmatrix} 1 & -\mu & -\mu \\ -\mu & 1 & -\mu \\ -\mu & -\mu & 1 \end{bmatrix}\begin{bmatrix} \mathrm{D}\sigma_r' \\ \mathrm{D}\sigma_\theta' \\ \mathrm{D}\sigma_z' \end{bmatrix} \tag{3.21}$$

where $\varepsilon_r^{\mathrm{e}}$, $\varepsilon_\theta^{\mathrm{e}}$ and $\varepsilon_z^{\mathrm{e}}$ denote the elastic components of radial, circumferential and vertical strains; $u = r - r_0$ is the radial displacement of a material point whose initial radial position is r_0; μ denotes Poisson's ratio; $E = 3(1-2\mu)vp'/\kappa$ represents the elastic modulus.

For cavity expansion in an infinite soil thickness, $E(v,p')$ does not change in the elastic zone because the mean effective stress always equals its initial value (Collins et al., 1992; Chen, S.L. and Abousleiman, Y.N., 2013; Mo and Yu, 2018; Chen, H. et al., 2020b). On the other hand, $E(v,p')$ varies with the loading process if the finite soil thickness around the cavity is considered, which makes it difficult to directly solve Eq. (3.21). This results in one of the main novelties in this chapter.

3.3.1 Validation of a conclusion

Before solving Eq. (3.21), it is necessary to show a conclusion that

$$\begin{cases} \dfrac{\mathrm{d}}{\mathrm{d}r}(\mathrm{D}\sigma_r' + \mathrm{D}\sigma_\theta') = 0 \\ \dfrac{\mathrm{d}}{\mathrm{d}r}\left[\mathrm{D}(S_{\mathrm{r}}s)\right] = 0 \end{cases} \tag{3.22}$$

The validation of Eq. (3.22) is shown as follows.

The compatibility equations related to strains and stresses can be derived from Eq. (3.21) as

$$\frac{\mathrm{d}(\mathrm{D}\varepsilon_\theta)}{\mathrm{d}r} + \frac{\mathrm{D}\varepsilon_\theta - \mathrm{D}\varepsilon_r}{r} = 0 \tag{3.23}$$

$$\frac{\mathrm{d}}{\mathrm{d}r}\left[-\mu\mathrm{D}\sigma_r' + (1-\mu)\mathrm{D}\sigma_\theta'\right] + \frac{\mathrm{D}\sigma_\theta' - \mathrm{D}\sigma_r'}{r} = 0 \tag{3.24}$$

With the effective stress definition, we can transform the equilibrium equation into

$$\frac{\mathrm{d}(\mathrm{D}\sigma_r')}{\mathrm{d}r}-\frac{\mathrm{d}\left[\mathrm{D}(S_{\mathrm{r}}s)\right]}{\mathrm{d}r}+\frac{\mathrm{D}\sigma_r'-\mathrm{D}\sigma_\theta'}{r}=0 \tag{3.25}$$

Combining Eqs. (3.24) and (3.25) gives

$$\frac{\mathrm{d}}{\mathrm{d}r}\left[(1-\mu)(\mathrm{D}\sigma_r'+\mathrm{D}\sigma_\theta')-\mathrm{D}(S_{\mathrm{r}}s)\right]=0 \tag{3.26}$$

It will be proved that Eq. (3.26) holds only if when Eq. (3.22) is satisfied.

As $\mathrm{D}\sigma_z'=\mu(\mathrm{D}\sigma_r'+\mathrm{D}\sigma_\theta')$ in plane strain conditions, the mean effective stress satisfies

$$\mathrm{D}p'=\frac{(1+\mu)(\mathrm{D}\sigma_r'+\mathrm{D}\sigma_\theta')}{3} \tag{3.27}$$

From Eq. (3.20) the specific volume can be expressed as a function of $\mathrm{D}p'$ as

$$v=v_0-\kappa\ln(1+\mathrm{D}p'/p_0') \tag{3.28}$$

Eqs. (3.27) and (3.28) indicate that Dv is determined by $(\mathrm{D}\sigma_r'+\mathrm{D}\sigma_\theta')$, and then $\mathrm{D}(S_{\mathrm{r}}s)$ can also be fully linked by $(\mathrm{D}\sigma_r'+\mathrm{D}\sigma_\theta')$ with the aid of Eqs. (3.13) and (3.14). As a result, there will be one basic unknown (i.e. $\mathrm{D}\sigma_r'+\mathrm{D}\sigma_\theta'$) in Eq. (3.26). If Eq. (3.26) always holds during the loading process, we can get that:

$$\frac{\mathrm{d}}{\mathrm{d}r}(\mathrm{D}\sigma_r'+\mathrm{D}\sigma_\theta')=0 \tag{3.29}$$

Finally, Eq. (3.22) can be proven by combining Eqs. (3.26) and (3.29).

3.3.2 Stress analysis

Eq. (3.22) implies that ($\mathrm{D}\sigma_r'+\mathrm{D}\sigma_\theta'$) does not change with the radial position for a given time (but it varies with time). For convenience, $\sigma_r'+\sigma_\theta'$ can be expressed as

$$\sigma_r'+\sigma_\theta'=2(\sigma_{\mathrm{h}}'-C_\rho) \tag{3.30}$$

where σ_{h}'=effective radial stress at the outer boundary; C_ρ is a constant determined by the elastoplastic boundary.

Combining Eqs. (3.3), (3.21), (3.22) and (3.30), the stresses in the elastic zone can be derived as

$$\begin{cases} \sigma'_r = \sigma'_{\mathrm{h}} + C_\rho \left[(b/r)^2 - 1 \right] \\ \sigma'_\theta = \sigma'_{\mathrm{h}} - C_\rho \left[(b/r)^2 + 1 \right] \\ \sigma'_z = \sigma'_{\mathrm{v0}} + 2\mu \left(\sigma'_{\mathrm{h}} - \sigma'_{\mathrm{h0}} - C_\rho \right) \end{cases} \tag{3.31}$$

$$C_\rho = \frac{\sigma'_{r\rho} - \sigma'_{\mathrm{h}}}{(b/\rho)^2 - 1} \tag{3.32}$$

$$p' = p'_0 + \frac{2}{3}(1+\mu)\left(\sigma'_{\mathrm{h}} - \sigma'_{\mathrm{h0}} - C_\rho \right) \tag{3.33}$$

where σ'_{h0} =effective vertical stress before loading; $\sigma'_{r\rho}$ denotes the radial effective stress at the elastoplastic boundary (r=ρ). Eq. (3.33) shows that the mean effective stress is constant in the elastic zone for a given time (e.g. a given ρ) but varies during the loading process. This is one of the main differences from self-similar cavity expansion problems.

The integral constants σ'_{h} and C_ρ can be determined by the boundary conditions at $r = \rho$ and $r = b$. Since the total radial stress at $r = b$ remains unchanged (i.e. σ_{h0}), combination of Eqs. (3.2) and (3.4) gives

$$S_{\mathrm{r}} s - S_{\mathrm{r0}} \cdot s_0 = \sigma'_{\mathrm{h}} - \sigma'_{\mathrm{h0}} \tag{3.34}$$

where S_{r0} =initial degree of saturation and s_0 =initial suction. At the elastoplastic boundary, the stress states ought to be on the initial yield surface so that the initial yield stress $p'_{\mathrm{c0}}(s_0)$ at $r = \rho$ could be back-calculated from Eq. (3.15) and Table 3.1., as

$$p'_{\mathrm{c0}}(s_0) = R_0 f^{-1}(p'_0, q_0) \tag{3.35}$$

where R_0 = initial overconsolidation ratio of soils; q_0 = initial deviatoric stress.

3.3.3 Displacement analysis

The incremental form of the radial displacement of a material point can be obtained by

combining Eqs. (3.21), (3.31) and (3.33) as

$$\frac{\mathrm{D}u(r)}{r}=\frac{\mu-1+2\mu^2}{E(v,p')}\mathrm{D}\left(\sigma'_{\mathrm{h}}-\sigma'_{\mathrm{h0}}\right)+\frac{1+\mu}{E(v,p')}\left[1-2\mu+(b/r)^2\right]\mathrm{D}C_{\rho} \tag{3.36}$$

From Eq. (3.33), we can get

$$\mathrm{D}C_{\rho}=\mathrm{D}\sigma'_{\mathrm{h}}-\frac{3}{2(1+\mu)}\mathrm{D}p' \tag{3.37}$$

Substituting Eq. (3.37) into Eq. (3.36), the radial displacement can be expressed as

$$\frac{\mathrm{D}u(r)}{r}=\frac{(1+\mu)}{E(v,p')}\left(\frac{b}{r}\right)^2\mathrm{D}\left(\sigma'_{\mathrm{h}}-\sigma'_{\mathrm{h0}}\right)-\frac{3}{2E(v,p')}\left[1-2\mu+(b/r)^2\right]\mathrm{D}p' \tag{3.38}$$

Substituting Eqs. (3.20) and (3.34) into Eq. (3.38) and then integrating Eq. (3.38) following the loading history of a material point, the radial displacement becomes

$$\frac{u(r)}{r}=\int_{p'_0}^{p'}\frac{(1+\mu)\kappa}{3(1-2\mu)}\left(\frac{b}{r}\right)^2\frac{\partial(S_{\mathrm{r}}s)}{\partial p'}\frac{\mathrm{D}p'}{vp'}+\int_{p'_0}^{p'}\frac{-\kappa\left[1-2\mu+(b/r)^2\right]}{2(1-2\mu)}\frac{\mathrm{D}p'}{vp'} \tag{3.39}$$

As the small strain theory is adopted in the elastic zone, the current radial position of a material point can be replaced by its initial value (i.e. $r=r_0$) in the calculation of elastic displacement (this assumption will be proven in Section 3.7.1). Hence, Eq. (3.39) can be integrated as

$$\frac{u(r)}{r}=\frac{(1+\mu)\kappa}{3(1-2\mu)}\left(\frac{b}{r}\right)^2\cdot\int_{p'_0}^{p'}\frac{\partial(S_{\mathrm{r}}s)}{\partial p'}\frac{\mathrm{D}p'}{vp'}+\frac{1-2\mu+(b/r)^2}{2(1-2\mu)}\ln\left(1-\frac{\kappa}{v_0}\ln\frac{p'}{p'_0}\right) \tag{3.40}$$

The integral of the first term in Eq. (3.40) mainly depends on the complexity of SWRCs and controlled suction or water content conditions. For example, if the degree of saturation is just suction dependent (i.e. $S_{\mathrm{r}}=S_{\mathrm{r}}(s)$), the first term on the right hand of Eq. (3.40) will become zero under constant suction conditions. In the other cases, numerical integration techniques will be required to integrate it.

The displacements at the elastoplastic boundary and the outer cylinder wall can be computed by Eq. (3.40) with $r=\rho$ and $r=b$, respectively, as

$$\frac{u(\rho)}{\rho}=\frac{(1+\mu)\kappa}{3(1-2\mu)}\left(\frac{b}{\rho}\right)^2\cdot\int_{p_0'}^{p'}\frac{\partial(S_{\mathrm{r}}s)}{\partial p'}\frac{\mathrm{D}p'}{vp'}+\frac{1-2\mu+(b/\rho)^2}{2(1-2\mu)}\ln\left(1-\frac{\kappa}{v_0}\ln\frac{p'}{p_0'}\right) \quad (3.41)$$

$$\frac{u(b)}{b}=\frac{(1+\mu)\kappa}{3(1-2\mu)}\cdot\int_{p_0'}^{p'}\frac{\partial(S_{\mathrm{r}}s)}{\partial p'}\frac{\mathrm{D}p'}{vp'}+\frac{1-\mu}{1-2\mu}\ln\left(1-\frac{\kappa}{v_0}\ln\frac{p'}{p_0'}\right) \quad (3.42)$$

3.3.4 Calculation procedures for the elastic stresses and displacements

The elastic solution for stresses and displacements is much more complex than conventional self-similar cavity expansion problems (Collins et al., 1992; Chen, S.L. and Abousleiman, Y.N., 2013; Mo and Yu, 2018; Chen, H. et al., 2020b; Yang, C. et al., 2021). The solution also provides the information (i.e. current radius, stresses, and specific volume) at the elastoplastic boundary, which serves as the boundary values for the analysis in the plastic zone. Elastic stresses and displacements can be calculated following the procedure below:

(i) Input initial parameters, including: b_0/a_0, ρ_0; $\sigma'_{\mathrm{h}0}$, $\sigma'_{\mathrm{v}0}$, $S_{\mathrm{r}0}$, s_0, R_0, v_0; λ_{sr}, λ_{se}, κ_{sr}, κ, M, s_{I}, s_{D};

(ii) Calculate p'_0 and q_0 with the initial horizontal and vertical stresses; calculate $p'_{\mathrm{c}0}(s_0)$ by Eq. (3.35);

(iii) For a given ρ_0 (the undeformed radius of elastoplastic interface whose current radius is ρ), set p' as the basic unknown and substitute Eqs. (3.13) (or (3.14)), (3.20), and (3.31)~(3.35) into Eq. (3.15); solve Eq. (3.15) and obtain p';

(iv) Then, calculate v by Eq. (3.20); calculate S_{r} by Eq. (3.13) for constant suction case (or S_{r} and s by Eq. (3.14) for constant water content case);

(v) Finally, calculate σ'_{h} by Eq. (3.34); calculate C_ρ by Eq. (3.33); calculate σ'_r, σ'_θ and σ'_z by Eq. (3.31).

3.4 Solutions in the plastic zone

3.4.1 Governing PDEs in the plastic zone

There are five unknowns (r, σ'_r, σ'_θ, σ'_z and v) for the analysis in the plastic zone ($a \le r < \rho$). Five governing equations are required to be established by combining the compatibility equations, the equilibrium equations, the SWRC and stress-strain relationships of soils as follows. These equations are divided into two groups as both Eulerian and Lagrangian descriptions are involved.

3.4.1.1 PDEs in the Eulerian description

Logarithmic strain definitions are adopted to account for large deformation in the plastic zone, which are expressed as

$$\varepsilon_r = -\ln\left(\mathrm{d}r/\mathrm{d}r_0\right) \tag{3.43}$$

$$\varepsilon_\theta = -\ln\left(r/r_0\right) \tag{3.44}$$

$$\varepsilon_v = \varepsilon_r + \varepsilon_\theta = -\ln\left(v/v_0\right) \tag{3.45}$$

The compatibility equation in terms of r and v can be derived by combining Eqs. (3.43), (3.44) and (3.45):

$$\mathrm{d}r = \frac{vr_0}{v_0 r}\mathrm{d}r_0 \tag{3.46}$$

Substituting the SWRC into the stress equilibrium equation (3.3) gives

$$\mathrm{d}\sigma'_r - \frac{\partial\left(S_r s\right)}{\partial v}\mathrm{d}v = \left(\sigma'_\theta - \sigma'_r\right)\frac{\mathrm{d}r}{r} \tag{3.47}$$

Eqs. (3.46) and (3.47) are the two PDEs defined for a given time in the Eulerian description.

3.4.1.2 PDEs in the Lagrangian description

For a given material point, the incremental form of the stress-strain relationships is defined in the Lagrangian description and can be finally written as

$$\begin{bmatrix} a_{21} & a_{22} & a_{23} & a_{24} \\ a_{31} & a_{32} & a_{33} & a_{34} \\ a_{41} & a_{42} & a_{43} & a_{44}+1/v \end{bmatrix} \begin{bmatrix} \mathrm{D}\sigma'_r \\ \mathrm{D}\sigma'_\theta \\ \mathrm{D}\sigma'_z \\ \mathrm{D}v \end{bmatrix} = \begin{bmatrix} -\mathrm{D}r/r \\ 0 \\ 0 \end{bmatrix} \tag{3.48}$$

The derivation of Eq. (3.48) and related coefficients are detailed below.

In the plastic zone, the stress-strain relationship can be written in the incremental form as

$$\mathrm{D}\varepsilon_{ii}^{\mathrm{p}} = \Lambda B_{ii} = \Lambda \frac{\partial g}{\partial \sigma'_{ii}} = \Lambda \left(\frac{\partial g}{\partial p'} \frac{\partial p'}{\partial \sigma'_{ii}} + \frac{\partial g}{\partial q} \frac{\partial q}{\partial \sigma'_{ii}} \right) \tag{3.49}$$

$$\mathrm{D}\varepsilon_{v}^{\mathrm{p}} = \Lambda \frac{\partial g}{\partial p'} = \Lambda B_p \tag{3.50}$$

where $\varepsilon_{ii}^{\mathrm{p}}$ represents the plastic component of ε_{ii} (ii=r, θ, z); Λ is a scalar multiplier.

Differentiating the yield function (3.15) gives:

$$\frac{\partial f}{\partial p'} \mathrm{D}p' + \frac{\partial f}{\partial q} \mathrm{D}q + \frac{\partial f}{\partial p'_c(s)} \frac{\partial p'_c(s)}{\partial s} \mathrm{D}s + \frac{\partial f}{\partial p'_{\mathrm{c}}(s)} \frac{\partial p'_{\mathrm{c}}(s)}{\partial p'_{\mathrm{c}}(0)} \mathrm{D}p'_{\mathrm{c}}(0) = 0 \tag{3.51}$$

Substituting the Eqs. (3.17), (3.19) and (3.50) into Eq. (3.51) leads to:

$$\frac{\partial f}{\partial p'} \mathrm{D}p' + \frac{\partial f}{\partial q} \mathrm{D}q + \frac{\partial f}{\partial p'_c(s)} \frac{\partial p'_c(s)}{\partial s} \mathrm{D}s + \frac{\partial f}{\partial p'_{\mathrm{c}}(s)} \frac{\partial p'_{\mathrm{c}}(s)}{\partial p'_{\mathrm{c}}(0)} \frac{v p'_{\mathrm{c}}(0)}{\lambda(0)-\kappa} \Lambda \frac{\partial g}{\partial p'} = 0 \tag{3.52}$$

Then Λ can be expressed as

$$\Lambda = \frac{1}{K_{\mathrm{p}}} \left(A_r \mathrm{D}\sigma'_r + A_\theta \mathrm{D}\sigma'_\theta + A_{\mathrm{z}} \mathrm{D}\sigma'_{\mathrm{z}} + A_{\mathrm{s}} \mathrm{D}s \right) \tag{3.53}$$

where A_{ii} (ii=r, θ, z), A_{s} and K_{p} can be generally expressed as

$$A_{ii} = \frac{\partial f}{\partial \sigma'_{ii}} = \frac{\partial f}{\partial p'} \frac{\partial p'}{\partial \sigma'_{ii}} + \frac{\partial f}{\partial q} \frac{\partial q}{\partial \sigma'_{ii}} \tag{3.54}$$

$$A_{\mathrm{s}} = \frac{\partial f}{\partial s} = \frac{\partial f}{\partial p'_{\mathrm{c}}(s)} \frac{\partial p'_{\mathrm{c}}(s)}{\partial s} \tag{3.55}$$

$$K_{\mathrm{p}} = -\frac{\partial f}{\partial p'_{\mathrm{c}}(s)} \frac{\partial p'_{\mathrm{c}}(s)}{\partial p'_{\mathrm{c}}(0)} \frac{v p'_{\mathrm{c}}(0)}{\lambda(0)-\kappa} B_p \tag{3.56}$$

Substituting Eq. (3.53) into Eqs. (3.49) and (3.50), the plastic strains can be shown as

$$\begin{bmatrix} \mathrm{D}\varepsilon_\theta^{\mathrm{p}} \\ \mathrm{D}\varepsilon_z^{\mathrm{p}} \\ \mathrm{D}\varepsilon_v^{\mathrm{p}} \end{bmatrix} = \frac{1}{K_{\mathrm{p}}} \begin{bmatrix} A_r B_\theta & A_\theta B_\theta & A_z B_\theta & A_v B_\theta \\ A_r B_z & A_\theta B_z & A_z B_z & A_v B_z \\ A_r B_p & A_\theta B_p & A_z B_p & A_v B_p \end{bmatrix} \begin{bmatrix} \mathrm{D}\sigma_r' \\ \mathrm{D}\sigma_\theta' \\ \mathrm{D}\sigma_z' \\ \mathrm{D}v \end{bmatrix} \tag{3.57}$$

where

$$A_v = \frac{\partial f}{\partial v} = A_s \frac{\partial s}{\partial v} \tag{3.58}$$

The total strain is the sum of elastic and plastic strain components, which can be obtained by combining Eqs. (3.20), (3.21) and (3.57):

$$\begin{bmatrix} \mathrm{D}\varepsilon_\theta \\ \mathrm{D}\varepsilon_z \\ \mathrm{D}\varepsilon_v \end{bmatrix} = \begin{bmatrix} a_{21} & a_{22} & a_{23} & a_{24} \\ a_{31} & a_{32} & a_{33} & a_{34} \\ a_{41} & a_{42} & a_{43} & a_{44} \end{bmatrix} \begin{bmatrix} \mathrm{D}\sigma_r' \\ \mathrm{D}\sigma_\theta' \\ \mathrm{D}\sigma_z' \\ \mathrm{D}v \end{bmatrix} \tag{3.59}$$

where

$$a_{21} = \frac{-\mu}{E} + \frac{A_r B_\theta}{K_{\mathrm{p}}} \tag{3.60}$$

$$a_{22} = \frac{1}{E} + \frac{A_\theta B_\theta}{K_{\mathrm{p}}} \tag{3.61}$$

$$a_{23} = \frac{-\mu}{E} + \frac{A_z B_\theta}{K_{\mathrm{p}}} \tag{3.62}$$

$$a_{24} = \frac{A_v B_\theta}{K_{\mathrm{p}}} \tag{3.63}$$

$$a_{31} = \frac{-\mu}{E} + \frac{A_r B_z}{K_{\mathrm{p}}} \tag{3.64}$$

$$a_{32} = \frac{-\mu}{E} + \frac{A_\theta B_z}{K_{\mathrm{p}}} \tag{3.65}$$

$$a_{33} = \frac{1}{E} + \frac{A_z B_z}{K_{\mathrm{p}}} \tag{3.66}$$

$$a_{34} = \frac{A_v B_z}{K_p} \tag{3.67}$$

$$a_{41} = \frac{1-2\mu}{E} + \frac{A_r B_p}{K_p} \tag{3.68}$$

$$a_{42} = \frac{1-2\mu}{E} + \frac{A_\theta B_p}{K_p} \tag{3.69}$$

$$a_{43} = \frac{1-2\mu}{E} + \frac{A_z B_p}{K_p} \tag{3.70}$$

$$a_{44} = \frac{A_v B_p}{K_p} \tag{3.71}$$

Finally, by substituting Eqs. (3.44), (3.45) and $\mathrm{D}\varepsilon_z = 0$ into Eq. (3.59), we can obtain Eq. (3.48).

For convenient references Table 3.2 and Table 3.3 list the coefficients related to the constitutive equations for the MCC-based and CASM-based unsaturated models.

Table 3.2 Coefficients related to constitutive equations for the MCC-based unsaturated model

Coefficients	Functions
B_{ii}	$\frac{M^2-\eta^2}{3M^2p'}+\frac{3(\sigma'_{ii}-p')}{M^2(p')^2}$
B_p	$\frac{M^2-\eta^2}{M^2p'}$
A_{ii}	$\frac{M^2-\eta^2}{3M^2p'}+\frac{3(\sigma'_{ii}-p')}{M^2(p')^2}$
$\frac{\partial f}{\partial p'_c(s)}$	$-\frac{1}{p}$
$p'_{\mathrm{c}}(0)$	$p'_{\mathrm{n}}\left[\frac{p'_{\mathrm{c}}(s)}{p'_{\mathrm{n}}}\right]^{\frac{\lambda(s)-\kappa}{\lambda(0)-\kappa}}$
$\frac{\partial p'_{\mathrm{c}}(s)}{\partial p'_{\mathrm{c}}(0)}$	$\frac{\lambda(0)-\kappa}{\lambda(s)-\kappa}\left[\frac{p'_{\mathrm{c}}(0)}{p'_{\mathrm{n}}}\right]^{\frac{\lambda(0)-\lambda(s)}{\lambda(0)-\kappa}}$
$\frac{\partial p'_{\mathrm{c}}(s)}{\partial s}$	$\beta(1-\alpha)e^{-\beta s}p'_{\mathrm{c}}(s)\lambda(0)\frac{\lambda(0)-\kappa}{\left[\lambda(s)-\kappa\right]^2}\ln\left[\frac{p'_{\mathrm{c}}(0)}{p'_{\mathrm{n}}}\right]$
A_s	$-\frac{p'_c(s)}{p'}\lambda(0)\beta(1-\alpha)e^{-\beta s}\frac{\lambda(0)-\kappa}{\left[\lambda(s)-\kappa\right]^2}\ln\left[p'_c(0)\right]$
K_{p}	$\frac{vp'_{\mathrm{c}}(0)}{\lambda(s)-\kappa}\left[\frac{p'_{\mathrm{c}}(0)}{p'_{\mathrm{n}}}\right]^{\frac{\lambda(0)-\lambda(s)}{\lambda(0)-\kappa}}\frac{M^2-\eta^2}{M^2(p')^2}$

Table 3.3 Coefficients related to constitutive equations for the CASM-based unsaturated model

Coefficients	Functions
B_{ii}	$\dfrac{9\left[M-\eta+\left(9+3M-2M\eta\right)\left(\sigma'_{ii}-p'\right)/2q\right]}{p'\left(2\eta+3\right)\left(3-\eta\right)}$
B_p	$\dfrac{27\left(M-\eta\right)}{p'\left(2\eta+3\right)\left(3-\eta\right)}$
A_{ii}	$\dfrac{1-n^*\ln r^*\left(\eta/M\right)^2}{3\ln r^* p'}+\dfrac{3\left(\sigma'_{ii}-p'\right)n^*\eta^{n^*-1}}{2M^{n^*}qp'}$
$\dfrac{\partial f}{\partial p'_c\left(s\right)}$	$\dfrac{-1}{\ln r^* p'_c\left(s\right)}=\dfrac{-1}{\ln r^* p' r^* \exp\left(\eta/M\right)^{n^*}}$
$p'_{\mathrm{c}}\left(0\right)$	$p'_{\mathrm{n}}\left[\dfrac{p'_{\mathrm{c}}\left(s\right)}{p'_{\mathrm{n}}}\right]^{\frac{\lambda(s)-\kappa}{\lambda(0)-\kappa}}$
$\dfrac{\partial p'_{\mathrm{c}}\left(s\right)}{\partial p'_{\mathrm{c}}\left(0\right)}$	$\dfrac{\lambda\left(0\right)-\kappa}{\lambda\left(s\right)-\kappa}\left[\dfrac{p'_{\mathrm{c}}\left(0\right)}{p'_{\mathrm{n}}}\right]^{\frac{\lambda(0)-\lambda(s)}{\lambda(0)-\kappa}}$
$\dfrac{\partial p'_{\mathrm{c}}\left(s\right)}{\partial s}$	$\beta\left(1-\alpha\right)e^{-\beta s}p'_{\mathrm{c}}\left(s\right)\lambda\left(0\right)\dfrac{\lambda\left(0\right)-\kappa}{\left[\lambda\left(s\right)-\kappa\right]^2}\ln\left[\dfrac{p'_{\mathrm{c}}\left(0\right)}{p'_{\mathrm{n}}}\right]$
A_s	$\dfrac{p'_c\left(s\right)}{p'e^{\ln r^*\left(\eta/M\right)^n}}\lambda\left(0\right)\beta\left(1-\alpha\right)e^{-\beta s}\dfrac{\lambda\left(0\right)-\kappa}{\left[\lambda\left(s\right)-\kappa\right]^2}\ln\left[p'_c\left(0\right)\right]$
K_{p}	$\dfrac{vp'_{\mathrm{c}}\left(0\right)}{\ln r^* p'_c\left(s\right)}\dfrac{1}{\lambda\left(s\right)-\kappa}\left[\dfrac{p'_{\mathrm{c}}\left(0\right)}{p'_{\mathrm{n}}}\right]^{\frac{\lambda(0)-\lambda(s)}{\lambda(0)-\kappa}}\dfrac{27\left(M-\eta\right)}{p'\left(2\eta+3\right)\left(3-\eta\right)}$

3.4.2 HEL approach and calculation procedures

Five first-order PDEs are obtained for the analysis in the plastic zone, where Eqs. (3.46) and (3.47) are given in the Eulerian description (i.e. for a given time) and Eq. (3.48) is in the Lagrangian description (i.e. for a given particle). A novel HEL approach is developed to solve the complicated system of PDEs as follows.

The hollow cylinder can be discretized into (m-1) concentric annuli with m nodes while the whole loading process can be discretized into a few load steps. Figure 3.3 shows the nonlinear distribution of nodes in load step (0) (i.e. before loading), and the radial position of node (i) satisfies:

$$\begin{cases} r_{(i+1)}^{(0)} = \omega r_{(i)}^{(0)} = \omega^{i-1}\, a_0 \\ \omega = \left(b_0/a_0\right)^{1/(m-1)} \end{cases} \tag{3.72}$$

where the subscript "$_{(i)}$" (i=1, 2, 3, …, m) denotes the node number and the superscript "$^{(0)}$" denotes the load step number.

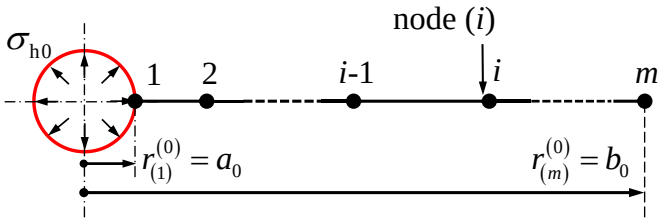

Figure 3.3 Definition of nodes before loading

During the loading process (i.e. the load step increases from (0) to (j)), the initial radial position of node (i) is defined as $r_{(i)}^{(0)}$ and the current information (r, σ_r', σ_θ', σ_z', and v) at node (i) is updated in each step. For convenience, a vector is introduced to store the node information:

$$\mathbf{x}_{(i)}^{(j)} = \left[r_{(i)}^{(j)}, \sigma_{r(i)}'^{(j)}, \sigma_{\theta(i)}'^{(j)}, \sigma_{z(i)}'^{(j)}, v_{(i)}^{(j)} \right]^{\mathrm{T}} \tag{3.73}$$

where the superscript "$^{(j)}$" denotes load step (j).

In order to deal with the PDEs, it is defined that the elastoplastic boundary expands to node (j) at the end of load step (j) (i.e. $\rho_0^{(j)} = r_{(j)}^{(0)}$ and $\rho^{(j)} = r_{(j)}^{(j)}$). Consequently, the distribution (along the radial axis at a given time) and evolution (along the time scale of each material point) of stresses and displacements can be associated via the elastoplastic boundary, and the change of $\mathbf{x}_{(i)}^{(j)}$ with nodes and load steps can be seen in Figure 3.4. In Figure 3.4 (a), the information vector $\mathbf{x}_{(i)}^{(j)}$ in the elastic zone (i.e. $i > j$) can be calculated by the elastic solution in Section 4, while $\mathbf{x}_{(i)}^{(j)}$ in the plastic zone (i.e. $i < j$) needs to be computed by solving the governing PDEs. At the elastoplastic boundary, $\mathbf{x}_{(j)}^{(j)}$ can also be derived by the elastic solution with $r = \rho_0^{(j)}$, which serves as the known boundary values for the plastic analysis.

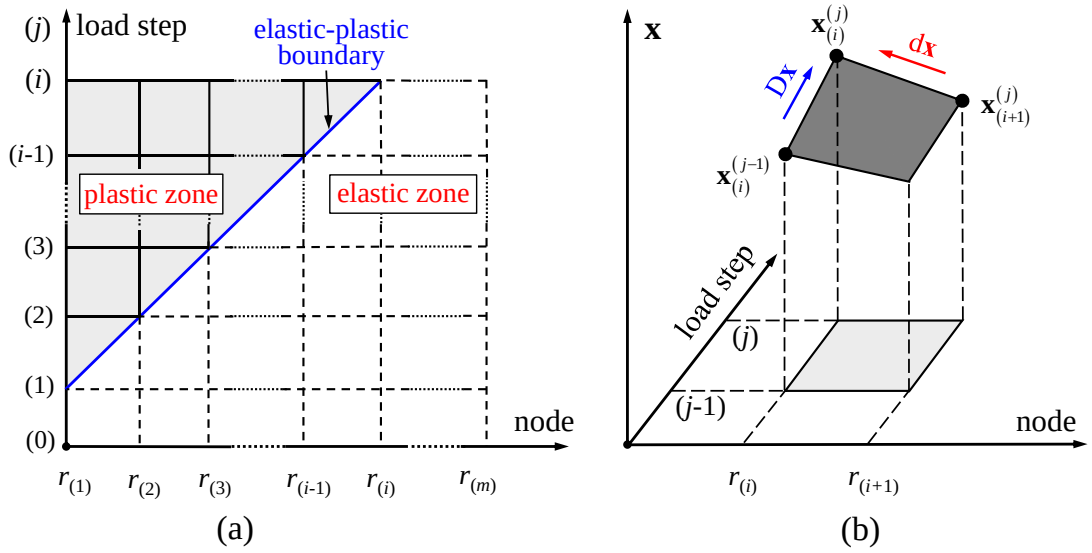

Figure 3.4 $\mathbf{x}_{(i)}^{(j)}$ with nodes and load steps:

(a) two-dimensional schematic; (b) three-dimensional schematic

For self-similar cavity expansion problems, the increments of $\mathbf{x}$ (i.e. D$\mathbf{x}$ and d$\mathbf{x}$ in Figure 3.4 (b)) can be unified into either the Eulerian description or the Lagrangian description (Collins et al., 1992; Chen, S.L. and Abousleiman, Y.N., 2013). Instead, for the present non-self-similar expansion problem, the increments of $\mathbf{x}$ are solved in the

forms of both Eulerian and Lagrangian descriptions in the advanced HEL approach. When the (i)-th node is loaded from load step ($j-1$) to load step (j), D$\mathbf{x}$ should be

$$\mathrm{D}\mathbf{x} = \mathbf{x}_{(i)}^{(j)} - \mathbf{x}_{(i)}^{(j-1)} \tag{3.74}$$

On the other hand, in the (j)-th load step, the increment of $\mathbf{x}$ from node (i+1) to node (i) is defined as

$$\mathrm{d}\mathbf{x} = \mathbf{x}_{(i)}^{(j)} - \mathbf{x}_{(i+1)}^{(j)} = \mathrm{D}\mathbf{x} + \mathbf{x}_{(i)}^{(j-1)} - \mathbf{x}_{(i+1)}^{(j)} \tag{3.75}$$

Combining Eqs. (3.47), (3.48) and (3.75), the PDEs can be transformed into

$$\mathbf{K}\left[\mathrm{D}\sigma_r', \mathrm{D}\sigma_\theta', \mathrm{D}\sigma_z', \mathrm{D}v\right]^{\mathrm{T}} = \left[F_1, F_2, 0, 0\right]^{\mathrm{T}} \tag{3.76}$$

where $\mathbf{K}$, F_1, and F_2 are defined respectively as

$$\mathbf{K} = \begin{bmatrix} 1 & 0 & 0 & a_{14} \\ a_{21} & a_{22} & a_{23} & a_{24} \\ a_{31} & a_{32} & a_{33} & a_{34} \\ a_{41} & a_{42} & a_{43} & a_{44} + 1/v \end{bmatrix} \tag{3.77}$$

$$a_{14} = -\frac{\partial\left(S_{\mathrm{r}} s\right)}{\partial v} \tag{3.78}$$

$$F_1 = \left(\sigma_\theta' - \sigma_r'\right)\frac{\mathrm{d}r}{r} + \sigma_{r(i+1)}'^{(j)} - \sigma_{r(i)}'^{(j-1)} + a_{14}\left(v_{(i+1)}^{(j)} - v_{(i)}^{(j-1)}\right) \tag{3.79}$$

$$F_2 = -\mathrm{D}r/r \tag{3.80}$$

The modified Euler's method with second-order accuracy is chosen to solve the PDEs (3.46) and (3.76), and the procedures are detailed as follows:

(i) Calculate an approximate value of $\mathrm{d}r$ by Eq. (3.46) with $\mathrm{d}r_0 = (1-\omega)r_{(i)}^{(0)}$ and $\mathbf{x}$=$\mathbf{x}_{(i+1)}^{(j)}$; then calculate approximate $r_{(i)}^{(j)}$ by $r_{(i)}^{(j)} = r_{(i+1)}^{(j)} + \mathrm{d}r$;

(ii) Calculate $\mathrm{D}r$ by $\mathrm{D}r = r_{(i)}^{(j)} - r_{(i)}^{(j-1)}$; calculate approximate values of $\left[\mathrm{D}\sigma_r', \mathrm{D}\sigma_\theta', \mathrm{D}\sigma_z', \mathrm{D}v\right]^{\mathrm{T}}$ by Eq. (3.76) with $\mathbf{x}$=$\mathbf{x}_{(i)}^{(j-1)}$ in $\mathbf{K}$ and F_2, and $\mathbf{x}$=$\mathbf{x}_{(i+1)}^{(j)}$ in F_1;

(iii) Update $\mathbf{x}$=$\mathbf{x}_{(i)}^{(j)}$ with $\left[\mathrm{D}\sigma_r', \mathrm{D}\sigma_\theta', \mathrm{D}\sigma_z', \mathrm{D}v\right]^{\mathrm{T}}$ and $\mathbf{x}_{(i)}^{(j)} = \mathbf{x}_{(i)}^{(j-1)} + \mathrm{D}\mathbf{x}$;

(iv) Back-calculate more accurate values of $\mathbf{x}_{(i)}^{(j)}$ by Eqs. (3.46) and (3.76) with $\mathbf{x}=\left(\mathbf{x}_{(i)}^{(j-1)}+\mathbf{x}_{(i)}^{(j)}\right)/2$ and $\mathbf{x}=\left(\mathbf{x}_{(i)}^{(j)}+\mathbf{x}_{(i+1)}^{(j)}\right)/2$ for those related to the Lagrangian and Eulerian descriptions, respectively;

(v) In load step (j), calculate $\mathbf{x}_{(i)}^{(j)}$ node-by-node from the elastoplastic boundary to the inner cavity wall (i.e. from $\mathbf{x}_{(j)}^{(j)}$ to $\mathbf{x}_{(1)}^{(j)}$), and the information of all the nodes in the (j)-th load step can be determined;

(vi) Finally, increase the load step from (j) to (j+1) and let $\rho_0^{(j+1)}=r_{(j+1)}^{(0)}$; calculate $\mathbf{x}_{(i)}^{(j+1)}$ node-by-node following procedures (i)-(v). For the whole loading process, gradually increase (j) until the inner cavity radius reaches a final value, a_{end}.

3.4.3 Analysis in the fully plastic expansion stage

The fully plastic expansion stage, namely the loading-induced plastic zone expanding to the outer cylinder wall (i.e. $\rho_0=b_0$), may occur once the thickness of the soil cylinder is finite. In this case, the governing PDEs (3.46) and (3.76) still hold, while their boundary values at $r=\rho$ should be changed to those at $r=b$.

For a given b ($b>r_{(m)}^{(m)}$), $\mathrm{D}\left(\sigma_r'-S_{\mathrm{r}}s\right)$ remains zero at $r=b$ since the total radial stress is constant at $r=b$. Together with Eq. (3.48), it gives

$$\mathbf{K}\left[\mathrm{D}\sigma_r',\mathrm{D}\sigma_\theta',\mathrm{D}\sigma_z',\mathrm{D}v\right]^{\mathrm{T}}=\left[0,-\mathrm{D}b/b,0,0\right]^{\mathrm{T}} \tag{3.81}$$

The boundary values at $r=b$ can be derived from Eq. (3.81), and $\mathbf{x}_{(i)}^{(j)}$ can be calculated node-by-node from $\mathbf{x}_{(m)}^{(j)}$ to $\mathbf{x}_{(1)}^{(j)}$ following the above procedures.

3.5 Comparison of Eulerian, Lagrangian and HEL approaches

The differences and connections between the proposed HEL approach and other commonly used methods for large strain cavity expansion analysis are compared and

discussed as follows.

In the Eulerian approach for self-similar expansion problems (e.g. assume $b=\infty$ in Figure 3.1), the loading history of a particle at $r=a$ is equivalent to the field distribution from $r=\infty$ to $r=a$ due to the self-similarity of stresses and deformation (e.g. Figure 3.5(a)). Therefore, the cavity expansion analysis can be performed by tracing the loading history of a material point with auxiliary variables (i.e. path AC) (Chen, S.L. and Abousleiman, Y.N., 2013; Su, 2021), or by focusing on field distributions for a given time with proper timescales (i.e. path BC) (Hill, 1950; Collins et al., 1992; Yu and Carter, 2002; Zhou et al., 2021a; Carter and Yu, 2022). Overall, the information of j nodes in the plastic zone at the end of (j)-th load step can be determined via path AC (or BC) due to the self-similarity.

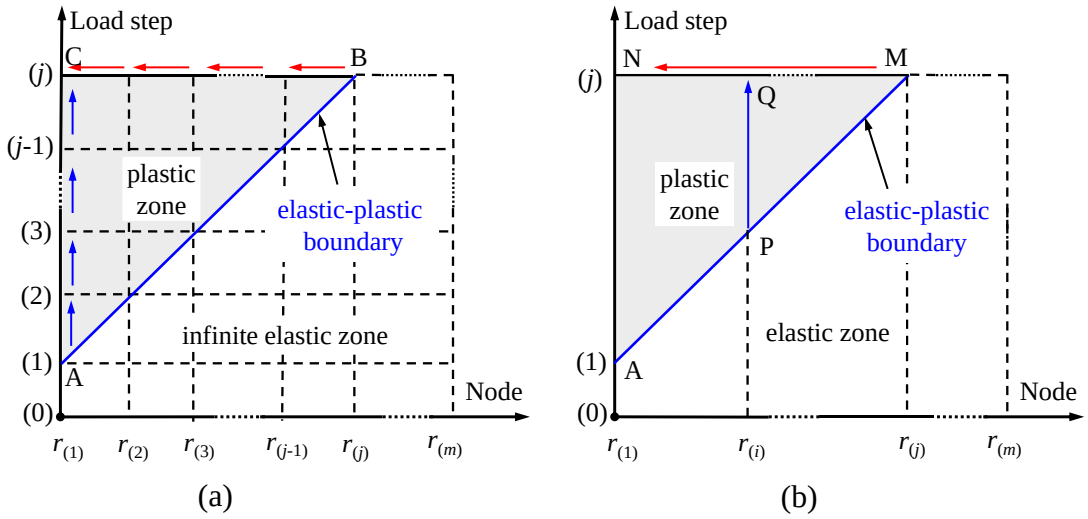

Figure 3.5 Schematic of Eulerian and Lagrangian approaches: (a) Eulerian approach; (b) Lagrangian approach

In the Lagrangian approach (see Figure 3.5(b)), the relationship between the effective stress and total strain for node (i) should be given analytically to account for path PQ. For drained cavity expansion in Mohr-Coulomb materials, the stress distribution following path MN can be directly calculated by combining the yield function and stress equilibrium equation, and then the deformation distribution can be obtained with the known stress field and the analytical stress-total strain relationships (Chadwick, 1959; Yu and Houlsby, 1991; Yu, 1992; Yu, 1993). Similarly, for cavity expansion in undrained saturated Cam

Clay soils, the deformation (or strain) distribution following path MN can be readily determined relying on the constant-volume assumption. Then the stress distribution can be back-solved from the strain field and the stress-total strain relationships (Collins and Yu, 1996; Zhuang et al., 2021).

The HEL approach, in which the PDEs are expressed in the forms of both Eulerian and Lagrangian descriptions and are solved simultaneously (Figure 3.4(a)), is powerful for cavity expansion analysis under various conditions, including drained/undrained conditions, soil cylinder of finite/infinite thickness, saturated/unsaturated state of soils, and various constitutive models. The HEL approach tends to have higher computation efficiency than common numerical methods. For example, when studying drained cavity expansion with critical state models, Osinov and Cudmani (2001) searched the stress fields that satisfy stress boundary conditions and equilibrium equations by multiple iterations and then calculated strain fields node-by-node. This method is relatively time-consuming as it needs to calculate the information of a total of $m \times j \times$ iteration times nodes. Comparing to the finite element/difference methods that need to calculate the deformation energies in the whole region (i.e. $m \times j$ nodes), the HEL approach is also more efficient (calculate the information of $j(j-1)/2$ nodes) because of the analytical solutions in the elastic zone.

3.6 Special cases

The aforementioned elastoplastic cavity expansion analysis is unified and general in that different drainage conditions, the finite cylinder thickness, saturated and unsaturated states of soil, and various constitutive models are considered. Particularly, the influence of these factors is involved in a general matric that governs the elastoplastic cavity expansion behaviour in the plastic zone. In some special cases the governing PDEs and the elastic solution can be simplified more or less and can be reduced to some published solutions. Three main special cases will be discussed in the following.

3.6.1 Case 1: Self-similar cavity expansion problems

If the cylinder thickness is infinite (i.e. $b_0/a_0=\infty$), the considered cylinder in this chapter will behave in a self-similar manner and the Eulerian approach is most widely used for cavity expansion analyses, especially for those with complex constitutive models. It will be proven that the present solution can also reproduce the self-similar solutions derived by the Eulerian approach, and the relationship between the auxiliary variable approach and the HEL approach will be further discussed.

3.6.1.1 Solution in the elastic zone

For cavity expansion in an infinite thickness of soil, the stresses and displacement in saturated/unsaturated soils share the same form (Chen, S.L. and Abousleiman, 2012; Chen, S.L. and Abousleiman, Y.N., 2013; Chen, H. et al., 2020b):

$$\sigma_r'=\sigma_{\mathrm{h0}}'+\left(\sigma_{r\rho}'-\sigma_{\mathrm{h0}}'\right)\left(\rho/r\right)^2 \tag{3.82}$$

$$\sigma_\theta'=\sigma_{\mathrm{h0}}'-\left(\sigma_{r\rho}'-\sigma_{\mathrm{h0}}'\right)\left(\rho/r\right)^2 \tag{3.83}$$

$$\sigma_z'=\sigma_{\mathrm{v0}}' \tag{3.84}$$

$$S_{\mathrm{r}}=S_{\mathrm{r0}} \tag{3.85}$$

$$s=s_0 \tag{3.86}$$

$$v=v_0 \tag{3.87}$$

$$\sigma_{r\rho}'=\sigma_{\mathrm{h0}}'+\sqrt{\frac{q_\rho^2-q_0^2}{3}} \tag{3.88}$$

$$\sigma_{\theta\rho}'=\sigma_{\mathrm{h0}}'-\sqrt{\frac{q_\rho^2-q_0^2}{3}} \tag{3.89}$$

$$q_\rho=f^{-1}\left[p_0',p_{\mathrm{c0}}'(s)\right] \tag{3.90}$$

$$\frac{u}{r}=\frac{(1+\mu)\left(\sigma_{r\rho}'-\sigma_{\mathrm{h0}}'\right)}{E\left(v_0,p_0'\right)}\left(\frac{\rho}{r}\right)^2 \tag{3.91}$$

where $\sigma_{\theta\rho}'$ and q_ρ are the circumferential effective stress and deviatoric stress at the

elastoplastic boundary. Eqs. (3.82)~(3.91) can be proven as follows:

(i) At a sufficiently large area, the stresses and displacements can hardly be affected by the internal loading at the inner cavity wall. Therefore, we have $\mathrm{D}\sigma_r' + \mathrm{D}\sigma_\theta' = 0$;

(ii) According to Eq. (3.22), $\mathrm{D}\sigma_r' + \mathrm{D}\sigma_\theta'$ does not vary with the radius so that $\mathrm{D}\sigma_r' + \mathrm{D}\sigma_\theta' = 0$ is satisfied in the whole elastic zone;

(iii) Then the mean effective stress and specific volume, according to Eqs. (3.27) and (3.28), are also unchanged during the loading process;

(iv) With the constant volume in the elastic zone, the degree of saturation and suction are also constants and equal to their initial values, respectively, so Eqs. (3.85) and (3.86) are proven;

(v) Once the mean effective stress does not vary with the loading process, Eq. (3.33) can be transformed into $\sigma_\mathrm{h}' - C_\rho = \sigma_{\mathrm{h}0}'$. Substituting this equation and Eq. (3.32) into Eq. (3.31), it can be found Eqs. (3.82)~(3.84) are proven;

(vi) Eq. (3.88) can be easily derived by substituting Eqs. (3.82)~(3.84) into Eq. (3.8), and Eq. (3.89) will then be obtained with Eqs. (3.83) and (3.88);

(vi) Finally, substituting $\sigma_\mathrm{h}' - C_\rho = \sigma_{\mathrm{h}0}'$ and $\mathrm{D}p' = 0$ into Eq. (3.38) leads to the proof of Eq. (3.91).

3.6.1.2 Solution in the plastic zone

It is well-known that the governing PDEs in the plastic zone can be transformed into a set of ODEs with the aid of an auxiliary variable or a proper time scale (e.g. $(r - r_0)/r$, r_0/r, and r/ρ) (Hill, 1950; Collins et al., 1992; Chen, S.L. and Abousleiman, Y.N., 2013; Su, 2021). To clear the relationship between the HEL approach and the Eulerian approach, the latter method can be understood as follows:

(i) Due to the self-similar characteristic, the load history of a material point at *r*=*a* is equivalent to the field distribution from $r = \infty$ to $r = a$. It means there is a

special loading pattern that can link the load history and field movement by $\mathrm{D}\mathbf{x}=\mathrm{d}\mathbf{x}$ (but $\mathrm{D}r\neq\mathrm{d}r$ since $\mathrm{D}r>0>\mathrm{d}r$).

(ii) Under this special loading pattern, the cavity expansion analysis can be conducted merely by tracing the load history of a material point (or by calculating the field movement for a given time). In other words, the PDEs in terms of time and spatial derivatives can be transformed into the ODEs in either the Lagrangian description or the Eulerian description.

(iii) To reduce the PDEs into the ODEs, a proper auxiliary variable ξ is usually chosen to eliminate dr (or Dr) by $\mathrm{d}\xi=\mathrm{D}\xi$, and ξ should be monotonous in terms of time and radius.

There are several available auxiliary variables to link Dr and dr, for example, r/ρ, $\left(r-r_0\right)/r$, and r_0/r (Collins et al., 1992; Chen, S.L. and Abousleiman, 2012; Su, 2021). What is the link among them? For self-similar problems, Chen, S.L. and Abousleiman, Y.N. (2013) have found the unknowns in the information vector are the functions of a single variable ε_θ. In fact, $\mathrm{D}\mathbf{x}=\mathrm{d}\mathbf{x}$ means that the increases of stress components in terms of time and space are the same. As strains can be fully determined by stresses (Eq. (3.48)), $\mathrm{D}\mathbf{x}=\mathrm{d}\mathbf{x}$ indicates $\mathrm{D}\varepsilon_\theta=\mathrm{d}\varepsilon_\theta$, which gives

$$\frac{\mathrm{D}r}{r}=\frac{\mathrm{d}r}{r}-\frac{\mathrm{d}r_0}{r_0} \tag{3.92}$$

It is interesting to find Eq. (3.92) can also be derived with other auxiliary variables such as $\left(r-r_0\right)/r$ and r_0/r, which indicates ε_θ is the most fundamental auxiliary variable and other variables are its extension or transformation. Therefore, a new, fundamental auxiliary variable ε_θ is chosen here to transform the governing PDEs into ODEs.

Combining Eqs. (3.46) and (3.92), a relationship between dr and Dr is obtained as

$$\frac{\mathrm{d}r}{r}=\frac{1}{1-\left(r/r_0\right)^2\left(v_0/v\right)}\frac{\mathrm{D}r}{r} \tag{3.93}$$

Substituting Eq. (3.93) and $\mathrm{D}\mathbf{x}=\mathrm{d}\mathbf{x}$ into Eq. (3.76), we can derive that

$$\mathbf{K}\begin{bmatrix}\mathrm{D}\sigma_r'\\ \mathrm{D}\sigma_\theta'\\ \mathrm{D}\sigma'\\ \mathrm{D}v\end{bmatrix}=\frac{\mathrm{D}r}{r}\begin{bmatrix}\dfrac{\left(\sigma_\theta'-\sigma_r'\right)}{1-\left(r/r_0\right)^2\left(v_0/v\right)}\\ -1\\ 0\\ 0\end{bmatrix} \tag{3.94}$$

The governing PDEs (3.76) are totally transformed into ODEs (3.94) in terms of $\mathrm{D}r/r$ (i.e. $-\mathrm{D}\varepsilon_\theta$) with the Lagrangian descriptions, from which $\left[\mathrm{D}\sigma_r',\mathrm{D}\sigma_\theta',\mathrm{D}\sigma_z',\mathrm{D}v\right]^{\mathrm{T}}$ can be readily obtained. Actually, the commonly used auxiliary variables such as $\left(r-r_0\right)/r$, and r_0/r (Chen, S.L. and Abousleiman, Y.N., 2013; Su, 2021) are also mainly used to eliminate $\mathrm{d}r/r$ in F_1 (see Eq. (3.79)). From this point of view, the Eulerian approach is a special case of the HEL approach when $\ln\left(r/r_0\right)$ is chosen as the auxiliary variable and b_0/a_0 becomes infinite.

3.6.2 Case 2: Cavity expansions in dry soils (S_r=0)

While a cavity expands in ideally dry soils (i.e. S_r=0), the proposed solution can be further simplified as $\sigma_{\mathrm{h0}}'=\sigma_{\mathrm{h}}'$ and $S_r s$ =0.

Solutions for analysis in the elastic zone can be obtained by substituting $\sigma_{\mathrm{h0}}'=\sigma_{\mathrm{h}}'$ into Eqs. (3.31), (3.33) and (3.40):

$$\begin{cases}\sigma_r'=\sigma_{\mathrm{h}}'+C_\rho\left[\left(b/r\right)^2-1\right]\\ \sigma_\theta'=\sigma_{\mathrm{h}}'-C_\rho\left[\left(b/r\right)^2+1\right]\\ \sigma_z'=\sigma_{\mathrm{v0}}'-2\mu C_\rho\end{cases} \tag{3.95}$$

$$p'=p_0'-\frac{2}{3}\left(1+\mu\right)C_\rho \tag{3.96}$$

$$\frac{u(r)}{r}=\frac{1-2\mu+(b/r)^2}{2(1-2\mu)}\ln\left(1-\frac{\kappa}{v_0}\ln\frac{p'}{p'_0}\right) \tag{3.97}$$

For the plastic analysis, K_{p}, **K** and F_1 in Eqs. (3.56) and (3.76) can be simplified with $S_{\mathrm{r}}s=0$ as

$$K_{\mathrm{p}}=-\frac{\partial f}{\partial p'_{\mathrm{c}}(0)}\frac{vp'_{\mathrm{c}}(0)}{\lambda(0)-\kappa}B_p \tag{3.98}$$

$$\mathbf{K}=\begin{bmatrix}1 & 0 & 0 & 0\\ a_{21} & a_{22} & a_{23} & 0\\ a_{31} & a_{32} & a_{33} & 0\\ a_{41} & a_{42} & a_{43} & 1/v\end{bmatrix} \tag{3.99}$$

$$F_1=(\sigma'_\theta-\sigma'_r)\frac{\mathrm{d}r}{r}+\sigma'^{(j)}_{r(i+1)}-\sigma'^{(j-1)}_{r(i)} \tag{3.100}$$

The simplified K_{p} for selected Cam Clay models are listed in Table 3.4.

Table 3.4 K_{p} for the selected Cam Clay models under fully drained conditions

Model	OCC	MCC	CASM
K_{p}	$\frac{v}{\lambda-\kappa}\frac{M-\eta}{Mp'}$	$\frac{v}{\lambda-\kappa}\frac{M^4-\eta^4}{M^4p'}$	$\frac{v}{\lambda-\kappa}\frac{1}{\ln r^*}\frac{27(M-\eta)}{p(3+2\eta)(3-\eta)}$

Combining Eqs. (3.76), (3.99) and (3.100), the calculation of $[\mathrm{D}\sigma'_r,\mathrm{D}\sigma'_\theta,\mathrm{D}\sigma'_z,\mathrm{D}v]^{\mathrm{T}}$ can be simplified as:

$$\mathrm{D}\sigma'_r=(\sigma'_\theta-\sigma'_r)\frac{\mathrm{d}r}{r}+\sigma'^{(j)}_{r(i+1)}-\sigma'^{(j-1)}_{r(i)} \tag{3.101}$$

$$\begin{bmatrix}\mathrm{D}\sigma_\theta\\ \mathrm{D}\sigma_{\mathrm{z}}\end{bmatrix}=-\begin{bmatrix}a_{22} & a_{23}\\ a_{32} & a_{33}\end{bmatrix}^{-1}\begin{bmatrix}a_{21} & 1\\ a_{31} & 0\end{bmatrix}\begin{bmatrix}\mathrm{D}\sigma_r\\ \mathrm{D}r/r\end{bmatrix} \tag{3.102}$$

$$\frac{\mathrm{D}v}{v}=-(a_{41}\mathrm{D}\sigma'_r+a_{42}\mathrm{D}\sigma'_\theta+a_{43}\mathrm{D}\sigma'_z) \tag{3.103}$$

Finally, the node information can be calculated following the same procedures of Section 3.4.2.

3.6.3 Case 3: Undrained analysis in fully saturated soils (S_r=1 and s=0)

For cavity expansion in fully saturated soils (S_r=1 and s=0) under undrained conditions, the specific volume of soils keeps constant (i.e. $v = v_0$). This special case can also be recovered from the present solution.

In the elastic zone, the mean effective stress remains unchanged (i.e. $p' = p'_0$), and the stress components, pore water pressure, and displacements can be obtained by substituting $p' = p'_0$ and $S_r s = -u_w$ into Eqs. (3.31), (3.33), (3.34) and (3.38):

$$\sigma'_{h0} = \sigma'_h - C_\rho \tag{3.104}$$

$$\begin{cases} \sigma'_r = \sigma'_{h0} + C_\rho \left(b/r\right)^2 \\ \sigma'_\theta = \sigma'_{h0} - C_\rho \left(b/r\right)^2 \\ \sigma'_z = \sigma'_{v0} \end{cases} \tag{3.105}$$

$$u_w = \sigma_{h0} - \sigma'_h = u_{w0} - C_\rho \tag{3.106}$$

$$C_\rho = \sqrt{\frac{q_\rho^2 - q_0^2}{3}} \left(\frac{\rho}{b}\right)^2 \tag{3.107}$$

$$q_\rho = f^{-1}\left(p'_0, p'_{c0}\right) \tag{3.108}$$

$$\frac{u}{r} = \frac{C_\rho (1+\mu)}{E\left(v_0, p_0\right)} \left(\frac{b_0}{r_0}\right)^2 \tag{3.109}$$

where u_{w0} denotes the initial water pressure.

Meanwhile, the PDEs Eqs. (3.46), (3.47) and (3.48) for the plastic analysis can be simplified with the conditions of Dv=0 and $du_w = \left(\partial u_w / \partial v\right) \cdot dv$, as

$$dr = \frac{r_0}{r} dr_0 \tag{3.110}$$

$$d\sigma'_r + du_w = \left(\sigma'_\theta - \sigma'_r\right) \frac{dr}{r} \tag{3.111}$$

$$\begin{bmatrix} a_{21} & a_{22} & a_{23} \\ a_{31} & a_{32} & a_{33} \\ a_{41} & a_{42} & a_{43} \end{bmatrix} \begin{bmatrix} \mathrm{D}\sigma_r' \\ \mathrm{D}\sigma_\theta' \\ \mathrm{D}\sigma_z' \end{bmatrix} = \begin{bmatrix} -\mathrm{D}r/r \\ 0 \\ 0 \end{bmatrix} \tag{3.112}$$

The new system of PDEs in Eqs. (3.110)~(3.112) can be calculated following similar procedures in Section 3.4.2. It is interesting to find that the changes in effective stresses are only related to $\mathrm{D}r/r$ (see Eq. (3.112)) and thereby the effective stresses evolve in a self-similar manner even if the cylinder thickness is finite in this special case (Zhuang et al., 2021). It is found that the Lagrangian, Eulerian, and HEL approaches are all suitable for the analysis in this special case, and the advantages and limitations of these approaches will be further discussed in Section 3.10.3.

3.7 Results and discussion

3.7.1 Validation of the HEL approach

The proposed HEL approach is validated at first by comparing with some existing solutions in special cases of saturated and unsaturated soil with an infinite radial extent as follows.

3.7.1.1 Comparison with Chen and Abousleiman (2012; 2013)

Chen, S.L. and Abousleiman (2012) and Chen, S.L. and Abousleiman, Y.N. (2013) proposed exact solutions for expansion analysis of a cylindrical cavity in an infinite soil thickness under ideally undrained and drained conditions, respectively, adopting the MCC model. As discussed in Section 3.6, these solutions can be regarded as two special cases of the proposed solution when $b_0/a_0 \to \infty$. Cavity expansion curves predicted by their solutions and the present solution are compared in Figure 3.6~Figure 3.9, taking the same parameters for Boston Blue clay (i.e. Table 3.5). In the calculations with the proposed solution, b_0/a_0 is set as 2000 to eliminate the outer boundary effect, and the ideally drained conditions are simulated with $S_r = 0$ for simplicity. Figure 3.6~Figure 3.9 show

that the results calculated by the proposed solution are identical to those published by Chen and Abousleiman (2012, 2013) in these two typical cases, which proves the accuracy of the proposed HEL approach and the assumption of replacing r with r_0 in Eq. (3.40).

Table 3.5 MCC Parameters for Boston Blue clay (Chen and Abousleiman 2012)

R_0	σ'_{h0} /kPa	σ'_{v0} /kPa	p'_0 /kPa	q_0 /kPa	$\sigma'_{h0}/\sigma'_{v0}$	v_0
1	100	160	120	60	0.625	2.09
3	120	120	120	0	1.0	1.97
10	144	72	120	72	2.0	1.80

Note: M=1.2, $\lambda(0)$=0.15, κ=0.03, μ=0.278, and Γ=2.74 (the specific volume at p'=1kPa). The initial ambient pore water pressure is 100kPa for the undrained case.

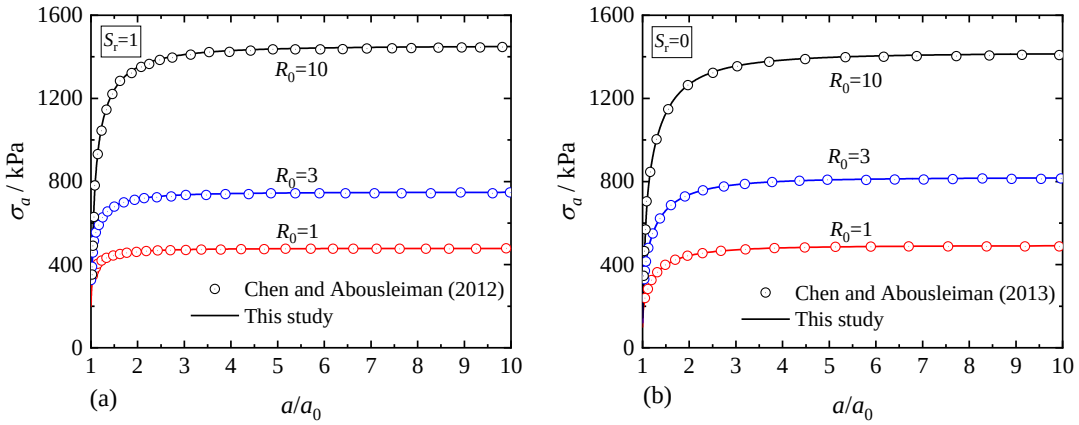

Figure 3.6 Comparison of cavity expansion curves: (a) undrained conditions; (b) drained conditions.

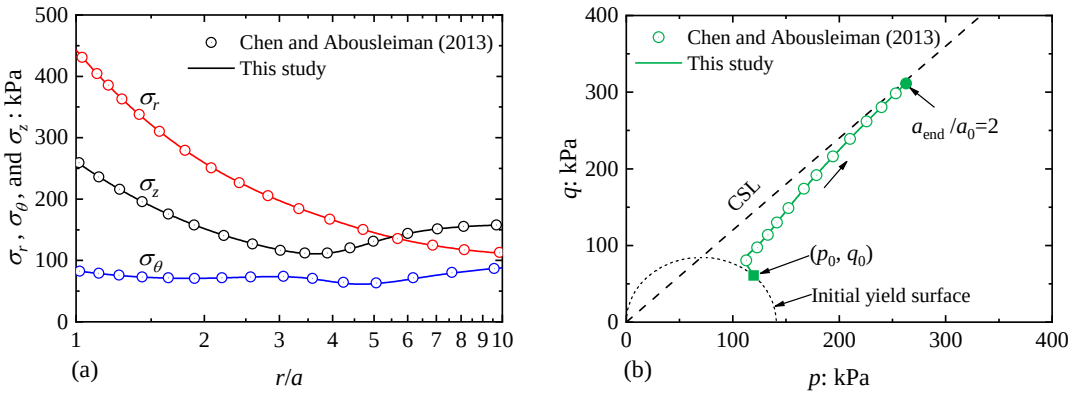

Figure 3.7 Stress distributions and stress paths under drained conditions for R_0=1: (a) stress distributions; (b) stress paths at the inner cavity wall

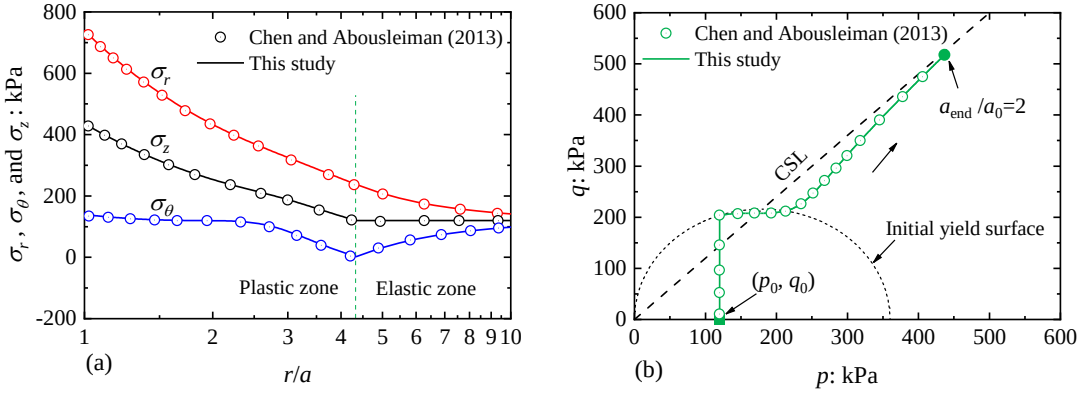

Figure 3.8 Stress distributions and stress paths under drained conditions for R_0=3: (a) stress distributions; (b) stress paths at the inner cavity wall

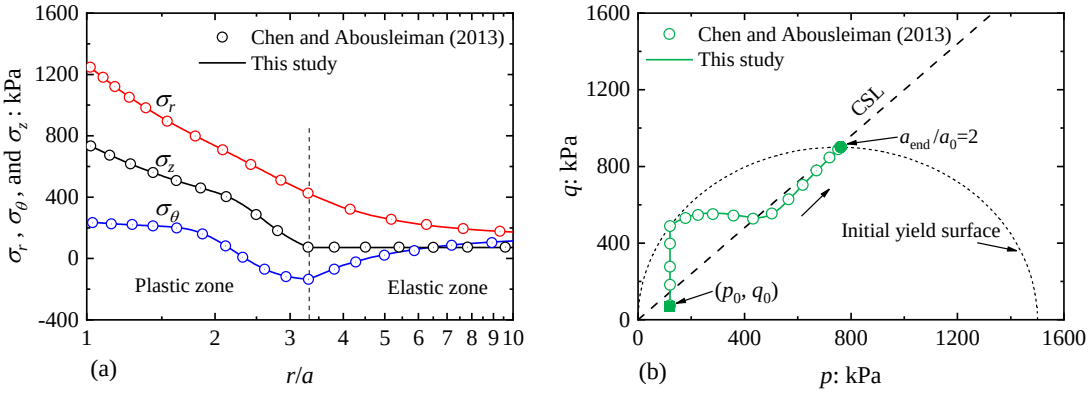

Figure 3.9 Stress distributions and stress paths under drained conditions for R_0=10: (a) stress distributions; (b) stress paths at the inner cavity wall

3.7.1.2 Comparison with Chen, H. et al. (2020b)

Using the Eulerian approach, Chen, H. et al. (2020b) proposed a solution for cylindrical cavity expansion analysis in infinite unsaturated soils under both constant suction and

constant water content conditions. To reproduce the results of Chen, H. et al. (2020b), the same soil parameters (i.e. Table 3.6) are used and b_0/a_0 is set as 2000 in the proposed solution. Predicted cavity expansion curves and stress distribution curves at the instant of a/a_0 =2 for constant suction and constant water content conditions are compared in Figure 3.10~Figure 3.12. It is shown that the results calculated by the proposed solution agree well with those of Chen, H. et al. (2020b) while $b_0/a_0 \to \infty$, which further validates the aurracy of the HEL approach. It is also found that the constant suction or constant water content conditions marginally affect the cavity expansion curves. This can be explained by that the coefficients related to drainages conditions (i.e. a_{14}, a_{24}, a_{34}, and a_{44} in Eqs. (3.76) and (3.77)) apply minimal influence on $\mathrm{D}\sigma'_{ii}$ (ii=r, θ, z) for small changes in v.

Table 3.6 UCSM Parameters for unsaturated soils (after Chen, H. et al. (2020b))

R_0	σ'_{h0} /kPa	σ'_{v0} /kPa	p_{net0} /kPa	q_0 /kPa	$\sigma'_{\mathrm{h0}}/\sigma'_{\mathrm{v0}}$
1	160	220	120	60	0.73
3	180	180	120	0	1.0
5	190	160	120	30	1.19

Note: M=1.2, $\lambda(0)$=0.15, κ=0.03, μ=0.3, α=0.65, β=0.125, λ_{se}=0.21, λ_{sr}=0.13, κ_{sr}=0.13, p'_n=10kPa, s_0=100kPa, S_{r0}=0.6, v_0=2.1. $p_{\mathrm{net0}} = p'_0 - S_{\mathrm{r0}}s_0$, which denotes the initial net mean stress.

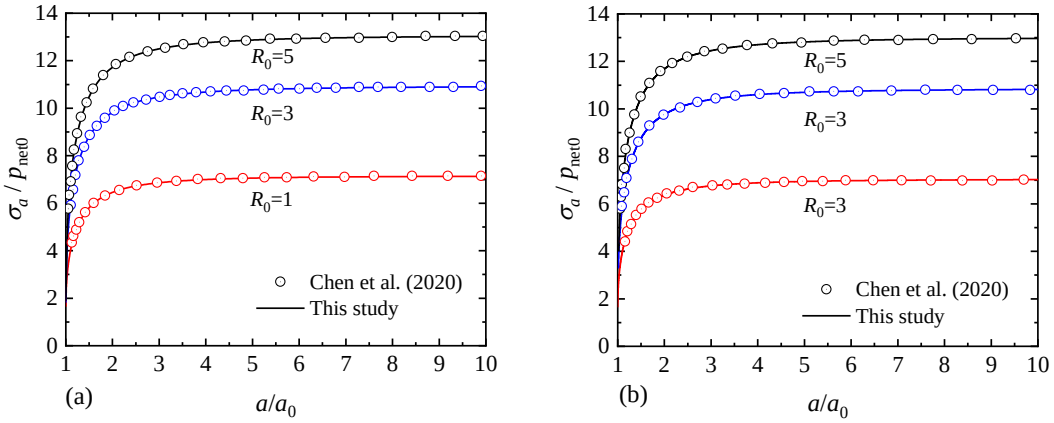

Figure 3.10 Comparison of cavity expansion curve with Chen et al. (2020): (a) constant suction conditions; (b) constant water content conditions.

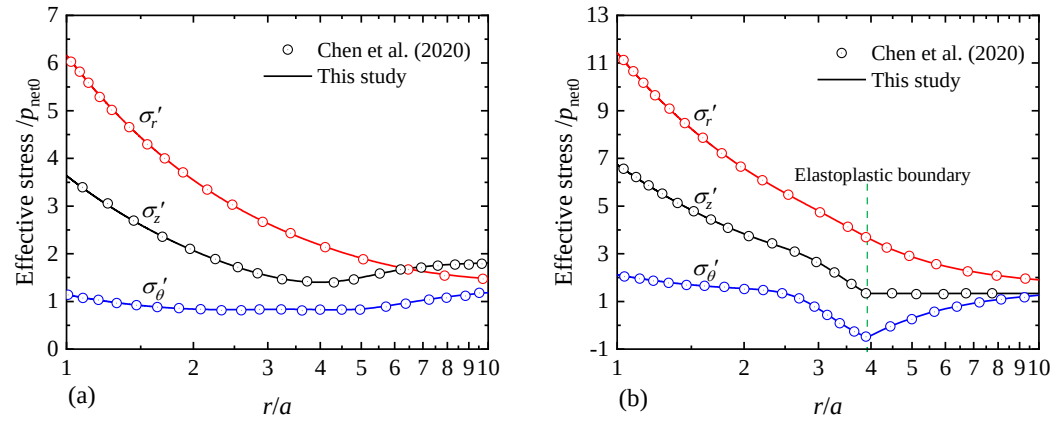

Figure 3.11 Comparison of stress distribution with Chen et al. (2020) under constant suction conditions: (a) R_0=1; (b) R_0=5.

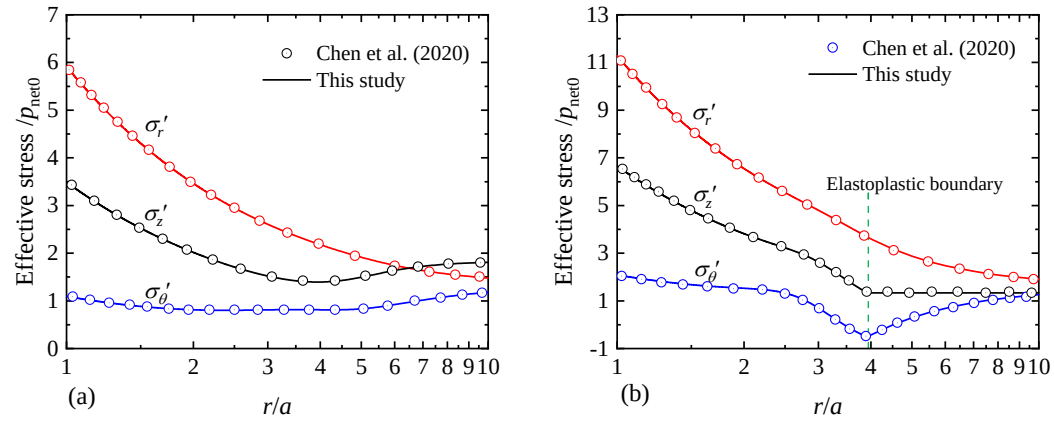

Figure 3.12 Comparison of stress distribution with Chen et al. (2020) under constant water content conditions: (a) R_0=1; (b) R_0=5.

3.7.1.3 Comparison with FEM

The HEL approach is further validated by comparison with FEM via Abaqus 2020 for cavity expansion in a finite soil thickness. The numerical model established in Abaqus can refer to Figure 3.13 with MCC soil parameters in Table 3.5 and b_0/a_0=20 . Note that only the cases of cavity expansion in fully saturated and completely dry soils are simulated (suction is not considered), which is because the MCC has been well implemented in Abaqus. Other information for the numerical simulations can be summarised as

(i) The initial inner cavity radius a_0 is set as 1m and the outer radius is 20m (i.e. $b_0/a_0 = 20$). A total of 1112 elements are adopted, and the element type is CAX8R for the drained dry case and CAX8RP for the fully saturated.

(ii) The cavity expansion process is displacement-controlled in Abaqus. Firstly, the initial fields are defined by inputting the initial void ratio and initial stress field. Then a radial stress σ_{h0} is applied to the right boundary and the displacement is restricted at the left, top, and bottom boundaries, after which the stress and displacement field is balanced. Finally, the left boundary (inner cavity wall) is controlled by gradually increasing the displacement ($a-a_0$) at a rate of 1mm/s (dynamic forces are neglected for the quasi-static problem).

(iii) In the case of cavity expansion in undrained saturated soils, the soil permeability is set as 1.7×10^{-9} m/s (Zhou et al., 2021a).

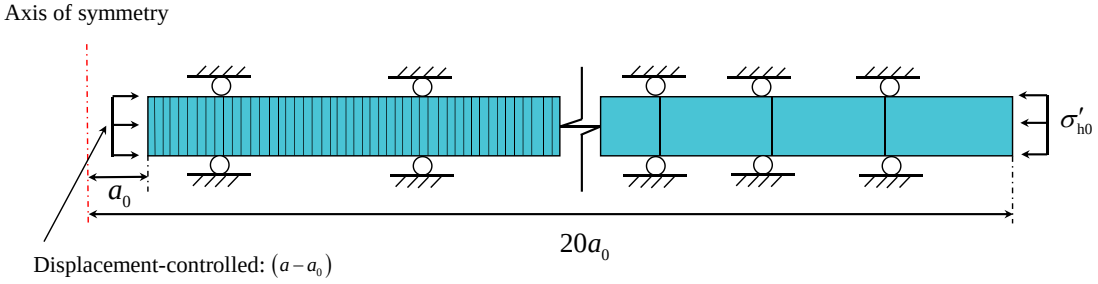

Figure 3.13 FEM model in Abaqus

Figure 3.14 shows the comparison of cavity expansion curves calculated by the HEL approach and FEM, and identical results are capable of providing further verification of the present approach. Besides, the cavity expansion curves in undrained saturated soils are more sensitive to the boundary effect than those in drained dry soils, especially for a higher R_0. This indicates that the existence of excess water pressure can help weaken the boundary effect in the cavity expansion process.

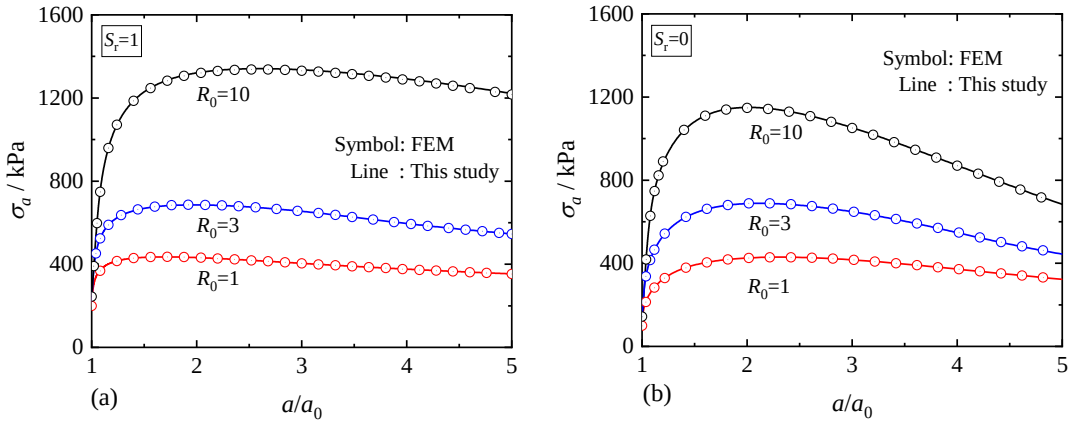

Figure 3.14 Comparison of cavity expansion curves: (a) undrained conditions; (b) drained conditions.

3.7.2 Cavity expansion in finite dry soils

3.7.2.1 Non-self-similar cavity expansion behaviour

For comparison, stress and deformation paths of soil material points at different radial positions (e.g. $r_0 = a_0$, $5a_0$, $15a_0$ and $30a_0 = b_0$) are captured during the expansion process. The MCC model is adopted with the parameters in Table 3.6. The results are plotted both in the $p-q$ and $v-\ln p$ planes as shown in Figure 3.15~Figure 3.17, in which the solid squares and circles mark the origin and end of loading (i.e. a_{end}/a_0=5), respectively.

During the continuous expansion process, it is known that all material points around the cavity share the same stress and deformation paths for self-similar cavity expansion problems (e.g. a cylindrical cavity in an infinite soil thickness of axisymmetric stress conditions) (Collins et al., 1992; Chen, S.L. and Abousleiman, Y.N., 2013; Mo and Yu, 2018). On the contrary, Figure 3.15~Figure 3.17 show that these paths differ significantly for particles at different radial positions, which corroborates the non-self-similar nature of cavity expansion in soils with a finite radial extent.

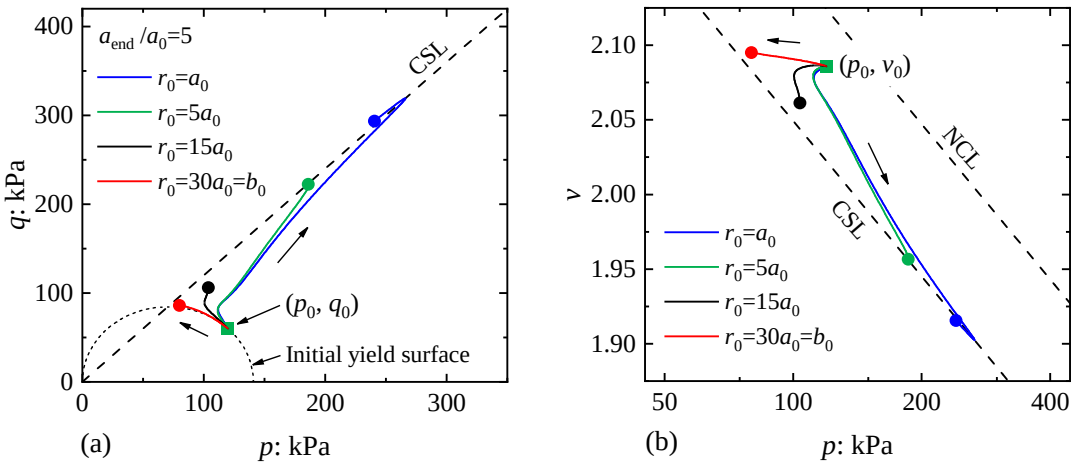

Figure 3.15 Stress paths of various material points for R_0=1: (a) *p*-*q* plane; (b) *v*-ln*p* plane

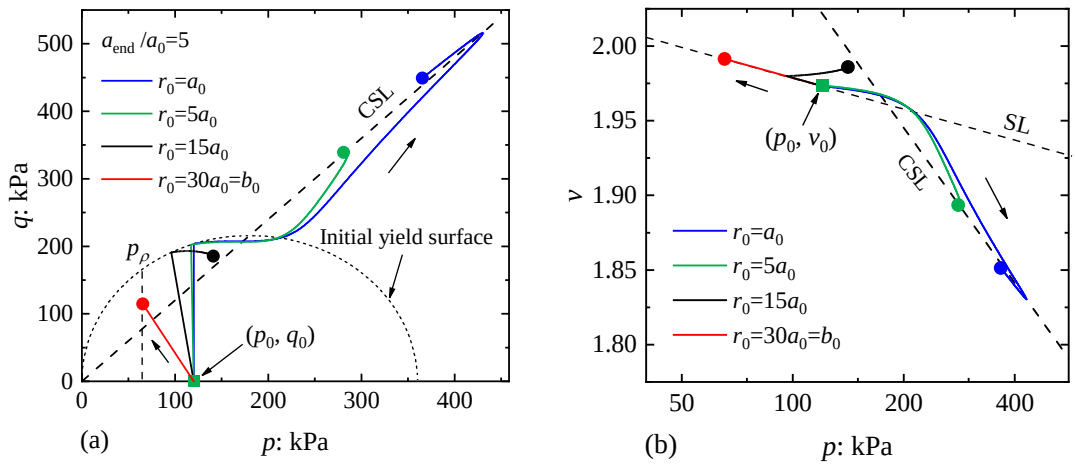

Figure 3.16 Stress paths of various material points for R_0=3: (a) *p*-*q* plane; (b) *v*-ln*p* plane

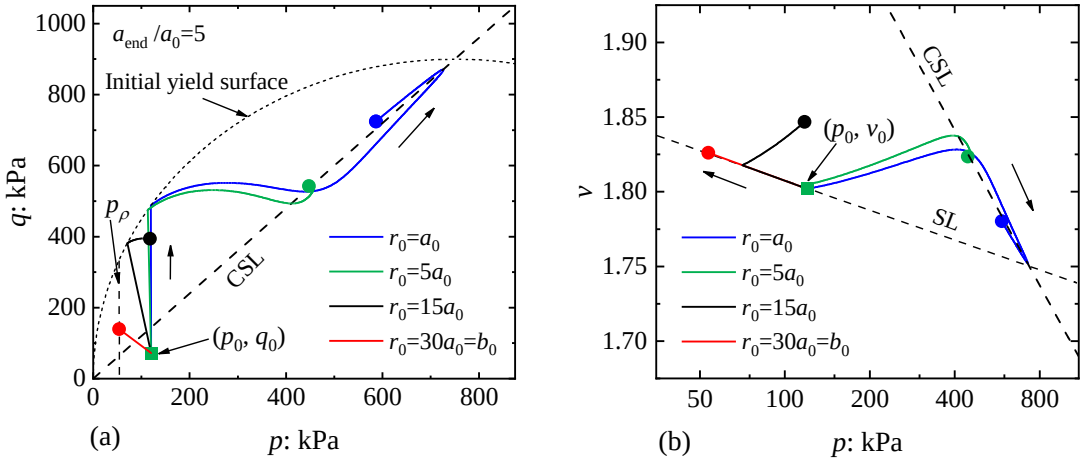

Figure 3.17 Stress paths of various material points for R_0=10: (a) *p*-*q* plane; (b) *v*-ln*p* plane

For the present non-self-similar problem, the stress states of soil material points closely relate to the level of expansion, the radial distance to the cavity wall, and the initial overconsolidation ratio. Figure 3.15~Figure 3.17 indicate the closer to the cavity wall the earlier the stress state reaches the critical state, and soil material points with larger initial radii generally take shorter paths to the CSL. With the same level of expansion, material points near the outer boundary may enter the plastic state in normally consolidated soils (e.g. $R_0=1$), whereas only elastic deformation occurs (e.g. within the initial yield surface in the $p-q$ plane or purely move along the SL in the $v-\ln p$ plane) in overconsolidated soils (e.g. R_0 =3 and 10). The stress paths prior to yielding are approximately straight lines in the $p-q$ plane but vary with the radial positions of material points. In the purely elastic stage, the mean stress reduces upon loading, and the reduction becomes greater as the particle radius increases. This is also greatly different to what happens in a self-similar cavity expansion process (Chen, S.L. and Abousleiman, Y.N., 2013; Mo and Yu, 2018).

3.7.2.2 Boundary effect for cavity expansion

Cavity expansion curves (i.e. σ_a/σ_h versus a/a_0) with various b_0/a_0 ratios and R_0 values are calculated and plotted in Figure 3.18~Figure 3.20. In these figures the triangles

on some cavity expansion curves indicate the moment that the elastic-plastic boundary just reaches the outer boundary of the hollow cylinder (i.e. $\rho_0 = b_0$).

The outer boundary effect becomes more significant with the increase of the overconsolidation ratio of soil (i.e. R_0). For example, setting a_{end}/a_0 =5, the inner cavity pressure for b_0/a_0 =30 is 84.3% of that for $b_0/a_0 = \infty$ in the case of R_0 =1, and this ratio becomes 76.8% and 70.7% in the cases of R_0 =3 and 10, respectively.

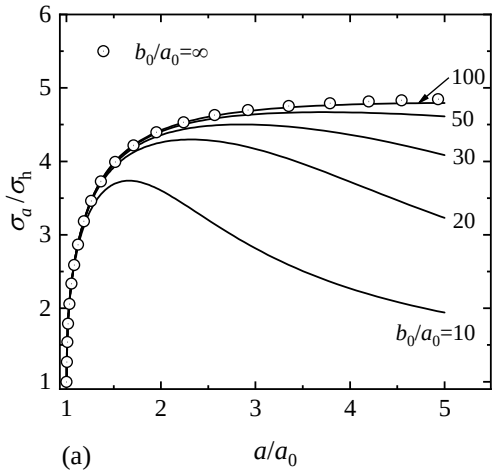

Figure 3.18 Cavity expansion curves for R_0=1

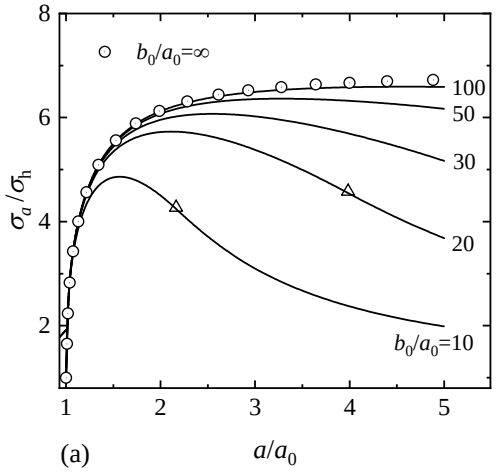

Figure 3.19 Cavity expansion curves for R_0=3

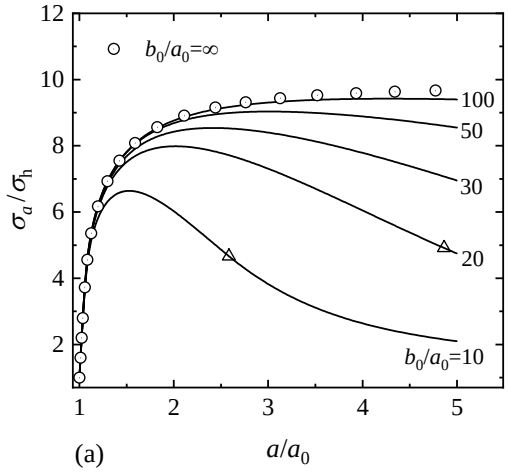

Figure 3.20 Cavity expansion curves for R_0=10

3.7.3 Revisiting undrained cavity expansion in finite, fully saturated soils

Using Lagrangian method, Zhuang et al. (2021) proposed a semi-analytical solution for undrained analysis of a thick-wall soil cylinder with Cam-Clay soil models, adopting approximate definitions of stress invariants from Collins and Yu (1996):

$$p' = \left(\sigma'_r + \sigma'_\theta\right)/2 \tag{3.113}$$

$$q = \sigma'_r - \sigma'_\theta \tag{3.114}$$

In order to evaluate the influences of the stress definitions, their solution is compared with the proposed solution that adopts rigorous stress definitions, taking the same soil model (i.e. MCC) and input parameters for London Clay: Γ=2.759, $\lambda(0)$=0.161, κ=0.062, M=0.773, v_0=2.0, μ=0.3, $a_{\text{end}}/a_0 = 4$, and $u_{\text{w0}} = 0$ (Collins and Yu, 1996; Zhuang et al., 2021).

3.7.3.1 Boundary effect for cavity expansion

The total cavity pressure σ_a and water pressure u_{w} at the inner cavity wall predicted by these two solutions are compared in Figure 3.21 and Figure 3.22 with R_0=1 and 16, respectively. σ_a and u_{w} calculated by the two solutions vary in the same trend with a/a_0, while the values predicted by the present solution are mostly larger than those by Zhuang et al. (2021). For example, setting a_{end}/a_0=4 and b_0/a_0=1000, the approximate

definition of stress invariants led to 8% and 11% underestimation of the total pressure with R_0=1 and 16, respectively. Similar trends were also found by Wang, X. and Chen (2022) for cavity expansion in undrained, fully saturated MCC soils of an infinite radial extent. Differences of σ_a between these two solutions become smaller in cases of a smaller b_0/a_0 and a larger a/a_0. After the peak, the total pressure and the water pressure predicted by the rigorous solution may decrease faster than those by the approximate one for a small b_0/a_0. This is due mainly to that:

(i) When b_0/a_0 is small, the entire soil may reach the critical state and $\sigma_r \to \sigma_{h0}$ (i.e. confining pressure at r=b) (Zhuang et al., 2021));

(ii) At the critical state, the effective radial stress in the rigorous solution ($\sigma'_r = p' + q/\sqrt{3}$) is larger than that in the approximate solution ($\sigma'_r = p' + q/2$), so u_w decreases relatively faster in the rigorous solution.

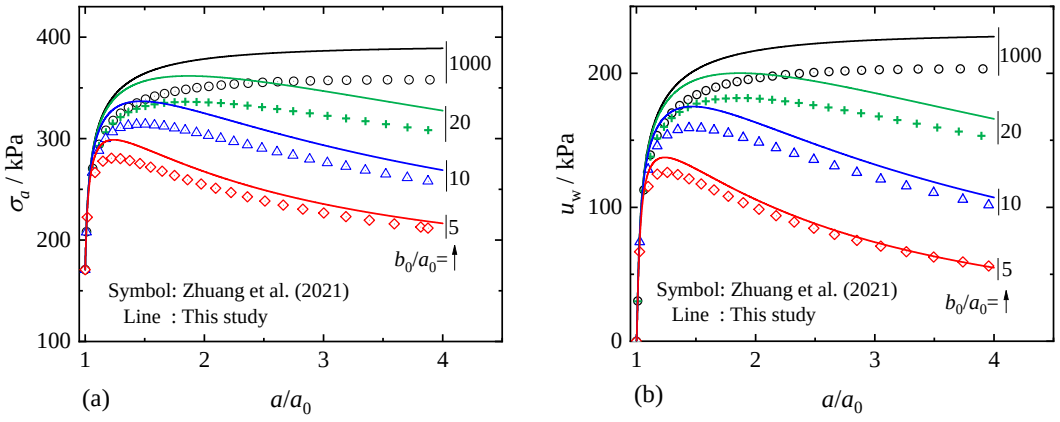

Figure 3.21 Cavity expansion response at the inner cavity wall with R_0=1: (a) total pressure; (b) excess water pressure

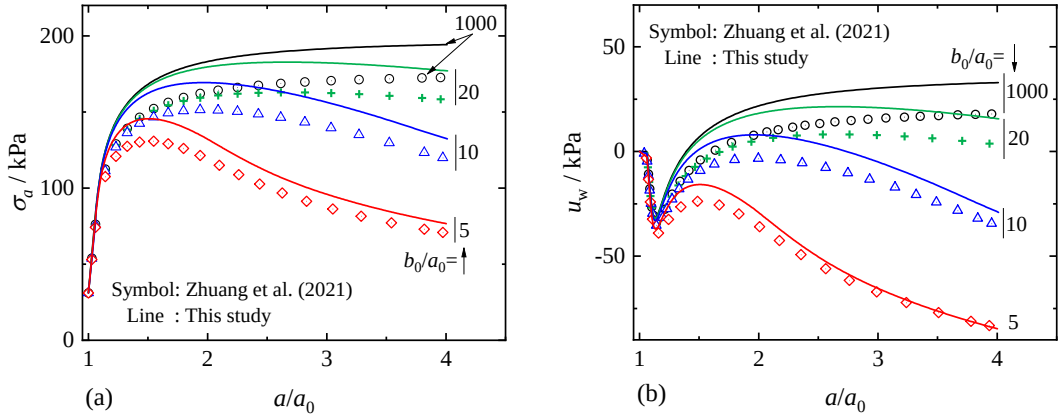

Figure 3.22 Cavity expansion response at the inner cavity wall with R_0=16: (a) total pressure; (b) excess water pressure

3.7.3.2 Non-self-similar cavity expansion behaviour

Figure 3.23 and Figure 3.24 plot the effective and total stress paths at the inner cavity wall predicted by the present solution and the solution of Zhuang et al. (2021) with the MCC. b_0/a_0 was set as 2 or 1000, and a_{end}/a_0 =4. Figure 3.23 shows that the effective stress paths coincide in all conditions. This is because the deviatoric stress totally depends on the mean effective stress under constant-volume conditions (Collins and Yu, 1996; Zhuang et al., 2021), as indicated by Eq. (3.115):

$$q(p') = Mp'\sqrt{R_0\left(p'/p_0'\right)^{-1/\Omega} - 1} \tag{3.115}$$

where $\Omega = 1-\kappa/\lambda(0)$. Derivation of Eq. (3.115) is detailed in Appendix A.

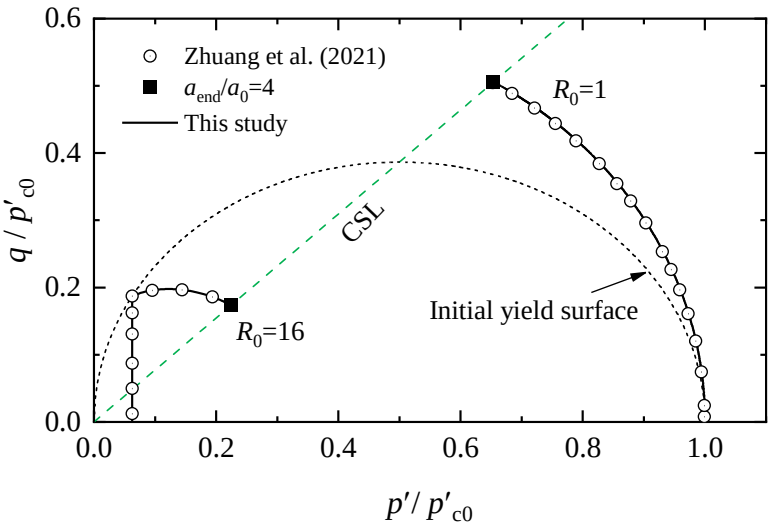

Figure 3.23 Effective stress path at the inner cavity wall

On the contrary, the total stress paths obtained by these two solutions are significantly different in the normalised p-q plane as shown in Figure 3.24, and it is explained as follows. Under the constant-volume conditions ($\mathrm{D}\varepsilon_\theta = -\mathrm{D}\varepsilon_r$), Eq. (3.112) is equivalent to that obtained by Wang, X. and Chen (2022) with rigorous stress definitions, which is

$$\mathrm{D}\varepsilon_\theta = \frac{\kappa}{v_0}\left[\frac{\sqrt{3}\eta}{M^2-\eta^2} - \frac{\sqrt{3}(1+\mu)}{9(1-2\mu)}\frac{\partial q}{\partial p'}\right]\frac{\mathrm{D}p'}{p'} \tag{3.116}$$

With approximate stress invariants, the incremental circumferential strain $\mathrm{D}\tilde{\varepsilon}_\theta$ becomes

$$\mathrm{D}\tilde{\varepsilon}_\theta = \frac{2}{\sqrt{3}}\frac{\kappa}{v_0}\left[\frac{2\eta}{M^2-(4/3)\eta^2} - \frac{1}{4(1-2\mu)}\frac{\partial q}{\partial p'}\right]\frac{\mathrm{D}p'}{p'} \tag{3.117}$$

Derivation of Eqs. (3.116) and (3.117) is detailed in Appendix B. The difference between Eqs. (3.116) and (3.117) results in the different total stress paths with different stress definitions. It also needs to be noted that the stresses (e.g. σ_a) in Collins and Yu (1996) are normalised by the undrained shear strength $\tilde{s}_u$, which is different to the standard one s_u ($\tilde{s}_u = \sqrt{3}/2\, s_u \approx 0.866 s_u$). As a result, the difference between the rigorous and the approximate solutions in the normalised expansion curves was found minimal (Sheng et al., 2000). It is also necessary to mention that this conclusion hold mainly for undrained cavity expansion with isotropic stress states, and care should be taken when adopting the

approximate definition of stress invariants to those cavity expansion problems in drained conditions or anisotropic stress states.

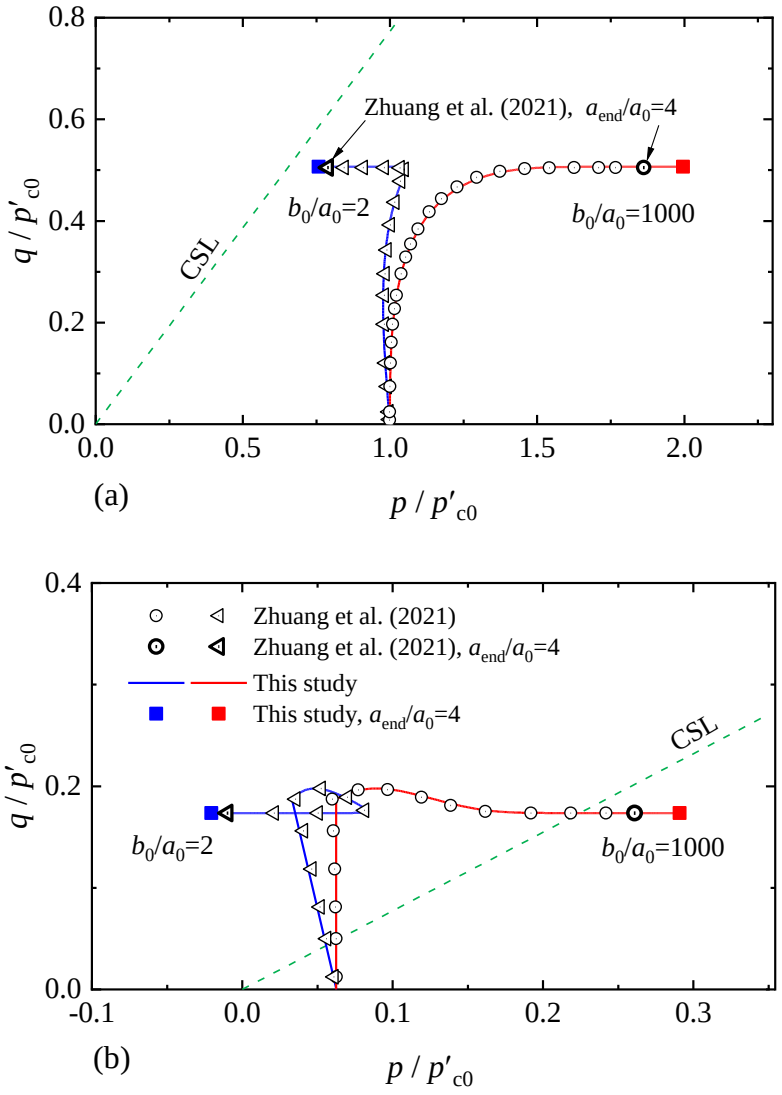

Figure 3.24 Total stress path at the inner cavity wall: (a) R_0=1; (b) R_0=16

Apart from the HEL approach, the applicability of the Eulerian and Lagrangian approaches in this special case is further discussed. Eqs. (3.112) and (3.115) indicate the effective stress paths are self-similar, but the Eulerian approach may still not be applicable because the total stress paths are not self-similar and the outer boundary conditions are difficult to be determined during the fully plastic expansion stage (Wang, C.-L. et al., 2022). In addition, is it possible to use the Lagrangian approach with rigorous definitions of (p',q)? Based on Wang, X. and Chen (2022) that solved Eq. (3.116) by numerical

method, this paper goes a step further by integrating Eq. (3.116) analytically, as

$$\int \mathrm{D}\varepsilon_\theta = \frac{\sqrt{3}\kappa}{v_0}\left[\frac{\Omega}{M}\left(\tan^{-1}\frac{\eta}{M}-\tanh^{-1}\frac{\eta}{M}\right)-\frac{(1+\mu)}{9(1-2\mu)}\left(\eta-2\Omega\eta+2M\Omega\tan^{-1}\frac{\eta}{M}\right)\right] \tag{3.118}$$

Once the analytical stress-total strain relationship is generated, the Lagrangian approach can be readily applied to the analysis of this problem following the same procedures of Zhuang et al. (2021).

3.7.4 Cavity expansion behaviour in finite unsaturated soils

The expansion behaviour of a cylindrical cavity in unsaturated soils of a finite radial extent is investigated in this subsection with a particular focus on the finite outer boundary effect and the non-self-similar characteristics. The soil parameters in Table 3.6 are adopted here, and the analysis is performed only under constant suction conditions for brevity as similar cavity expansion curves can be expected for undrained analysis (e.g. Figure 3.10~Figure 3.12). The cavity expansion level is up to a_{end}/a_0 =5 and the stresses are normalised by p_{net0}=120kPa.

3.10.4.1 Boundary effect and non-self-similarity for cavity expansion

The pressure-expansion curves and effective stress paths at the inner wall are shown in Figure 3.25 and Figure 3.26 for R_0=1 and 5, respectively, with various b_0/a_0 ratios. For the curves with a smaller b_0/a_0, the inner cavity pressure first increases to reach a peak value, and then decreases upon further loading. It proves that the finite cylinder thickness may play an important role in the cavity expansion behaviour, which is consistent with other studies (Yu, 1992; Zhuang et al., 2021; Cheng, Y. et al., 2022; Wang, C.-L. et al., 2022). Different from the expansion behaviour in saturated soils under undrained conditions (see Section 3.10.3), the boundary effect can also influence the effective stress path for unsaturated soils. In Figure 3.25 (b) and Figure 3.26 (b), the effective stress paths in the p'-q plot for b_0/a_0=10 and 30 turn around after reaching the peak values, which drop along the CSL with p' and q reducing, rather than getting steady as that may

happen during counterpart cavity expansion analysis with $b_0/a_0=\infty$.

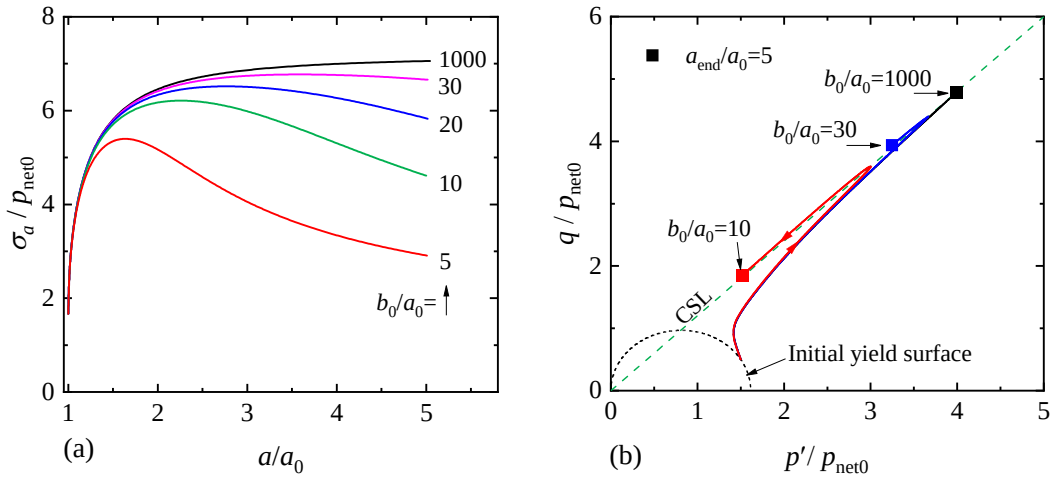

Figure 3.25 Cavity expansion curves and stress paths at the inner cavity wall for R_0=1: (a) cavity expansion curves; (b) stress path

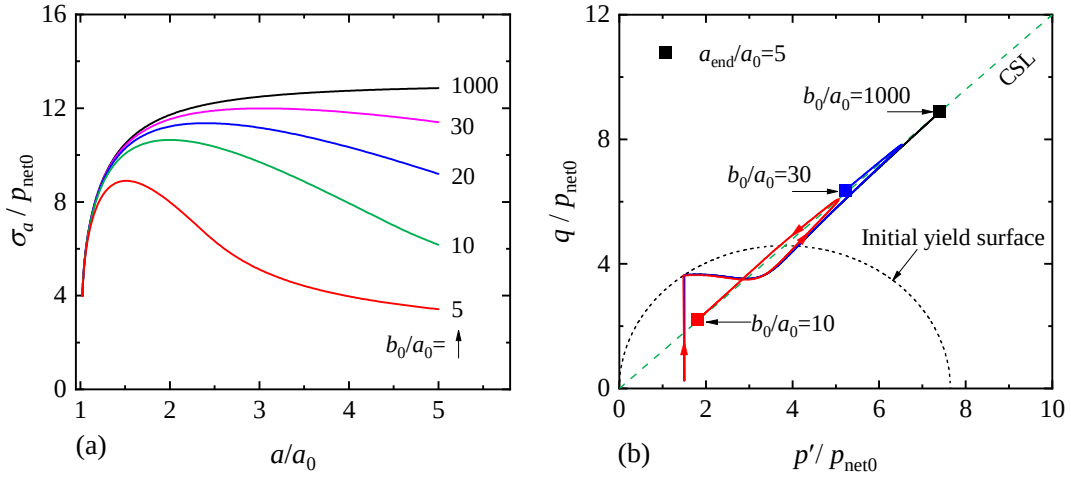

Figure 3.26 Cavity expansion curves and stress paths at the inner cavity wall for R_0=5: (a) cavity expansion curves; (b) stress path

To further highlight the non-self-similar properties, the deformation paths of material points at various radial positions are depicted in Figure 3.27, taking b_0/a_0 =30 as an example. It can be seen that material points at different radial positions within the soil cylinder take various paths from the initial states to the critical states, which verifies the non-self-similarity nature in the expansion process of thick-wall soil cylinders.

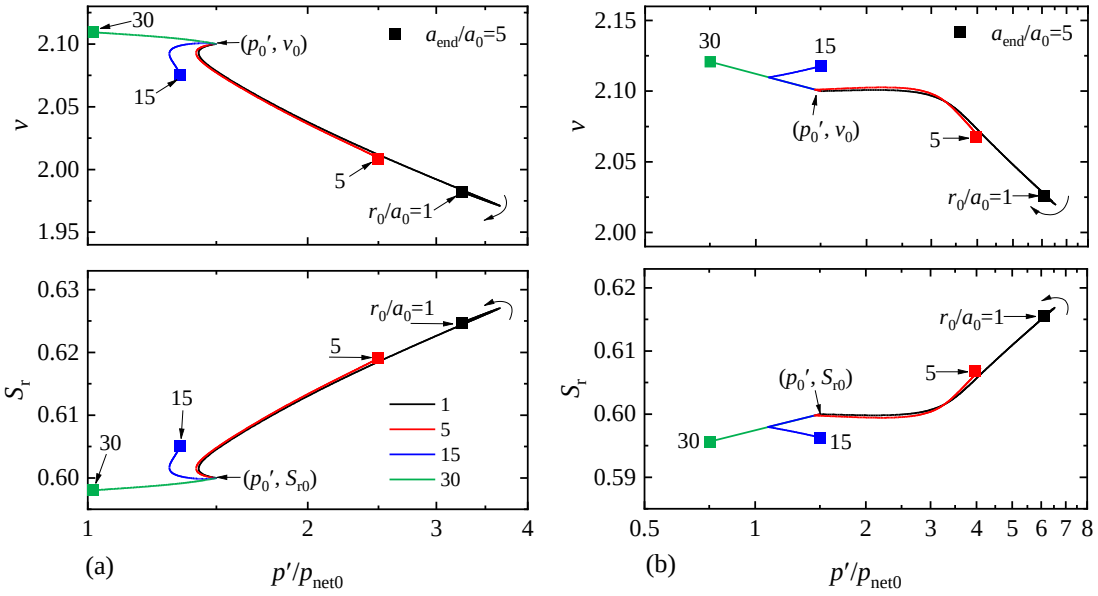

Figure 3.27 Deformation paths of various material points: (a) R_0=1; (b) R_0=5

3.10.4.2 Comparison between HEL and Eulerian approaches

It was mentioned that the self-similar-based Eulerian approach has also been used in the expansion analysis of a cavity in finite soils under drained conditions (Pournaghiazar et al., 2013; Cheng et al., 2018; Cheng and Yang, 2019), which are actually approximate solutions as the expansion proves to be non-self-similar. To highlight the significance of the HEL approach in non-self-similar cavity expansion problems, cavity expansion curves and stress paths at the inner cavity wall are calculated by the HEL approach and the suggested Eulerian approach. The same soil model (i.e. UCSM) and soil parameters (i.e. Table 3.6) are adopted in the two approaches, and the comparison results are shown in Figure 3.28. Two thickness ratios of the cylinder (i.e. b_0/a_0 =10 and 1000) are selected and ρ_0/b_0 is set as 0.6 in the suggested Eulerian approach in the case of b_0/a_0 =10.

Not surprisingly, the cavity expansion curves predicted by the two approaches are identical while b_0/a_0 is large enough (e.g. b_0/a_0 =1000 in Figure 3.28 (a)). However, the predicted pressure-expansion curves vary with each other while b_0/a_0 is small (e.g. b_0/a_0 =10) as the expansion process is no longer self-similar. In addition, ρ_0/b_0 is

assumed as a constant in the suggested Eulerian approach. Consequently, the inner pressure predicted by the Eulerian approach keeps increasing with a/a_0, which in fact ought to drop after peak values as predicted by the present solution. Significant differences are also shown in the stress paths (Figure 3.28 (b)), especially in the purely elastic loading process. Hence, considerable errors may be involved by the common Eulerian approach for the expansion analysis of a thick-wall cylinder of soils.

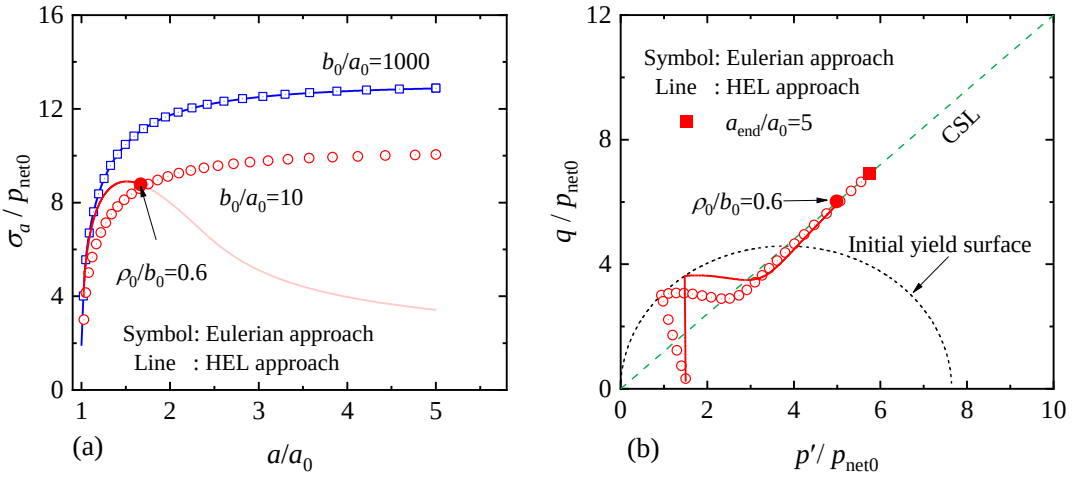

Figure 3.28 Cavity expansion curves and stress path at the inner cavity wall for R_0=5:(a) cavity expansion curves; (b) stress path

3.8 Application to pressuremeter test in calibration chambers

A simple case study is shown to indicate the potential application of the proposed non-self-similar solution to the pressuremeter tests in the laboratory. Fahey (1986) conducted a series of pressuremeter tests in a small-sized calibration chamber that is 200mm high and 400mm in diameter ($2b_0$), as shown in Figure 3.29. The pressuremeter used is 200mm long (L) and 40mm in diameter ($2a_0$) which gives b_0/a_0=10 and $L/2a_0$=5. The small ratios of b_0/a_0 and $L/2a_0$ indicate the lateral boundary effect of the chamber and the end effect of the pressuremeter would impose an important impact on the pressuremeter curves. Five tests with isotropic initial stress state in Fahey (1986) (i.e. tests SC5, SC6, SC7, RC1, and RC2) are selected in the present section, where the lateral boundary pressure was kept as 90kPa and the initial vertical stress was also 90kPa. In tests SC5,

SC6, and SC7, the bottom and top plates of the chamber were smooth to eliminate the end effect of the pressuremeter, while in tests RC1 and RC2 the plates were rough to study the end effect. The tested soil is well-documented Leighton Buzzard sand 14/25 and the initial specific volume is 1.512±0.016. The CASM is adopted to describe the constitutive behaviour of the sand, and the input parameters are: Γ=2 , λ =0.035, and $\varphi_{cs}=(1.0\sim1.2)\times30°$ (Wroth, 1984; Sladen et al., 1985; Chang et al., 1999), κ=0.003 (by fitting the initial shear moduli), n^*=2.5 and $r^* = 200$ (by fitting the triaxial tests in Lee, S.Y. (1990).

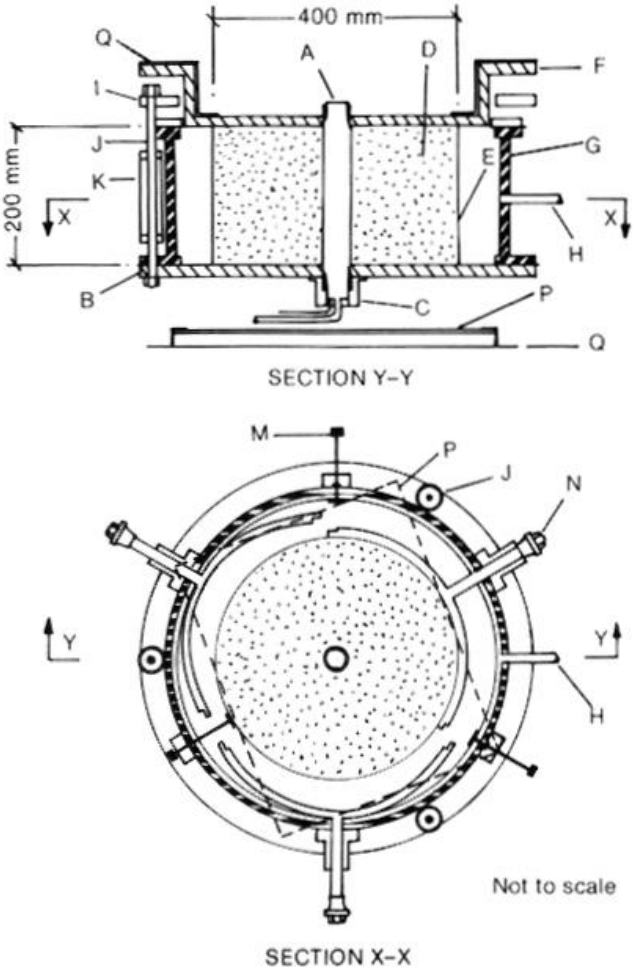

Figure 3.29 Thick cylinder test apparatus in Fahey (1986) on Leighton Buzzard sand 14/25 (Fahey, 1986)

Figure 3.30 shows the comparison of experimental pressuremeter curves with predicted curves by cavity expansion solutions. From the experimental results it can be seen that

the rough plates of the chamber (tests RC) can cause stiffer pressuremeters curves than smooth plates (tests SC), mainly due to principle stress rotation by the soil-plate friction (Fahey, 1986). The predicted pressuremeter curves by the cavity expansion solution in a finite soil thickness are in the same trend as experimental results, although slightly higher limit pressuremeter pressure is predicted than tests SC. Apart from the possible errors induced by the selected constitutive model, the reason may be that a sheet of latex rubber was attached to the smooth plates in the SC tests (Fahey, 1986) and thus the plain strain assumption may not be perfectly satisfied. On the other hand, the pressuremeter pressure would be highly overestimated by the cavity expansion solution if the boundary effect is ignored, which indicates the importance of the present semi-analytical solution.

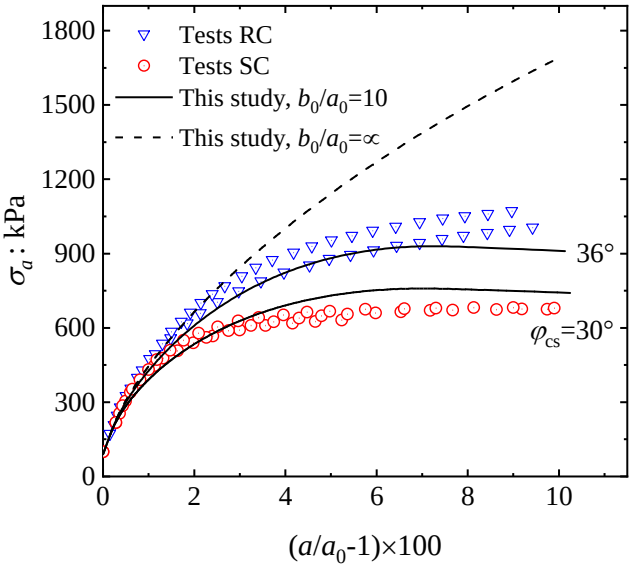

Figure 3.30 Comparison of experimental and theoretical pressuremeter expansion curves

Yu (1994) proposed a method of interpreting in-situ pressuremeter tests using a cavity expansion solution with a state-parameter-based critical state model. Yu found the pressuremeter expansion curve is nearly linear on the logarithmic scale when $a/a_0 \in [1.02, 1.15]$. The slope of the expansion curve (i.e. S_d) is almost linear with the initial state parameter (i.e. $\xi_0 = v_0 + \lambda \ln p - \Gamma$), but is rarely influenced by the soil

moduli. However, Yu's method may not be directly applied to pressuremeter tests in small-sized calibration chambers due to the finite boundary effect. To make it clear, the pressuremeter expansion curves for Leighton Buzzard sand (φ_{cs}=30° and K_0=1) are calculated by the present solution and are plotted in Figure 3.31 on the logarithmic scale with various b_0/a_0 ratios. The expansion curves are almost linear in the range of $a/a_0 \in [1.02,\ 1.15]$ when $b_0/a_0 \geq 20$, but curve curvature is obvious when $b_0/a_0 < 20$. This means the slope S_d may heavily rely on the soil stiffness (i.e. G_0/p_0, G_0 is the initial shear modulus). For example, the variation of S_d with G_0/p_0 and b_0/a_0 can be seen in Figure 3.32 within the range of $a/a_0 \in [1.02,\ 1.06]$. When b_0/a_0=20, S_d is shown to decrease linearly with the increase of ξ_0, and it is hardly affected by the soil stiffness. When b_0/a_0=10, on the other hand, there is a linear relationship between S_d and ξ_0 for G_0/p_0=300, but S_d cannot be obtained from the pressuremeter curves for G_0/p_0=1000 owing to curve curvature. Therefore, care must be taken if the pressuremeter tests in very small-sized chambers are interpreted by Yu (1994)'s method and the b_0/a_0 ratios of calibration chambers are recommended to be larger than 20. Otherwise, interpretation of pressuremeter tests may require curve fitting techniques and it is necessary to adopt more "realistic" descriptions of soil moduli in the constitutive modelling.

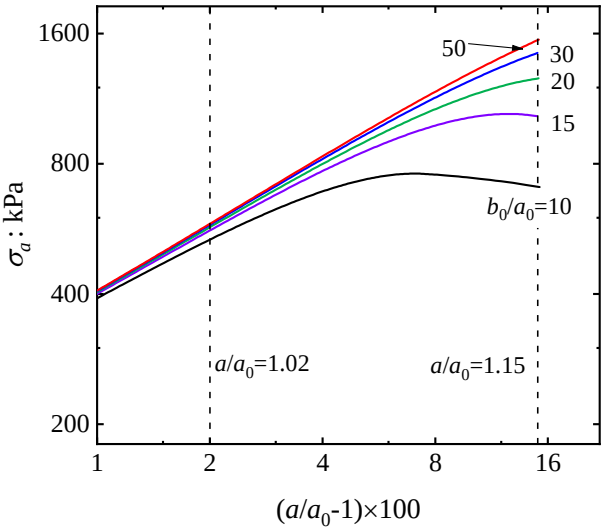

Figure 3.31 Pressuremeter expansion curves with different b_0/a_0 ratios

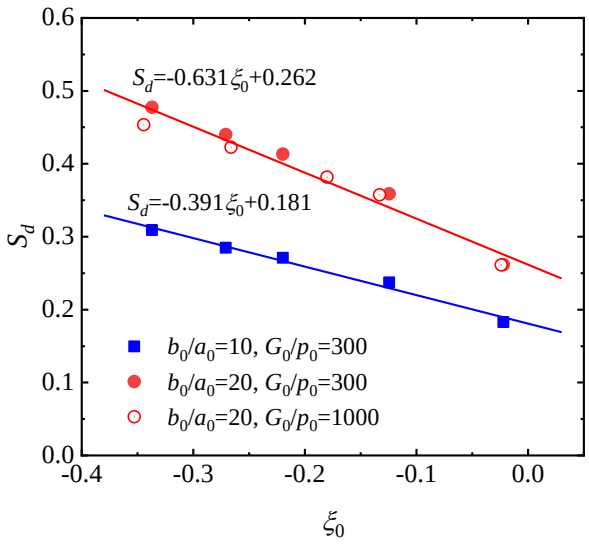

Figure 3.32 Slope of the pressuremeter expansion curve with the initial state parameter

3.9 Chapter summary

This chapter proposes a novel Hybrid Eulerian-Lagrangian (HEL) approach for the expansion analysis of a thick cylinder of soils with arbitrary saturate states. A closed-form solution for elastic stresses and displacements is developed, considering the finite thickness of the soil cylinder and stress-dependent soil moduli. In the plastic zone, the non-self-similar cavity expansion problem is expressed into five first-order PDEs in terms of both Eulerian and Lagrangian descriptions, and they are solved by a novel algorithm

of high efficiency. The following conclusions are drawn:

(i) It proves that the Eulerian approach is a special case of the HEL approach if the cylinder thickness becomes infinite and the Lagrangian approach can be recovered from the HEL approach when the analytical stress-total strain relationship is obtained.

(ii) The commonly used approximate definitions of the stress invariant (i.e. $p' = (\sigma'_r + \sigma'_\theta)/2$ and $q = \sigma'_r - \sigma'_\theta$) may lead to moderate underestimation of the required expansion pressure in some extreme cases.

(iii) The finite thickness of the soil cylinder may greatly influence the cavity expansion behaviour, which leads to the non-self-similar behaviour during the cavity expansion process. As a result, the self-similar-based Eulerian approach can only provide approximate solutions for this problem, especially for cylinders with small thickness ratios.

(iv) A simple case study shows that the new solution may provide useful tools for interpreting pressuremeter tests in small-sized calibration chambers.

Chapter 4 Hydro-mechanical cavity expansion in a poro-elasto-plastic medium under partially drained conditions

This chapter proposes a closed-form solution for cylindrical cavity expansion in intermediately permeable soils under partially drained conditions. The mechanical behaviour is modelled by the elastoplastic Tresca model while the hydraulic behaviour obeys Darcy's law. Then two partial differential equations (PDEs) are established in the elastic and plastic zones, respectively, and are solved by the variable transformation method. On the basis of the theoretical solution, a new normalised penetration rate is proposed by considering the influence of rigidity index. It is found that a unique backbone curve exists with the new normalised rate, and the curve matches well with a database of numerical and experimental results. Finally, a method is presented to estimate the consolidation coefficient of soils from multi-rate CPTU (penetration stage), which can provide guidance and redundancy in the interpretation of CPTU dissipation tests.

Related publications	(i) **Yang, H.**, Zhuang, P.-Z., Yu, H.-S., Mo, P.-Q., Ma, Y., Chen, X. and Schnaid, F. 2024. Cylindrical cavity expansion analysis under partially drained conditions for normalisation of excess water pressure in CPTU. *Canadian Geotechnical Journal*. (Under review)

4.1 Problem Definition and Assumptions

4.1.1 Cavity expansion model for the CPTU analysis

Modelling penetration problems with simplified geometries and boundary conditions can help understand the mechanisms of the CPTU penetration process. Following former studies on CPTU under partially drained conditions (Silva et al., 2006; Dienstmann et al., 2018b; Mafra and Dienstmann, 2022), the changes in radial stresses, deformation, and EWP around the cone tip during the penetration process is modelled by a time-dependent expansion of a cylindrical cavity, as shown in Figure 4.1. The rates of CPTU penetration and radial cavity expansion are denoted as V_{cptu} and V_a, respectively, and they can be related by $V_a = V_{\text{cptu}} \tan(\vartheta/2)$ (ϑ is the cone tip angle).

At the beginning (i.e. initial state before penetration/cavity expansion), total horizontal and vertical stresses (σ_{h0}, σ_{v0}) act throughout the soil that is homogenous, isotropic, and fully saturated. When the piezocone moves through section XX (see Figure 4.1), the inner cavity radius will expand from a_0 to a and the inner cavity pressure will increase from σ_{h0} to σ_a. For convenience, the cavity expansion problem is regarded as a plane strain problem (infinitely long in the vertical direction) and a cylindrical coordinate (r, θ, z) with the origin at the cavity centre is used for performing the theoretical analysis.

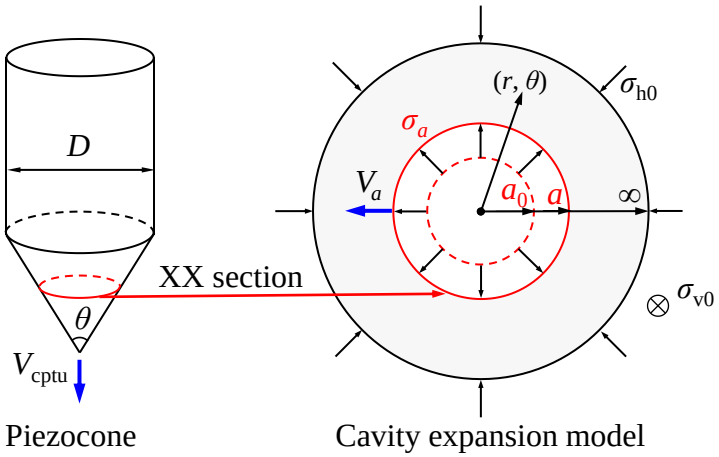

Figure 4.1 Relation between the piezocone penetration and cavity expansion

4.1.2 Equilibrium equations

Ignoring body forces and taking compression as positive, the radial equilibrium equation during cavity expansions can be written in two typical forms as

$$\frac{\mathrm{d}\sigma_r}{\mathrm{d}r}+\frac{\sigma_r-\sigma_\theta}{r}=0 \tag{4.1}$$

$$\frac{\mathrm{d}\sigma'_r}{\mathrm{d}r}+\frac{\sigma'_r-\sigma'_\theta}{r}+\frac{\mathrm{d}U}{\mathrm{d}r}=0 \tag{4.2}$$

in which σ_r and σ_θ denote the total radial and circumferential stresses, respectively; σ'_r and σ'_θ represent the effective radial and circumferential stresses, respectively; r is the current radial position of a material point whose initial value is r_0; U means EWP relative to the initial ambient water pressure u_{w0}.

4.1.3 Stress-strain relationship

In order to obtain a closed-form solution for the cavity expansion analysis under partially drained conditions, the soil is modelled as a perfectly elastoplastic Tresca model following the well-known work of Teh and Houlsby (1991) (dissipation stage of CPTU). The elastic behaviour of soils is assumed to follow the small strain theory and Hooke's law, as

$$\begin{cases}\varepsilon_r^{\mathrm{e}}=-\dfrac{\partial u}{\partial r}=\dfrac{1-\mu}{2G}\left[\left(\sigma'_r-\sigma'_{\mathrm{h0}}\right)-\dfrac{\mu}{1-\mu}\left(\sigma'_\theta-\sigma'_{\mathrm{h0}}\right)\right]\\ \varepsilon_\theta^{\mathrm{e}}=-\dfrac{u}{r}=\dfrac{1-\mu}{2G}\left[\left(\sigma'_\theta-\sigma'_{\mathrm{h0}}\right)-\dfrac{\mu}{1-\mu}\left(\sigma'_r-\sigma'_{\mathrm{h0}}\right)\right]\end{cases} \tag{4.3}$$

where $\varepsilon_r^{\mathrm{e}}$ and $\varepsilon_\theta^{\mathrm{e}}$ are the elastic radial and circumferential strains, respectively; $u=r-r_0$ denotes the radial displacement of the soil; G and μ are the shear modulus and Poisson's ratio; $\sigma'_{\mathrm{h0}}=\sigma_{\mathrm{h0}}-u_{\mathrm{w0}}$ denotes the initial horizontal effective stress.

Once yielding occurs, the soil obeys the Tresca yielding criteria with an associated flow rule, which can be defined as

$$\sigma_r' - \sigma_\theta' = 2s_{\mathrm{u}} \tag{4.4}$$

$$\frac{\mathrm{D}\varepsilon_r^{\mathrm{p}}}{\mathrm{D}\varepsilon_\theta^{\mathrm{p}}} = \frac{\mathrm{D}\varepsilon_r - \mathrm{D}\varepsilon_r^{\mathrm{e}}}{\mathrm{D}\varepsilon_\theta - \mathrm{D}\varepsilon_\theta^{\mathrm{e}}} = -1 \tag{4.5}$$

where s_{u} is the shear strength of soils; $\varepsilon_r^{\mathrm{p}}$ and $\varepsilon_\theta^{\mathrm{p}}$ are the plastic radial and circumferential strains, respectively; ε_r and ε_θ are the total radial and circumferential strains, respectively. Note that in Eq. (4.5) the vertical stress is taken as the intermediate principal stress for simplification (Carter et al., 1979; Carter et al., 1986; Yu and Houlsby, 1991).

4.1.4 Water flow equation

It is assumed that material points and water in soils are incompressible during the penetration process and water flow in the porous soils obeys Darcy's law:

$$V_{\mathrm{Darcy}} = -\frac{k}{\gamma_{\mathrm{w}}}\frac{\partial U}{\partial r} \tag{4.6}$$

where V_{Darcy} is Darcy's velocity; k represents the permeability coefficient of soil (soil anisotropy is not considered); γ_{w} represents the specific gravity of water.

For the mass balance of water in saturated soils, the volume change is related to the net water flow. Let us select an annulus element as shown in Figure 4.2. For a small increment of time, the volume of water that flows into and out of the element can be expressed as

$$-2\pi r \frac{k}{\gamma_w}\frac{\partial U}{\partial r}\bigg|_r \mathrm{D}t \qquad \text{(flow in)} \tag{4.7}$$

$$-2\pi\left(r+\mathrm{d}r\right)\frac{k}{\gamma_w}\frac{\partial U}{\partial r}\bigg|_{r+\mathrm{d}r} \mathrm{D}t \qquad \text{(flow out)} \tag{4.8}$$

where t denotes time and t=0 for the initial state before loading.

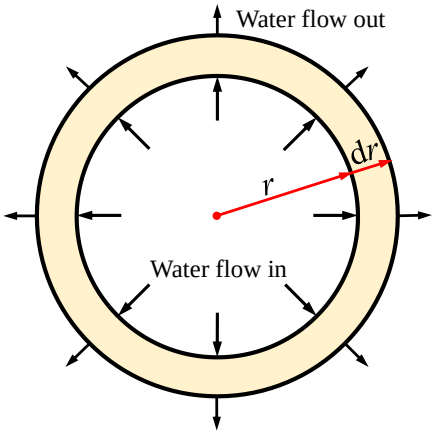

Figure 4.2 Volume change of an annulus element

The volume change of the element equals the volume of water that flows in minus that flows out, which is:

$$\mathrm{D}v = 2\pi \frac{k}{\gamma_w}\left[(r+\mathrm{d}r)\frac{\partial U}{\partial r}\bigg|_{r+\mathrm{d}r} - r\frac{\partial U}{\partial r}\bigg|_{r}\right]\mathrm{D}t \tag{4.9}$$

The increment of volume strain can be defined as

$$\mathrm{D}\varepsilon_v = -\frac{\mathrm{D}v}{v} = -\frac{\mathrm{D}v}{2\pi r\mathrm{d}r} \tag{4.10}$$

where ε_v is the total volumetric strain. Combining Eqs. (4.9) and (4.10), the mass balance equation can be obtained (Soderberg, 1962; Randolph and Wroth, 1979):

$$\frac{\partial \varepsilon_v}{\partial t} = -\frac{k}{\gamma_w}\frac{1}{r}\frac{\partial}{\partial r}\left(r\frac{\partial U}{\partial r}\right) = -\frac{k}{\gamma_w}\left(\frac{\partial^2 U}{\partial r^2} + \frac{1}{r}\frac{\partial U}{\partial r}\right) \tag{4.11}$$

It is necessary to mention that a convection term is neglected in Eq. (4.11) for large strain cavity expansion problem. Yu and Carter (2002) demonstrated that the error induced from this simplification is insignificant for small friction and dilation angles, and is less than 1% for Tresca model.

4.1.5 Boundary conditions and initial conditions

At t=0, the initial conditions for the defined problem can be written as

$$\begin{cases}\sigma_r = \sigma_\theta = \sigma_{\mathrm{h0}} \\ U = 0\end{cases} \quad \text{for} \quad r \geq a_0 \quad \text{and} \quad t=0 \tag{4.12}$$

The boundary conditions at $r=\infty$ and $r=a$ can be summarised as

$$\begin{cases}\sigma_r = \sigma_\theta = \sigma_{\mathrm{h0}} \\ U = 0\end{cases} \quad \text{for} \quad r = \infty \quad \text{and} \quad t \geq 0 \tag{4.13}$$

$$\partial U / \partial r = 0 \qquad \text{for} \quad r = a \quad \text{and} \quad t \geq 0 \tag{4.14}$$

where Eq. (4.14) means the surface of a piezocone is impermeable (Soderberg, 1962; Randolph and Wroth, 1979).

4.2 Solution in the elastic loading stage

At the early stage of cavity expansion, the stress state in soils is elastic and the cavity expansion process is in the purely elastic loading stage. The solution in this loading stage is firstly discussed.

4.2.1 Governing PDE for excess water pressure

The compatibility equation in terms of stresses can be derived from Eq. (4.3) as

$$\frac{\mathrm{d}}{\mathrm{d}r}\left[-\mu\sigma_r' + (1-\mu)\sigma_\theta'\right] + \frac{\sigma_\theta' - \sigma_r'}{r} = 0 \tag{4.15}$$

Combining Eqs. (4.2) and (4.15), we can find that:

$$\frac{\mathrm{d}}{\mathrm{d}r}\left[(1-\mu)(\sigma_r' + \sigma_\theta') + U\right] = 0 \tag{4.16}$$

For a given time, Eq. (4.16) indicates that the above combination of stresses and EWP does not change with radial positions of material points. When substituting Eq. (4.13) into Eq. (4.16), we can obtain the compatibility equation as follows.

$$(1-\mu)(\sigma_r' + \sigma_\theta') + U = 2(1-\mu)\sigma_{\mathrm{h0}}' \tag{4.17}$$

The mean effective stress under plane strain conditions can be determined by the radial and circumferential effective stresses as

$$\frac{\mathrm{D}p'}{\mathrm{D}t} = \frac{(1+\mu)}{3}\frac{\mathrm{D}(\sigma_r' + \sigma_\theta')}{\mathrm{D}t} \tag{4.18}$$

On the other hand, the volumetric strain in the elastic zone is the function of mean effective stress:

$$\frac{\mathrm{D}\varepsilon_v}{\mathrm{D}t}=\frac{3(1-2\mu)}{2G(1+\mu)}\frac{\mathrm{D}p'}{\mathrm{D}t} \tag{4.19}$$

Combining Eqs. (4.11), (4.17), (4.18) and (4.19), we can get the governing PDE for EWP in the elastic region:

$$\frac{\partial U}{\partial t}=c_{\mathrm{he}}\frac{1}{r}\frac{\partial}{\partial r}\left(r\frac{\partial U}{\partial r}\right)=c_{\mathrm{he}}\left(\frac{\partial^2 U}{\partial r^2}+\frac{1}{r}\frac{\partial U}{\partial r}\right) \tag{4.20}$$

$$c_{\mathrm{he}}=2G\frac{k}{\gamma_w}\times\frac{1-\mu}{1-2\mu} \tag{4.21}$$

where c_{he} may be named as the “elastic” coefficient of consolidation.

4.2.2 Stresses, displacement, and water pressure

With the initial conditions and boundary conditions defined by Eqs. (4.12) and (4.14), the solution for the PDE (4.20) is:

$$U(r,t)=0 \tag{4.22}$$

$$u_{\mathrm{w}}=u_{\mathrm{w0}} \tag{4.23}$$

Therefore, there is no EWP generated in the elastic loading stage

Once the initial pore water pressure is found, the effective stress components can be solved as follows. Combining Eqs. (4.17) and (4.22), the stress components satisfy:

$$\sigma'_r+\sigma'_\theta=2\sigma'_{\mathrm{h0}} \tag{4.24}$$

Combing Eqs. (4.2), (4.13), (4.22) and (4.24), the radial and circumferential stresses are derived as (Yu, 2000)

$$\sigma'_r=\sigma'_{\mathrm{h0}}+(\sigma'_a-\sigma'_{\mathrm{h0}})(\rho/r)^2 \tag{4.25}$$

$$\sigma'_\theta=\sigma'_{\mathrm{h0}}-(\sigma'_a-\sigma'_{\mathrm{h0}})(\rho/r)^2 \tag{4.26}$$

Then the radial displacement will be obtained by substituting Eqs. (4.25) and (4.26) into Eq. (4.3)

$$\frac{u}{r}=\frac{\sigma'_a-\sigma'_{\mathrm{h0}}}{2G}\left(\frac{a}{r}\right)^2 \tag{4.27}$$

4.3 Solution in the elastoplastic loading stage: Elastic zone

As the cavity expands, the surrounding soil is initially in the purely elastic stage. Then a plastic region is formed stemming from the inner cavity wall to ρ, where ρ denotes the current radius of the elastoplastic interface. This section shows the analytical solution for the effective stresses, EWP, and displacements in the elastic zone ($r>\rho$).

The PDE (4.20) for EWP in the elastic loading stage also holds for cavity expansion in the elastic zone in the elastoplastic loading stage, because of the same governing equations. With the boundary condition at $r=\infty$ (i.e. Eq. (4.13)), the solution of (4.20) can be expressed as

$$U=A_{\mathrm{e}}\mathrm{E}_1\left(r^2/4c_{\mathrm{he}}t\right) \tag{4.28}$$

$$\mathrm{E}_1(y)=\int_y^{\infty}\frac{e^{-x}}{x}\mathrm{d}x,\ y>0 \tag{4.29}$$

$$\frac{\partial U}{\partial r}=-2\frac{A_{\mathrm{e}}}{r}\exp\left(\frac{-r^2}{4c_{\mathrm{he}}t}\right) \tag{4.30}$$

where A_{e} can be determined by the continuity conditions of EWP at the elastoplastic interface; E_1 is known as the exponential integral.

Combining the stress equilibrium equation (4.2) and compatibility equation (4.17), the two equations in terms of σ'_r and σ'_θ can be obtained as

$$\frac{\partial\sigma'_r}{\partial r}+\frac{2}{r}\sigma'_r=\frac{1}{r}\left[2\sigma'_{\mathrm{h0}}-\frac{U}{1-\mu}+2A_{\mathrm{e}}\exp\left(\frac{-r^2}{4c_{\mathrm{he}}t}\right)\right] \tag{4.31}$$

$$\sigma'_\theta=2\sigma'_{\mathrm{h0}}-\sigma'_r-\frac{U}{1-\mu}=2\sigma'_{\mathrm{h0}}-\sigma'_r-\frac{A_{\mathrm{e}}}{1-\mu}\Omega\left(\frac{r^2}{4c_{\mathrm{he}}t}\right) \tag{4.32}$$

Eq. (4.31) can be readily solved with the boundary conditions (4.13) and EWP (4.28)

$$\sigma_r' = \sigma_{\mathrm{h0}}' + B_{\mathrm{e}}\frac{\rho^2}{r^2} - \frac{U}{2(1-\mu)} + F(r) \tag{4.33}$$

$$\sigma_\theta' = \sigma_{\mathrm{h0}}' - B_{\mathrm{e}}\frac{\rho^2}{r^2} - \frac{U}{2(1-\mu)} - F(r) \tag{4.34}$$

$$F(r) = \frac{4\mu-2}{1-\mu}\frac{A_{\mathrm{e}}c_{\mathrm{he}}t}{r^2}\exp\left(\frac{-r^2}{4c_{\mathrm{he}}t}\right) \tag{4.35}$$

where B_{e} can be determined by the yield function (4.4) at the elastoplastic boundary as

$$B_{\mathrm{e}} = s_{\mathrm{u}} - F(\rho) \tag{4.36}$$

Then substituting Eqs. (4.33) and (4.34) into Eq. (4.3), the radial displacement can be expressed as

$$\frac{u}{r} = \frac{1}{2G}\left[B_{\mathrm{e}}\frac{\rho^2}{r^2} + \frac{(1-2\mu)U}{2(1-\mu)} + F(r)\right] \tag{4.37}$$

In particular, the radial displacement at the elastoplastic boundary can be derived by substituting $r=\rho$ into Eq. (4.37):

$$\frac{u(\rho)}{\rho} = \frac{1}{2G}\left[s_{\mathrm{u}} + \frac{(1-2\mu)U_\rho}{2(1-\mu)}\right] \tag{4.38}$$

where U_ρ denotes the EWP at $r=\rho$.

4.4 Solution in the elastoplastic loading stage: Plastic zone

This section derives the solution for the radial effective stress in the plastic zone ($a<r<\rho$) following the large strain theory.

4.4.1 Stress analysis

Eq. (4.5) indicates the plastic volumetric strain remains as zero (i.e. $\varepsilon_r^{\mathrm{p}} + \varepsilon_\theta^{\mathrm{p}} = 0$) so that ε_v can be expressed as

$$\varepsilon_{\mathrm{v}} = \varepsilon_r^{\mathrm{e}} + \varepsilon_\theta^{\mathrm{e}} \tag{4.39}$$

Then ε_v can be related to σ_r' in the rate form by substituting Eqs. (4.3) and (4.4) into Eq. (4.39) as

$$\frac{\partial \varepsilon_v}{\partial t} = \frac{1-2\mu}{G}\frac{\partial \sigma_r'}{\partial t} \tag{4.40}$$

Combining Eqs. (4.2) and (4.4), the gradient of EWP can be expressed as

$$\frac{\partial U}{\partial r} = -\frac{2s_u}{r} - \frac{\partial \sigma_r'}{\partial r} \tag{4.41}$$

Substituting Eqs. (4.40) and (4.41) into Eq. (4.11) and eliminating U and ε_v, the PDE in terms of σ_r' can be derived as

$$\frac{\partial \sigma_r'}{\partial t} = c_{hp}\left(\frac{\partial^2 \sigma_r'}{\partial r^2} + \frac{1}{r}\frac{\partial \sigma_r'}{\partial r}\right) \tag{4.42}$$

$$c_{hp} = \frac{k}{\gamma_w}\frac{G}{1-2\mu} = \frac{c_{he}}{2(1-\mu)} \tag{4.43}$$

Here c_{hp} may be named as the "plastic" coefficient of consolidation. Accordingly, the boundary conditions for PDE (4.42) can be obtained by combining Eqs. (4.14) and (4.41) as

$$\frac{\partial \sigma_r'}{\partial r} = \frac{-2s_u}{a} \quad \text{for} \quad r=a<\rho \tag{4.44}$$

The elastoplastic stress analysis during cavity expansions under partially drained conditions was formulated as two conduction-type PDEs (i.e. Eqs. (4.20) and (4.42)) with moving boundary conditions at the elastoplastic interface, which is actually a typical Stefan problem (Gupta, 2017). A detailed description of the solutions for the Stefan problems was summarised by Gupta (2017) with various governing PDEs and boundary conditions. Gupta (2017) demonstrated that, in the cylindrical coordinate system, exact analytical solutions for the Stefan problems exist only for some specific boundary conditions. Since $a(t)$ in Eq. (4.44) increases continuously with time, it is hard to get a rigorous solution, if not impossible, for the present problem with the complex boundary conditions. Alternatively, it is found that an approximate solution can be derived by the

variable transformation method as shown below.

For the sake of convenience, the current radius r is transformed to a normalised radius $\tilde{r}$, following:

$$\tilde{r} = \frac{r}{2\sqrt{c_{\mathrm{hp}} t}} = \frac{r}{2\sqrt{c_{\mathrm{hp}}}} t^{-\frac{1}{2}} \tag{4.45}$$

Then we have the following expressions by the chain rule:

$$r = 2\sqrt{c_{\mathrm{hp}} t}\tilde{r} \tag{4.46}$$

$$\frac{\partial \tilde{r}}{\partial r} = \frac{1}{2\sqrt{c_{\mathrm{hp}} t}} \tag{4.47}$$

$$\frac{\partial \tilde{r}}{\partial t} = -\frac{1}{4}\frac{r}{\sqrt{c_{\mathrm{hp}}}} t^{-\frac{3}{2}} = -\frac{1}{4}\frac{r}{t\sqrt{c_{\mathrm{hp}} t}} = -\frac{1}{2}\frac{\tilde{r}}{t} \tag{4.48}$$

$$\frac{1}{r}\frac{\partial r}{\partial t} = \frac{1}{2\sqrt{c_{\mathrm{hp}} t}\tilde{r}} 2\tilde{r}\sqrt{c_{\mathrm{hp}}}\frac{1}{2\sqrt{t}} = \frac{1}{2t} \tag{4.49}$$

$$\frac{\partial \sigma_r'}{\partial r} = \frac{\partial \sigma_r'}{\partial \tilde{r}}\frac{\partial \tilde{r}}{\partial r} = \frac{\partial \sigma_r'}{\partial \tilde{r}}\frac{1}{2\sqrt{c_{\mathrm{hp}} t}} \tag{4.50}$$

$$\frac{\partial^2 \sigma_r'}{\partial r^2} = \frac{\partial \sigma_r'}{\partial \tilde{r}}\frac{\partial \tilde{r}}{\partial r} = \frac{1}{2\sqrt{c_{\mathrm{hp}} t}}\frac{\partial^2 \sigma_r'}{\partial \tilde{r}\partial r} = \frac{1}{2\sqrt{c_{\mathrm{hp}} t}}\frac{\partial^2 \sigma_r'}{\partial \tilde{r}^2}\frac{\partial \tilde{r}}{\partial r} = \frac{1}{4c_{\mathrm{hp}} t}\frac{\partial^2 \sigma_r'}{\partial \tilde{r}^2} \tag{4.51}$$

$$\frac{1}{r}\frac{\partial \sigma_r'}{\partial r} = \frac{1}{2\sqrt{c_{\mathrm{hp}} t}\tilde{r}}\frac{\partial \sigma_r'}{\partial \tilde{r}}\frac{1}{2\sqrt{c_{\mathrm{hp}} t}} = \frac{1}{4c_{\mathrm{hp}} t\tilde{r}}\frac{\partial \sigma_r'}{\partial \tilde{r}} \tag{4.52}$$

$$\frac{\partial \sigma_r'}{\partial t} = \frac{\partial \sigma_r'}{\partial \tilde{r}}\frac{\partial \tilde{r}}{\partial t} = -\frac{1}{2}\frac{\tilde{r}}{t}\frac{\partial \sigma_r'}{\partial \tilde{r}} \tag{4.53}$$

Substituting Eqs. (4.45)~(4.53) into PDE (4.42) gives

$$\tilde{r}\frac{\partial^2 \sigma_r'}{\partial \tilde{r}^2} + \left(1 + 2\tilde{r}^2\right)\frac{\partial \sigma_r'}{\partial \tilde{r}} = 0 \tag{4.54}$$

For the present Stefan problem, it should be noted that Eq. (4.42) can be transformed into Eq. (4.54) because the boundary condition is defined in the type of Eq. (4.44). If the boundary condition is shown in other forms (e.g. $\partial \sigma_r'/\partial r = \left(\sigma_\theta' - \sigma_r'\right)/a$) with more

complex constitutive models (e.g. MCC and MC models), transformation of Eq. (4.42) may involve some limitations as clearly stated in Russell et al. (2023).

The radial effective stress can be obtained by solving Eq. (4.54):

$$\sigma_r' = A_\mathrm{p}\mathrm{E}_1\left(\tilde{r}^2\right) + B_\mathrm{p} \tag{4.55}$$

where A_p and B_p are integral constants that should be determined by the boundary conditions at the inner cavity wall and elastoplastic boundary. With boundary conditions (4.44) and the stress continuity at the elastoplastic interface, the radial effective stress can finally be derived as

$$\sigma_r' = \sigma_{r\rho}' + s_\mathrm{u} e^{\tilde{a}^2}\left[\mathrm{E}_1\left(\tilde{r}^2\right) - \mathrm{E}_1\left(\tilde{\rho}^2\right)\right] \tag{4.56}$$

where $\sigma_{r\rho}'$ denotes the radial effective stress at $r=\rho$ and $\tilde{a}$ is the normalised inner radius. Here Eq. (4.56) is approximate because $a(t)$ is dependent on t and the boundary condition (4.44) cannot be rigorously transformed into a function which is only dependent on $\tilde{r}$ (Gupta, 2017). However, it is later demonstrated that the error induced by this simplification is negligible by comparison with numerical simulations.

The total radial stress can be obtained by integrating Eq. (4.1) from $\tilde{\rho}$ to $\tilde{r}$ as:

$$\sigma_r = \sigma_{r\rho} + 2s_\mathrm{u}\ln\left(\tilde{\rho}/\tilde{r}\right) \tag{4.57}$$

where $\sigma_{r\rho}$ denotes the total radial stress at $r=\rho$. Then the total radial stress at the inner cavity wall (i.e. σ_a) can be calculated from Eq. (4.57) with $\tilde{r}=\tilde{a}$, and the EWP in the plastic zone can be obtained from Eqs. (4.56) and (4.57) as:

$$U = U_\rho + 2s_\mathrm{u}\ln\left(\tilde{\rho}/\tilde{r}\right) - s_\mathrm{u}e^{\tilde{a}^2}\left[\mathrm{E}_1\left(\tilde{r}^2\right) - \mathrm{E}_1\left(\tilde{\rho}^2\right)\right] \tag{4.58}$$

Determination of $\sigma_{r\rho}'$, $\sigma_{r\rho}$ and U_ρ relies on the continuity conditions of stresses and EWP at the elastoplastic boundary.

4.4.2 Displacement analysis

Logarithmic strain definitions are adopted to account for the large deformation in the plastic zone (Chadwick, 1959; Yu and Houlsby, 1991), and they can be expressed as Eqs. (4.59) and (4.60) for the present axisymmetric expansion problem.

$$\varepsilon_r = -\ln\left(\mathrm{d}\tilde{r}/\mathrm{d}\tilde{r}_0\right) \tag{4.59}$$

$$\varepsilon_\theta = -\ln\left(\tilde{r}/\tilde{r}_0\right) \tag{4.60}$$

Substituting Eqs. (4.39), (4.56), (4.59) and (4.60) into Eq. (4.40) leads to

$$\varepsilon_r + \varepsilon_\theta = -\ln\frac{\tilde{r}\mathrm{d}\tilde{r}}{\tilde{r}_0\mathrm{d}\tilde{r}_0} = \frac{1-2\mu}{G}\left[s_\mathrm{u}e^{\tilde{a}^2}\left[\mathrm{E}_1\left(\tilde{r}^2\right)-\mathrm{E}_1\left(\tilde{\rho}^2\right)\right]\right] \tag{4.61}$$

In Eq. (4.61) the slight volume change for a material point going the purely elastic deformation is ignored. If the variation of $\sigma'_{r\rho}$ along the radial direction is also simplified to be contant (e.g. $\sigma'_{\mathrm{h}0}+s_\mathrm{u}$), Eq. (4.61) will be simplified as

$$\ln\frac{\tilde{r}\mathrm{d}\tilde{r}}{\tilde{r}_0\mathrm{d}\tilde{r}_0} = -\omega e^{\tilde{a}^2}\left[\mathrm{E}_1\left(\tilde{r}^2\right)-\mathrm{E}_1\left(\tilde{\rho}^2\right)\right] \tag{4.62}$$

$$\omega = \left(1-2\mu\right)/I_\mathrm{r} \tag{4.63}$$

where $I_\mathrm{r} = G/s_\mathrm{u}$ =rigidity index. Eq. (4.62) can be further rewritten as

$$\exp\left\{\omega e^{\tilde{a}^2}\left[\mathrm{E}_1\left(\tilde{r}^2\right)-\mathrm{E}_1\left(\tilde{\rho}^2\right)\right]\right\}\mathrm{d}\tilde{r}^2 = \mathrm{d}\tilde{r}_0^2 \tag{4.64}$$

Integrating Eq. (4.64) over the interval $[\tilde{a},\ \tilde{\rho}]$ gives:

$$\int_{\tilde{a}^2}^{\tilde{\rho}^2}\exp\left[\omega e^{\tilde{a}^2}\mathrm{E}_1\left(y\right)\right]\mathrm{d}y = \exp\left[\omega e^{\tilde{a}^2}\mathrm{E}_1\left(\tilde{\rho}^2\right)\right]\left(\tilde{\rho}_0^2-\tilde{a}_0^2\right) \tag{4.65}$$

where ρ_0 denotes the initial radial position of the elastoplastic interface.

Once $a(t)$ or $\tilde{a}$ is given, $\tilde{\rho}$ can be calculated from Eq. (4.65) by simple iterations via the classical Newton-Raphson-type method. For displacement analysis, $\sigma'_{r\rho}$ in Eq. (4.62) is simplified to be $\sigma'_{\mathrm{h}0}+s_\mathrm{u}$ and ρ_0 in Eq. (4.65) should be conjugately replaced

by $\rho_0=\rho\left(1-0.5/I_r\right)$ (Gibson and Anderson, 1961; Yu, 2000). This simplification is rigorously satisfied only for fully drained and undrained conditions (Yu, 2000), but the induced error proves to be insignificant as shown later in this paper.

4.5 Solution at the elastoplastic interface

The EWP as well as its gradient calculated by the elastic and plastic solutions should satisfy the continuity conditions at the elastoplastic interface. Combining Eqs (4.28), (4.41) and (4.56), A_e in Eq. (4.28) can be derived as

$$A_e = s_u \exp\left(\frac{\rho^2}{4c_{he}t}\right)\left(1-e^{\tilde{a}^2-\tilde{\rho}^2}\right) \tag{4.66}$$

Then EWP, radial effective stress and total radial stress at $r=\rho$ can be obtained from Eqs. (4.28) and (4.33) yielding the following expressions:

$$U_\rho = s_u \exp\left(\frac{\rho^2}{4c_{he}t}\right)\left(1-e^{\tilde{a}^2-\tilde{\rho}^2}\right)\mathrm{E}_1\left(\frac{\rho^2}{4c_{he}t}\right) \tag{4.67}$$

$$\sigma'_{r\rho} = \sigma'_{h0} + s_u - \frac{1}{2(1-\mu)}U_\rho \tag{4.68}$$

$$\sigma_{r\rho} = \sigma_{h0} + s_u + \frac{1-2\mu}{2(1-\mu)}U_\rho \tag{4.69}$$

When $\tilde{\rho}$ and ρ are determined from Eq. (4.65) for a given $\tilde{a}$, the information at $r=\rho$ can be calculated by Eqs. (4.67), (4.68) and (4.69), and finally the stresses and EWP in the plastic zone can be calculated by Eqs. (4.4), (4.56), (4.57) and (4.58).

4.6 Numerical algorithm for the exponential integral

4.6.1 Series expansion of the exponential integral

For a large value of $\tilde{a}$ (e.g. larger than 25), $e^{\tilde{a}^2}$ in Eqs. (4.56), (4.58) and (4.65) may be very large and will be remarked as infinite in MATLAB (used in this thesis). Therefore, it is necessary to show the numerical algorithm for dealing with the exponential integral

and $e^{\tilde{a}^2}$. For a rather small value of y (e.g. $0<y<10$), the exponential integral can be expanded into the series form as

$$\mathrm{E}_1(y) = -\zeta - \ln y - \sum_{n=1}^{\infty} \frac{(-y)^n}{nn!}, \quad 0 < y < 10 \tag{4.70}$$

where ζ is the Euler-Mascheroni constant and approximate to 0.5772156649. For $0<y<10$, the first 50 terms of the series are selected and the series solution are compared with exact values calculated by the exponential integral function inclined in MATLAB, as shown in Figure 4.3. The maximum error is less than 5×10^{-7} and thereby the accuracy of the series solution is acceptable.

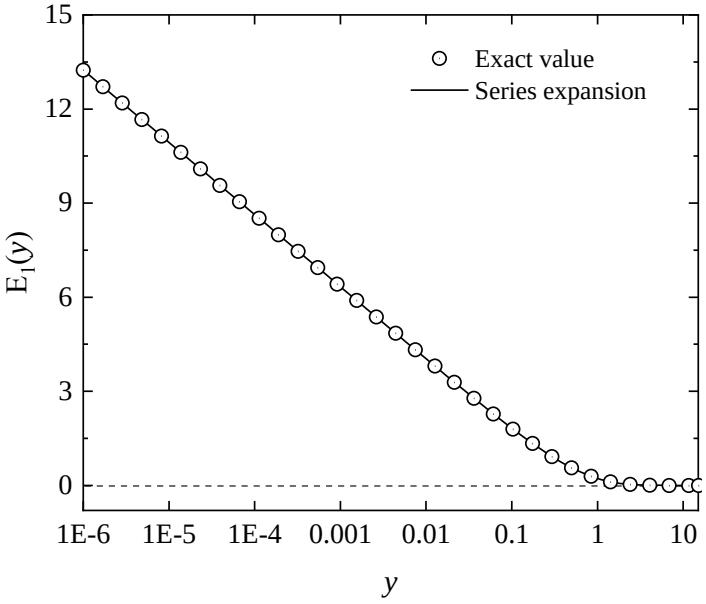

Figure 4.3 The exponential integral for 0<*y*<10

With the increase of y in Eq. (4.70), there may be too many terms required to calculate the exponential integral $\mathrm{E}_1(y)$, which causes unnecessary cost of calculation efficiency. $\mathrm{E}_1(y)$ is found to approach 0 when $y \geq 10$, and can be approximately captured by the asymptotic series:

$$\Omega(y) = \frac{e^{-y}}{y}\left[1 + \sum_{n=1}^{10} \frac{n!}{(-y)^n}\right], \qquad y \geq 10 \tag{4.71}$$

It is worthwhile to note that the asymptotic series is not convergence and only the first 10 terms are chosen for calculation. The comparison results between the series results

derived by Eq. (4.71) and the exact results calculated by MATLAB are depicted in Figure 4.4 . The maximum error is less than 2×10^{-4} when $y\to10$, which will be proven to satisfy the calculation accuracy.

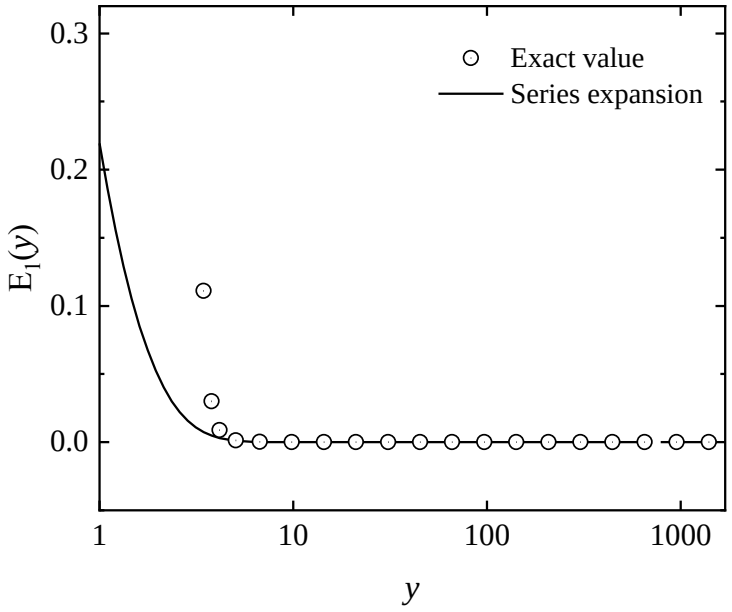

Figure 4.4 Exact and series solution of the exponential integral for *y*>10

4.6.2 Numerical integration of the exponential integral

After showing the series solution of the exponential integral, this subsection will validate that the series solution meets the calculation accuracy of numerical integration of Eq. (4.65) and discusses how to deal with the problem of $e^{\tilde{a}^2}\to\infty$ with the aid of Eq. (4.71).

From the point of view of the exponential integral, there are three possible ways to integral the left hand of Eq. (4.65) by MATLAB, including:

(i) directly using the integral functions inclined in MATLAB. Although this way seems to be quite convenient, the main shortcoming is that the integral tends to become infinite when $e^{\tilde{a}^2}\to\infty$.

(ii) changing the integral to.

$$\int_{\tilde{r}^2}^{\tilde{\rho}^2} \exp\left[\omega e^{\tilde{a}^2}\Omega(y)\right]\mathrm{d}y = \int_{\tilde{r}^2}^{\tilde{\rho}^2} \exp\left(\omega\int_{y}^{\infty}\frac{e^{\tilde{a}^2-x}}{x}\mathrm{d}x\right)\mathrm{d}y \tag{4.72}$$

Since $\tilde{a}^2 \le \tilde{r}^2 \le \tilde{\rho}^2$, $e^{\tilde{a}^2-x}$ will be less than 1 and the integral can be calculated by MATLAB regardless of what the value of $\tilde{a}$ is. However, it can be time-consuming to integrate Eq. (4.72) by numerical integration methods inclined in MATLAB, and Eq. (4.72) should be integrated in each iteration to find an "accurate" ρ.

(iii) changing $\mathrm{E}_1(y)$ by Eq. (4.70) or (4.71). The approximate series solution can help improve the calculation efficiency and prevent the computational capacity when $e^{\tilde{a}^2} \to \infty$. This integral method is followed in this chapter owing to the convenience of solving Eq. (4.65) by iterations.

Figure 4.5 shows the change of the integrand (i.e. $\exp\left[\omega e^{\tilde{a}^2}\mathrm{E}_1(y)\right]$) with various y in the logarithmic scale, and the results computed by the way (ii) for exact values and way (iii) for approximate values are compared. For various $\tilde{a}$ and y, it can be found that the errors can be ignored when replacing the exponential integral with the series expansion.

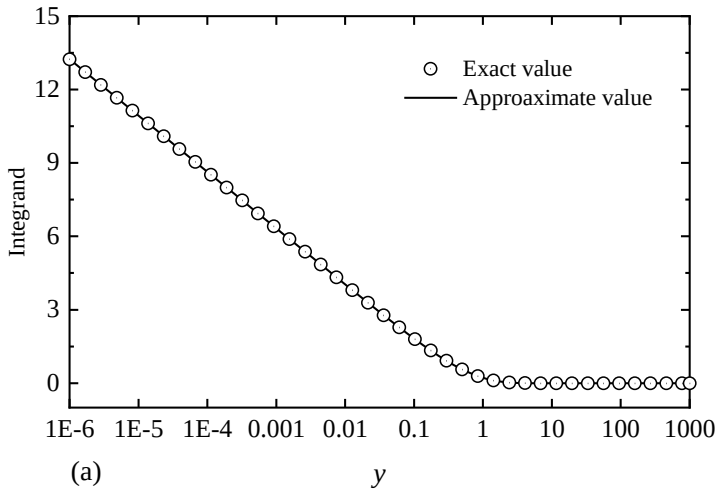

(a)

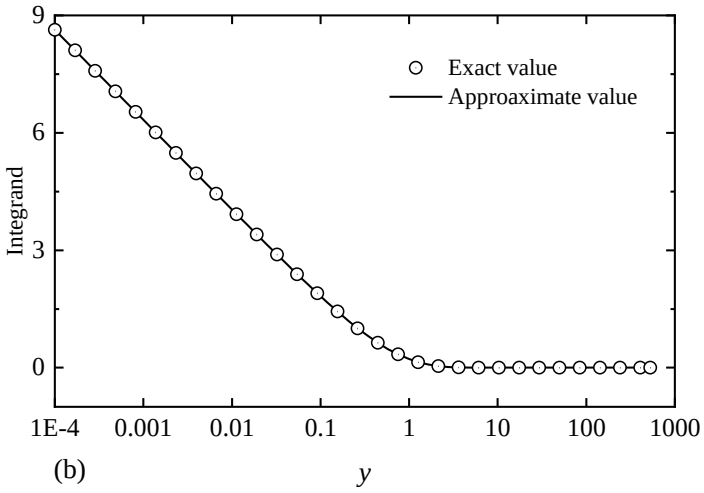

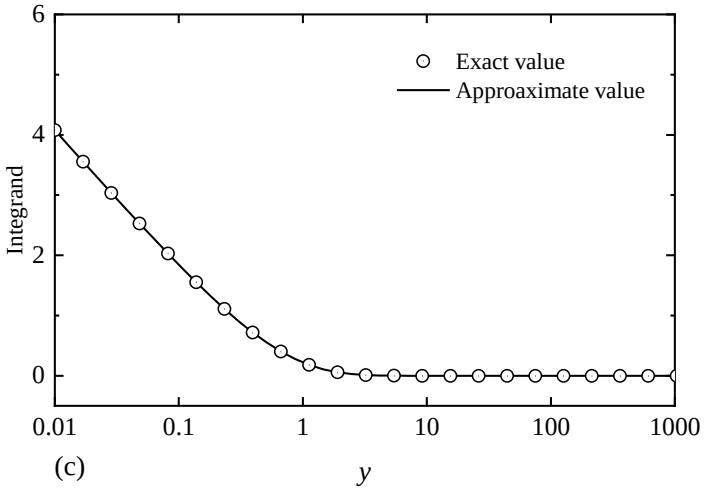

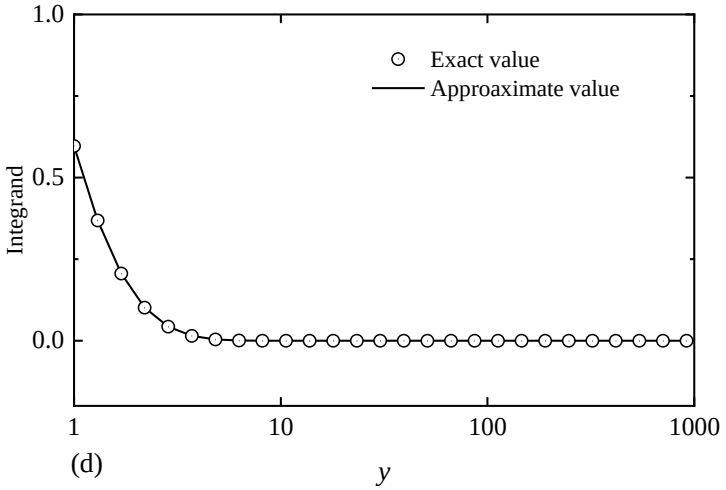

Figure 4.5 Comparison of exact and approximate values of the integrand:

(a) $\tilde{a} = 0.001$; **(b)** $\tilde{a} = 0.01$; **(a)** $\tilde{a} = 0.1$; **(a)** $\tilde{a} = 1$.

For a given time, the simple and practical secant method is used to find the roots of Eq. (4.65) (i.e. $\tilde{\rho}$), which is one of the iteration methods for non-linear equations. The reason for choosing the secant method is that the lower and upper limits of the roots are provided by the cases of cavity expansion in fully drained and undrained conditions. To avoid repetitive calculation of the integrals in each iteration, the integrals of the left hands of Eq. (4.65) are computed numerically by the trapezoidal rule instead of using inclined integral functions in MATLAB. Besides, in the range of upper and lower bounds of $\tilde{\rho}$, Simpson's rule that provides the degree of exactness of 3 is used to minimise the error induced by the step size. For easy referencing, the Matlab code is detailed in Appendix C.

4.7 Special cases: fully undrained and drained cases

While the solution for cavity expansion under partially drained conditions is given in the above sections, two special cases for ideally drained and undrained conditions can be deduced from the given solution by taking $c_{\mathrm{hp}} \to 0$ (ideally undrained) and $c_{\mathrm{hp}} \to \infty$ (ideally drained). These two cases can provide useful initial values for iterations of Eq. (4.65) by Newton-Raphson-type methods.

4.7.1 Fully undrained case

Under undrained conditions ($c_{\mathrm{hp}} \to 0$ and $\tilde{r} \to \infty$), the exponential integral can be approximately replaced by the asymptotic series:

$$e^{\tilde{a}^2}\mathrm{E}_1\left(\tilde{r}^2\right) \approx \frac{e^{\tilde{a}^2-\tilde{r}^2}}{\tilde{r}^2}\left[1+\sum_{n=1}^{10}\frac{n!}{\left(-\tilde{r}^2\right)^n}\right] < \frac{1}{\tilde{a}^2} \tag{4.73}$$

When $\tilde{a} \to \infty$, Eqs. (4.56) and (4.69) can be simplified as:

$$\sigma_r' = \sigma_{r\rho}' = \sigma_{\mathrm{h}0}' + s_{\mathrm{u}} \tag{4.74}$$

and Eq. (4.65) is recovered to be

$$a^2 - a_0^2 = \rho^2 - \rho_0^2 \tag{4.75}$$

Combining Eqs. (4.57) and (4.75), the inner cavity pressure can be expressed as

$$\sigma_a = \sigma_{\mathrm{h}0} + s_{\mathrm{u}} + s_{\mathrm{u}} \ln\left[I_{\mathrm{r}}\left(1-a_0^2/a^2\right)\right] \tag{4.76}$$

which is identical to the solution of Gibson and Anderson (1961). When a_0=0, the EWP under fully undrained conditions can be derived from Eq. (4.76):

$$U_{\mathrm{ref}} = s_{\mathrm{u}} \ln I_{\mathrm{r}} \tag{4.77}$$

For the Tresca model, U_{ref} can be seen as the reference EWP for the normalisation of EWP in CPTU.

4.7.2 Fully drained case

Under fully drained conditions ($c_{\mathrm{hp}} \to \infty$ and $\tilde{r} \to 0$), the exponential integral can be expanded into the series form as

$$\mathrm{E}_1\left(\tilde{r}^2\right) = -\zeta - 2\ln\tilde{r} - \sum_{n=1}^{\infty} \frac{\left(-\tilde{r}^2\right)^n}{nn!} \approx -\zeta - 2\ln\tilde{r} \tag{4.78}$$

where ζ (=0.577215…) is the Euler-Mascheroni constant. Substituting Eq. (4.78) into Eqs. (4.56), (4.65), (4.67) and (4.68), we can get the analytical solution under fully drained conditions, as

$$\sigma_r' = \sigma_{\mathrm{h0}}' + s_{\mathrm{u}} + 2s_{\mathrm{u}} \ln\left(\tilde{\rho}/\tilde{r}\right) \tag{4.79}$$

$$U = 0 \tag{4.80}$$

$$\left(\frac{\tilde{r}}{\tilde{\rho}}\right)^{2-2\omega} - 1 = \left(1-\omega\right)\left[\left(\frac{\tilde{r}_0}{\tilde{\rho}}\right)^2 - \left(\frac{\tilde{\rho}_0}{\tilde{\rho}}\right)^2\right] \tag{4.81}$$

4.8 Results and Discussion

For illustration this section explores the cavity expansion response and EWP evolution during cavity expansion with a constant expansion rate and a constant normalised inner radius. Unless stated otherwise, the following input parameters are adopted in this section: a_0=1m, u_{w0}=0kPa, σ_{h0}=σ_{v0}=10kPa, s_{u}=10kPa, I_{r}=100, μ=0.3.

4.8.1 Numerical Simulations and Validation

Numerical simulations for cavity expansion under partially drained conditions are conducted by Comsol Multiphysics 6.0 (CM6) that is a kind of finite element software

for multi-coupling analyses. The proposed solution in this chapter is validated by comparing the theoretical and numerical results.

4.8.1.1. Model geometry

Due to the axial-symmetry of the problem, the numerical model is established by choosing an annular sector of $1°$, as shown in Figure 4.6. The initial inner radius (a_0) of the annular is 1m while the initial outer radius (b_0) is set as 1000m to simulate the infinite soil thickness around the cavity. When the cavity expansion level is up to $a_{\text{end}}/a_0 = 10$, b_0/a_0 =1000 is sufficiently large to eliminate the possible outer boundary effect of the annular sector. It is necessary to mention that the infinite element domain is not used to simplify the numerical model. This is mainly because the element size should be carefully restricted in the hydro-mechanical coupling process (will be shown below).

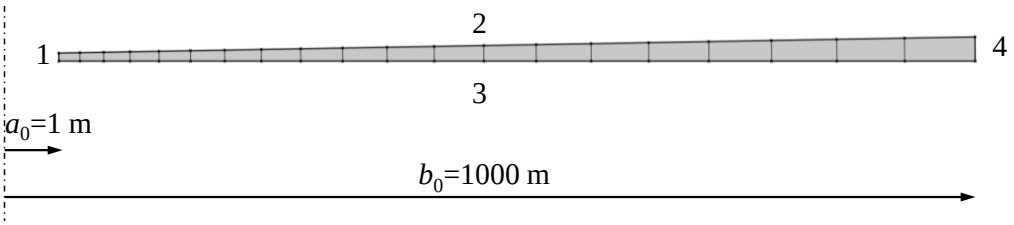

Figure 4.6 Schematic of the numerical model

4.8.1.2. Mesh generation and time step

Quadrilateral meshes are generated by the mapped function in the radial direction and the meshes are highly structured because of the symmetry. Since driven forces are also in the radial direction, the meshes are not distorted in the large strain cavity expansion and there is no need to add the moving mesh. The nodes on sides 2 and 3 are nonlinearly distributed that satisfy Eq. (4.82):

$$r_{(i+1)} = 1.01 r_{(i)} \tag{4.82}$$

To make it stable in the calculation of EWP, the time step and the maximum element size

should satisfy:

$$\mathrm{D}t > \frac{\gamma_{\mathrm{w}}}{12G(1+\mu)k}(\mathrm{d}r)^2 \tag{4.83}$$

Therefore, the total element number is not a constant and is dependent on the soil properties. For completely dry conditions that do not consider the hydraulic behaviour, the total number of 1000 is found to be suitable for numerical simulations, but more than 10000 elements may be required for low permeable clays with hydro-mechanical coupling in CM6.

4.8.1.3. Mechanical behaviour

The numerical model is established under the plane strain conditions. Quasi-static analysis is selected which means dynamic forces are ignored, and the second-order Lagrangian element is adopted for displacement fields. The solid domain is modelled by the perfectly elastoplastic Tresca model which is the same as the theoretical analysis. The elastic parameters of the clay are set as: E=26000kPa and μ=0.3. The soil density is set as 2000kg/m^3 and this parameter has no influence on the simulation results due to the ignorance of body forces. The initial yield stress is chosen as 20 kPa and the kinematic hardening is not considered.

Large strains are selected for the plasticity to account for the large deformation. However, this will automatically cause the geometric nonlinearity in the elastic zone. The different definitions of strains in the elastic zone may result in slight differences between the present theoretical solution (small strain definition) and FEM numerical results (large strain definition). For example, positive EWP may be predicted in CM6, especially for the clays with a low rigidity index.

4.8.1.4. Hydraulic behaviour

Fluid flow (i.e. water in this chapter) is assumed to obey Darcy's law and be uncompressible. The permeability of clay varies in different simulations while the water density is constant as 1000 kg/m^3. The clay is seen as the poroelastic medium to model

the water flow. Considering tensile as positive in CM6, the porosity of the soil skeleton is the user-defined function:

$$1-\frac{\exp\left(-\varepsilon_v\right)}{2} \tag{4.84}$$

where Eq. (4.84) means that the initial specific volume is 2.0.

4.8.1.5. Boundary conditions

For the solid part, the tangential displacement on sides 2 and 3 in Figure 4.6 is restricted and the radial displacement is prescribed at the inner cavity wall (side 1 in Figure 4.6):

$$a = a_0 + V_a t \tag{4.85}$$

V_a is the velocity of cavity expansion that the inner cavity radius increases linearly with time. In this chapter, V_a=1 m/s is applied to the numerical model, and the drainage conditions are mainly controlled by the soil permeability.

For simplification, the initial stress σ'_{h0} is set as 0.1Pa in the numerical model to avoid the balance of initial geostatic stresses. The soundness of this simplification is that the stiffness, strength, and dilatancy of soils do not rely on the stress level in the elastoplastic Tresca model. On the other hand, for Darcy's flow, sides 1, 2 and 3 in Figure 4.6 are set as impermeable boundaries, while side 4 is set as the permeable boundary with zero EWP.

4.8.1.6. Hydro-mechanical coupling

The embedded hydro-mechanical coupling analysis in CM6 is directly adopted by adding The Multiphysics Branch. The reference water pressure is selected as 0 and the Biot-Willis coefficient is set as 1.

4.8.1.7. Time-dependent solver and calculation

The above numerical model is solved by the MUltifrontal Massively Parallel Sparse Direct Solver (MUMPS) built-in Comsol and is computed by the fully coupled approach. The relative tolerance is user-defined as 0.001, and the Jacob matrix is updated in each

iteration step with more cost of time but improvement of the stability of calculation. After calculation, the data are extracted by creating a point probe at the inner cavity wall, including the displacement, radial effective stress and EWP.

4.8.2 Cavity expansion with a constant expansion rate

Cavity expansion behaviour with a constant expansion rate is firstly investigated and the inner cavity radius in this loading pattern can be defined as Eq. (4.85) (Silva et al., 2006; Mafra and Dienstmann, 2022).

To highlight the influences of V_a and relative soil permeability (i.e. k/γ_w), Figure 4.7 shows the cavity expansion curves and EWP at the cavity wall calculated by the present solution with $k/\gamma_w = 10^{-6}$ and 10^{-9} $m^2s^{-1}Pa^{-1}$ and various V_a. Cavity expansion curves under fully drained and undrained conditions are calculated by Eqs. (4.76), (4.79) and (4.81) and they serve as the lower and upper boundaries of the shadow areas in Figure 4.7. Numerical simulation results, taking the same soil model and input soil parameters, are computed by CM6 software with $k/\gamma_w = 10^{-6}$ $m^2s^{-1}Pa^{-1}$ and are also added for comparison.

Figure 4.7 shows that the total inner pressure under partially drained conditions is restricted within the shadow area. With the present parameters, σ_a/s_u under undrained conditions (upper bound of the shadow area) is about 4% higher than that under drained conditions (lower bound of the shadow area), which reveals that σ_a/s_u is minimally affected by the drainage conditions and expansion rate. It can be found that:

(i) For cavity expansion in a high velocity in a low permeable media (e.g. $V_a = 10^{-1}$ and $10^{-9} m^2s^{-1}Pa^{-1}$), the cavity behaves in an undrained manner, and the difference between σ_a/s_u and U/s_u is a constant ($\sigma'_{h0}/s_u + 1$ as shown by Eq. (4.74)) when plasticity occurs.

(ii) For cavity expansion in a low velocity in a high permeable media (e.g. $V_a = 10^{-4}$ m/s and $10^{-6}\text{m}^2\text{s}^{-1}\text{Pa}^{-1}$), the cavity shows ideally drained behaviour and U/s_u vanishes as indicated by Eq. (4.80).

(iii) U/s_u at the cavity wall increases with $V_a a\gamma_w/k$ under partially drained conditions, indicating the significant influence of the partially drained effect. Therefore, partial drainage mainly influences the proportion of effective stresses and EWP, without significantly changing the sum of the two components (i.e. the total stress).

(iv) Comparing the EWPs in Figure 4.7 (a) ($k/\gamma_w = 10^{-6}\text{m}^2\text{s}^{-1}\text{Pa}^{-1}$) and Figure 4.7 (d) ($k/\gamma_w = 10^{-9}\text{m}^2\text{s}^{-1}\text{Pa}^{-1}$), it is interesting to find that U/s_u is the same for the same a/a_0 and $V_a\gamma_w/k$. This finding will be further discussed for the normalisation of EFP under partially drained conditions.

(vi) Finally, σ_a/s_u and U/s_u predicted by the present analytical solution agrees well with those calculated from numerical simulations, which validates the accuracy of the approximate solution.

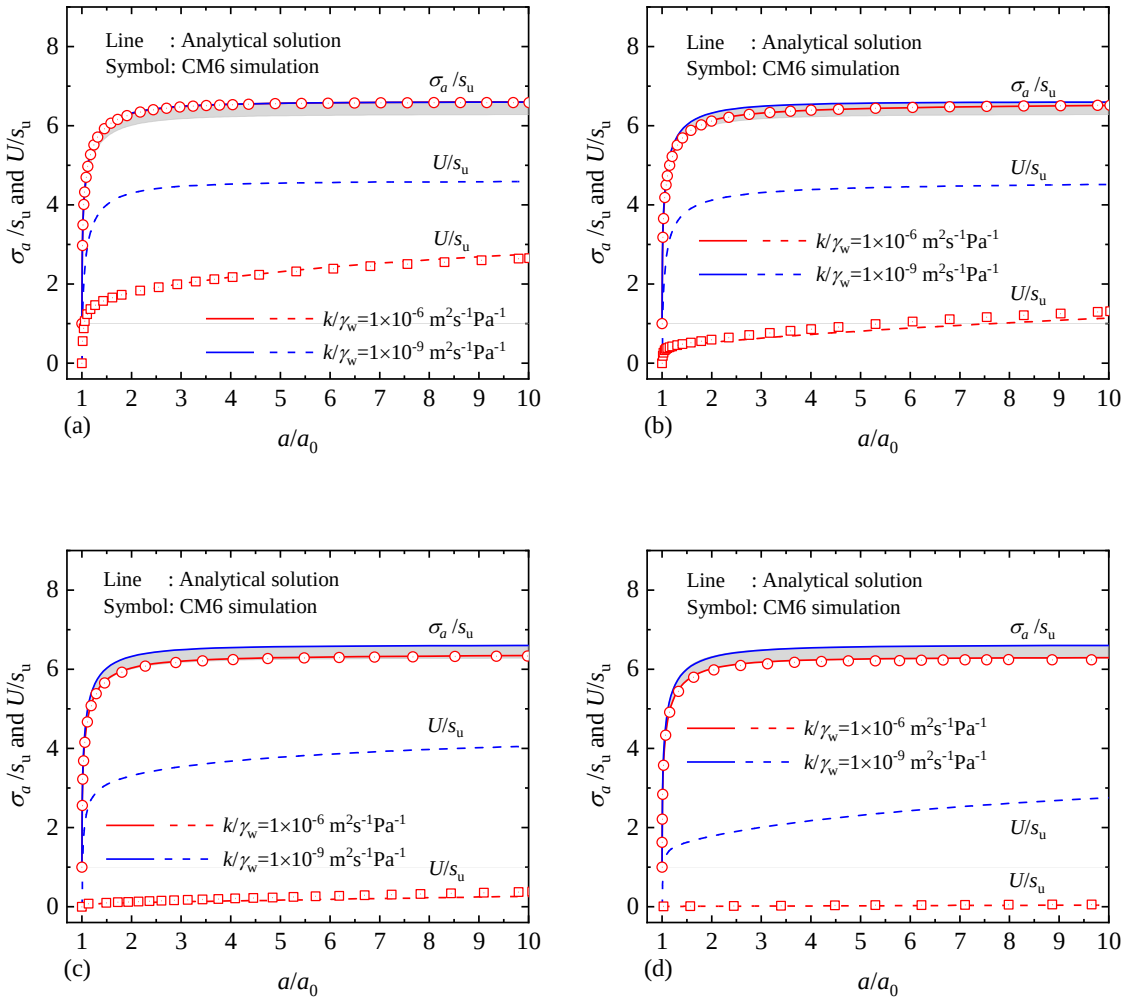

Figure 4.7 Cavity expansion curves and EWP with various expansion rates:

(a) $V_a = 10^{-1}$ **m/s; (b)** $V_a = 10^{-2}$ **m/s; (c)** $V_a = 10^{-3}$ **m/s; (d)** $V_a = 10^{-4}$ **m/s**

4.8.3 Cavity expansion with a constant normalised radius

This subsection discusses the case of a cavity expanding with a constant normalised inner radius (i.e. constant $\tilde{a}=\delta$), in which the inner cavity radius in this loading pattern is defined as

$$a=2\delta\sqrt{c_{hp}t},\ \rho \geq a \tag{4.86}$$

$$\tilde{a}=\delta,\ \rho \geq a \tag{4.87}$$

where δ is a constant that controls the expansion "rate". Substituting Eqs. (4.45) and (4.86) into Eq. (4.44), the boundary conditions at $r=a$ can be simplified to

$$\frac{\partial \sigma'_r}{\partial \tilde{r}} = \frac{-2s_u}{\delta} \quad \text{for} \quad \tilde{r}=\tilde{a}<\tilde{\rho} \tag{4.88}$$

In this case the right-hand of Eq. (4.88) is a constant and it will be proved later that the cavity expansion behaviour is independent of k/γ_w (or c_{hp}) as long as δ is given.

The total inner pressure and EWP at the cavity wall with various δ are computed by the present solution and are plotted in Figure 4.8. Initially both σ_a/s_u and U/s_u increase with a/a_0 to later reaching limit values for a/a_0 larger than 3. Due to the influence of partially drained conditions, the limit values of σ_a/s_u and U/s_u increase with δ. The cavity expansion curves get close to those under fully drained conditions for small δ (e.g. less than 0.01) and fully undrained conditions for large δ (e.g. larger than 10). Compared with the case for constant V_a, U/s_u computed in the case of constant $\tilde{a}$ gets steady much earlier, rather than progressively increases with a/a_0 (see Figure 4.7). For a given value of δ, the curves for constant $\tilde{a}$ are found to be independent of k/γ_w, which represents another difference from the case for constant V_a. This characteristic means that δ can be back-calculated from the measured U/s_u, and then c_{hp} may be obtained by Eq. (4.86) with a and t recorded in pressuremeter tests.

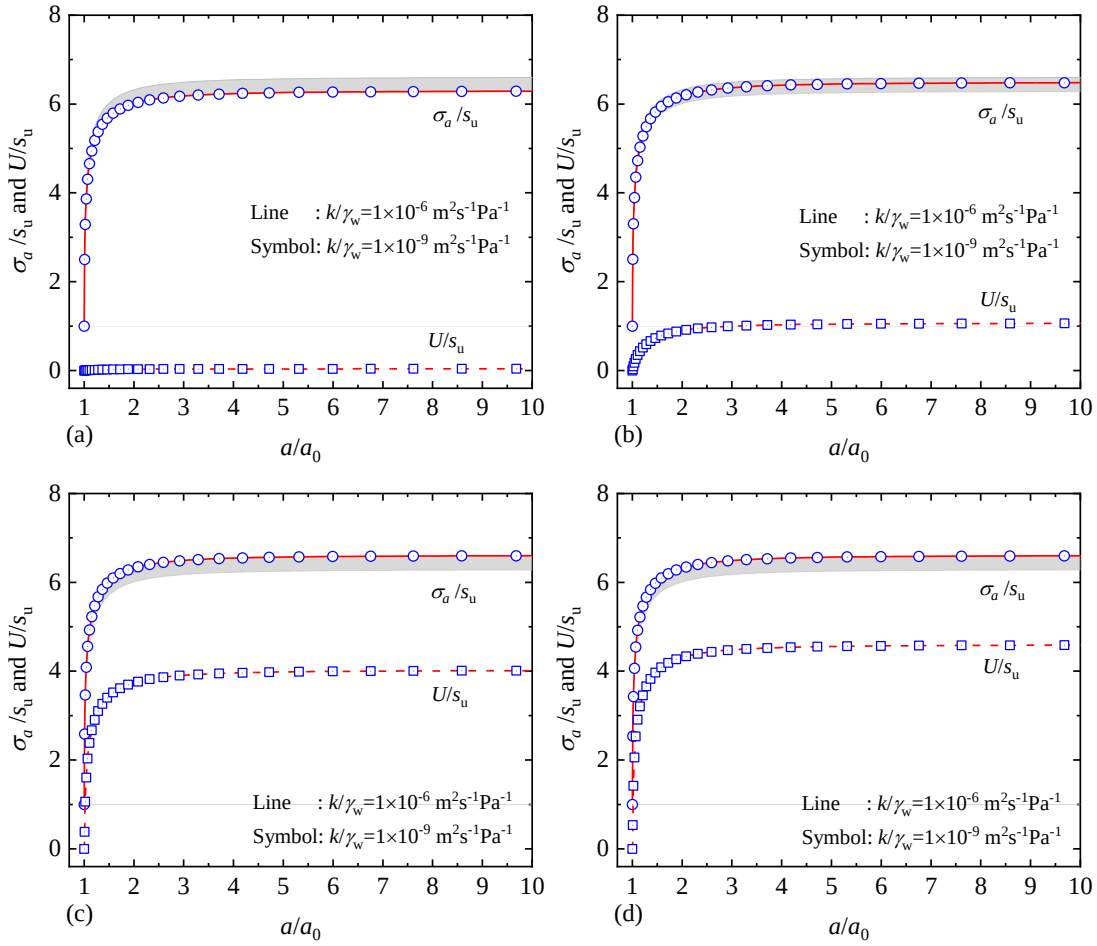

Figure 4.8 Cavity expansion curves and EWP with various δ:

(a) δ =0.01; (b) δ =0.1; (c) δ =1; (d) δ =10

4.9 Penetration rate normalisation in CPTU

Normalisation of cone penetration rate is an important step for assessment of soil properties and for comparisons of data from different sites. The normalisation of penetration rate in CPTU is discussed in this section with due consideration of partial drainage and soil rigidity variation.

4.9.1 Modified normalised rate and backbone curve

First of all, the theoretical basis of $\overline{V}_0$ for quantifying the partially drained effect in CPTU is proven based on the present solution. Combining Eqs. (4.43), (4.45), and (4.85) with $a_0 \to 0$, the normalised radius at $r = a = D/2$ can be expressed as

$$\tilde{a}^2 = \frac{V_a D}{8c_{\mathrm{hp}}} = \tan\left(\frac{\vartheta}{2}\right)\frac{V_{\mathrm{cptu}} D}{8c_{\mathrm{hp}}} = \tan\left(\frac{\vartheta}{2}\right)\frac{\bar{V}_0}{8} \tag{4.89}$$

$$\bar{V}_0 = \frac{V_{\mathrm{cptu}} D}{c_{\mathrm{hp}}} \tag{4.90}$$

where $\bar{V}_0$ is the original normalised penetration rate in CPTU (Randolph and Hope, 2004; DeJong and Randolph, 2012) and is the function of $\tilde{a}^2$ only (ϑ is usually 60°). Once $\tilde{a}^2$ (or $\bar{V}_0$) and I_{r} are given, $\tilde{\rho}^2$ can be fully determined from Eq. (4.65). Then the normalised EWP, $\bar{U}$ (see Eq. (4.91)), can also be known by Eqs. (4.58), (4.67) and (4.77).

$$\bar{U} = U/U_{\mathrm{ref}} \tag{4.91}$$

Therefore, the backbone curve (i.e. $\bar{U}-\bar{V}_0$ curve) is unique for a given soil (i.e. given I_{r}), and $\bar{V}_0$ can be used to account for the partial drainage conditions.

Eq. (4.65) and some former publications (Dienstmann et al., 2018b; Mafra and Dienstmann, 2022) show that the evolution of EWP is also affected by I_{r}. When $\bar{U}$=0.5, for example, Dienstmann et al. (2018b) reported that $\bar{V}_0 \approx 0.01$ for I_{r}=900 while $\bar{V}_0 \approx$ 0.03 for I_{r}=100. Therefore. $\bar{V}_0$ may not be able to fully quantify the partial drainage effect for a wide range of soils with various I_{r}. Moreover, Figure 4.9 (a) plots 6 series of $\bar{U}-\bar{V}_0$ curves calculated by the present solution with input parameters in Table 4.1. It is clearly shown that under partially drained conditions $\bar{U}$ increases with I_{r} for a given $\bar{V}_0$, and the backbone curves are noticeably dependent on I_{r}.

To consider the influence of I_{r} in the penetration process, a modified normalised penetration rate, $\bar{V}$, is defined in this thesis as

$$\bar{V} = \bar{V}_0 I_r^{\bar{m}} = \frac{V_{cptu} D}{c_{hp}} I_r^{\bar{m}} = \frac{1}{\tan(\vartheta/2)} \frac{V_a D}{c_{hp}} I_r^{\bar{m}} \tag{4.92}$$

where $\bar{m}$ is a curve fitting parameter in the range of 0.45~0.5. The calculated backbone curves are replotted in Figure 4.9 (a) with the modified $\bar{V}$ ($\bar{m}$=0.5), and it is shown the modified backbone curves ($\bar{U} - \bar{V}$) converge to a narrow band that can be fitted by the following expression (DeJong and Randolph, 2012):

$$\bar{U} = 1 - \frac{1}{1 + (\bar{V}/8.1)^{0.7}} \tag{4.93}$$

The uniqueness of Eqs. (4.92) and (4.93) for normalisation of partially drained effect is clearly illustrated.

Table 4.1 Input parameters for the normalisation of rate effect

Series	G : kPa	s_u : kPa	I_r	U_{ref}/s_u
S1	200	10	20	3.00
S2	500	10	50	3.91
S3	1000	10	100	4.60
S4	2000	10	200	5.29
S5	5000	10	500	6.20
S6	10000	10	1000	6.90

Note: $V_a = 10^{-2}$ m/s, $k/\gamma_w = 10^{-5} \sim 10^{-15} \mathrm{m^2 s^{-1} Pa^{-1}}$, μ=0.3, a_0=0, and D=0.04m

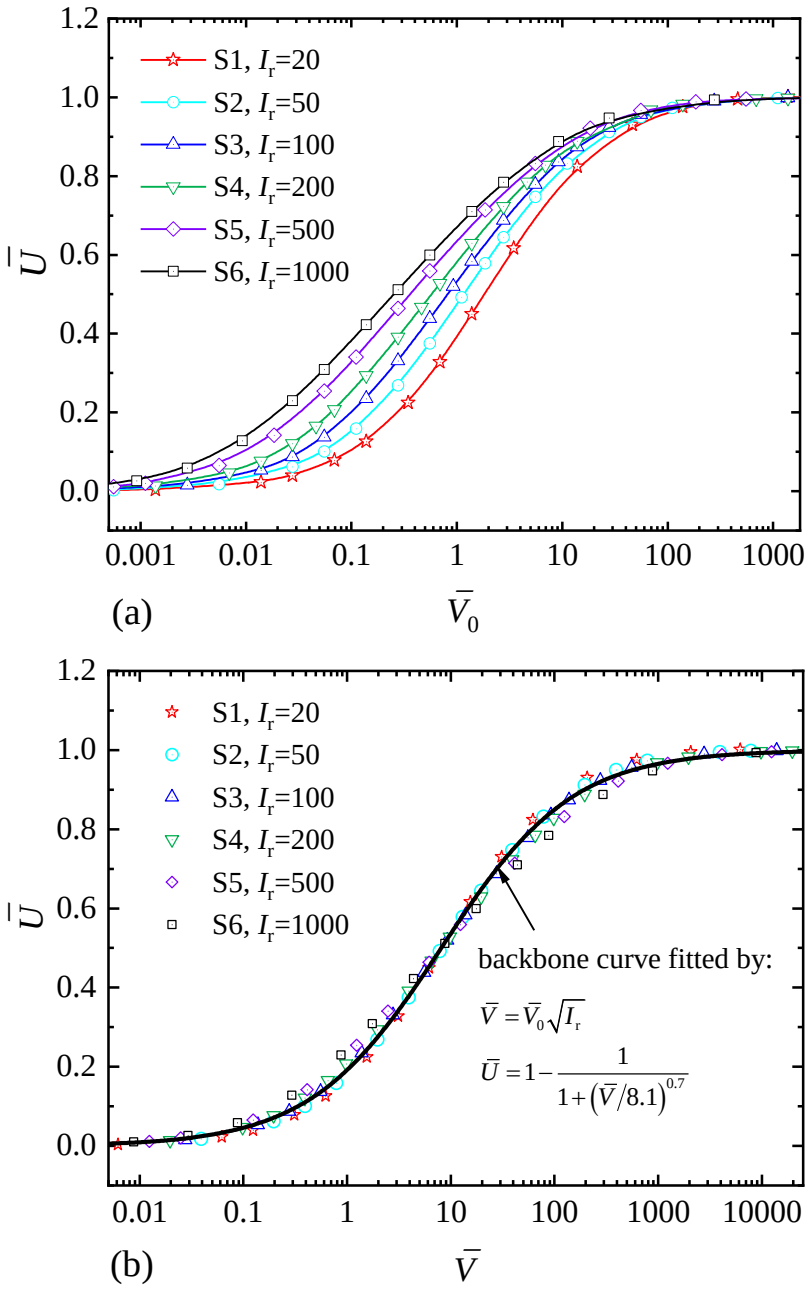

Figure 4.9 Backbone curves in CPTU: (a) based on $\bar{V}_0$; (b) based on $\bar{V}$

4.9.2 Validation of the backbone curve and potential applications

The new backbone curve defined in Eq. (4.93) is validated by comparison with a database containing experimental and numerical results, as summarised in Table 4.2. In the database a total number of 109 in-situ tests in silts-gold tailings (Fazenda Brasileiro Mine, Brazil) and 101 Centrifuge model tests (40g) in normally consolidated UWA Kaolin Clay are collated. Numerical simulation results were mainly calculated by FEM and MPM, and

the DP model and MCC were used for constitutive modelling of soils (e.g. Kaolin clays and Malaysian Kaolin silt). Some CPTU data are modified/ excluded, and the reasons and discussions are detained in Appendix D. Overall, the database covers a wide range of I_r from 32 to 874.

The data in the database are plotted in Figure 4.10 for comparison with the proposed solution (see Eq. (4.93)). The scatter of the database comes mainly from in-situ tests in silts-gold tailings, which may be attributed to the wide spatial dispersion of testing sites, deposition conditions, and material segregation, among other factors (Dienstmann et al., 2018b; Mafra and Dienstmann, 2022). When compared with the database, the new backbone curve predicted by the present solution is able to capture well the partially drained effect in CPTU. Besides, the present backbone curve gives an overestimation of $\bar{U}$ for a small $\bar{V}$ (i.e. approximately less than 3), and it may be induced by the neglection of EWP dissipation and soil deformation in the vertical direction (Soderberg, 1962; Robertson and Campanella, 1983; Zhang, Y. et al., 2022). The vertical EWP dissipation may be partially described by a corresponding solution in the spherical scenario and this will be developed in a further study combining with the normalisation of cone tip resistance. Figure 4.10 also shows the comparison of the backbone curves predicted by Mafra and Dienstmann (2022) and this study via the cavity expansion method. The two curves show similar trends but the curve of Mafra and Dienstmann (2022) tends to overestimate $\bar{U}$. This difference may result from the imposed initial EWP distribution predefined in Mafra and Dienstmann (2022), which is not required in the proposed solution.

Table 4.2 Database and cavity expansion method for partially drained effect in CPTU

References	Soil type/ model	Numbers	I_r	c_{he}/c_v	μ	Method
Bedin (2006)	Silty-gold tailing	16	874[&]	—	0.3	In-situ tests
Klahold (2013)	Silty-gold tailing	14	874[&]	—	0.3	
Sosnoski (2016)	Silty-gold tailing	79	874[&]	—	0.3	
Randolph and Hope (2004)	Kaolin clay	50	76*	4.66*	0.3	Centrifuge tests
Schneider et al. (2007)	Kaolin clay	21	76*	4.66*	0.3	
Mahmoodzadeh and Randolph (2014)	Kaolin clay	30	76*	4.66*	0.3	
Liyanapathirana (2009)	MCC	9	74	4.66*	0.3	FEM
Yi et al. (2012)	DP	40	74/148	1	0.3	
Sheng et al. (2014)	MCC	23	32[§]	—	0.33	
Liu et al. (2022)	MCC	24	59[†]	4.7[‡]	0.3	
Ceccato and Simonini (2017)	MCC	—	108	3	0.25	MPM
Mafra and Dienstmann (2022)**	DP	—	874	—	0.3	Cavity expansion
This study	Tresca	—		—	0.3	Cavity expansion

[&]Refer to Dienstmann et al. (2017), Dienstmann et al. (2018b), and Schnaid et al. (2020);

*Refer to Mahmoodzadeh, Hamed and Randolph (2014) and Mahmoodzadeh, H et al. (2015);

[‡]Variation of c_{he}/c_v with $\bar{V}_0$ is not considered;

[§]Refer to Obrzud et al. (2011);

[†]Refer to Zhang, Y. et al. (2022);

**The curve without correction is selected (i.e. $I_r \approx 874$).

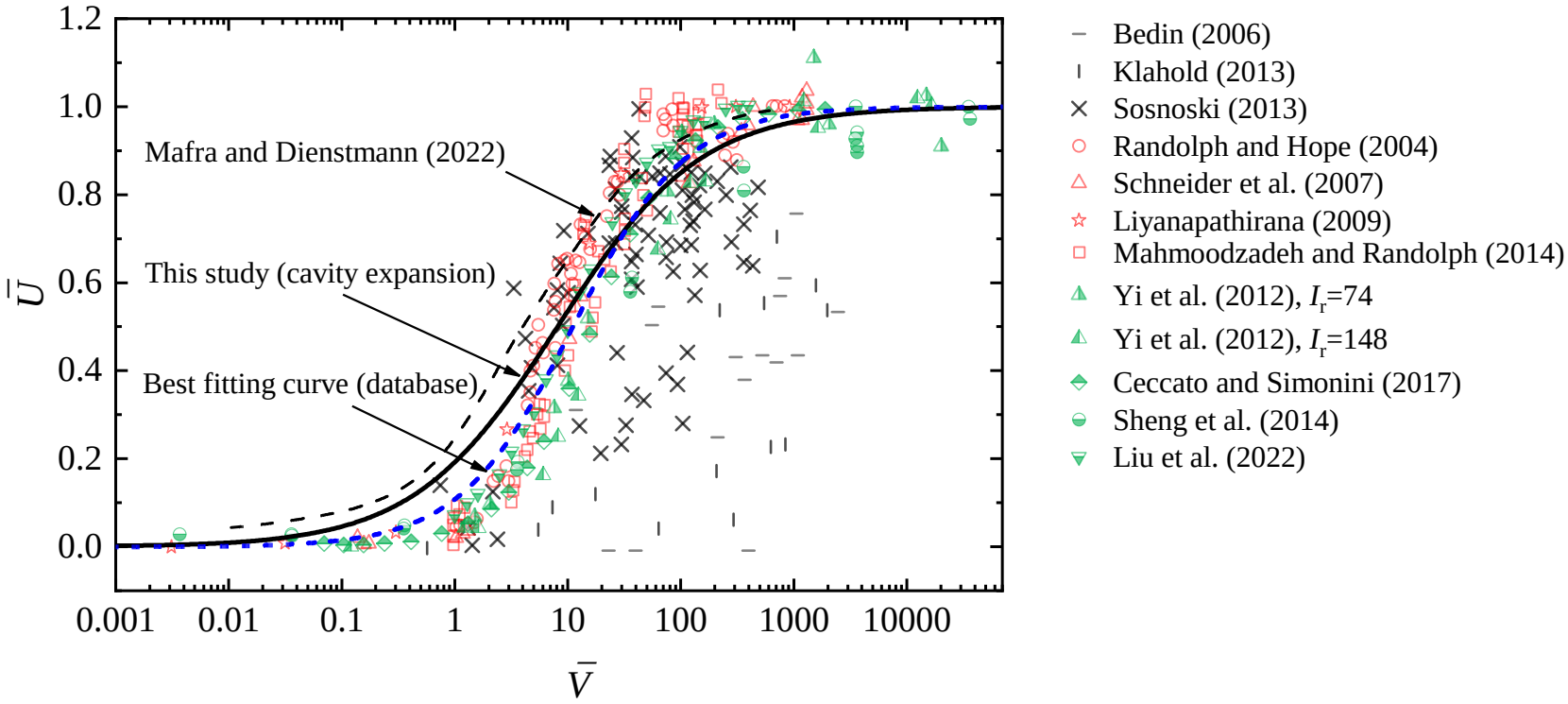

Figure 4.10 Predicted backbone curve versus experimental and numerical results

The unique backbone curve ($\bar{U}-\bar{V}$) may provide a potential approach to assess the in-situ consolidation coefficient of soils from multi-rate CPTU (Fahey and Goh, 1995; House et al., 2001; Randolph and Hope, 2004), following:

(i) Carry out multi-rate CPTU with different penetration rates and measure EWPs.

(ii) Interpret I_r by conventional methods (e.g. Mayne et al. (2022); Khodayari and Ahmadi (2022)).

(iii) Combine Eqs. (4.92) and (4.93) to calculate c_{hp} by Eq. (4.94) with I_r and the measured EWPs.

$$c_{hp}=\frac{V_{cptu}D\sqrt{I_r}}{8.1}\left(\frac{1-\bar{U}}{\bar{U}}\right)^{1.43} \tag{4.94}$$

In the future multi-rate CPTU and subsequent dissipation tests can be performed in the field and in the laboratory, and it is expected that more reliable values of c_h can be obtained by combining the interpretation of CPTU in the penetration and dissipation stages. Finally, it is worth noticing that although the partially drained effect in CPTU is only quantified herein by the normalised EWP, due to the limitation of paper length, further research will concentrate on the normalisation of cone tip resistance by $\bar{V}$.

4.10 Discussion on the selected Tresca model

The major limitation of the present solution is the selection of the Tresca model for cavity expansion under partially drained conditions. The inherent shortcomings of the Tresca model are therefore inclined in the solution:

(i) The equivalent shear strength and shear modulus are input parameters rather than dependent on stress and volume changes. Therefore, the state-dependent soil strength and stiffness are beyond the scope of this chapter.

(ii) The soil model fails to encompass the consequence of volumetric change on the soil mechanical behaviour because the plastic volumetric strain is always zero with the associated plastic flow rule. Accordingly, parameters controlling the compressibility of a normally consolidated clay have not been included in the

calculation of "plastic" coefficient of consolidation.

However, an elastoplastic, hydro-mechanical coupled solution for cavity expansion has not been reported so far in a straightforward form, even using such a simple Tresca model. The advantages of the present solution lie in that:

(i) From the mathematical point of view, the Tresca model enables the cavity expansion analysis to be formulated into a standard Stefan problem and solved by the variable transformation method. When more advanced soil models are adopted (e.g. MCC in the time-stepping solution of Russell et al. (2023)), it may not be suitable to solve the complex governing equations by the variable transformation method.

(ii) From the perspective of solution form, choosing the Tresca model can enable the solution to be expressed in a concise straightforward form. Only in this concise form can the normalisation of EWP be deeply understood with the superiority of the solution in dimensional analysis.

(iii) From the practical point of view, there is an urgent need to modify the original normalised penetration rate for CPTU by considering I_r. Since I_r is the function of s_u and G, it can be more convenient to pay attention to these two parameters and Tresca model will be a valuable choice. The validation of the new normalised penetration rate and backbone are also helpful to demonstrate the reasonability of this simplification.

(iv) In view of the comparison of different soil models, the backbone curves behave in a similar trend as shown in Figure 4.10. It may be explained by: the generation and dissipation of the normalised EWP are mainly controlled by Darcy's law that is adopted in the database with different soil models. Therefore, this may be the reason why the present solution with the simple Tresca model can predict the new backbone curve successfully.

In summary, this paper contributes to the development of the cavity expansion theory

under partially drained conditions and its application in geotechnical engineering by selecting the Tresca model as a starting point.

4.11 Chapter summary

This chapter proposes a hydro-mechanical coupled solution for large strain cylindrical cavity expansion under partially drained conditions. The mechanical behaivour of the porous media is modelled as a perfectly elastoplastic material with Tresca yield criterion, while the hydraulic behaviour is assumed to obey Darcy's law. The defined cavity expansion problem is formulated into two partial differential equations (PDEs) in the elastic and plastic zones with an interface of Stefan-type moving boundary (i.e. elastopalstic boundary). A closed-form solution is obtained by the variable transformation method and is validated by comparison with numerical simulations. Finally, the proposed solution is applied to the normalisation of EWP in CPTU. It is found that:

(i) The partially drained effect has an important influence on EWP but little on the total inner pressure. EWP increases with the increase of cavity expansion velocity and decrease of permeability under partially drained conditions until it reaches the reference EWP under ideally undrained conditions.

(ii) For cavity expansion with a constant normalised radius δ, EWP increases with δ under partially drained conditions and is independent of hydraulic permeability as long as δ is given.

(iii) A modified normalised penetration rate is defined by considering the influence of the rigidity index of soils. With the new normalised rate, a unique backbone curve is found and validated by a database of experimental tests and numerical simulation results. Finally, a method for interpreting multi-rate CPTU (penetration stage) is suggested to measure the coefficient of consolidation of soils.

Overall the chapter contributes to quantifying the partially drained effect in CPTU to enhance the interpretation of CPTU in the dissipation stage. The new solution and backbone curve can also have potential applications to predict the EWP generated in animals' burrowing and pile installation in saturated soils, etc.

Chapter 5 Transient thermo-elastic cavity expansion solution for radial interaction between energy piles and soils

This chapter proposes an analytical solution for the calculation of thermo-elastic stresses and displacements during cavity expansion under transient temperature fields. Firstly, transient temperature distributions are shown and then applied to surrounding soil that is modelled as the linear elastic model. The solution is a modification of Kandil et al. (1995) by giving an analytical form and considering a radial displacement boundary at the pile-soil interface. It is therefore more suitable for RIEPS analysis in geotechnical engineering considering the combined effects of transient soil temperatures and energy pile expansion. Finally, the radial contact stress at the pile-soil interface is revisited focusing on the influences of soil temperature distributions and soil moduli.

Related publications	**Yang, H.**, Zhuang, P.-Z., Mo, P.-Q., Yu, H.-S. and Chen, X. 2024. Analytical Solution for Transient Radial Interaction Between Energy Piles and Soils: Thermo-Elastic Cavity Expansion Analysis. *Geomechanics for Energy and the Environment*. **39**, article no: 100572 [no pagination]

5.1 Problem Definition and Assumptions

The radial interaction between an energy pile and the surrounding soil during heating/cooling is modelled by the expansion/contraction of a cylindrical cavity (Olgun et al., 2014; Fuentes et al., 2016). As shown in Figure 5.1, a single energy pile with the diameter of $2a$ is embedded in a homogeneous and isotropic soil of infinite radial extent. Initially, the soil is subjected to a hydrostatic stress σ_0 and the ambient temperature of pile and soil is denoted as T_0. When t=0 (t denotes time), the energy pile is heated/cooled and soil temperature is assumed to be T_a at the pile-soil interface. Later, the energy pile will expand and the soil temperature will increase during the heating process (or the energy pile will contract and the soil temperature will decrease during the cooling process). In this period, stresses and displacements in the soil will change during the heating/cooling process (Olgun et al., 2014; Faizal et al., 2019b; Lv et al., 2020). Prior to showing the detailed derivation, necessary assumptions are introduced as follows and their reasonability and/or limitations are also demonstrated.

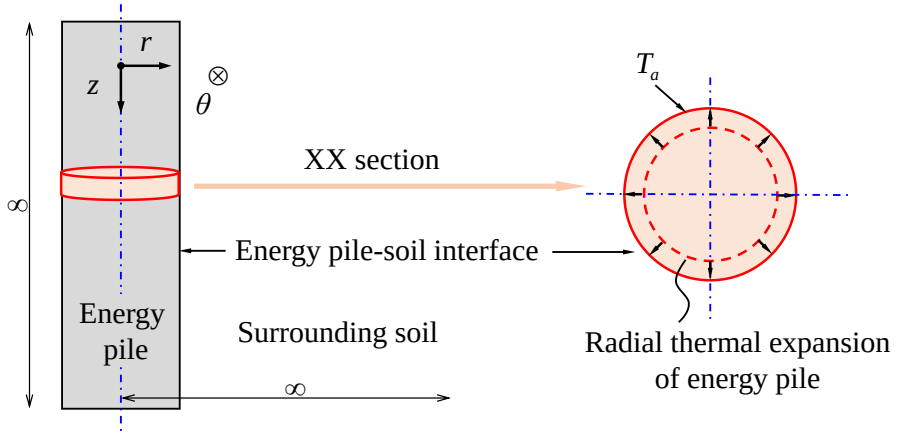

Figure 5.1 Schematic of radial energy pile-soil interaction

The length-to-diameter ratios of piles are usually large enough and the radial energy pile-soil interaction can be studied by concerning a certain horizontal plane under plane strain and axisymmetric conditions (i.e XX section in Figure 5.1) (Olgun et al., 2014; Fuentes

et al., 2016; Chen, H. et al., 2021; Pang et al., 2024). The cylindrical coordinate system (r,θ,z) is adopted for convenience with the origin at the pile centre.

The thermal expansion coefficients of soils and energy piles are usually in the order of 10^{-6}~10^{-5}/°C (Olgun et al., 2014; Bourne-Webb, P. et al., 2019), and thermal strains of soils could be in the order of 10^{-4}~10^{-5} for $|T_a - T_0| \leq 30$°C. Hence, the thermal-induced stresses and strains may be assumed to obey small strain definitions and Hooke's law (i.e. linear elastic stress-strain relationship) to simplify the solution derivation. The plasticity will be discussed in Section 5.3.4.

Assumptions in terms of soil temperatures can be summarised into three main aspects. At first, the change of soil temperature is mainly resulted from radial heat conduction, rather than heat radiation and convection. By comparing the finite and infinite line/cylinder sources, Philippe et al. (2009) validated that pile-soil heat conduction is mainly in the radial direction for a short period (i.e. several days for thermo-mechanical behaviour of energy piles). Secondly, the temperature at the pile-soil interface, T_a, is assumed to be uniform in the vertical direction, as field test results showed a slight variation of this temperature with depth, less than 0.5 °C/m (Faizal et al., 2018). Finally, to derive an analytical form of transient temperature distributions, constant T_a is applied to soils at $r = a$ when t=0. In reality T_a may slightly increase/decrease with time during the heating/cooling process until a steady temperature is reached, but this kind of thermal boundary condition would make it difficult to find analytical-form solutions of transient temperature distributions. As reviewed in Bourne-Webb, P. et al. (2019), the boundary of constant T_a is preferred in most publications to simplify the analyses of energy pile-soil interaction.

All the input parameters for energy piles and soils are assumed to be independent of temperature, stress state, and time (Olgun et al., 2014; Fuentes et al., 2016). Changes in stresses and displacement are caused by the radial thermal expansion of energy piles and soil temperature changes. Heat generated/consumed by soil deformation is excluded for small deformation of piles/soils during the quasi-static heating/cooling process. Moreover, pore water pressure generation, water flow, and phase changes are beyond the scope of this paper.

5.2 Solution for transient thermal stresses and displacement

This section shows the analytical solution for transient thermo-mechanical stresses and displacements in the radial pile-soil interaction system. Transient temperature distributions are calculated and applied to soils to derive transient thermal stresses and displacements in soils.

5.2.1 Transient temperature distribution

As the vertical heat flow is neglected, the partial differential equation (PDE) for soil temperature in the radial direction can be obtained by Fourier's law (Carslaw and Jaeger, 1947), as

$$\frac{\partial(\Delta T)}{\partial t}=c_{\mathrm{ht}}\left[\frac{\partial^2(\Delta T)}{\partial r^2}+\frac{1}{r}\frac{\partial(\Delta T)}{\partial r}\right] \tag{5.1}$$

where ΔT denotes the temperature change related to T_0; r means the current radial position of a material point; $c_{\mathrm{ht}}=k_{\mathrm{T}}/c\rho$ is soil thermal diffusivity, in which k_{T}, c, and ρ are the thermal conductivity, specific heat, and density of soil, respectively.

As defined in Section 2, the initial and boundary conditions for temperature can be expressed as

$$\Delta T=0, \quad \text{for } r>a \text{ and } t=0 \tag{5.2}$$

$$\Delta T=0, \quad \text{for } r=\infty \text{ and } t\geq 0 \tag{5.3}$$

$$\Delta T = \Delta T_a, \quad \text{for} \quad r = a \quad \text{and} \quad t \geq 0 \tag{5.4}$$

where $\Delta T_a = T_a - T_0$.

With the given PDE, initial conditions and boundary conditions, transient temperature distributions in the surrounding soil can be derived following Carslaw and Jaeger (1947):

$$\Delta T = \Delta T_a \frac{\ln(b/r)}{\ln(b/a)} + \Delta T_a \pi \sum_{n=1}^{\infty} \frac{J_0(\beta_n a) J_0(\beta_n b) U_0(\beta_n r)}{J_0^2(\beta_n a) - J_0^2(\beta_n b)} \exp\left(-c_{\text{ht}} \beta_n^2 t\right) \tag{5.5}$$

$$U_0(\beta_n r) = J_0(\beta_n r) Y_0(\beta_n b) - J_0(\beta_n b) Y_0(\beta_n r) \tag{5.6}$$

where J_0 and Y_0 are the first and second kinds of Bessel functions of zero order, respectively; $U_0(\beta_n r)$ is the composite Bessel function defined by Eq. (5.6) and β_n is the *n*-th root of $U_0(\beta_n a) = 0$ (counted from 0 to infinite); b is a sufficiently large radius to replace the infinity boundary condition of (5.3) (e.g. $50a$ in this study). The method to find the roots of $U_0(\beta_n a) = 0$ can be seen in Appendix E.

5.2.2 Transient stress and displacement analyses

As the initial and current stresses are in equilibrium states, stress increments should also be in equilibrium in the radial direction, as

$$\frac{\partial(\Delta\sigma_r)}{\partial r} + \frac{\Delta\sigma_r - \Delta\sigma_\theta}{r} = 0 \tag{5.7}$$

where $\Delta\sigma_r$ and $\Delta\sigma_\theta$ are the changes in radial and circumferential stresses, respectively, during the heating/cooling process.

The total of soil strains may be induced by the changes of both stresses and soil temperatures. Taking compression as positive for stresses and strains, the stress-strain relationship can be expressed as

$$\varepsilon_r = -\frac{\partial u}{\partial r} = \frac{1}{E}\left[\Delta\sigma_r - \mu(\Delta\sigma_\theta + \Delta\sigma_z)\right] - \alpha\Delta T \tag{5.8}$$

$$\varepsilon_\theta = -\frac{u}{r} = \frac{1}{E}\left[\Delta\sigma_\theta - \mu\left(\Delta\sigma_r + \Delta\sigma_z\right)\right] - \alpha\Delta T \tag{5.9}$$

$$\varepsilon_z = 0 = \frac{1}{E}\left[\Delta\sigma_z - \mu\left(\Delta\sigma_r + \Delta\sigma_\theta\right)\right] - \alpha\Delta T \tag{5.10}$$

where ε_r, ε_θ and ε_z are the total radial, circumferential, and vertical strains, respectively; u denotes the radial displacement of a material point; E, μ and α are the elastic modulus and Poisson's ratio and thermal expansion coefficient of the soil.

The compatibility equation regarding strains can be derived by combining Eqs. (5.8) and (5.9):

$$\frac{\partial\varepsilon_\theta}{\partial r} + \frac{\varepsilon_\theta - \varepsilon_r}{r} = 0 \tag{5.11}$$

Substituting Eqs. (5.8) and (5.9) into Eq. (5.11), the compatibility equation will be transformed into:

$$\frac{\partial}{\partial r}\left(\Delta\sigma_\theta - \mu\Delta\sigma_r - \mu\Delta\sigma_z - E\alpha\Delta T\right) + \left(1+\mu\right)\frac{\Delta\sigma_\theta - \Delta\sigma_r}{r} = 0 \tag{5.12}$$

With the aid of Eq. (5.10), the vertical stress change can be expressed as

$$\Delta\sigma_z = \mu\left(\Delta\sigma_r + \Delta\sigma_\theta\right) + E\alpha\Delta T \tag{5.13}$$

Substituting Eqs. (5.7) and (5.13) into Eq. (5.12) gives

$$\frac{\partial}{\partial r}\left[\Delta\sigma_\theta - \mu\Delta\sigma_r - \mu\Delta\sigma_z - E\alpha\Delta T\right] + \left(1+\mu\right)\frac{\partial\Delta\sigma_r}{\partial r} = 0 \tag{5.14}$$

$$\frac{\partial}{\partial r}\left[\left(1-\mu\right)\left(\Delta\sigma_r + \Delta\sigma_\theta\right) - E\alpha\Delta T\right] = 0 \tag{5.15}$$

Integrating Eq. (5.15) along the radial direction, one can get that

$$\left(1-\mu\right)\left(\Delta\sigma_r + \Delta\sigma_\theta\right) = E\alpha\Delta T \tag{5.16}$$

Eq. (5.16) can be helpful to eliminate $\Delta\sigma_\theta$ as

$$\Delta\sigma_\theta = \frac{E\alpha\Delta T}{1-\mu} - \Delta\sigma_r \tag{5.17}$$

By putting Eq. (5.17) into Eq. (5.7), the ODE regarding $\Delta\sigma_r$ can be obtained as

$$\frac{\partial(\Delta\sigma_r)}{\partial r}+\frac{2}{r}\Delta\sigma_r=\frac{1}{r}\frac{E\alpha\Delta T}{1-\mu} \tag{5.18}$$

The stress components in soils can then be solved by combining Eqs. (5.10), (5.18) and (5.16), as

$$\Delta\sigma_r=\frac{A_a}{r^2}+\frac{E\alpha}{1-\mu}\frac{1}{r^2}\int\Delta T\cdot r\mathrm{d}r \tag{5.19}$$

$$\Delta\sigma_\theta=\frac{E\alpha\Delta T}{1-\mu}-\frac{A_a}{r^2}-\frac{E\alpha}{1-\mu}\frac{1}{r^2}\int\Delta T\cdot r\mathrm{d}r \tag{5.20}$$

$$\Delta\sigma_z=\frac{E\alpha\Delta T}{1-\mu} \tag{5.21}$$

where A_a is an integral constant that can be determined by the boundary condition at $r=a$. $\int\Delta T\cdot r\mathrm{d}r$ can be integrated after combination with Eq. (5.5), as

$$\begin{aligned}\int\Delta T\cdot r\mathrm{d}r=&\frac{\Delta T_a r^2}{2\ln(b/a)}\left(\frac{1}{2}+\ln\frac{b}{r}\right)+\\&\Delta T_a\pi\sum_{n=1}^{\infty}\frac{J_0(\beta_n a)J_0(\beta_n b)}{J_0^2(\beta_n a)-J_0^2(\beta_n b)}\exp\left(-c_{\mathrm{ht}}\beta_n^2 t\right)\frac{rU_1(\beta_n r)}{\beta_n}\end{aligned} \tag{5.22}$$

in which

$$U_1(\beta_n r)=\frac{\beta_n}{r}\int U_0(\beta_n r)\cdot r\mathrm{d}r=J_1(\beta_n r)Y_0(\beta_n b)-J_0(\beta_n b)Y_1(\beta_n r) \tag{5.23}$$

where J_1 and Y_1 are the first and second kinds of Bessel functions of first order, respectively. Note that integral of Eq. (5.22) is achieved with the following relationships of Bessel functions:

$$\int J_0(\beta_n r)r\mathrm{d}r=\frac{J_1(\beta_n r)r}{\beta_n} \tag{5.24}$$

$$\int Y_0(\beta_n r)r\mathrm{d}r=\frac{Y_1(\beta_n r)r}{\beta_n} \tag{5.25}$$

$$\int U_0(\alpha_n r)r\mathrm{d}r=\int\left[J_0(\alpha_n r)Y_0(\alpha_n b)-J_0(\alpha_n b)Y_0(\alpha_n r)\right]r\mathrm{d}r=\frac{r}{\alpha_n}U_1(\alpha_n r) \tag{5.26}$$

$$U_1(\alpha_n r) = J_1(\alpha_n r)Y_0(\alpha_n b) - J_0(\alpha_n b)Y_1(\alpha_n r) \tag{5.27}$$

When substituting Eqs. (5.19), (5.20), and (5.21) into Eq. (5.9), the radial displacement of a given material point can be obtained as

$$\begin{aligned} u = -r\varepsilon_\theta &= \alpha T r + \frac{r}{E}\left(\mu\Delta\sigma_r + \mu\Delta\sigma_z - \Delta\sigma_\theta\right) \\ &= \alpha T r + \frac{r}{E}\left(\begin{array}{l} \mu\dfrac{A_a}{r^2} + \dfrac{\mu E\alpha}{1-\mu}\dfrac{1}{r^2}\int \Delta T \cdot r\mathrm{d}r \\ + \dfrac{\mu E\alpha\Delta T}{1-\mu} \\ - \dfrac{E\alpha\Delta T}{1-\mu} + \dfrac{A_a}{r^2} + \dfrac{E\alpha}{1-\mu}\dfrac{1}{r^2}\int \Delta T \cdot r\mathrm{d}r \end{array}\right) \\ &= \frac{1+\mu}{E}\frac{A_a}{r} + \frac{1+\mu}{1-\mu}\frac{\alpha}{r}\int \Delta T \cdot r\mathrm{d}r \end{aligned} \tag{5.28}$$

where A_a should be determined by the boundary conditions at the pile-soil interface:

$$\frac{u(a)}{a} = \alpha_{\text{pile}}\Delta T_a - \frac{1-\mu_{\text{pile}}-2\mu_{\text{pile}}^2}{E_{\text{pile}}}\Delta\sigma_{\text{n}}. \tag{5.29}$$

where E_{pile}, μ_{pile} and α_{pile} are the thermal expansion coefficient, Poisson's ratio and elastic modulus of energy piles, respectively, and the derivation of Eq. (5.29) is detailed in Appendix F. The first term on the right hand represents the thermal-induced radial strain at the pile-soil interface while the second term accounts for the mechanical radial strain generated by soil restriction.

By combining Eqs. (5.28) and (5.29), we have

$$\frac{u(a)}{a} = \alpha_{\text{pile}}\Delta T_a - \frac{1-\mu_{\text{pile}}-2\mu_{\text{pile}}^2}{E_{\text{pile}}}\Delta\sigma_{\text{n}}. \tag{5.30}$$

$$\frac{u(a)}{a} = \frac{1+\mu}{E}\frac{A_a}{a^2} + \frac{1+\mu}{1-\mu}\frac{\alpha}{a^2}\int \Delta T \cdot r\mathrm{d}r = \alpha_{\text{pile}}\Delta T_a - \frac{1-\mu_{\text{pile}}-2\mu_{\text{pile}}^2}{E_{\text{pile}}}\Delta\sigma_{\text{n}} \tag{5.31}$$

Then A_a can be obtained from Eq. (5.31) as

$$A_a = \frac{E\alpha_{\text{pile}}\Delta T_a a^2}{1+\mu} - \frac{E\left(1-\mu_{\text{pile}}-2\mu_{\text{pile}}^2\right)}{E_{\text{pile}}\left(1+\mu\right)}\Delta\sigma_{\text{n}}a^2 - \frac{E\alpha}{1-\mu}\int \Delta T\cdot r\mathrm{d}r \tag{5.32}$$

Finally, transient thermo-elastic stresses and displacements in the soil can be simplified by substituting Eq. (5.32) into Eqs. (5.19), (5.20), (5.21), and (5.28):

$$\Delta\sigma_r = \frac{E\alpha_{\text{pile}}\Delta T_a}{1+\mu}\frac{a^2}{r^2} - \frac{E\left(1-\mu_{\text{pile}}-2\mu_{\text{pile}}^2\right)}{E_{\text{pile}}\left(1+\mu\right)}\Delta\sigma_{\text{n}}\frac{a^2}{r^2} + \frac{E\alpha}{1-\mu}\frac{1}{r^2}\int_a^r \Delta T\cdot r\mathrm{d}r \tag{5.33}$$

$$\Delta\sigma_\theta = \frac{E\alpha\Delta T}{1-\mu} - \frac{E\alpha_{\text{pile}}\Delta T_a}{1+\mu}\frac{a^2}{r^2} + \frac{E\left(1-\mu_{\text{pile}}-2\mu_{\text{pile}}^2\right)}{E_{\text{pile}}\left(1+\mu\right)}\Delta\sigma_{\text{n}}\frac{a^2}{r^2} - \frac{E\alpha}{1-\mu}\frac{1}{r^2}\int_a^r \Delta T\cdot r\mathrm{d}r \tag{5.34}$$

$$\Delta\sigma_z = \frac{E\alpha\Delta T}{1-\mu} \tag{5.35}$$

$$u = \alpha_{\text{pile}}\Delta T_a\frac{a^2}{r} - \frac{1-\mu_{\text{pile}}-2\mu_{\text{pile}}^2}{E_{\text{pile}}}\Delta\sigma_{\text{n}}\frac{a^2}{r} + \frac{1+\mu}{1-\mu}\frac{\alpha}{r}\int_a^r \Delta T\cdot r\mathrm{d}r \tag{5.36}$$

5.2.3 Special cases

Three special cases of the present solution are discussed in this subsection, including cavity expansion under purely mechanical loading pattern, thermal loading pattern, and combined thermal-mechanical loading pattern without soil restriction on radial expansion of energy piles.

When removing the transient temperature field and applying a radial displacement $\alpha_{\text{pile}}\Delta T_a a$ at $r=a$, the present solution can be reduced to the conventional elastic solution for cavity expansion in isothermal soils (Yu, 2000), namely

$$\Delta\sigma_r = \frac{E\alpha_{\text{pile}}\Delta T_a}{1+\mu}\frac{a^2}{r^2} \tag{5.37}$$

$$\Delta\sigma_\theta = -\frac{E\alpha_{\text{pile}}\Delta T_a}{1+\mu}\frac{a^2}{r^2} \tag{5.38}$$

$$\Delta\sigma_z = 0 \tag{5.39}$$

$$u = \alpha_{\text{pile}} \Delta T_a \frac{a^2}{r} \tag{5.40}$$

If the radial contact stress at the soil-pile interface is removed, (i.e. $\Delta\sigma_n$ =0), the present solution recovers to the solution of Kandil et al. (1995) as

$$A_a = -\frac{E\alpha}{1-\mu}\int \Delta T \cdot r \mathrm{d}r \tag{5.41}$$

$$\Delta\sigma_r = \frac{E\alpha}{1-\mu}\frac{1}{r^2}\int_a^r \Delta T \cdot r \mathrm{d}r \tag{5.42}$$

$$\Delta\sigma_\theta = \frac{E\alpha\Delta T}{1-\mu} - \frac{E\alpha}{1-\mu}\frac{1}{r^2}\int_a^r \Delta T \cdot r \mathrm{d}r \tag{5.43}$$

$$\Delta\sigma_z = \frac{E\alpha\Delta T}{1-\mu} \tag{5.44}$$

$$u = \frac{1+\mu}{1-\mu}\frac{\alpha}{r}\int_a^r \Delta T \cdot r \mathrm{d}r \tag{5.45}$$

Note that in this chapter $\int \Delta T \cdot r \mathrm{d}r$ is integrated analytically with the temperature distributions of Eq. (5.5), instead of using numerical integration techniques in Kandil et al. (1995).

Since E_{pile} is much larger than E, radial thermal expansion of the energy pile can hardly be prevented by the surrounding soil. Therefore, the particle displacement at the pile-soil interface, defined by Eq. (5.29), can be simplified as

$$\frac{u(a)}{a} = \alpha_{\text{pile}} \Delta T_a \tag{5.46}$$

Following the similar procedures in Section 3.2, stresses and displacements in the soil are simplified to be

$$A_a = \frac{E\alpha_{\text{pile}}\Delta T_a a^2}{1+\mu} - \frac{E\alpha}{1-\mu}\int \Delta T \cdot r\mathrm{d}r \tag{5.47}$$

$$\Delta\sigma_r = \frac{E\alpha_{\text{pile}}\Delta T_a}{1+\mu}\frac{a^2}{r^2} + \frac{E\alpha}{1-\mu}\frac{1}{r^2}\int_a^r \Delta T \cdot r\mathrm{d}r \tag{5.48}$$

$$\Delta\sigma_\theta = \frac{E\alpha\Delta T}{1-\mu} - \frac{E\alpha_{\text{pile}}\Delta T_a}{1+\mu}\frac{a^2}{r^2} - \frac{E\alpha}{1-\mu}\frac{1}{r^2}\int_a^r \Delta T \cdot r\mathrm{d}r \tag{5.49}$$

$$\Delta\sigma_z = \frac{E\alpha\Delta T}{1-\mu} \tag{5.50}$$

$$u = \alpha_{\text{pile}}\Delta T_a \frac{a^2}{r} + \frac{1+\mu}{1-\mu}\frac{\alpha}{r}\int_a^r \Delta T \cdot r\mathrm{d}r \tag{5.51}$$

It is interesting that the cavity expansion solution under the thermal-mechanical loading (Eqs. (5.48)~(5.51)) is the sum of the solutions under purely mechanical loading (Eqs. (5.37)~(5.40)) and purely thermal loading (Eqs. (5.42)~(5.45)). This can be explained by that the linear elastic model is adopted which enables stresses and displacements to satisfy the superposition principle.

5.3 Results and Discussion

This section shows validation and parametric studies of the proposed solution. Unless stated otherwise, the following input parameters are adopted: $E = 5\times10^4\,\text{kPa}$, $E_{\text{pile}} = 3\times10^7\,\text{kPa}$, $\alpha = 5\times10^{-5}/°\text{C}$, $\alpha_{\text{pile}} = 1\times10^{-5}/°\text{C}$, μ=0.3 and μ_{pile}=0.15 (Olgun et al., 2014); a=1m, b=50m, and $\Delta T_a = 20°\text{C}$.

5.3.1 Solution validation

The proposed solution is validated by comparison with FEM via Comsol Multiphysics 6.0 (CM6) software. The numerical model established in CM6 is a two-dimensional axisymmetric model, as shown in Figure 5.2. Initially, the numerical model is free of stresses, strains, and temperature change. Then at the left boundary (i.e. $r = a$), there is a radial displacement $\alpha_{\text{pile}}\Delta T_a a$ representing thermal expansion of the energy pile and a

constant temperature ΔT_a for heating/cooling at the pile-soil interface. Vertical heat flow and displacements are restricted at the top and bottom boundaries to simulate plane strain conditions in terms of the vertical direction, and the right boundary (i.e. $r = b$) is free of stress and temperature. The soil model and input parameters are the same as those used in the proposed solution, and the mesh number is set as 400. Thermo-mechanical coupling is undertaken by the thermal expansion model built in CM. Figure 5.3 shows the distributions of temperatures, stresses and displacements calculated by the present solution and FEM when $c_{\mathrm{ht}}t = 1\ \mathrm{m}^2$. The results predicted by the present solution match well with those calculated by FEM, thereby validating the solution accuracy.

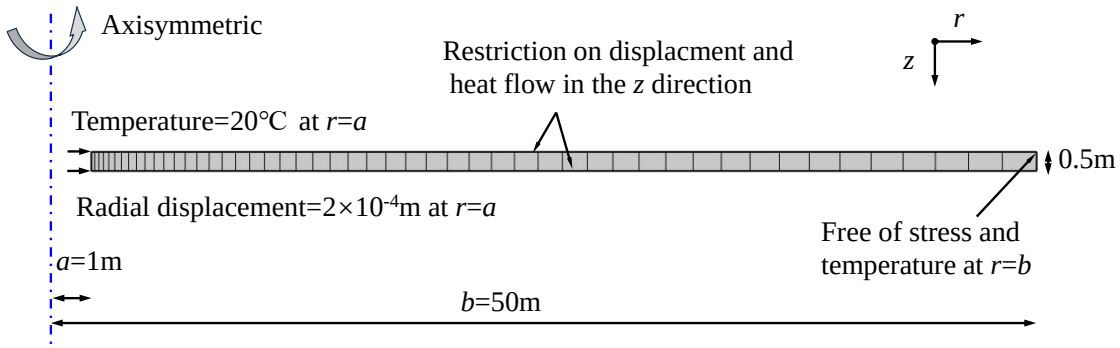

Figure 5.2 Numerical simulation model in CM

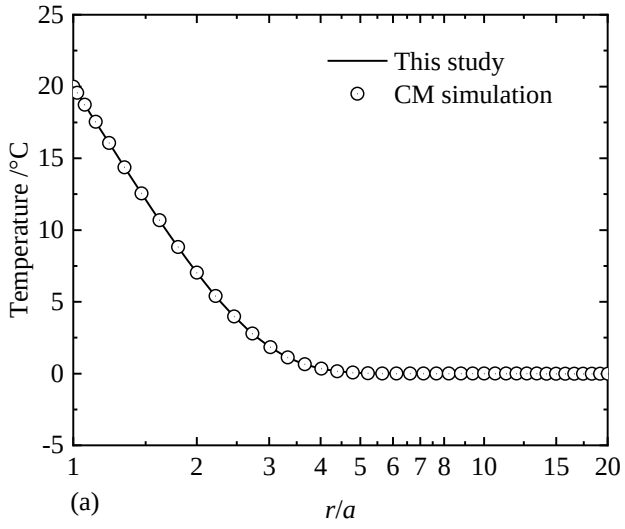

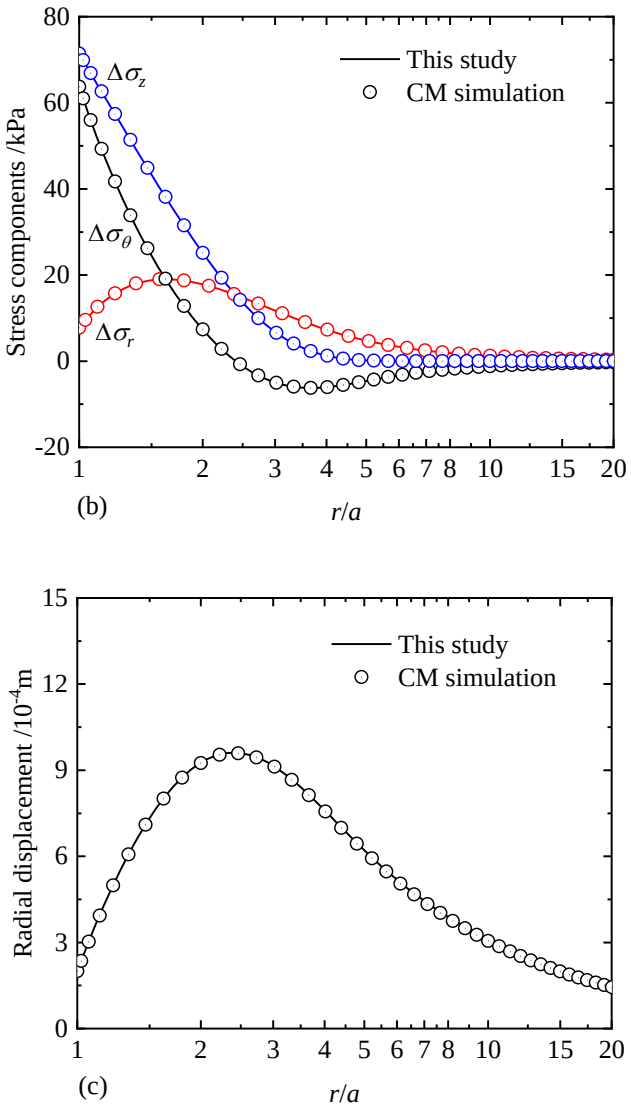

Figure 5.3 Results calculated by the present solution and FEM: (a) temperature distribution; (b) stress distribution; (c) radial displacement distribution

5.3.2 Cavity expansion under the mechanical loading, thermal loading, and thermal-mechanical loading patterns

Figure 5.4 shows the stress and displacement distributions for cavity expansion under three loading patterns shown in Section 5.2.3. The stresses and displacements under thermal-mechanical loading pattern are determined by the competitive relationship between those under mechanical loading and thermal loading patterns. Mechanical loading plays an important role in the stresses and displacements in the (approximate)

range of $a \le r \le 4a$, out of which mechanical loading effect becomes insignificant. Thermal loading dominates the increase/decrease of stresses and displacements under thermal-mechanical loading pattern with the present input parameters. For example, the radial stresses under thermal loading and thermal-mechanical loading patterns show a similar trend that $\Delta\sigma_r$ first increases and then decrease with radial positions.

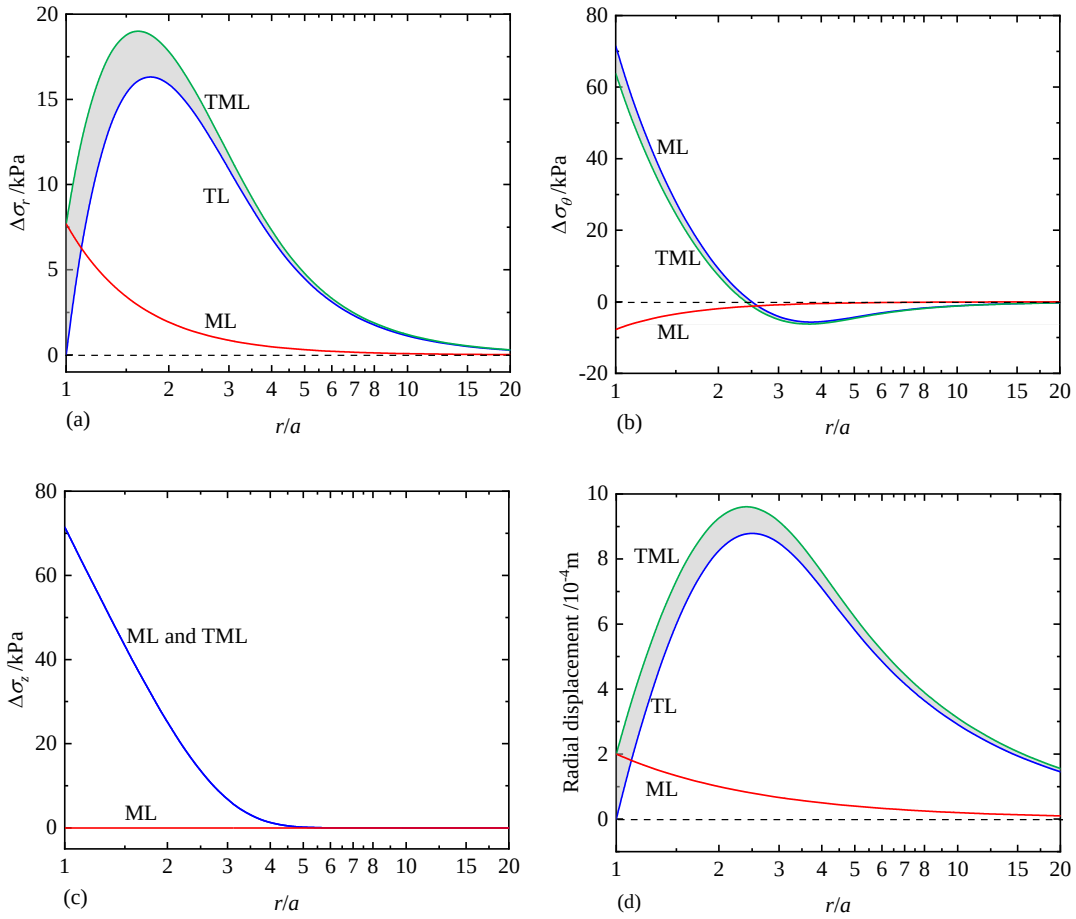

Figure 5.4 Stress and displacement distributions under mechanical loading, thermal loading and thermal-mechanical loading patterns:

(a) radial stress; (b) circumferential stress;

(c) vertical stress; (d) radial displacement.

When comparing Eqs. (5.37)~(5.39) under mechanical loading pattern and Eqs. (5.42)~(5.44) under thermal loading pattern, the stress components are proportional to soil moduli, indicating that soil moduli do not affect the competition between these two

loading patterns. However, the stresses and displacements under mechanical loading patterns heavily rely on the thermal expansion coefficients of energy piles (α_{pile}), while the stresses and displacements under thermal loading patterns depend on thermal expansion coefficients of soils (α). In other words, the competitive relationship between thermal loading and mechanical loading patterns is primarily determined by the relative values of α_{pile} and α.

5.3.3 Transient temperature, stress, strain, and displacement distributions

Figure 5.5 shows the transient distributions of temperatures, strains, stresses, and displacements in soils, which are predicted by the present solution. In Figure 5.5 (a) the soil temperature remains $20°C$ at $r = a$, and gradually decreases with radius and increases with time. Similar trends can also be observed for vertical stress distributions as shown in Figure 5.5 (d). This is because the vertical stress $\Delta\sigma_z$ is proportional to soil temperature if pile and soil parameters are given (see Eq. (5.21)).

On the contrary, the radial stress $\Delta\sigma_r$ in Figure 5.5 (b) firstly increases and then decreases with the increase of the radius, which is consistent with the observations in Olgun et al. (2014) by FEM. The maximum value of $\Delta\sigma_r$ increases with time and appears at a larger radial position for a longer time. As a result, the thermal expansion and heat conduction of energy piles may impose an increasingly significant impact on adjacent geo-structures (e.g. pile groups) if transient temperature fields are considered. It is also worth noting that the maximum value of $\Delta\sigma_r$ could not increase infinitely with time, because temperature distributions will eventually be in a steady state (Philippe et al., 2009; Ghasemi-Fare and Basu, 2013).

Figure 5.5 (c) shows that $\Delta\sigma_\theta$ firstly decreases and then increases with radius, and the

minimum value of $\Delta\sigma_\theta$ is negative. This exactly reflects the competitive relationship between the impacts of energy pile expansion (mechanical loading) and transient temperature distributions (thermal loading). It is also for this reason that radial displacements and radial strains firstly increase and then decrease with the increasing radius, as shown in Figure 5.5 (e) and (f).

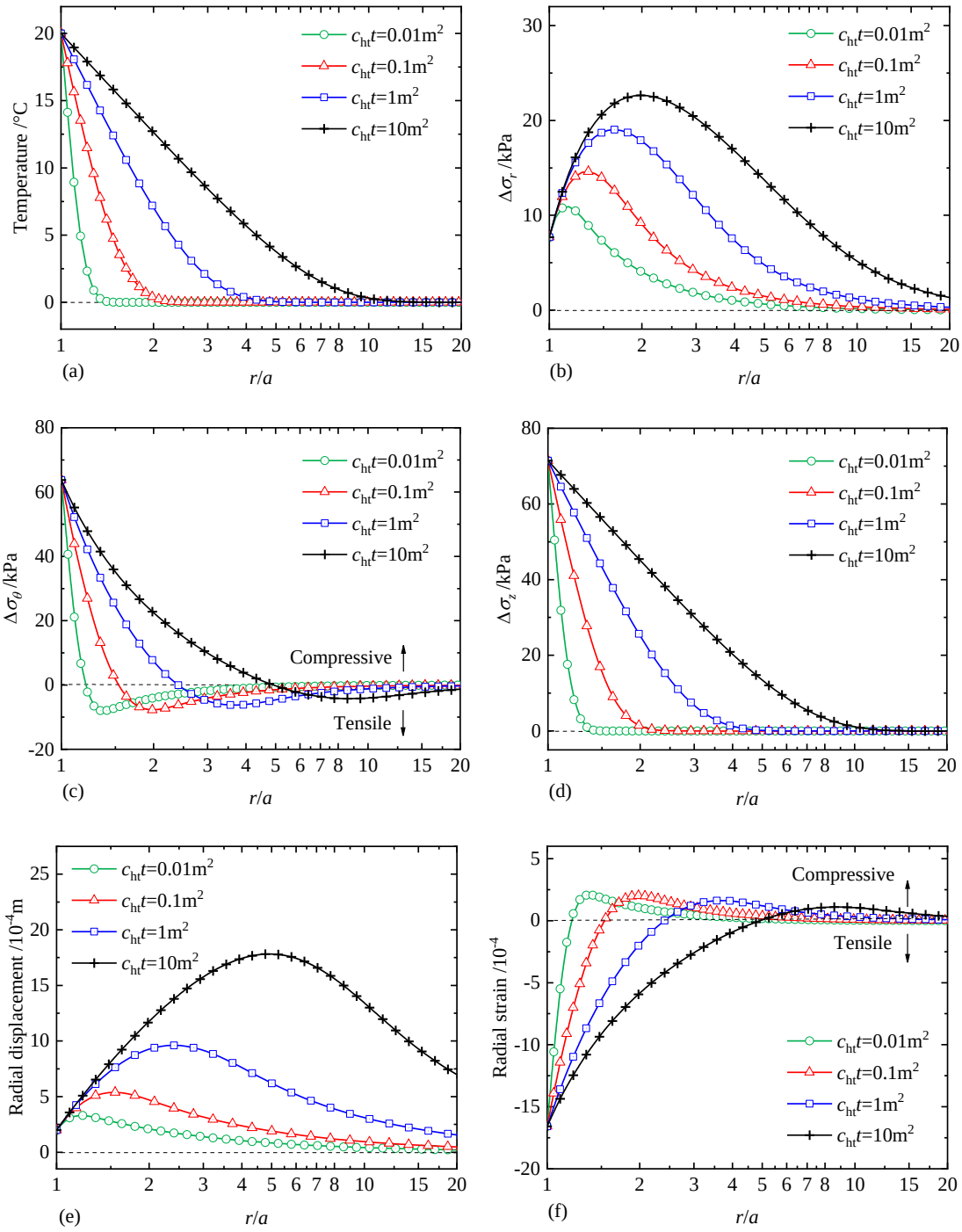

Figure 5.5 Field distributions with time:

(a) temperature; (b) radial stress; (c) circumferential stress;

(d) vertical stress; (e) radial displacement; (f) radial strain

5.3.4 Validation of the elastic assumption

In this chapter the stress-strain relationship is assumed to be linear and the reasonability is discussed in this sub-section. Following the numerical simulation of Olgun et al. (2014) where the soil plasticity was modelled by Tresca yield criteria, the potential yielding may firstly occur at the pile-soil interface where σ_z and σ_r could be major and minor principal stresses. If the soils around energy piles are in the elastic state (as assumed in this paper), we can get Eq. (5.52) by combining Eqs. (5.48) and (5.50):

$$\left|\Delta T_a\left(\frac{\alpha}{1-\mu}-\frac{\alpha_{\text{pile}}}{1+\mu}\right)\right|<\frac{2s_{\text{u}}}{E} \tag{5.52}$$

Since Poisson's ratio of soils is usually in the range of 0~0.5, we can get the inequality:

$$\left|\Delta T_a\right|\left(\frac{\alpha}{1-\mu}-\frac{\alpha_{\text{pile}}}{1+\mu}\right)<\frac{\left|\Delta T_a\right|\cdot\max\left(\alpha,\alpha_{\text{pile}}\right)}{\left(1-\mu\right)}<2\left|\Delta T_a\right|\cdot\max\left(\alpha,\alpha_{\text{pile}}\right)<\frac{2s_{\text{u}}}{E} \tag{5.53}$$

For typical thermal expansion coefficients of soils and piles in the order of $10^{-6}/°\text{C}$, the assumption of elastic soil behaviour can be satisfied with typical E/s_{u} ratios of soils, for example, 1000 in Olgun et al. (2014).

5.3.5 Influence of thermal expansion coefficient of the soil

As mentioned above, the evolution of stresses and strains in the soils is dependent on the competitive relationship between α and α_{pile}. The competitive relationship is discussed be showing the influence of various α on stress and displacement distributions, as shown in Figure 5.6 ($c_{\text{ht}}t$ =1 m^2).

It shows that the radial stress change and radial displacement remain the same at the pile-soil interface, owing to the given displacement boundary conditions at $r=a$. However, $\Delta\sigma_r$ and $u(r)$ increase with the increase of α, and there are no extremum points for a small α (e.g. $\alpha=5\times10^{-6}/°\text{C}$). It proves that the mechanical loading gradually

becomes dominant with the increase of α. Similar conclusions can also be drawn from the changes of circumferential stress and vertical stress, as shown in Figure 5.6 (b) and (c). Both $\Delta\sigma_\theta$ and $\Delta\sigma_z$ at the pile-soil interface increase with α, and the influenced zone caused by thermal-mechanical loading is also larger for a higher α value.

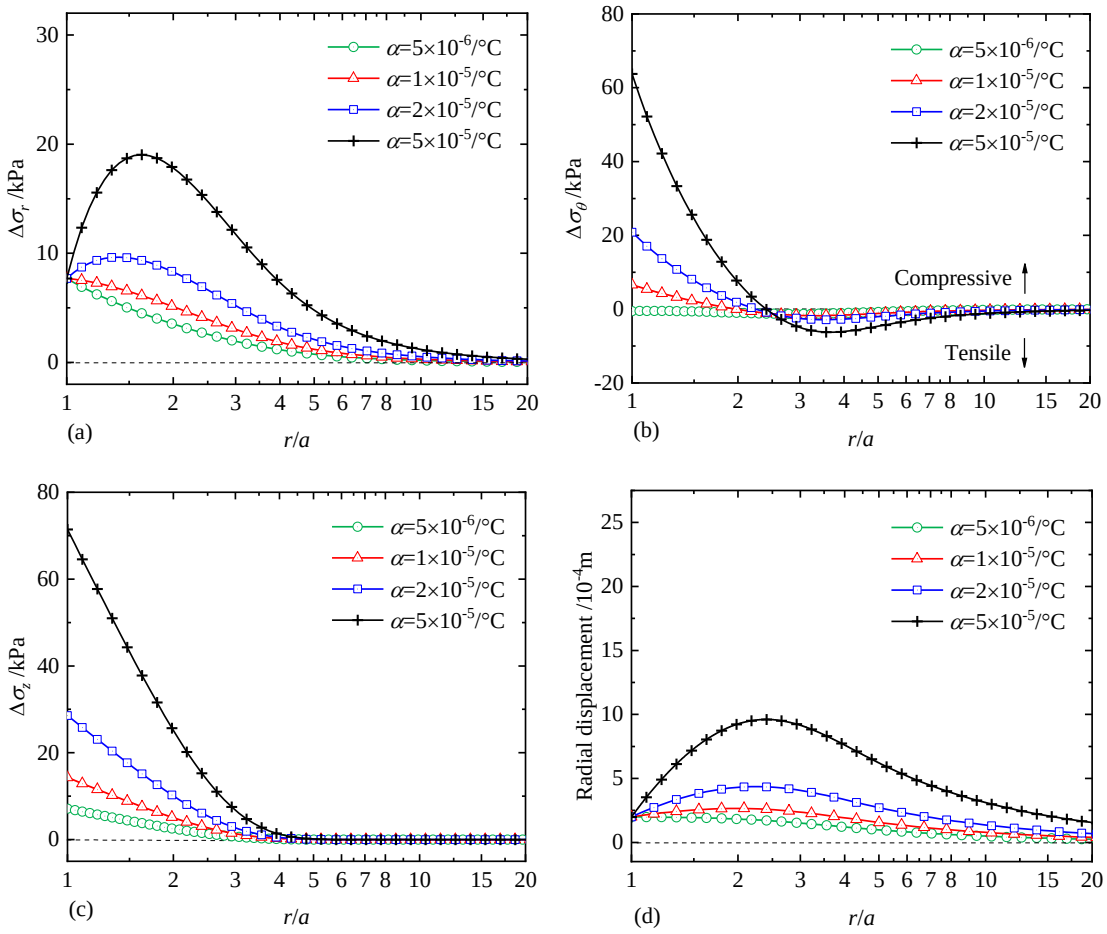

Figure 5.6 Field distributions with various thermal expansion coefficients of soils:

(a) radial stress; (b) circumferential stress;

(c) vertical stress; (d) radial displacement

5.4 Radial contact stress at the energy pile-soil interface

If energy piles can expand freely without the radial restriction from surrounding soils, the radial stress change at the pile-soil interface ($r = a$) can be derived from Eq. (5.48) as

$$\Delta\sigma_{\mathrm{n}}=\frac{E\alpha_{\mathrm{pile}}\Delta T_a}{1+\mu}=\frac{E\,\varepsilon_\theta\big|_{r=a}}{1+\mu} \tag{5.54}$$

While Eq. (5.54) has been used to estimate $\Delta\sigma_{\mathrm{n}}$ (Faizal et al., 2018; Lv et al., 2020), it is revisited here based on the present solution to discuss the applicability of Eq. (5.54).

Firstly, Eq. (5.54) is quite general regarding various temperature fields, although specific temperature distributions are adopted in this paper. This conclusion can be proved as follows. By setting $r=a$ into Eq. (5.37), $\Delta\sigma_{\mathrm{n}}$ under the mechanical loading pattern is the same as Eq. (5.54). Similarly, $\Delta\sigma_{\mathrm{n}}$ is zero under the thermal loading pattern after substituting $r=a$ into Eq. (5.42). Based on the superposition principle, $\Delta\sigma_{\mathrm{n}}$ is determined by the radial displacement at $r=a$, but is not affected by different temperature distributions. Therefore, Eq. (5.54) could be applied to estimate $\Delta\sigma_{\mathrm{n}}$ with various temperature distributions, as long as the radial displacement can be obtained.

Secondly, energy pile expansion may be prevented by surrounding soils in real field conditions, and $\Delta\sigma_{\mathrm{n}}$ will be expressed as Eq. (5.55) after substituting $r=a$ into Eq. (5.33).

$$\Delta\sigma_{\mathrm{n}}=\frac{E\alpha_{\mathrm{pile}}\Delta T_a}{1+\mu+\left(1-\mu_{\mathrm{pile}}-2\mu_{\mathrm{pile}}^2\right)\left(E/E_{\mathrm{pile}}\right)} \tag{5.55}$$

Figure 5.7 presents the variation of $\Delta\sigma_{\mathrm{n}}$ with soil moduli, taking $E_{\mathrm{pile}}=3\times10^7\,\mathrm{kPa}$, $\mu_{\mathrm{pile}}=0.15$, and $\Delta T_a=10^{\circ}\mathrm{C}$. The figure shows that Eq. (5.55) predicts similar $\Delta\sigma_{\mathrm{n}}$ as that in Olgun et al. (2014), and the difference lies in Poisson's ratio effect (plane strain assumption in this study and plane stress assumption in Olgun et al. (2014)). For typical soil moduli within the range of $10^3\sim10^5\,\mathrm{kPa}$, Eq. (5.55) for $\Delta\sigma_{\mathrm{n}}$ can be simplified as Eq. (5.54), revealing that energy piles can expand with negligible restrictions from the

surrounding soils. In this case the mechanism that $\Delta\sigma_n$ increases with E can therefore be explained by Eq. (5.37) that the radial stress change is proportional to E, but it is hardly relevant to soil restriction on radial expansion of energy piles. Moreover, Eq. (5.55) indicates that the soil restriction is mainly dependent on the soil-to-pile modulus ratio, which may become important when energy piles are installed into hard rocks with high elastic moduli.

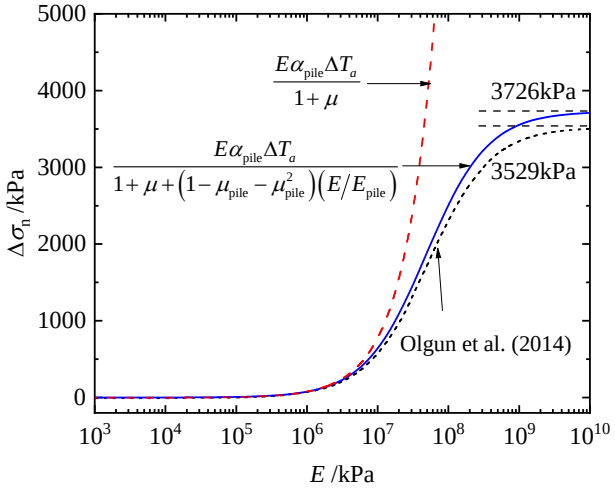

Figure 5.7 Variation of radial stress at the pile-soil interface with soil moduli

Overall, Eq. (5.54) may be able to estimate $\Delta\sigma_n$ with consideration of various temperature distributions and pile/soil moduli. Figure 5.8 shows the comparison of $\Delta\sigma_n$ predicted by Eq. (5.54) and measured by field tests that were conducted in red cliff sand with E=60MPa and μ=0.3 at the Melbourne test site (Faizal et al., 2018; Faizal et al., 2019b; Moradshahi et al., 2022) and hard clay with E=6.9MPa and μ=0.35 at Nanjing Liuhe test site (Lv et al., 2020). Good agreement can be seen between measured and predicted $\Delta\sigma_n$, thereby validating the accuracy of Eq. (5.54) for quantifying the RIEPS. In practical capacity design of energy piles, $\Delta\sigma_n$ can be neglected for soft soils under low temperature change, while it may become noticeable for stiff soils under high temperature change. Finally, care should be taken because Eq. (5.54) was derived by

assuming that soil deformation is purely elastic. Soil plasticity may occur as the stress states may be disturbed by energy pile installation and be influenced by energy pile expansion in the vertical direction.

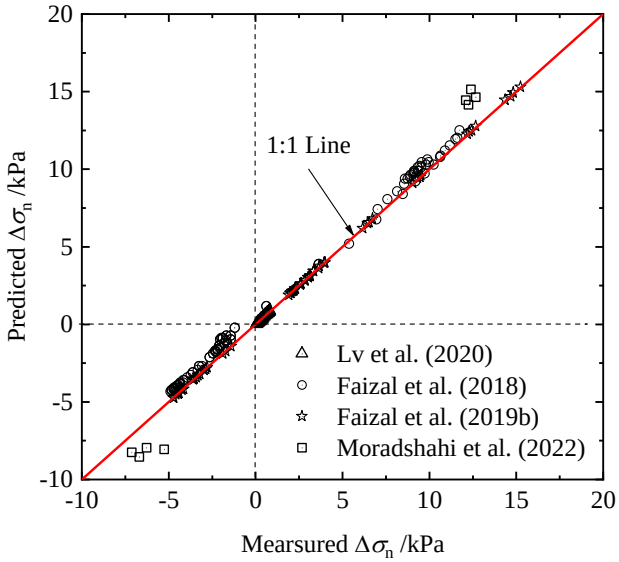

Figure 5.8 Comparison of predicted and measured radial stress changes

5.5 Chapter summary

This chapter proposes a thermo-elastic cavity expansion solution for radial interaction between energy piles and soils (RIEPS), considering transient temperature distributions and radial displacement boundary at the pile-soil interface. The solution is adopted to investigate transient stresses and displacements in soils and analyse the radial contact stress change at the pile-soil interface. It is found that:

(i) The cavity expansion solution under the combined thermo-mechanical loading pattern is the linear superposition of the solutions under purely mechanical loading and thermal loading patterns.

(ii) The thermal-mechanical stresses and displacements in soils depend on the competitive relationship between mechanical loading and thermal loading patterns, more specifically, the thermal expansion coefficients of soils and energy piles. For this reason the stresses and displacements in soils evolve with time and

radial positions in various ways.

(iii) The change in radial contact stress at the pile-soil interface is revisited with a particular focus on the influences of transient temperature distributions and soil/pile moduli. After showing parametric studies and comparison with field test data, Eq. (5.54) may be utilised to estimate the change of radial contact stress at the energy pile-soil interface.

Chapter 6 Conclusions and Recommendations

6.1 Conclusions

While traditional self-similar cavity expansion theory (CET) has been becoming mature, it is necessary to develop non-self-similar CET for the applications to in-lab pressuremeter tests (SBPs) and cone penetration tests (CPTs), piezocone penetration tests (CPTU), jet grouting, energy pile-soil interaction, etc. This thesis primarily studies the theory and applications of non-self-similar expansion of a cylindrical cavity in geotechnical engineering. Three main factors that can lead to the non-self-similarity during cavity expansion are investigated in Chapters 3, 4 and 5, including the finite thickness of the cylinder, the hydro-mechanical coupling and thermo-mechanical coupling. The key conclusions of this thesis are presented below.

6.1.1 Cavity expansion in finite soil thickness

Due to the "complexity" of saturated/unsaturated critical state soil models, a novel hybrid Eulerian-Lagrangian (HEL) approach is proposed in Chapter 3 for non-self-similar cavity expansion problems. It is found that:

(i) There is a closed-form solution for cavity expansion in the elastic zone, even if the soil cylinder thickness is finite and the soil modulus is stress-dependent. In the plastic zone, on the other hand, the cavity expansion problem should be formulated into a set of five first-order partially differential equations (PDEs) in terms of both Eulerian and Lagrangian descriptions, which should be solved by the HEL approach.

(ii) The HEL approach is general for cavity expansion in finite/infinite soil thickness, saturated/unsaturated soils, drained/undrained condition, and various constitutive models of soils.

(iii) The commonly used Eulerian approach and Lagrangian approach can be seen as special cases of the HEL approach. It is proven that the HEL approach can recover

to the Eulerian approach if the cavity expansion process is self-similar (e.g. infinite cylinder thickness) and the $\ln(r/r_0)$ is chosen as an auxiliary variable. Meanwhile, the HEL approach can be reduced to the Lagrangian approach if the effective stress-total strain relationship can be integrated analytically.

(iv) Approximate definitions of stress invariants (i.e. $p'=(\sigma'_r+\sigma'_\theta)/2$ and $q=\sigma'_r-\sigma'_\theta$) that were normally used in cavity expansion analyses may lead to underestimation of the required expansion pressure in the case of undrained saturated soils. However, the rigorous definitions of stress invariants are recommended because approximate definitions are not suitable in many other cases. Using rigorous definitions of p' and q, Chapter 3 of this thesis proves that cavity expansion solutions can still be found by Eulerian, Lagrangian, and HEL approaches.

(v) The finite thickness of the soil cylinder may greatly influence the cavity expansion behaviour, and the non-self-similarity caused by this factor is illustrated. It is also proven that the self-similar-based Eulerian approach can not provide rigorous solutions for the expansion of a cylinders with finite thickness ratios.

6.1.2 Cavity expansion a poro-elasto-plastic medium under partially drained conditions

A hydro-mechanical coupling solution is proposed in Chapter 4 for cylindrical cavity expansion in saturated soils under partially drained conditions. This new solution is derived by assuming perfectly elastoplastic Tresca model for mechanical behaviour and Darcy's law for hydraulic behaviour. It is found that:

(i) The cavity expansion under partially drained conditions can be transformed into a Stefan problem: two PDEs in the elastic and plastic zones with a moving boundary at the elastoplastic interface. There are no rigorous solutions, if not impossible, for the PDEs, but an approximate solution is given in Chapter 4 by the variable transformation method. The new solution is validated by numerical simulations conducted by Comsol Multiphysics.

(ii) Parametric studies show that the partially drained effect has an important influence on EWP evolution but little on the total inner pressure for Tresca model. Under partially drained conditions, EWP increases with the increases of loading rate V_a and decrease of k/γ_w for the case of cavity expansion with a constant expansion rate, while EWP increase with δ for cavity expansion with a constant normalised inner radius.

(iii) The application of the new solution is illustrated by quantifying the partially drained effect in piezocone penetration tests (CPTU). The physical meaning of the existing normalised penetration rate, $\bar{V}_0$, is proven based on the present solution. Also, the limitations of $\bar{V}_0$ are discussed, which lie mainly in the ignoration of the influence of soil rigidity index I_r.

(iv) A new normalised penetration rate, $\bar{V} = \bar{V}_0 I_r^{0.5}$, is defined in Chapter 4 and a unique backbone curve is found. The new backbone curve is validated by a database of experimental tests and numerical simulation results. Finally, a method for interpreting multi-rate CPTU (penetration stage) is suggested to measure the coefficient of consolidation of soils.

6.1.3 Transient thermo-elastic solution for cavity expansion radial interaction between energy piles and soils

In Chapter 5 a transient thermo-elastic solution is proposed with an application to quantify the radial interaction between energy piles and soils (RIEPS). The new solution is able to capture the effects of transient temperature distributions and radial displacement boundary at the pile-soil interface. It is found that:

(i) The cavity expansion solution under the combined thermo-mechanical loading pattern is the linear superposition of the solutions under purely mechanical loading and thermal loading patterns. The competition between mechanical loading and thermal loading patterns results in various changes of stresses and displacements.

(ii) The new solution can provide a simple equation for the change of radial contact stress at the pile-soil interface, with the consideration of transient temperature distributions and soil/pile moduli. The simple equation is validated by comparison with field test data of energy pile-soil interactions.

6.2 Recommendations

The thesis serves as a start for developing CET with a particular focus on non-self-similar characteristics. There will be some aspects left that may need to be investigated in the future, and a few of them are listed below to provide suggestions for future work.

(i) Some other factors may lead to non-self-similarity during the cavity expansion process, such as the loading-unloading history and chemical reactions. These factors can be considered by extending the solution methods shown in this thesis.

(iii) For cavity expansion under partially drained conditions, this thesis models the mechanical behaviour of soil by perfectly elastoplastic model with Tresca failure criterion in order to derive elegant analytical solutions. This model is greatly simplified because the soil strength and dilation cannot be well captured. It is necessary to develop the hydro-mechanical cavity expansion solutions using some more "realistic" models.

(iv) In Chapter 4 a method for interpreting multi-rate CPTU (penetration stage) is suggested to measure the coefficient of consolidation of soils. This method needs to be further validated by in-situ CPTU for back-interpretation of the consolidation coefficient of soils.

(v) In the penetration stage, the modified normalised penetration rate is $\bar{V} = \bar{V}_0 I_r^{0.5}$ and in the dissipation stage Teh and Houlsby (1991) suggested that a modified time factor was $T^* = \frac{4c_{he}t}{D^2 I_r^{0.5}}$. Comparing the modified normalised penetration rate and dissipation time, it may not be a coincidence that both $\bar{V}$ and T^* are the functions of $\sqrt{I_r}$ and the inherent mechanism can be explored in the future.

(vi) There may be a potential way to measure the coefficient of consolidation of soils by pressuremeter tests equipped with water pressure gauges. Different to CPTU, however, the pressuremeter tests should be loaded with a constant expansion rate, but a constant normalised inner radius. This is mainly because the initial radius of pressuremeter probe is not zero, and EWP normalisation in CPTU cannot be directly applied to the EWP normalisation in pressuremeter tests. Luckily, the results shown in Section 4.8.3 prove that EWP can still be normalised as long as the inner radius is linearly proportional to $\sqrt{t}$. This finding in the thesis may help back-calculate soil permeability from the pressuremeter test results.

(vii) In Chapter 5, the transient thermo-elastic solution is developed by neglecting the hydraulic influence and soil plasticity. The solution method shown in Chapter 5 can also be modified to consider these factors.

Appendix A Derivation of Eq. (3.115) for MCC

The total volumetric strain is the sum of elastic and plastic volumetric strains, which can be expressed as

$$\varepsilon_v = \varepsilon_v^{\mathrm{e}} + \varepsilon_v^{\mathrm{p}} \tag{A.1}$$

Substituting Eqs. (3.19) and (3.20) into Eq. (A.1), we have

$$\mathrm{D}\varepsilon_v^{\mathrm{p}} = \int_{p_0'}^{p'} \frac{\kappa}{v_0 p'} \mathrm{D}p' + \frac{\lambda(0)-\kappa}{v_0} \int_{p_{\mathrm{c}0}'}^{p_{\mathrm{c}}'} \frac{\mathrm{D}p_{\mathrm{c}}'(0)}{p_{\mathrm{c}}'(0)} = 0 \tag{A.2}$$

Integration of Eq. (A.2) leads to

$$\kappa \ln \frac{p'}{p_0'} + \left[\lambda(0)-\kappa\right] \ln \frac{p_{\mathrm{c}}'}{p_{\mathrm{c}0}'} = 0 \tag{A.3}$$

With the aid of $p_{\mathrm{c}0}' = R_0 p_0'$, p_{c}' will be

$$\frac{p_{\mathrm{c}}'}{p'} = R_0 \frac{p_0'}{p'} \left(\frac{p_0'}{p'} \right)^{\frac{1}{\frac{\lambda(0)}{\kappa}-1}} = R_0 \left(\frac{p_0'}{p'} \right)^{\frac{1}{\Omega}} \tag{A.4}$$

Finally, Eq. (3.115) can be derived from Eq. (3.15)

$$q(p') = Mp' \sqrt{R_0 \left(p'/p_0'\right)^{-1/\Omega} - 1} \tag{A.5}$$

Appendix B Derivation of Eqs. (3.116) and (3.117)

The soil volume does not change for fully saturated soils under undrained conditions, thereby giving:

$$\varepsilon_v = \varepsilon_r + \varepsilon_\theta = 0 \tag{B.1}$$

the circumferential strain can be expressed as the function of deviatoric strain as

$$\mathrm{D}\varepsilon_\theta = -\frac{\sqrt{3}}{2}\mathrm{D}\varepsilon_q = -\frac{\sqrt{3}}{2}\left(\mathrm{D}\varepsilon_q^{\mathrm{e}} + \mathrm{D}\varepsilon_q^{\mathrm{p}}\right) \tag{B.2}$$

where $\varepsilon_q^{\mathrm{e}}$ and $\varepsilon_q^{\mathrm{p}}$ are the elastic and plastic deviatoric strains that satisfy

$$\mathrm{D}\varepsilon_q^{\mathrm{e}} = \frac{\mathrm{D}q}{3G} = \frac{2(1+\mu)}{9(1-2\mu)}\frac{\kappa}{v_0 p'}\frac{\partial q}{\partial p'}\mathrm{D}p' \tag{B.3}$$

$$\mathrm{D}\varepsilon_q^{\mathrm{p}} = \frac{\partial g/\partial q}{\partial g/\partial p'}\mathrm{D}\varepsilon_v^{\mathrm{p}} = -\frac{\partial g/\partial q}{\partial g/\partial p'}\mathrm{D}\varepsilon_v^{\mathrm{e}} = \frac{-2\eta}{M^2-\eta^2}\frac{\kappa}{v_0 p'}\mathrm{D}p' \tag{B.4}$$

By putting Eqs. (B.3) and (B.4) into Eq. (B.2), Eq. (3.116) will be derived as

$$\mathrm{D}\varepsilon_\theta = \frac{\sqrt{3}\kappa}{v_0}\left(\frac{\eta}{M^2-\eta^2} - \frac{1+\mu}{9(1-2\mu)}\frac{\partial q}{\partial p'}\right)\frac{\mathrm{D}p'}{p'} \tag{B.5}$$

In conjunction with the approximate definitions of stress invariants, the deviatoric strain should be adjusted to (Collins and Yu, 1996):

$$\tilde{\varepsilon}_q = \tilde{\varepsilon}_r - \tilde{\varepsilon}_\theta \tag{B.6}$$

where $\tilde{\varepsilon}_q$ and $\tilde{\varepsilon}_r$ are the approximate deviatoric strain and radial strain, respectively. By combining Eqs. (B.1) and (B.6), the circumferential strain can be shown as

$$\mathrm{D}\tilde{\varepsilon}_\theta = -\frac{1}{2}\mathrm{D}\tilde{\varepsilon}_q = -\frac{1}{2}\left(\mathrm{D}\tilde{\varepsilon}_q^{\mathrm{e}} + \mathrm{D}\tilde{\varepsilon}_q^{\mathrm{p}}\right) \tag{B.7}$$

where $\tilde{\varepsilon}_q^{\mathrm{e}}$ and $\tilde{\varepsilon}_q^{\mathrm{p}}$ are the approximate definitions of elastic and plastic deviatoric strains, which are

$$\mathrm{D}\tilde{\varepsilon}_q^{\mathrm{e}} = \frac{\mathrm{D}q}{2G} = \frac{\mathrm{D}q}{2(1-2\mu)}\frac{\kappa}{v_0 p'} \tag{B.8}$$

$$\mathrm{D}\varepsilon_q^{\mathrm{p}} = \frac{\partial g/\partial q}{\partial g/\partial p'}\mathrm{D}\varepsilon_v^{\mathrm{p}} = -\frac{\partial g/\partial q}{\partial g/\partial p'}\mathrm{D}\varepsilon_v^{\mathrm{e}} = \frac{2}{\sqrt{3}}\frac{-4\eta}{M^2 - 4\eta^2/3}\frac{\kappa}{v_0 p'}\mathrm{D}p' \tag{B.9}$$

Eq. (3.117) can be finally obtained by substituting Eqs. (B.8) and (B.9) into Eq. (B.7):

$$\mathrm{D}\tilde{\varepsilon}_\theta = \frac{2\kappa}{\sqrt{3}v_0}\left(\frac{2\eta}{M^2 - 4\eta^2/3} - \frac{1}{4(1-2\mu)}\frac{\partial q}{\partial p'}\right)\frac{\mathrm{D}p'}{p'} \tag{B.10}$$

Appendix C Matlab code for cavity expansion analysis in Chapter 4

Although the solution shown in Chapter 4 is quite concise, calculation of stresses and displacement may involve some difficulties for dealing with exponential integral and Newton-Raphson iteration. For easy reference, reproduction, and modification, the Matlab code for Chapter 4 is shown in this appendix.

Matlab code:

```
%%   Fully Drained Cavity Expansion in Tresca Materials
%%   He Yang      21/12/2022      University of Leeds
clc; clear all
format long e
tic
%%   1--Input Parameters
% %   (a) Cavity shape
a0=1;               % initial inner cavity radius, m
Va=1e-2;          % inner cavity expansion velocity, m/s
% %   (b) Initial stress state
Sig0=1e+4;      % initial confining pressure
% %   (c) Strength and stiffness
G=1e+6;           su=1e+4;         mu=0.3;
% %   (d) Permeability
k=1e-6;     % permeability/gamma_w
% %   (e) Mesh
a_end=10;              %   final inner radius, m
incr_a=1.005;          %   increase of inner cavity radius
error=1e-4;           %   Iteration error
incr_r=1.01;           %   increase of radius when integration
options=optimset('TolFun',1e-8,'MaxIter',5000,'MaxFunEvals',5000,'display','off');

%%   2--Derived Parameters
Ir=G/su;                    % rigidity index (Houlsby, 1988);
w=(1-2*mu)/Ir;
Cp=G*k/(1-2*mu);
Ce=2*G*k*(1-mu)/(1-2*mu);
max=ceil(log(a_end/a0)/log(incr_a));

%%   3--Elastic Expansion
a_lim1=a0/(1-0.5/Ir);
```

```
TT(1,1)=(a_lim1-a0)/Va;
RR(1,1)=a_lim1;
SR(1,1)=Sig0+su;
SO(1,1)=Sig0-su;
UU(1,1)=0;
SRe(1,1)=Sig0+su;
%%   4--Elastic-Plastic Expansion
a=a_lim1
for i=2:1:max

      % (a) Give the boundary value
      a=a*incr_a^(min(0.6*i,20));
      if a>a_end
          a=a_end
      end

      t=(a-a0)/Va;

      % (b) Calculate two limit cases, fully drained and undrained
      rou_u=((a^2-a0^2)/(1-(1-0.5/Ir)^2))^0.5;
      syms x
      Eqr=matlabFunction((a/x)^(2-2*w)-1+(w-1)*((a0/x)^2-(1-0.5/Ir)^2));
      rou_d=fsolve(Eqr, rou_u, options);

      % (c) Normalised radius
      a0_t=a0/2/(Cp*t)^0.5;
      a_t=a/2/(Cp*t)^0.5;
      rou_ut=rou_u/2/(Cp*t)^0.5;
      rou_dt=rou_d/2/(Cp*t)^0.5;

     % (d)   fully undrained
      if a_t>=100
          rou=rou_u;
          rou_t=rou/2/(Cp*t)^0.5;
          RR(i,1)=a;
          SR(i,1)=Sig0+su+2*su*log(rou_t/a_t);
          SO(i,1)=SR(i,1)-2*su;
          UU(i,1)=2*su*log(rou_t/a_t);
          SRe(i,1)=SR(i,1)-UU(i,1);
          TT(i,1)=t;

     % (e)   fully drained
      elseif a_t<0.01/(Ir)^0.5
```

```
            rou=rou_d;
            rou_t=rou/2/(Cp*t)^0.5;
            RR(i,1)=a;
            SR(i,1)=Sig0+su+2*su*log(rou_t/a_t);
            SO(i,1)=SR(i,1)-2*su;
            UU(i,1)=0;
            SRe(i,1)=Sig0+su;
            TT(i,1)=t;

        % (f) Partially drained conditions
        else
            % (e-1): initial value for iteration
                        % using rou_dt
            % (e-2): numerical integration
            YZ(1,1)=a_t^2;                  %   Lower bound of integration
            YZ(1,2)=exp(E1fun(w, a_t^2, YZ(1,1)));
            N=ceil(2*log(rou_dt/a_t)/log(incr_r));
            for ii=2:1:N+1
                if YZ(ii-1,1)*incr_r<rou_dt^2;
                    YZ(ii,1)=YZ(ii-1,1)*incr_r;      % YZ(k,1)=rou_t^2
                else
                    YZ(ii,1)=rou_dt^2;
                end
                YZ(ii,2)=exp(E1fun(w, a_t^2, YZ(ii,1)));
            end
            Left0=trapz(YZ(:,1),YZ(:,2));

            % (e-3): find the exact value of rou:   % Newton Method
            % First Point
            XX(1,1)=rou_dt^2;
            Left=Left0;
            rou_dt0=rou_dt*(1-0.5/Ir);
            Right=exp(E1fun(w, a_t^2, rou_dt^2))*(rou_dt0^2-a0_t^2)*exp(w);
            FF(1,1)=Left-Right;
            % Second Point
            XX(2,1)=rou_ut^2;       YZ(N+2,1)=XX(2,1);
            YZ(N+2,2)=exp(E1fun(w, a_t^2, YZ(N+2,1)));
            Left=Left0+(YZ(N+2,1)-YZ(N+1,1))/6*(YZ(N+1,2)+YZ(N+2,2)+...

4*exp(E1fun(w, a_t^2, (YZ(N+1,1)+YZ(N+2,1))/2)));

            rou_ut0=rou_ut*(1-0.5/Ir);
            Right=exp(E1fun(w, a_t^2, rou_ut^2))*(rou_ut0^2-a0_t^2)*exp(w);
```

```
            FF(2,1)=Left-Right;
            %   Netown Iteration
            kk=2;       Error=1;
            while Error>error;
                XX(kk+1,1)=XX(kk,1)-FF(kk,1)/(FF(kk,1)-FF(kk-1,1))*(XX(kk,1)-
XX(kk-1,1));
                YZ(N+2,1)=XX(kk+1,1);    %   XX=rou_t^2
                YZ(N+2,2)=exp(E1fun(w, a_t^2, YZ(N+2,1)));
                Left=Left0+(YZ(N+2,1)-YZ(N+1,1))/6*(YZ(N+1,2)+YZ(N+2,2)+...

4*exp(E1fun(w, a_t^2, (YZ(N+1,1)+YZ(N+2,1))/2)));

                rou_t0=YZ(N+2,1)^0.5*(1-0.5/Ir);
                Right=exp(E1fun(w, a_t^2, YZ(N+2,1)))*(rou_t0^2-a0_t^2)*exp(w);

                FF(kk+1,1)=Left-Right;
                Error=abs((XX(kk+1,1)-XX(kk,1))/XX(kk,1));
                kk=kk+1;
            end
            rou_t=(YZ(N+2,1)^0.5);
            clear FF XX   YZ   kk   Left Right   U_rou   rou_t0
        end

        U_rou=su*(1-exp(a_t^2-rou_t^2))*E1fun(1, rou_t^2*Cp/Ce, rou_t^2*Cp/Ce);
        RR(i,1)=a;
        SR(i,1)=Sig0+su+2*su*log(rou_t/a_t)+(1-2*mu)/2/(1-mu)*U_rou;
        SO(i,1)=SR(i,1)-2*su;
        SRe(i,1)=Sig0+su-U_rou/2/(1-mu)+su*(E1fun(1, a_t^2, a_t^2)-E1fun(1, a_t^2,
rou_t^2));
        UU(i,1)=SR(i,1)-SRe(i,1);
        TT(i,1)=t;

        if a>=a_end
            break
        end
    end
toc
AAPP(:,1)=RR(:,1);
AAPP(:,2)=SR(:,1)/su;
AAPP(:,3)=UU(:,1)/su;
AAPP(:,4)=SRe(:,1)/su;

k
```

```
Va

%%   5--Results
subplot(1,3,1)
hold on
plot(RR(:,1),SR(:,1)/su,'r-')
subplot(1,3,2)
hold on
plot(RR(:,1),SRe(:,1)/su,'r-')
subplot(1,3,3)
hold on
plot(RR(:,1),UU(:,1)/su,'r-')



function [ E1_Int_Fun] = E1fun(w, y, x)

% %   E1fun=w*exp(y)*Int('exp(-x)/x', x, inf)
% %   Expotential integration function
% %   Similarity Solution
        if x>10000
            E1_Int_Fun=0;

        elseif x>10
             S=1;
             for n=1:1:10;
                   S=S+factorial(n)/(-x)^n;
             end
             E1_Int_Fun=w*exp(y-x)/x*S;

        else
             S=-0.577215664901533;
             for n=1:1:50;
                    S=S-(-x)^n/n/factorial(n);
             end
             E1_Int_Fun=w*exp(y)*(S-log(x));
        end
end
```

Appendix D Supplementary information for CPTU data

The available test data for CPTU under partially drained conditions may vary with different methods and different test sites. It is necessary to modify these data in accordance with the criteria shown in Chapter 4. The modification/exclusion of these data is detailed in this appendix.

Mafra and Dienstmann (2022) studied the backbone for EWP in CPTU by cavity expansion method, where their original normalised penetration rate should multiply $1.4\times\sqrt{3}$ to consider the influence of cone tip angle and the difference between c_{he} and c_{hp}.

The original normalised penetration rate in Mahmoodzadeh, Hamed and Randolph (2014) should be divided by

$$\frac{c_{\mathrm{hp}}}{c_{\mathrm{he}}}\frac{c_{\mathrm{he}}}{c_{\mathrm{v}}}=\frac{1}{1.4}\times 4.66=3.33 \tag{D.1}$$

This is mainly because the normalised penetration rate was defined by $\bar{V}_0=V_{\mathrm{cptu}}D/c_{\mathrm{v}}$ rather than $\bar{V}_0=V_{\mathrm{cptu}}D/c_{\mathrm{hp}}$.

Silva et al. (2006) and Zhou et al. (2021a) calculated some data based on the cavity expansion theory and finite element numerical simulations. Their data are not included in the database as the initial cavity radius is not zero. The centrifuge test data in Silva et al. (2006) are not included either due to the missing c_{hp}.

The numerical simulation data in Liu, Kehan et al. (2024) is also modified where their normalised penetration rate is divided by 4.7/1.4=3.36.

The data published in the thesis of Jaeger (2012) are excluded because:

(i) There was no reference EWP;

(ii) The value of c_{hp}/c_v was not given for the tested sandy silt.

The constitutive model in Yi et al. (2012) is the DP model that may lead to different definitions of c_{hp}. Besides, the reference EWP was not given and the maximum EWP is selected as the reference EWP in this thesis.

In Schneider et al. (2007), the data for tests on overconsolidated clay are not included in the database owing to the missing values of I_r and c_{hp}/c_v.

The experimental data in (Kim et al., 2008) and the numerical simulation data in (Monforte et al., 2021) are not included due to the missing values of I_r.

For easy conference, the CPTU data used in Chapter 4 are available from:

URL: https://pan.baidu.com/s/1lanerGx6hmAnMDgtk8idQQ

PIN: YANG

Appendix E Bessel functions

When $r \gg 1/4$, the first and second kinds of Bessel functions of zero order can be approximately replaced by

$$J_0(r) = \sqrt{\frac{2}{\pi r}} \cos\left(r - \frac{\pi}{4}\right) \tag{E.1}$$

$$Y_0(r) = \sqrt{\frac{2}{\pi r}} \sin\left(r - \frac{\pi}{4}\right) \tag{E.2}$$

The error is no more than 2% when $20 < r < 200$ and the error is no more than 1% when $r > 200$.

When *a*=1 and *b*=50, the roots of the composite Bessel function U_0 can be roughly estimated by combining Eq. (5.6), (E.1) and (E.2):

$$J_0(\alpha_n) Y_0(50\alpha_n) = J_0(50\alpha_n) Y_0(\alpha_n) \tag{E.3}$$

$$\sqrt{\frac{2}{\pi\alpha_n}} \cos\left(\alpha_n - \frac{\pi}{4}\right) \sqrt{\frac{2}{\pi 50\alpha_n}} \sin\left(\alpha_n - \frac{\pi}{4}\right) = \sqrt{\frac{2}{\pi 50\alpha_n}} \cos\left(50\alpha_n - \frac{\pi}{4}\right) \sqrt{\frac{2}{\pi\alpha_n}} \sin\left(\alpha_n - \frac{\pi}{4}\right) \tag{E.4}$$

Eq. (E.4) can be simplified as

$$\cos\left(\alpha_n - \frac{\pi}{4}\right) \sin\left(50\alpha_n - \frac{\pi}{4}\right) - \cos\left(50\alpha_n - \frac{\pi}{4}\right) \sin\left(\alpha_n - \frac{\pi}{4}\right) = 0 \tag{E.4}$$

or

$$\sin(49\alpha_n) = 0 \tag{E.5}$$

Then the roots of U_0 can be approximately seen as the roots of Eq. (E.5), as

$$\alpha_n = \frac{n\pi}{49} = 0.0641n \tag{E.6}$$

Eq. (E.6) can be severed as the initial iteration value to find the exact roots of U_0.

Finally, it is worthwhile to show the error analysis that can determine the maximum value

of the roots of U_0. The term in Eq. (5.5) can be approximately expressed as

$$\sum_{n=1}^{\infty} \frac{J_0(\alpha_n a) J_0(\alpha_n b) U_0(\alpha_n r)}{J_0^2(\alpha_n a) - J_0^2(\alpha_n b)} \approx \frac{J_0(\alpha_n 50) U_0(\alpha_n r)}{J_0(\alpha_n)} \approx \frac{U_0(\alpha_n r)}{\sqrt{50}} \tag{E.7}$$

For the maximum error of 10^{-4}, we can get:

$$\left|U_0(\alpha_n r)\right|_{\max} \le 7 \times 10^{-3} \tag{E.8}$$

It can be proven that when α_n >120, Eq. (E.8) will be satisfied.

Appendix F Derivation of Eq. (5.29)

The radial deformation of energy pile at $r = a$ the pile-soil interface may be split into thermal expansion part $\alpha_{\text{pile}} \Delta T_a a$ and soil restriction part with a confining pressure $\Delta\sigma_{\text{n}}$ at $r = a$. The latter induced by soil restriction can be derived as follows.

The stress equilibrium equation remains the same as Eq. (5.7), and elastic stress-strain relationship for energy piles can be simplified as

$$\varepsilon_r = -\frac{\partial u}{\partial r} = \frac{1}{E_{\text{pile}}}\left[\Delta\sigma_r - \mu_{\text{pile}}\left(\Delta\sigma_\theta + \Delta\sigma_z\right)\right] \tag{F.1}$$

$$\varepsilon_\theta = -\frac{u}{r} = \frac{1}{E_{\text{pile}}}\left[\Delta\sigma_\theta - \mu_{\text{pile}}\left(\Delta\sigma_r + \Delta\sigma_z\right)\right] \tag{F.2}$$

$$\varepsilon_z = 0 = \frac{1}{E_{\text{pile}}}\left[\Delta\sigma_z - \mu_{\text{pile}}\left(\Delta\sigma_r + \Delta\sigma_\theta\right)\right] \tag{F.3}$$

As the boundary conditions that $\Delta\sigma_r = \Delta\sigma_{\text{n}}$ at $r = a$ and $\Delta\sigma_r \neq \infty$ at $r = 0$ should be satisfied, the stress components will be

$$\Delta\sigma_r = \Delta\sigma_\theta = \Delta\sigma_{\text{n}} \tag{F.4}$$

$$\Delta\sigma_z = 2\mu_{\text{pile}}\Delta\sigma_{\text{n}} \tag{F.5}$$

The radial displacement at $r = a$, which are resulted from soil restriction, can be derived by substituting Eqs. (F.4) and (F.5) into Eq. (F.2):

$$u(a) = -\frac{\left(1-2\mu_{\text{pile}}\right)\left(1+\mu_{\text{pile}}\right)}{E_{\text{pile}}}\Delta\sigma_{\text{n}} a \tag{F.6}$$

Finally, the radial displacement of piles at $r = a$ can be obtained by adding $\alpha_{\text{pile}}\Delta T a$ and Eq. (F.6), thereby giving the expression of Eq. (5.29):

$$\frac{u(a)}{a} = \alpha_{\text{pile}}\Delta T_a - \frac{1-\mu_{\text{pile}}-\mu_{\text{pile}}^2}{E_{\text{pile}}}\Delta\sigma_{\text{n}} \tag{F.7}$$

List of References

Abbas, I.A. 2014. Nonlinear transient thermal stress analysis of thick-walled FGM cylinder with temperature-dependent material properties. *Meccanica.* **49**(7), pp.1697-1708.

Abu-Farsakh, M., Tumay, M. and Voyiadjis, G. 2003. Numerical parametric study of piezocone penetration test in clays. *International Journal of Geomechanics.* **3**(2), pp.170-181.

Akbari, A. 2021. Analytical solution of elastic–plastic stress for double-layer FGM spherical shell subjected to pressure and temperature load. *Journal of the Brazilian Society of Mechanical Sciences and Engineering.* **43**(2), article no: 79 [no pagination].

Alexandrov, S. and Jeng, Y.-R. 2020. An elastic/plastic solution for a hollow sphere subject to thermo-mechanical loading considering temperature dependent material properties. *International Journal of Solids and Structures.* **200**, pp.23-33.

Alonso, E.E., Gens, A. and Josa, A. 1990. A constitutive model for partially saturated soils. *Géotechnique.* **40**(3), pp.405-430.

Alsiny, A., Vardoulakis, I. and Drescher, A. 1992. Deformation localization in cavity inflation experiments on dry sand. *Géotechnique.* **42**(3), pp.395-410.

Amatya, B., Soga, K., Bourne-Webb, P., Amis, T. and Laloui, L. 2012. Thermo-mechanical behaviour of energy piles. *Géotechnique.* **62**(6), pp.503-519.

Aptukov, V. 1991. Expansion of a spherical cavity in a compressible elastoplastic medium. Report 2. Effect of inertial forces. Temperature effects. *Strength of materials.* **23**(12), pp.1269-1274.

Araki, W., Adachi, T. and Yamaji, A. 2004. Thermal stress analysis of thermoviscoelastic hollow cylinder with temperature-dependent thermal properties. *Journal of Thermal Stresses.* **28**(1), pp.29-46.

Arefi, M. and Rahimi, G. 2013. Thermo elastic analysis of a functionally graded cylinder under internal pressure using first order shear deformation theory. *Scientific Research and Essays.* **5**(12), pp.1442-1454.

Arslan, E., Mack, W. and Apatay, T. 2021. Thermo-mechanically loaded steel/aluminum functionally graded spherical containers and pressure vessels. *International Journal of Pressure Vessels and Piping.* **191**, p104334.

Asgari, M. and Akhlaghi, M. 2010. Transient thermal stresses in two-dimensional functionally graded thick hollow cylinder with finite length. *Archive of Applied Mechanics.* **80**, pp.353-376.

Auton, L.C. 2018. *Large fluid-driven deformations of porous annuli: solutions via Chebyshev spectral collocation*. Ph.D. thesis, University of Oxford.

Auton, L.C. and MacMinn, C.W. 2019. Large poroelasto-plastic deformations due to radially outward fluid injection. *Journal of the Mechanics and Physics of Solids.* **132**, article no: 103690 [no pagination].

Baguelin, F., Jezequel, J.-F., Le, M. and LeMehaute, A. 1972. Expansion of cylindrical probes in cohesive soils. *Journal of Soil Mechanics and Foundations Division.* **98**(SM11), pp.1129-1142.

Bao, X., Qi, X., Cui, H., Tang, W. and Chen, X. 2022. Experimental study on thermal response of a PCM energy pile in unsaturated clay. *Renewable Energy.* **185**, pp.790-803.

Bedin, J. 2006. *Interpretation of Piezocone Test in Bauxite Residues*. Master thesis, Universidade Federal do Rio Grande do Sul.

Benslimane, A., Benchallal, R., Mammeri, S., Methia, M. and Khadimallah, M.A. 2020. Investigation of displacements and stresses in thick-walled FGM cylinder subjected to thermo-mechanical loadings. *International Journal for Computational Methods in Engineering Science and Mechanics.* **22**(2), pp.138-149.

Bhargava, R. and Sharma, C. 1964. Elasto-plastic medium containing a cylindrical cavity

under uniform internal pressure. *Journal of the Franklin Institute.* **277**(5), pp.422-427.

Bigoni, D. and Laudiero, F. 1989. The quasi-static finite cavity expansion in a non-standard elasto-plastic medium. *International Journal of Mechanical Sciences.* **31**(11-12), pp.825-837.

Bishop, A.W. and Blight, G. 1963. Some aspects of effective stress in saturated and partly saturated soils. *Géotechnique.* **13**(3), pp.177-197.

Bishop, R.F., Hill, R. and Mott, N.F. 1945. The theory of indentation and hardness tests. *Proceedings of the Physical Society.* **57**(3), pp.147-159.

Bland, D.R. 1956. Elastoplastic thick-walled tubes of work-hardening material subject to internal and external pressures and to temperature gradients. *Journal of the Mechanics and Physics of Solids.* **4**(4), pp.209-229.

Bolton, M.D. 1986. The strength and dilatancy of sands. *Geotechnique.* **36**(1), pp.65-78.

Borja, R.I. 2004. Cam-Clay plasticity. Part V: A mathematical framework for three-phase deformation and strain localization analyses of partially saturated porous media. *Computer methods in applied mechanics and engineering.* **193**(48-51), pp.5301-5338.

Bourne-Webb, P., Burlon, S., Javed, S., Kürten, S. and Loveridge, F. 2016. Analysis and design methods for energy geostructures. *Renewable and Sustainable Energy Reviews.* **65**, pp.402-419.

Bourne-Webb, P., Freitas, T.B. and Assunção, R.F. 2019. A review of pile-soil interactions in isolated, thermally-activated piles. *Computers and Geotechnics.* **108**, pp.61-74.

Bourne-Webb, P.J., Amatya, B., Soga, K., Amis, T., Davidson, C. and Payne, P. 2009. Energy pile test at Lambeth College, London: geotechnical and thermodynamic aspects of pile response to heat cycles. *Géotechnique.* **59**(3), pp.237-248.

Bourne-Webb, P.J., Freitas, T.M.B. and Assunção, R.M.F. 2016. Soil–pile thermal interactions in energy foundations. *Géotechnique.* **66**(2), pp.167-171.

Burenin, A., Tkacheva, A. and Shcherbatyuk, G. 2018. Calculation of the unsteady thermal stresses in elastoplastic solids. *Journal of Applied Mechanics and Technical Physics.* **59**(7), pp.1197-1210.

Cai, G., Liu, S. and Puppala, A.J. 2015. Consolidation parameters interpretation of CPTU dissipation data based on strain path theory for soft Jiangsu quaternary clays. *Marine Georesources & Geotechnology.* **33**(4), pp.310-319.

Cao, L.F., Teh, C.I. and Chang, M.F. 2001. Undrained cavity expansion in modified Cam clay. *Géotechnique.* **51**(4), pp.323-334.

Carslaw, H.S. and Jaeger, J.C. 1947. *Conduction of heat in solids.* 2nd ed. Oxford: The Clarendon Press.

Carter, J.P., Booker, J.R. and Yeung, S.K. 1986. Cavity expansion in cohesive frictional soils. *Géotechnique.* **36**(3), pp.349-358.

Carter, J.P., Randolph, M.F. and Wroth, C.P. 1979. Stress and pore pressure changes in clay during and after the expansion of a cylindrical cavity. *International Journal for Numerical and Analytical Methods in Geomechanics.* **3**(4), pp.305-322.

Carter, J.P. and Yu, H.-S. 2022. Cavity Expansion in Cohesive-Frictional Soils with Limited Dilation. *Géotechnique.* **73**(7), pp.629-635.

Castro, J. and Sivasithamparam, N. 2022. Theoretical solution for drained cylindrical cavity expansion in clays with fabric anisotropy and structure. *Acta Geotechnica.* **17**(5), pp.1917-1933.

Ceccato, F., Beuth, L. and Simonini, P. 2016. Analysis of piezocone penetration under different drainage conditions with the two-phase material point method. *Journal of Geotechnical and Geoenvironmental Engineering.* **142**(12), article no: 04016066 [no pagination].

Ceccato, F. and Simonini, P. 2017. Numerical study of partially drained penetration and pore pressure dissipation in piezocone test. *Acta Geotechnica.* **12**, pp.195-209.

Chadwick, P. 1959. The quasi-static expansion of a spherical cavity in metals and ideal soils. *The Quarterly Journal of Mechanics and Applied Mathematics.* **12**(1), pp.52-71.

Chadwick, P. 1963. Compression of a spherical shell of work-hardening material. *International Journal of Mechanical Sciences.* **5**(2), pp.165-182.

Chai, J.-C., Hossain, M.J., Yuan, D.-J., Shen, S.-l. and Carter, J.P. 2016. Pore pressures induced by piezocone penetration. *Canadian Geotechnical Journal.* **53**(3), pp.540-550.

Chai, J.-C., Sheng, D., Carter, J.P. and Zhu, H. 2012. Coefficient of consolidation from non-standard piezocone dissipation curves. *Computers and Geotechnics.* **41**, pp.13-22.

Chang, M.-F., Teh, C.I. and Cao, L. 1999. Critical state strength parameters of saturated clays from the modified Cam clay model. *Canadian Geotechnical Journal.* **36**(5), pp.876-890.

Chen, H., Li, L. and Li, J. 2020a. Elastoplastic solutions for cylindrical cavity expansion in unsaturated soils. *Computers and Geotechnics.* **123**, p103569.

Chen, H., Li, L. and Li, J. 2020b. Elastoplastic solutions for cylindrical cavity expansion in unsaturated soils. *Computers and Geotechnics.* **123**, article no: 103569 [no pagination].

Chen, H., Li, L., Li, J. and Sun, D.A. 2021. A rigorous elastoplastic load-transfer model for axially loaded pile installed in saturated modified Cam-clay soils. *Acta Geotechnica.* pp.1-17.

Chen, H. and Mo, P.-Q. 2022. An undrained expansion solution of cylindrical cavity in SANICLAY for K0-consolidated clays. *Journal of Rock Mechanics and Geotechnical Engineering.* **14**(3), pp.922-935.

Chen, H., Weng, X., Hou, L. and Sun, D.A. 2022. Elastoplastic analysis of cylindrical cavity expansion responses in anisotropic unsaturated soils under plane stress condition. *Journal of Rock Mechanics and Geotechnical Engineering.* **14**(6), pp.1989-2002.

Chen, S.-L. 2024. A Graphical Solution Framework for Elastoplastic Cylindrical Cavity Problem in Mohr–Coulomb Material. *Journal of Engineering Mechanics.* **150**(5), p04024016.

Chen, S.-L. and Liu, K. 2019. Undrained cylindrical cavity expansion in anisotropic critical state soils. *Géotechnique.* **69**(3), pp.189-202.

Chen, S.-L. and Wang, X. 2022. A graphical method for undrained analysis of cavity expansion in Mohr–Coulomb soil. *Géotechnique.* pp.1-13.

Chen, S. and Abousleiman, Y. 2013. Exact drained solution for cylindrical cavity expansion in modified Cam Clay soil. *Géotechnique.* **63**(6), pp.510-517.

Chen, S. and Abousleiman, Y. 2018. Cavity expansion in strain hardening frictional soils under drained condition. *International Journal for Numerical and Analytical Methods in Geomechanics.* **42**(1), pp.132-142.

Chen, S. and Abousleiman, Y. 2023. A graphical analysis-based method for undrained cylindrical cavity expansion in modified Cam Clay soil. *Géotechnique.* **73**(8), pp.736-746.

Chen, S., Abousleiman, Y. and Muraleetharan, K.K. 2022. Computational implementation of bounding surface model and its verification through cavity benchmark problems. *International Journal for Numerical and Analytical Methods in Geomechanics.* **46**(3), pp.553-569.

Chen, S.L. and Abousleiman, Y.N. 2012. Exact undrained elasto-plastic solution for cylindrical cavity expansion in modified Cam Clay soil. *Géotechnique.* **62**(5), pp.447-456.

Chen, S.L. and Abousleiman, Y.N. 2013. Exact drained solution for cylindrical cavity expansion in modified Cam Clay soil. *Géotechnique.* **63**(6), pp.510-517.

Chen, X. 2013. Constitutive unsaturated hydro-mechanical model based on modified mixture theory with consideration of hydration swelling. *International Journal of Solids*

and Structures. **50**(20-21), pp.3266-3273.

Cheng, W., Chen, R.P., Pereira, J.M. and Cui, Y.J. 2022. Undrained cylindrical cavity expansion/contraction in stiff clays using a two‐surface plasticity model. *International Journal for Numerical and Analytical Methods in Geomechanics.* **46**(3), pp.570-593.

Cheng, Y. and Yang, H.-W. 2019. Exact solution for drained spherical cavity expansion in saturated soils of finite radial extent. *International Journal for Numerical and Analytical Methods in Geomechanics.* **43**(8), pp.1594-1611.

Cheng, Y., Yang, H.-W. and Sun, D.A. 2018. Cavity expansion in unsaturated soils of finite radial extent. *Computers and Geotechnics.* **102**, pp.216-228.

Cheng, Y., Yang, H., Xu, Z. and Lu, C. 2022. Cavity expansion analysis of normal indention of rocks with lateral confinement. *Computers and Geotechnics.* **145**, article no: 104693 [no pagination].

Collins, I.F., Pender, M.J. and Wang, Y. 1992. Cavity expansion in sands under drained loading conditions. *International Journal for Numerical and Analytical Methods in Geomechanics.* **16**(1), pp.3-23.

Collins, I.F. and Stimpson, J.R. 1994. Similarity solutions for drained and undrained cavity expansions in soils. *Géotechnique.* **44**(1), pp.21-34.

Collins, I.F. and Yu, H.-S. 1996. Undrained cavity expansions in critical state soils. *International Journal for Numerical and Analytical Methods in Geomechanics.* **20**(7), pp.489-516.

Coussy, O. 2004. *Poromechanics.* John Wiley & Sons.

Cowper, G. 1960. The elastoplastic thick-walled sphere subjected to a radial temperature gradient. *J. Appl. Mechanics.* **27**, pp.496-500.

Cui, Y.J. and Delage, P. 1996. Yielding and plastic behaviour of an unsaturated compacted silt. *Géotechnique.* **46**(2), pp.291-311.

Dats, E., Mokrin, S. and Murashkin, E. 2015. Calculation of the residual stresses of hollow cylinder under unsteady thermal action. In: *Proceedings of the World Congress on Engineering*.

Davis, R.O., Scott, R.F. and Mullenger, G. 1984. Rapid expansion of a cylindrical cavity in a rate-type soil. *International Journal for Numerical and Analytical Methods in Geomechanics.* **8**(2), pp.125-140.

De Boer, R. 2012. *Theory of porous media: highlights in historical development and current state.* Springer Science & Business Media.

DeJong, J.T. and Randolph, M.F. 2012. Influence of partial consolidation during cone penetration on estimated soil behavior type and pore pressure dissipation measurements. *Journal of Geotechnical and Geoenvironmental Engineering.* **138**(7), pp.777-788.

Derrington, M. and Johnson, W. 1958. The onset of yield in a thick spherical shell subject to internal pressure and uniform heat flow. *Applied Scientific Research, Section A.* **7**(6), pp.408-420.

Dienstmann, G., Maghous, S. and Schnaid, F. 2017. Theoretical analysis and finite-element simulation for nonlinear poroelastic behavior of cylinder expansion in infinite media under transient pore-fluid flow conditions. *International Journal of Geomechanics.* **17**(7), article no: 04017001 [no pagination].

Dienstmann, G., Maghous, S. and Schnaid, F. 2018a. Assessment of Rate Effects in Piezocone Tests from Poroelastic Cavity Expansion Analysis. *Soils and Rocks.* **41**(3), pp.319-332.

Dienstmann, G., Schnaid, F., Maghous, S. and DeJong, J. 2018b. Piezocone penetration rate effects in transient gold tailings. *Journal of Geotechnical and Geoenvironmental Engineering.* **144**(2), article no: 04017116 [no pagination].

Durban, D. 1983. Thermo-elastic/plastic behaviour of a strain-hardening thick-walled sphere. *International Journal of Solids and Structures.* **19**(7), pp.643-652.

Durban, D. and Fleck, N.A. 1997. Spherical cavity expansion in a Drucker-Prager solid. [Online]. Available from: https://doi.org/https://www.researchgate.net/publication/245359343_Spherical_Cavity_Expansion_in_a_Drucker-Prager_Solid

Ecemis, N., Arik, M.S. and Taneri, H. 2023. Effect of drainage conditions on CPT resistance of silty sand: physical model and field tests. *Acta Geotechnica.* **18**(12), pp.6709-6724.

Ehteram, M., Sadighi, M. and Tabrizi, H.B. 2011. Analytical solution for thermal stresses of laminated hollow cylinders under transient nonuniform thermal loading. *Mechanics.* **17**(1), pp.30-37.

Eraslan, A.N. and Apatay, T. 2016. Analytical solution to thermal loading and unloading of a cylinder subjected to periodic surface heating. *Journal of Thermal Stresses.* **39**(8), pp.928-941.

Eraslan, A.N. and Orcan, Y. 2002. Computation of transient thermal stresses in elastic-plastic tubes: Effect of coupling and temperature-dependent physical properties. *Journal of thermal stresses.* **25**(6), pp.559-572.

Fahey, M. 1986. Expansion of a thick cylinder of sand: a laboratory simulation of the pressuremeter test. *Géotechnique.* **36**(3), pp.397-424.

Fahey, M. and Goh, A.L. 1995. A comparison of pressuremeter and piezocone methods of determining the coefficient of consolidation. In: *The Pressuremeter and its New Avenues,* Balkema: CRC Press, pp.153-160.

Fahey, M. and Randolph, M.F. 1984. Effect of disturbance on parameters derived from self-boring pressuremeter tests in sand. *Géotechnique.* **34**(1), pp.81-97.

Faizal, M., Bouazza, A., Haberfield, C. and McCartney, J.S. 2018. Axial and radial thermal responses of a field-scale energy pile under monotonic and cyclic temperature changes. *Journal of Geotechnical and Geoenvironmental Engineering.* **144**(10), article

no: 04018072 [no pagination].

Faizal, M., Bouazza, A. and McCartney, J.S. 2022. Thermal resistance analysis of an energy pile and adjacent soil using radial temperature gradients. *Renewable Energy.* **190**, pp.1066-1077.

Faizal, M., Bouazza, A., McCartney, J.S. and Haberfield, C. 2019a. Axial and radial thermal responses of energy pile under six storey residential building. *Canadian Geotechnical Journal.* **56**(7), pp.1019-1033.

Faizal, M., Bouazza, A., McCartney, J.S. and Haberfield, C. 2019b. Effects of cyclic temperature variations on thermal response of an energy pile under a residential building. *Journal of Geotechnical and Geoenvironmental Engineering.* **145**(10), p04019066.

Fuentes, R., Pinyol, N. and Alonso, E. 2016. Effect of temperature induced excess porewater pressures on the shaft bearing capacity of geothermal piles. *Geomechanics for Energy and the Environment.* **8**, pp.30-37.

Gaaloul, I., Montassar, S. and Frikha, W. 2021. Thermal effects on limit pressure in a cylindrical cavity expansion. *Innovative Infrastructure Solutions.* **6**, article no: 194 [no pagination].

Gamer, U. 1988. On the elastic-plastic deformation of a sphere subjected to spherically symmetrical temperature field. *Journal of Thermal Stresses.* **11**(3), pp.159-173.

Ghafghazi, M. and Shuttle, D. 2008. Interpretation of sand state from cone penetration resistance. *Géotechnique.* **58**(8), pp.623-634.

Gharsallaoui, H., Jafari, M. and Holeyman, A. 2020. Cavity expansion in rock masses obeying the “Hoek–Brown” failure criterion. *Rock Mechanics and Rock Engineering.* **53**(2), pp.927-941.

Ghasemi-Fare, O. and Basu, P. 2013. A practical heat transfer model for geothermal piles. *Energy and Buildings.* **66**, pp.470-479.

Gibson, R. 1974. The analytical method in soil mechanics. *Geotechnique.* **24**(2), pp.115-140.

Gibson, R. and Anderson, W.F. 1961. In-situ measurement of soil properties with pressuremeter. *Civil Engineering and Public Works Review.* **56**(658), pp.615-618.

Gupta, S.C. 2017. *The classical Stefan problem: basic concepts, modelling and analysis with quasi-analytical solutions and methods.* Elsevier.

Heydari, A. and Kazemi, M. 2015. Thermo-elasto-plastic analysis of functionally graded spherical reservoirs subjected to temperature gradient. In: *Proceedings of the 10th International Congress on Civil Engineering,* University of Tabriz, Iran.

Hill, R. 1950. *The mathematical theory of plasticity.* London: Oxford university press.

Houlsby, G.T. and Withers, N.J. 1988. Analysis of the cone pressuremeter test in clay. *Geotechnique.* **38**(4), pp.575-587.

House, A., Oliveira, J. and Randolph, M.F. 2001. Evaluating the coefficient of consolidation using penetration tests. *International Journal of Physical Modelling in Geotechnics.* **1**(3), pp.17-26.

Huang, M., Tong, S. and Shi, Z. 2021. Solution for spherical cavity expansion in state-dependent soils. *Acta Geotechnica.* **16**(6), pp.1773-1788.

Hughes, J.M.O., Wroth, C.P. and Windle, D. 1977. Pressuremeter tests in sands. *Geotechnique.* **27**(4), pp.455-477.

Ishikawa, H. 1977. Transient thermoelastoplastic stress analysis for a hollow sphere using the incremental theory of plasticity. *International Journal of Solids and Structures.* **13**(7), pp.645-655.

Jabbari, M., Sohrabpour, S. and Eslami, M.R. 2002. Mechanical and thermal stresses in a functionally graded hollow cylinder due to radially symmetric loads. *International Journal of Pressure Vessels and Piping.* **79**, pp.493-497.

Jaeger, R.A. 2012. *Numerical and experimental study on cone penetration in sands and intermediate soils*. Ph.D. thesis, University of California, Davis.

Jaeger, R.A., DeJong, J., Boulanger, R., Low, H. and Randolph, M.F. 2010. Variable penetration rate CPT in an intermediate soil. In: *Proc., 2nd Int. Symp. on Cone Penetration Testing*, *Huntington Beach, CA*. Omnipress, pp.2-50.

Jahanian, S. and Tavakoli, M. 1998. Inelastic stresses in spheres caused by thermal loading. *Materials at high temperatures.* **15**(1), pp.29-33.

Jefferies, M.G. 1988. Determination of horizontal geostatic stress in clay with self-bored pressuremeter. *Canadian Geotechnical Journal.* **25**(3), pp.559-573.

Jewell, R.J., Fahey, M. and Wroth, C.P. 1980. Laboratory studies of the pressuremeter test in sand. *Géotechnique.* **30**(4), pp.507-531.

Jin, Z.-H. and Noda, N. 1994. Transient thermal stress intensity factors for a crack in a semi-infinite plate of a functionally gradient material. *International journal of solids and structures.* **31**(2), pp.203-218.

Jing, Y., Li, J., Ren, P. and Chen, H. 2024. Analysis of effects of initial hydraulic state on undrained cylindrical cavity expansion response in unsaturated soils. *Computers and Geotechnics.* **175**, p106708.

Johnson, W. and Mellor, P.B. 1962. Elastic-plastic behaviour of thick-walled spheres of non-work-hardening material subject to a steady-state radial temperature gradient. *International Journal of Mechanical Sciences.* **4**(2), pp.147-158.

Johnson, W. and Mellor, P.B. 1983. *Engineering plasticity.* John Wiley & Sons.

Kamal, S., Dixit, U.S., Roy, A., Liu, Q. and Silberschmidt, V.V. 2017. Comparison of plane-stress, generalized-plane-strain and 3D FEM elastic–plastic analyses of thick-walled cylinders subjected to radial thermal gradient. *International Journal of Mechanical Sciences.* **131**, pp.744-752.

Kandil, A., El-Kady, A.A. and El-Kafrawy, A. 1995. Transient thermal stress analysis of thick-walled cylinders. *International Journal of Mechanical Sciences.* **37**, pp.721-732.

Kashkoli, M.D. and Nejad, M.Z. 2015. Time-dependent thermo-elastic creep analysis of thick-walled spherical pressure vessels made of functionally graded materials. *Journal of Theoretical and Applied Mechanics.* **53**(4), pp.1053-1065.

KAYA, Y. and ERASLAN, A.N. 2014. Thermoelastic response of a long tube subjected to periodic heating. *Mathematical Sciences and Applications E-Notes.* **2**(1), pp.14-27.

Khalili, N., Habte, M.A. and Zargarbashi, S. 2008. A fully coupled flow deformation model for cyclic analysis of unsaturated soils including hydraulic and mechanical hystereses. *Computers and Geotechnics.* **35**(6), pp.872-889.

Khalili, N., Romero, E. and Marinho, F.A. 2022. State of the Art Report. Advances in Unsaturated Soil Mechanics: Constitutive modelling, experimental investigation, and field instrumentation. In: *Proceedings of the 20th ICSMGE-State of the Art and Invited Lectures*, *Rahman and Jaksa, Sydney, Australia*. pp.297-348.

Khodayari, M.R. and Ahmadi, M.M. 2022. Self CPTU measurements for determining su and OCR in clay soils: Simulation and practical applications. *International Journal of Geomechanics.* **22**(11), article no: 04022209 [no pagination].

Kim, K., Prezzi, M., Salgado, R. and Lee, W. 2008. Effect of penetration rate on cone penetration resistance in saturated clayey soils. *Journal of Geotechnical and Geoenvironmental Engineering.* **134**(8), pp.1142-1153.

Klahold, P. 2013. *Interpretation of field tests on soils with intermediate permeability*. Master thesis, Universidade Federal do Rio Grande do Sul.

Knellwolf, C., Peron, H. and Laloui, L.J.C. 2011. Geotechnical analysis of heat exchanger piles. *Journal of Geotechnical and Geoenvironmental Engineering.* **137**(10), pp.890-902.

Kong, G., Fang, J., Huang, X., Liu, H. and Abuel-Naga, H. 2021a. Thermal induced horizontal earth pressure changes of pipe energy piles under multiple heating cycles.

Geomechanics for Energy and the Environment. **26**, article no: 100228 [no pagination].

Kong, G., Fang, J., Huang, X., Liu, H. and Abuel-Naga, H. 2021b. Thermal induced horizontal earth pressure changes of pipe energy piles under multiple heating cycles. *Geomechanics for Energy and the Environment.* **26**, p100228.

Kumar, J.S., Chaudhuri, A., Detournay, E. and Kandasami, R.K. 2024. Fluid injection-induced cavity expansion in dry porous medium. *International Journal for Numerical and Analytical Methods in Geomechanics.* **48**(1), pp.104-122.

Ladanyi, B. 1972. In-situ determination of undrained stress-strain behavior of sensitive clays with the pressuremeter. *Canadian Geotechnical Journal.* **9**(3), pp.313-319.

Lai, B.T., Wong, H., Fabbri, A. and Branque, D. 2016. A new constitutive model of unsaturated soils using bounding surface plasticity (BSP) and a non-associative flow rule. *Innovative Infrastructure Solutions.* **1**(1), p3.

Laloui, L. and François, B. 2009. ACMEG-T: soil thermoplasticity model. *Journal of engineering mechanics.* **135**(9), pp.932-944.

Laloui, L., Nuth, M. and Vulliet, L. 2006. Experimental and numerical investigations of the behaviour of a heat exchanger pile. *International Journal for Numerical and Analytical Methods in Geomechanics.* **30**(8), pp.763-781.

Lee, S.Y. 1990. *Centrifuge modelling of cone penetration testing in cohesionless soils*. Ph.D. thesis, University of Cambridge.

Lee, Z.-Y., Chen, C.o.-K. and Hung, C.-I. 2001. Transient thermal stress analysis of multilayered hollow cylinder. *Acta Mechanica.* **151**(1-2), pp.75-88.

Li, J., Gong, W., Li, L. and Liu, F. 2017. Drained elastoplastic solution for cylindrical cavity expansion in K0-consolidated anisotropic soil. *Journal of Engineering Mechanics.* **143**(11), article no: 04017133 [no pagination].

Li, L., Chen, H. and Li, J. 2021. An elastoplastic solution for cylindrical cavity expansion

under constant water content conditions in anisotropic unsaturated soils. *Computers and Geotechnics.* **139**, article no: 104323 [no pagination].

Li, R., Kong, G., Sun, G., Zhou, Y. and Yang, Q. 2021. Thermomechanical characteristics of an energy pile-raft foundation under heating operations. *Renewable Energy.* **175**, pp.580-592.

Liang, H. 2010. *Advances in Ellipsoidal Cavity Expansion with Tresca Material*. Ph.D. thesis, China University of Mining and technology.

Liu, H.-l., Wang, C.-l., Kong, G.-q. and Bouazza, A. 2019. Ultimate bearing capacity of energy piles in dry and saturated sand. *Acta Geotechnica.* **14**, pp.869-879.

Liu, H., Zhou, H., Kong, G., Qin, H. and Zha, Y. 2017. High pressure jet-grouting column installation effect in soft soil: Theoretical model and field application. *Computers and Geotechnics.* **88**, pp.74-94.

Liu, H., Zhou, H., Wang, Z. and Li, X. 2021. Theoretical Solution for Cavity Expansion in Crushable Soil. *International Journal of Geomechanics.* **21**(7), article no: 04021098 [no pagination].

Liu, K. and Chen, S. 2019. Analysis of cylindrical cavity expansion in anisotropic critical state soils under drained conditions. *Canadian Geotechnical Journal.* **56**(5), pp.675-686.

Liu, K., Wang, D. and Zheng, J. 2024. Determination of the coefficient of consolidation by piezocone tests under partially drained conditions. *Géotechnique.* **74**(9), pp.829-839.

Liu, S.-w., Zhang, Q.-q., Cui, W., Liu, G.-h. and Liu, J.-h. 2022. A simple method for analyzing thermomechanical response of an energy pile in a group. *Geomechanics for Energy and the Environment.* **32**, article no: 100309 [no pagination].

Liyanapathirana, D. 2009. Effect of penetration rate on piezocone tests in soft clay. In: *Proceedings of 62nd Canadian geotechnical society conference, Halifax, Canada*, pp.1070-1077.

Lomakin, V. 1960. One-Dimensional Problem of Temperature Stresses in an Elastoplastic Medium. *ARS Journal.* **30**(11), pp.1034-1036.

Lunne, T. 2012. The Fourth James K. Mitchell Lecture: The CPT in offshore soil investigations-a historic perspective. *Geomechanics and Geoengineering.* **7**(2), pp.75-101.

Lv, Z., Kong, G., Liu, H. and Ng, C.W. 2020. Effects of soil type on axial and radial thermal responses of field-scale energy piles. *Journal of Geotechnical and Geoenvironmental Engineering.* **146**(10), article no: 06020018 [no pagination].

Mafra, V. and Dienstmann, G. 2022. Cavity expansion solutions applied to help assess the partial drainage behavior characterization of the piezocone test. *Computers and Geotechnics.* **152**, article no: 105017 [no pagination].

Mahmoodzadeh, H. and Randolph, M.F. 2014. Penetrometer Testing: Effect of Partial Consolidation on Subsequent Dissipation Response. *Journal of Geotechnical and Geoenvironmental Engineering.* **140**(6), article no: 04014022 [no pagination].

Mahmoodzadeh, H., Wang, D. and Randolph, M.F. 2015. Interpretation of piezoball dissipation testing in clay. *Géotechnique.* **65**(10), pp.831-842.

Mahmoudi, H. and Atefi, G. 2012. Analytical solution for thermal stresses in a hollow cylinder under periodic thermal loading. *Proceedings of the Institution of Mechanical Engineers, Part C: Journal of Mechanical Engineering Science.* **226**(7), pp.1705-1724.

Mair, R.J. and Wood, D.M. 2013. *Pressuremeter testing: methods and interpretation.* Elsevier.

Manassero, M. 1989. Stress-strain relationships from drained self-boring pressuremeter tests in sand. *Geotechnique.* **39**(2), pp.293-307.

Mayne, P., Paniagua, P., Di Buò, B. and Agaiby, S. 2022. Evaluating geoparameters of Maine sensitive clay by CPTU. In: *Cone Penetration Testing 2022*. CRC Press, pp.552-558.

Mayne, P. and Peuchen, J. 2022. Undrained shear strength of clays from piezocone tests: A database approach. In: *Cone Penetration Testing 2022*. CRC Press, pp.546-551.

Mo, P.-Q., Chen, H. and Yu, H.-S. 2022. Undrained cavity expansion in anisotropic soils with isotropic and frictional destructuration. *Acta Geotechnica.* **17**(6), pp.2325-2346.

Mo, P.-Q., Gao, X.W., Yang, W. and Yu, H.S. 2020. A cavity expansion–based solution for interpretation of CPTu data in soils under partially drained conditions. *International Journal for Numerical and Analytical Methods in Geomechanics.* **44**(7), pp.1053-1076.

Mo, P.-Q., Marshall, A.M. and Yu, H.-S. 2014. Elastic-plastic solutions for expanding cavities embedded in two different cohesive-frictional materials. *International Journal for Numerical and Analytical Methods in Geomechanics.* **38**(9), pp.961-977.

Mo, P.-Q. and Yu, H.-S. 2017. Undrained cavity expansion analysis with a unified state parameter model for clay and sand. *Géotechnique.* **67**(6), pp.503-515.

Mo, P.-Q. and Yu, H.-S. 2018. Drained cavity expansion analysis with a unified state parameter model for clay and sand. *Canadian Geotechnical Journal.* **55**(7), pp.1029-1040.

Moheimani, R., Damadam, M., Nayebi, A. and Dalir, H. 2018. Thick-walled functionally graded material cylinder under thermo-mechanical loading. In: *2018 9th International Conference on Mechanical and Aerospace Engineering (ICMAE)*: IEEE, pp.505-510.

Monforte, L., Gens, A., Arroyo, M., Mánica, M. and Carbonell, J.M. 2021. Analysis of cone penetration in brittle liquefiable soils. *Computers and Geotechnics.* **134**, article no: 104123 [no pagination].

Moradshahi, A., Faizal, M., Bouazza, A. and McCartney, J.S. 2022. Thermomechanical Responses of Thermally Interacting Field-Scale Energy Piles. *International Journal of Geomechanics.* **22**(11), article no: 04022212 [no pagination].

Nabavi, S. and Shahani, A. 2009. Thermal stress intensity factors for a cracked cylinder under transient thermal loading. *International Journal of Pressure Vessels and Piping.* **86**(2-3), pp.153-163.

Nanda, S. and Patra, N.R. 2015. Undrained Cylindrical Cavity Expansion in Critical State Soils Considering Soil Structure. *Indian Geotechnical Journal.* **45**(2), pp.169-180.

Ng, C.W.W., Ma, Q. and Gunawan, A. 2016. Horizontal stress change of energy piles subjected to thermal cycles in sand. *Computers and Geotechnics.* **78**, pp.54-61.

Ng, C.W.W., Shi, C., Gunawan, A., Laloui, L. and Liu, H. 2015. Centrifuge modelling of heating effects on energy pile performance in saturated sand. *Canadian Geotechnical Journal.* **52**(8), pp.1045-1057.

Ng, C.W.W., Zhou, C. and Chiu, C.F. 2020. Constitutive modelling of state-dependent behaviour of unsaturated soils: an overview. *Acta Geotechnica.* **15**(10), pp.2705-2725.

Nguyen, V.T., Wu, N., Gan, Y., Pereira, J.-M. and Tang, A.M. 2019. Long-term thermo-mechanical behaviour of energy piles in clay. *Environmental Geotechnics.* **7**(4), pp.237-248.

Obrzud, R.F., Truty, A. and Vulliet, L. 2011. Numerical modeling and neural networks to identify model parameters from piezocone tests: I. FEM analysis of penetration in two-phase continuum. *International Journal for Numerical and Analytical Methods in Geomechanics.* **35**(16), pp.1703-1730.

Olgun, C.G., Ozudogru, T.Y. and Arson, C. 2014. Thermo-mechanical radial expansion of heat exchanger piles and possible effects on contact pressures at pile–soil interface. *Geotechnique Letters.* **4**, pp.170-178.

Orçan, Y. and Gamer, U. 1994. The elastic-plastic spherical shell with nonlinear hardening subject to a radial temperature gradient. *Acta mechanica.* **102**(1), pp.183-198.

Osinov, V.A. and Cudmani, R. 2001. Theoretical investigation of the cavity expansion problem based on a hypoplasticity model. *International Journal for Numerical and Analytical Methods in Geomechanics.* **25**(5), pp.473-495.

Ouyang, Y., Soga, K. and Leung, Y.F. 2011. Numerical back-analysis of energy pile test

at Lambeth College, London. *Geo-frontiers 2011: Advances in geotechnical engineering.* pp.440-449.

Ozturk, A. and Gulgec, M. 2011. Elastic–plastic stress analysis in a long functionally graded solid cylinder with fixed ends subjected to uniform heat generation. *International Journal of Engineering Science.* **49**(10), pp.1047-1061.

Ozudogru, T.Y., Olgun, C.G. and Arson, C.F. 2015. Analysis of friction induced thermo-mechanical stresses on a heat exchanger pile in isothermal soil. *Geotechnical and Geological Engineering.* **33**, pp.357-371.

Palmer, A. 1972. Undrained plane-strain expansion of a cylindrical cavity in clay: a simple interpretation of the pressuremeter test. *Geotechnique.* **22**(3), pp.451-457.

Pang, L., Chong, J., Zhang, C. and Shi, Z. 2023. Drained expansion analyses of a cylindrical cavity in sands incorporating the SANISAND model with fabric change effect. *Applied Mathematical Modelling.* **120**, pp.711-732.

Pang, L., Jiang, C. and Zhang, C. 2024. A rigorous analytical approach to predicting the load–settlement behavior of axially loaded piles embedded in sands incorporating the SANISAND model. *Acta Geotechnica.* **19**(6), pp.2823-2840.

Parvizi, A., Alikarami, S. and Asgari, M. 2016. Exact solution for thermoelastoplastic behavior of thick-walled functionally graded sphere under combined pressure and temperature gradient loading. *Journal of Thermal stresses.* **39**(9), pp.1152-1170.

Philippe, M., Bernier, M. and Marchio, D. 2009. Validity ranges of three analytical solutions to heat transfer in the vicinity of single boreholes. *Geothermics.* **38**(4), pp.407-413.

Potts, D.M. 2003. Numerical analysis: a virtual dream or practical reality? *Géotechnique.* **53**(6), pp.535-573.

Pournaghiazar, M., Russell, A.R. and Khalili, N. 2013. Drained cavity expansions in soils of finite radial extent subjected to two boundary conditions. *International Journal for*

Numerical and Analytical Methods in Geomechanics. **37**(4), pp.331-352.

Pournaghiazar, M., Russell, A.R. and Khalili, N. 2014. Cavity expansion in soil of finite radial extent. In: *Applied Mechanics and Materials*: Trans Tech Publ, pp.464-469.

Radu, V., Paffumi, E., Taylor, N. and Nilsson, K.-F. 2009. A study on fatigue crack growth in the high cycle domain assuming sinusoidal thermal loading. *International Journal of Pressure Vessels and Piping.* **86**(12), pp.818-829.

Radu, V., Taylor, N. and Paffumi, E. 2008. Development of new analytical solutions for elastic thermal stress components in a hollow cylinder under sinusoidal transient thermal loading. *International Journal of Pressure Vessels and Piping.* **85**(12), pp.885-893.

Randolph, M.F., Dolwin, R. and Beck, R. 1994. Design of driven piles in sand. *Géotechnique.* **44**(3), pp.427-448.

Randolph, M.F. and Hope, S. 2004. Effect of cone velocity on cone resistance and excess pore pressures. In: *Effect of cone velocity on cone resistance and excess pore pressures*: Yodogawa Kogisha Co. Ltd, pp.147-152.

Randolph, M.F. and Wroth, C.P. 1979. An analytical solution for the consolidation around a driven pile. *International Journal for Numerical and Analytical Methods in Geomechanics.* **3**(3), pp.217-229.

Rao, P.-P., Chen, Q., Li, L., Nimbalkar, S. and Cui, J. 2017. Elastoplastic solution for spherical cavity expansion in modified Cam-clay soil under drained condition. *International Journal of Geomechanics.* **17**(8), article no: 06017005 [no pagination].

Rash Ahmadi, S., Sheikhlou, M. and Gharebagh, V.M.J.A.m. 2011. Thermo-elastic/plastic semi-analytical solution of incompressible functionally graded spherical pressure vessel under thermo-mechanical loading. *Acta mechanica.* **222**(1), pp.161-173.

Reid, D. and Smith, K. 2021. Interpretation of state parameter in partially drained tailings: a case history examination. *Géotechnique Letters.* **11**(4), pp.276-280.

Robertson, P. and Campanella, R. 1983. Interpretation of cone penetration tests. Part II: Clay. *Canadian geotechnical journal.* **20**(4), pp.734-745.

Robertson, P., Sully, J., Woeller, D.J., Lunne, T., Powell, J. and Gillespie, D. 1992. Estimating coefficient of consolidation from piezocone tests. *Canadian Geotechnical Journal.* **29**(4), pp.539-550.

Rowe, P.W. 1962. The stress-dilatancy relation for static equilibrium of an assembly of particles in contact. *Proceedings of the Royal Society of London. Series A. Mathematical and Physical Sciences.* **269**(1339), pp.500-527.

Russell, A.R. and Khalili, N. 2006. On the problem of cavity expansion in unsaturated soils. *Computational mechanics.* **37**(4), pp.311-330.

Russell, A.R., Wang, Y. and Khalili, N. 2023. Cavity expansions in partially drained soils and a comparison to CPT results. *Computers and Geotechnics.* **158**, article no: 105381 [no pagination].

Saeedi, S., Kholdi, M., Loghman, A., Ashrafi, H. and Arefi, M. 2021. Thermo-elasto-plastic analysis of thick-walled cylinder made of functionally graded materials using successive approximation method. *International Journal of Pressure Vessels and Piping.* **194**, article no: 104481 [no pagination].

Saggu, R. and Chakraborty, T. 2015. Cyclic thermo-mechanical analysis of energy piles in sand. *Geotechnical and Geological Engineering.* **33**, pp.321-342.

Şahin, A.Z. 1995. Analytical solutions of transient heat conduction in semi-infinite solid with time varying boundary conditions by means of similarity transformation. *International communications in heat and mass transfer.* **22**(1), pp.89-97.

Salgado, R., Mitchell, J.K. and Jamiolkowski, M. 1998. Calibration chamber size effects on penetration resistance in sand. *Journal of Geotechnical and Geoenvironmental Engineering.* **124**(9), pp.878-888.

Schmitt, N., Baquet, E., Guillo, P. and Blond, E. 2007. Thermal stresses in a Drucker

Prager elastoplastic hollow cylinder subjected to thermal shock: influence of material and structure parameters. In: *Thermal Stresses 2007*: NTUST, pp.771-774.

Schnaid, F., Dienstmann, G., Odebrecht, E. and Maghous, S. 2020. A simplified approach to normalisation of piezocone penetration rate effects. *Géotechnique.* **70**(7), pp.630-635.

Schnaid, F. and Houlsby, G.T. 1991. An assessment of chamber size effects in the calibration of in situ tests in sand. *Géotechnique.* **41**(3), pp.437-445.

Schneider, J.A., Lehane, B.M. and Schnaid, F. 2007. Velocity effects on piezocone measurements in normally and over consolidated clays. *International Journal of Physical Modelling in Geotechnics.* **7**(2), pp.23-34.

Schrefler, B. 1984. *The finite element method in soil consolidation*. Ph.D. thesis, University College of Swansea.

Shahani, A. and Nabavi, S. 2007. Analytical solution of the quasi-static thermoelasticity problem in a pressurized thick-walled cylinder subjected to transient thermal loading. *Applied mathematical modelling.* **31**(9), pp.1807-1818.

Shao, Z.S. and Ma, G. 2008. Thermo-mechanical stresses in functionally graded circular hollow cylinder with linearly increasing boundary temperature. *Composite Structures.* **83**, pp.259-265.

Sheng, D. 2011. Review of fundamental principles in modelling unsaturated soil behaviour. *Computers and Geotechnics.* **38**(6), pp.757-776.

Sheng, D., Fredlund, D.G. and Gens, A. 2008. A new modelling approach for unsaturated soils using independent stress variables. *Canadian Geotechnical Journal.* **45**(4), pp.511-534.

Sheng, D., Kelly, R., Pineda, J. and Bates, L. 2014. Numerical study of rate effects in cone penetration test. In: *3rd international symposium on cone penetration testing, Las Vegas, Nevada, USA*. The CPT'14 Organizing Committee, pp.419-428.

Sheng, D., Sloan, S.W., Gens, A. and Smith, D.W. 2003. Finite element formulation and algorithms for unsaturated soils. Part I: Theory. *International journal for numerical and analytical methods in geomechanics.* **27**(9), pp.745-765.

Sheng, D., Sloan, S.W. and Yu, H.-S. 2000. Aspects of finite element implementation of critical state models. *Computational Mechanics.* **26**(2), pp.185-196.

Shi, X. and Shang, X. 2014. Growth of a spherical micro-void in an infinite elastoplastic body under thermal load. *Acta Mechanica.* **225**(11), pp.3237-3245.

Silva, M.F., White, D.J. and Bolton, M.D. 2006. An analytical study of the effect of penetration rate on piezocone tests in clay. *International journal for numerical and analytical methods in geomechanics.* **30**(6), pp.501-527.

Silvestri, V. 2001. Interpretation of pressuremeter tests in sand. *Canadian Geotechnical Journal.* **38**(6), pp.1155-1165.

Silvestri, V. and Abou-Samra, G. 2011. Application of the exact constitutive relationship of modified Cam clay to the undrained expansion of a spherical cavity. *International Journal for Numerical and Analytical Methods in Geomechanics.* **35**(1), pp.53-66.

Silvestri, V. and Abou-Samra, G. 2012. Analytical solution for undrained plane strain expansion of a cylindrical cavity in modified cam clay. *Geomechanics and Engineering.* **4**(1), pp.19-37.

Silvestri, V. and Tabib, C. 2018. Application of cylindrical cavity expansion in MCC model to a sensitive clay under K o consolidation. *Journal of Materials in Civil Engineering.* **30**(8), article no: 04018155 [no pagination].

Sim, L., Yeo, W., Purbolaksono, J., Saw, L. and Tey, J. 2021. Analytical solution of thermo-mechanical stresses of multi-layered hollow spherical pressure vessel. *International Journal of Pressure Vessels and Piping.* **191**, article no: 104355 [no pagination].

Sivasithamparam, N. and Castro, J. 2018. Undrained expansion of a cylindrical cavity in

clays with fabric anisotropy: theoretical solution. *Acta Geotechnica.* **13**(3), pp.729-746.

Sivasithamparam, N. and Castro, J. 2020. Undrained cylindrical cavity expansion in clays with fabric anisotropy and structure: Theoretical solution. *Computers and Geotechnics.* **120**, article no: 103386 [no pagination].

Sladen, J. 1989. Problems with interpretation of sand state from cone penetration test. *Géotechnique.* **39**(2), pp.323-332.

Sladen, J., D'hollander, R. and Krahn, J. 1985. The liquefaction of sands, a collapse surface approach. *Canadian geotechnical journal.* **22**(4), pp.564-578.

Sloan, S.W. 2013. Geotechnical stability analysis. *Géotechnique.* **63**(7), pp.531-572.

Soderberg, L.O. 1962. Consolidation theory applied to foundation pile time effects. *Geotechnique.* **12**(3), pp.217-225.

Song, X.-G., Yang, H., Yue, H.-Y., Guo, X., Yu, H.-S. and Zhuang, P.-Z. 2022. Closed-form solutions for large strain analysis of cavity contraction in a bounded Mohr-Coulomb medium. *European Journal of Environmental and Civil Engineering.* **26**(10), pp.4548-4575.

Sosnoski, J. 2016. *Interpretation of CPTU and DMT tests in intermediate permeability soils*. Master thesis, Universidade Federal do Rio Grande do Sul.

Stewart, M.A. and McCartney, J.S. 2014. Centrifuge modeling of soil-structure interaction in energy foundations. *Journal of Geotechnical and Geoenvironmental Engineering.* **140**(4), article no: 04013044 [no pagination].

Su, D. 2021. Drained solution for cylindrical cavity expansion in modified Cam Clay soil under constant vertical stress. *Canadian Geotechnical Journal.* **58**(2), pp.176-189.

Sun, D.A., Matsuoka, H., Yao, Y.-P. and Ichihara, W. 2000. An Elasto-Plastic Model for Unsaturated Soil in Three-Dimensional Stresses. *Soils and Foundations.* **40**(3), pp.17-28.

Sun, D.A., Sheng, D. and Sloan, S.W. 2007. Elastoplastic modelling of hydraulic and

stress–strain behaviour of unsaturated soils. *Mechanics of Materials.* **39**(3), pp.212-221.

Suzuki, Y. 2015. *Investigation and interpretation of cone penetration rate effects*. Ph.D. thesis, University of Western Australia Crawley, Australia.

Takabi, B. 2016. Thermomechanical transient analysis of a thick-hollow FGM cylinder. *Engineering Solid Mechanics.* **4**(1), pp.25-32.

Talaee, M., Alizadeh, M. and Bakhshandeh, S. 2014. An exact analytical solution of non-Fourier thermal stress in cylindrical shell under periodic boundary condition. *Engineering Solid Mechanics.* **2**(4), pp.293-302.

Teh, C. and Houlsby, G. 1991. An analytical study of the cone penetration test in clay. *Géotechnique.* **41**(1), pp.17-34.

Teixeira, M., Zilio, G., Mortean, M., de Paiva, K. and Oliveira, J. 2023. Experimental and numerical analysis of transient thermal stresses on thick-walled cylinder. *International Journal of Pressure Vessels and Piping.* **202**, p104884 article no: 104884 [no pagination].

Temesgen, A., Singh, S. and Pankaj, T. 2021. Elastoplastic analysis in functionally graded thick-walled rotating transversely isotropic cylinder under a radial temperature gradient and uniform pressure. *Mathematics and Mechanics of Solids.* **26**(1), pp.5-17.

Thakur, P. and Sethi, M. 2020. Elastoplastic deformation in an orthotropic spherical shell subjected to a temperature gradient. *Mathematics and Mechanics of Solids.* **25**(1), pp.26-34.

Tian, G., Yang, C. and Li, J. 2024. Coupled thermomechanical analysis for cavity expansion under non-isothermal conditions. *Computers and Geotechnics.* **168**, article no: 106120 [no pagination].

Vaughan, P.R. 1994. Assumption, prediction and reality in geotechnical engineering. *Géotechnique.* **44**(4), pp.573-609.

Vesic, A.S. 1972. Expansion of cavities in infinite soil mass. *Journal of Soil Mechanics*

and Foundations Division. **98**(SM3), pp.265-290.

Vrakas, A. 2016. A rigorous semi-analytical solution for undrained cylindrical cavity expansion in critical state soils. *International Journal for Numerical and Analytical Methods in Geomechanics.* **40**(15), pp.2137-2160.

Wang, C.-L., Zhou, H., Liu, H.-L. and Ding, X.-M. 2022. Analysis of undrained spherical cavity expansion in modified Cam Clay of finite radial extent. *European Journal of Environmental and Civil Engineering.* **26**(3), pp.952-963.

Wang, H., Li, L. and Li, J. 2022a. A numerical investigation on undrained expansion of a cylindrical cavity under biaxial in situ stresses using anisotropic S‐CLAY1 model. *International Journal for Numerical and Analytical Methods in Geomechanics.* **46**(18), pp.3402-3424.

Wang, H., Yang, C. and Li, J. 2022b. Spherical cavity expansion in overconsolidated unsaturated soil under constant suction condition. *Geomechanics and Engineering.* **29**(1), pp.1-11.

Wang, X. and Chen, S. 2022. Revisiting undrained cavity expansion problem in critical state soils: A simple graph‐based approach. *International Journal for Numerical and Analytical Methods in Geomechanics.* **46**(12), pp.2356-2374.

Wang, Y. and Russell, A.R. 2023. Cavity expansions in two silty tailings with high degrees of saturation and a comparison to CPT results. *Computers and Geotechnics.* **164**, article no: 105682 [no pagination].

Wang, Y., Zhang, F., Liu, F. and Wang, X. 2024. Full-scale in situ experimental study on the bearing capacity of energy piles under varying temperature and multiple mechanical load levels. *Acta Geotechnica.* **19**(1), pp.401-415.

Wang, Z.-F., Shen, S., Modoni, G. and Zhou, A. 2020. Excess pore water pressure caused by the installation of jet grouting columns in clay. *Computers and Geotechnics.* **125**,

article no: 103667 [no pagination].

Wheeler, S., Sharma, R. and Buisson, M. 2003. Coupling of hydraulic hysteresis and stress–strain behaviour in unsaturated soils. *Géotechnique.* **53**(1), pp.41-54.

Wroth, C.P. 1984. The interpretation of in situ soil tests. *Géotechnique.* **34**(4), pp.449-489.

Wu, S.-S. 1997. Analysis on transient thermal stresses in an annular fin. *Journal of thermal stresses.* **20**(6), pp.591-615.

Xiong, Z., Li, X., Zhao, P., Zhang, D. and Dong, S. 2021. An in-situ experimental investigate of thermo-mechanical behavior of a large diameter over length energy pile. *Energy and Buildings.* **252**, article no: 111474 [no pagination].

Yang, C., Chen, H. and Li, J. 2020. Drained cylindrical cavity expansion analysis in anisotropic soils considering 3D strength. *Géotechnique Letters.* **10**(2), pp.346-352.

Yang, C., Li, J., Li, L. and Sun, D.A. 2021. Expansion responses of a cylindrical cavity in overconsolidated unsaturated soils: A semi-analytical elastoplastic solution. *Computers and Geotechnics.* **130**, article no: 103922 [no pagination].

Yang, H., Yu, H.-S., Chen, X. and Zhuang, P.-Z. 2023. Rigorous solution for drained analysis of spherical cavity expansion in soils of finite radial extent. *Computers and Geotechnics.* **160**, article no: 105516 [no pagination].

Yazdani, S., Helwany, S. and Olgun, G. 2019. Investigation of thermal loading effects on shaft resistance of energy pile using laboratory-scale model. *Journal of Geotechnical and Geoenvironmental Engineering.* **145**(9), article no: 04019043 [no pagination].

Yi, J., Goh, S., Lee, F. and Randolph, M.F. 2012. A numerical study of cone penetration in fine-grained soils allowing for consolidation effects. *Géotechnique.* **62**(8), pp.707-719.

Yu, H.-S. 1992. Expansion of a thick cylinder of soils. *Computers and Geotechnics.* **14**(1), pp.21-41.

Yu, H.-S. 1993. Finite elastoplastic deformation of an internally pressurized hollow

sphere. *Acta Mech Solida Sinica.* **6**(1), pp.81-97.

Yu, H.-S. 1994. State parameter from self-boring pressuremeter tests in sand. *Journal of Geotechnical Engineering.* **120**(12), pp.2118-2135.

Yu, H.-S. 1996. Interpretation of pressuremeter unloading tests in sands. *Géotechnique.* **46**(1), pp.17-31.

Yu, H.-S. 2000. *Cavity expansion methods in geomechanics.* Springer Science & Business Media.

Yu, H.-S. 2007. *Plasticity and geotechnics.* Springer Science & Business Media.

Yu, H.-S. and Carter, J.P. 2002. Rigorous similarity solutions for cavity expansion in cohesive-frictional soils. *International Journal of Geomechanics.* **2**(2), pp.233-258.

Yu, H.-S. and Houlsby, G.T. 1991. Finite cavity expansion in dilatant soils: loading analysis. *Géotechnique.* **41**(2), pp.173-183.

Yu, H.-S. and Mitchell, J.K. 1998. Analysis of cone resistance: review of methods. *Journal of Geotechnical and Geoenvironmental Engineering.* **124**(2), pp.140-149.

Zhang, Q., He, W., Wang, H.-Y., Liu, R.-C., Lu, M.-M. and Jiang, B.-S. 2021. Elasto-plastic solutions for expanding cavities in strain-hardening and/or softening soils. *Tunnelling and Underground Space Technology.* **107**, article no: 103660 [no pagination].

Zhang, Y., Wang, H., Liu, T., Liu, H. and Deng, S. 2022. Interpretation of pore pressure dissipation of CPTu in intermediate soil considering partial drainage effect. *Ocean Engineering.* **266**, article no: 112956 [no pagination].

Zhou, H., Kong, G.-Q. and Liu, H.-L. 2016a. Pressure-controlled elliptical cavity expansion under anisotropic initial stress: Elastic solution and its application. *Science China Technological Sciences.* **59**(7), pp.1100-1119.

Zhou, H., Kong, G., Liu, H. and Laloui, L. 2018. Similarity solution for cavity expansion in thermoplastic soil. *International Journal for Numerical and Analytical Methods in*

Geomechanics. **42**(2), pp.274-294.

Zhou, H., Kong, G., Liu, H., Wu, Y. and Li, G. 2016b. A novel cavity expansion-based analytical tool and its potential application for energy pile foundation. In: *Proceedings of the 1st International Conference on Energy Geotechnics, ICEGT*, pp.359-365.

Zhou, H., Liu, H. and Li, Y. 2019. Analysis of dynamic spherical cavity expansion in undrained modified Cam Clay soil. *International Journal for Numerical and Analytical Methods in Geomechanics.* **43**(9), pp.1686-1703.

Zhou, H., Liu, H. and Wang, Z. 2022a. A semi-analytical solution for displacement-controlled elliptical cavity expansion in undrained MCC soil. *International Journal for Numerical and Analytical Methods in Geomechanics.* **46**(2), pp.339-373.

Zhou, H., Liu, H., Wang, Z. and Ding, X. 2021a. A unified and rigorous solution for quasi-static cylindrical cavity expansion in plasticity constitutive models. *Computers and Geotechnics.* **135**, article no: 104162 [no pagination].

Zhou, H., Sheil, B. and Liu, H. 2022b. Noncircular Cavity Expansion in Undrained Soil: Semi-Analytical Solution. *Journal of Engineering Mechanics.* **148**(7), article no: 04022032 [no pagination].

Zhou, H., Wang, Z., Liu, H., Shen, H. and Ding, X. 2021b. Undrained Cylindrical and Spherical Cavity Expansion in Elastic-Viscoplastic Soils. *Canadian Geotechnical Journal.* **58**(10), pp.1543-1557.

Zhou, Y., Kong, G. and Yang, Q. 2022. Field performances of energy pile based on the secondary utilization of sonic logging pipes. *Geomechanics for Energy and the Environment.* **32**, article no: 100280 [no pagination].

Zhuang, P.-Z. 2017. *Cavity expansion analysis with applications to cone penetration test and root-soil interaction*. Ph.D. thesis, University of Nottingham.

Zhuang, P.-Z., Sun, E.-C., Zhang, J.-L., Wu, Z.-X., Yu, H.-S. and Yang, H. 2024. CASM-

U: a unified critical state model for unsaturated clays and sands. *Acta Geotechnica.*

Zhuang, P.-Z. and Yu, H.-S. 2018. Uplift resistance of horizontal strip anchors in sand: a cavity expansion approach. *Géotechnique Letters.* **8**(4), pp.284-289.

Zhuang, P.-Z., Yu, H.-S., Mooney, S.J. and Mo, P.-Q. 2021. Loading and unloading of a thick-walled cylinder of critical-state soils: large strain analysis with applications. *Acta Geotechnica.* **16**, pp.237-261.